

**STRATEGIES FOR SELECTING COMPUTATIONAL PROTOCOLS IN
SUPPORT OF SMALL MOLECULE STRUCTURAL ANALYSIS BY ION
MOBILITY-MASS SPECTROMETRY**

SARAH MARKLEY STOW

Dissertation

Submitted to the Faculty of the
Graduate School of Vanderbilt University
in partial fulfillment of the requirements

for the degree of

DOCTOR OF PHILOSOPHY

in

Chemistry

August 2015

Nashville, Tennessee

Professor John A. McLean

Professor Terry P. Lybrand

Professor Brian O. Bachmann

Professor David M. Hercules

Professor Larry J. Marnett

ACKNOWLEDGEMENTS

I would like to thank my dissertation advisor, Dr. John A. McLean, for providing me with the opportunity to perform research within his laboratory and to pursue projects that are, at times, outside of the realm of the laboratory's focus. I am very thankful for his mentorship and collaborative skills that have provided the research group with countless opportunities.

I would also like to thank Dr. Terry P. Lybrand and Dr. David M. Hercules for their co-mentorship on many of my research projects. Dr. Lybrand's wealth of computational knowledge has been extremely beneficial over the years, and I am still amazed at how much I still learn from him during our meetings while discussing my research projects. I am also very grateful for the collaborative work I have performed with Dr. Hercules. I have enjoyed investigating polymer chemistry as well as many other aspects of the academic process with him.

Additionally, I would like to thank Dr. Brian O. Bachmann and Dr. Larry J. Marnett for serving on my dissertation committee. Our weekly subgroup meetings with Dr. Bachmann were particularly helpful during my early years in graduate school. I would also like to thank Dr. Marnett for his foresight in founding the Vanderbilt Institute of Chemical Biology, an organization that has made several of my collaborations possible.

I would like to thank all of my fellow McLean Group lab members for moving outside of their comfort zone to discuss my theoretical research and for helping me extensively when I moved outside of mine and attempted experimental research in the laboratory. In particular, Dr. Cody R. Goodwin, Dr. Michal Kliman, and Dr. Jody C. May

were especially useful when starting my dissertation project and have engaged in many theoretical discussions on IM research. Dr. Jay G. Forsythe and Ms. Nichole M. Lareau have provided significant experimental support for my theoretical calculations.

I would also like to thank my family and friends for being so supportive throughout this journey. They have been there to help me make tough decisions, listen to me complain, and celebrate major milestones in my graduate school career. Without each of them supporting me along the way I would not be where I am today.

Finally, I would like to thank the sources of funding that have made my research possible: the Vanderbilt University College of Arts and Sciences, the Vanderbilt Institute of Chemical Biology, the Vanderbilt Institute of Integrative Biosystems Research and Education, the National Institutes for Health (R01GM092218, UH2TR00491, S10RR019022), the Defense Threat Reduction Agency (HDTRA1-09-1-0013, DTRA100271 A-5186, DE-001165), the Defense Advanced Research Projects Agency (DARPA-11-73-MPSys-FP-011, W911NF-12-2-0036).

TABLE OF CONTENTS

ACKNOWLEDGEMENTS	ii
LIST OF TABLES	vi
LIST OF FIGURES	vii
LIST OF ABBREVIATIONS	ix
Chapter	
1. STRUCTURALLY INTERPRETING ION MOBILITY-MASS SPECTROMETRY WITH COMPUTATIONAL STRATEGIES	1
1.1. Ion Mobility-Mass Spectrometry	1
1.1.1. Instrumentation Arrangements.....	2
1.1.1.1. Fragmentation Capabilities	4
1.1.1.2. Ion Mobility Analyzes	5
1.2. Experimental Collision Cross Section Determination	6
1.3. Theoretical Collision Cross Section Determination	8
1.4. Computational Conformational Space Sampling.....	13
1.5. Applications	18
1.5.1. Polymers	20
1.5.2. Natural Products.....	21
1.5.3. Metabolites.....	23
1.6. Conclusion and Objectives	25
1.7. Acknowledgements.....	26
1.8. References.....	27
2. STRUCTURAL CHARACTERIZATION OF METHYLENEDIANILINE REGIOISOMERS BY ION MOBILITY-MASS SPECTROMETRY TANDEM MASS SPECTROMETRY, AND COMPUTATIONAL STRATEGIES	48
2.1. Introduction.....	48
2.2. Experimental Section.....	52
2.3. Results and Discussion for 2-Ring MDA	56
2.4. Results and Discussion for 3-Ring and 4-Ring MDA	73
2.5. Conclusions.....	89
2.6. Acknowledgements.....	92
2.7. References.....	93
3. DISTANCE GEOMETRY PROTOCOL TO GENERATE CONFORMATIONS OF NATURAL PRODUCTS AND METABOLITES TO STRUCTURALLY	

INTERPRET ION MOBILITY-MASS SPECTROMETRY COLLISION CROSS SECTIONS	98
3.1. Introduction.....	98
3.2. Experimental Section.....	101
3.3. Results and Discussion	107
3.4. Conclusions.....	119
3.5. Acknowledgements.....	120
3.6. References.....	121
4. OBTAINING THEORETICAL COLLISION CROSS SECTION RANGES FOR LARGE SETS OF METABOLITES TO AID IN IDENTIFICATION BY ION MOBILITY-MASS SPECTROMETRY	125
4.1. Introduction.....	125
4.2. Experimental Section.....	128
4.3. Results and Discussion	130
4.4. Conclusions.....	144
4.5. Acknowledgments.....	145
4.6. References.....	146
5. CONCLUSIONS AND FUTURE DIRECTIONS	149
5.1. Summary	149
5.2. Future Directions	150
5.2.1. Characterization of Methylenedianiline.....	150
5.2.2. Distance Geometry Applications	152
5.3. Conclusions.....	154
APPENDIX	
A. References of Adaption for Chapters.....	156
B. Supplementary Materials for Chapter II	157
C. Supplementary Materials for Chapter III.....	216
D. Supplementary Materials for Chapter IV.....	262
E. Curriculum Vitae	272

LIST OF TABLES

Table 1.1	Structural IM-MS Studies Combined with Computational Methods	16
Table 1.2	IM-MS Studies of Metabolites	24
Table 2.1	Structures of MDA Fragments.....	59
Table 2.2	CCS values of 2-Ring MDA.....	62
Table 2.3	CCS values of 3-Ring and 4-Ring MDA	78
Table 3.1	Representative IM-MS Structural Studies	99
Table 3.2	Advantages and Challenges for Distance Geometry and MD Strategies	116
Table 4.1	List of Metabolites Investigated	131
Table 4.2	Sources of Error for CCS Calculations	139

LIST OF FIGURES

Figure 1.1	IM-MS Instrument Schematics.....	3
Figure 1.2	Theoretical CCS Calculation Methods.....	9
Figure 1.3	IM-MS Biological Class Separation and Trends.....	19
Figure 1.4	PCA Plots of Synthesized Compounds and Natural Products.....	22
Figure 2.1	Structures of 2-Ring, 3-Ring, and 4-Ring MDA Isomers	49
Figure 2.2	Mass Spectra and Tandem Mass Spectra for 2-Ring MDA	57
Figure 2.3	Collision Induced Dissociation Curves for 2-Ring MDA	61
Figure 2.4	IM Traces and Conformational Sampling Plots for 2-Ring MDA	65
Figure 2.5	Collisionally Activated CCS Profiles for 2-Ring MDA.....	66
Figure 2.6	Cluster Representative Conformers for 2-Ring MDA Isomers.....	69
Figure 2.7	Fragmentation Mechanisms for 2-Ring MDA Isomers.....	71
Figure 2.8	Mass Spectra and Tandem Mass Spectra for 3- and 4-Ring MDA	74
Figure 2.9	CCS Profiles and CID Curves for 3- and 4-Ring MDA	76
Figure 2.10	IM Traces and Conformational Sampling Plots for 3- and 4-Ring MDA...80	
Figure 2.11	Cluster Representative Conformers for 3- and 4-Ring MDA	83
Figure 2.12	Fragmentation Mechanisms for 3- and 4-Ring MDA Isomers.....	87
Figure 3.1	Workflow for Distance Geometry and MD Sampling Approaches	102
Figure 3.2	Structures of Natural Products.....	108
Figure 3.3	Histogram Comparing CPU Time	110
Figure 3.4	Conformational Space Plots for Natural Products.....	112
Figure 3.5	IM Traces with Suggested Structures of Natural Products	114
Figure 4.1	Comparison of DTIM Experimental CCS with Theoretical CCS	133

Figure 4.2	Comparison of TWIM Experimental CCS with Theoretical CCS	135
Figure 4.3	Structures of Disagreeing Metabolites	137
Figure 4.4	Time Histogram for Distance Geometry Calculation.....	143
Figure 5.1	MALDI Spectra of 2-Ring, 3-Ring, and 4-Ring MDA	151
Figure 5.2	Comparison of CCS Experiment and Theory for Negative Ions.....	153

LIST OF ABBREVIATIONS

CCS	Collision Cross Section
CID	Collision Induced Dissociation
COM	Center of Mass
DFT	Density Functional Theory
DTIM	Drift Time Ion Mobility
ESI	Electrospray Ionization
ETMD	Elevated Temperature Molecular Dynamics
eV	Electron volts
GAFF	General Amber Force Field
IM	Ion Mobility
IM-MS	Ion Mobility-Mass Spectrometry
IM-MS/MS	Ion Mobility-Tandem Mass Spectrometry
MALDI	Matrix Assisted Laser Desorption Ionization
MD	Molecular Dynamics
MDA	Methylenedianiline
MDI	Methylene Diphenyl Diisocyanate
MMFF94x	Merck Molecular Force Field 94x
MS	Mass Spectrometry
MS/MS	Tandem Mass Spectrometry
M/Z	Mass-to-charge ratio
NMR	Nuclear Magnetic Resonance
PSA	Projection Superposition Approximation

QM	Quantum Mechanics
RESP	Restrained Electrostatic Potential
RMSD	Root Mean Squared Deviation
TM	Trajectory Method
TOF	Time of Flight
TWIM	Traveling Wave Ion Mobility

CHAPTER 1

STRUCTURALLY INTERPRETING ION MOBILITY-MASS SPECTROMETRY WITH COMPUTATIONAL STRATEGIES

1.1. Ion Mobility-Mass Spectrometry

Mass spectrometry (MS) is an analytical tool that separates gas phase ions based on their mass-to-charge ratio (m/z). While MS alone is a very powerful analytical tool, it greatly benefits from its ability to easily combine with other separation techniques. A separation technique that is often paired with MS is ion mobility (IM). IM is an electrophoretic separation where differential diffusion of ions occurs based on their gas phase structure. This additional measurement not only provides another dimension of separation, but also allows this analytical technique to offer structural information.¹⁻³

As the gas phase ions transverse the IM drift tube filled with a neutral buffer gas, the ions experience a number of elastic interactions based on the size of the ion. Smaller ions transverse the drift tube faster because they have fewer collisions with the buffer gas thus resulting in shorter drift times. As discussed in greater detail later in this chapter, a collision cross section (CCS) value is then calculated from the IM drift time measurements to provide a rotationally averaged surface area of the gas phase ion. This value allows for comparison with theoretically generated conformations to provide more detailed structural information.

This introductory chapter aims to discuss the analytical abilities of IM-MS as well as the theoretical methodology and techniques that allow this analytical separation technique to offer structural information. In Section 1.1, different orientations of IM-MS

instruments, as well as different IM analyzers, are discussed. How structural information is obtained from an IM-MS measurement is discussed in Section 1.2. Determination of a CCS from a theoretical conformation is described in Section 1.3. Computational methods that are utilized in support of structural IM-MS studies are discussed in Section 1.4. Section 1.5 discusses the applications of combining IM-MS experimental measurements with theoretical computational modeling. Finally, Section 1.6 concludes with a summary and description of the objectives of this dissertation research.

1.1.1. Instrumentation Arrangements

Because both IM and MS separations occur in the gas phase, IM-MS allows for some versatility in the ordering and arrangements of the IM and MS separations due to their correlation. Depending on the particular experimental goals, a number of configurations are possible. Generally, IM-MS instruments contain an ion source, ion mobility analyzer, and a mass analyzer. For IM-MS measurements, soft ionization sources such as electrospray ionization (ESI) or matrix assisted laser desorption ionization (MALDI) are typically utilized. Soft ionization sources generate gas phase ions while maintaining the structural integrity of the molecule. The three specific instrumentation arrangements that are used in this work are displayed in Figure 1.1. Prior to the first commercially available IM-MS instrument in 2006, most IM-MS measurements were obtained on instruments similar to the one shown in Figure 1.1a. The version of this instrument in our laboratory contains interchangeable ESI and MALDI ion sources followed by a ion mobility drift tube and time of flight (TOF) mass analyzer.⁴ The first commercially available IM-MS from Waters Corporation (Milford, MA) is

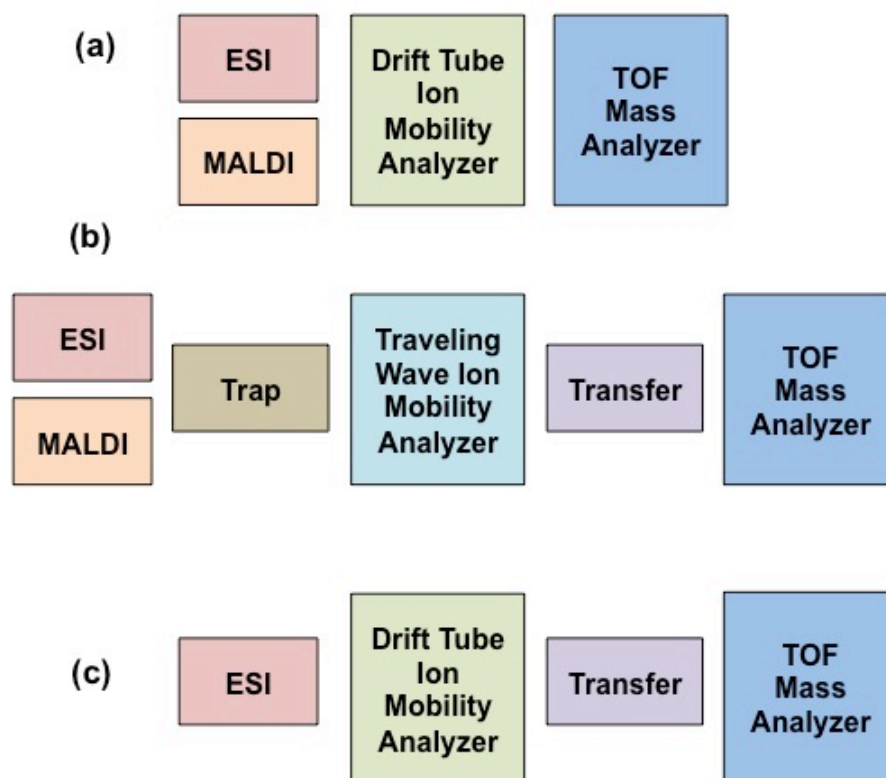


Figure 1.1. Instrument schematics are shown for the three IM-MS arrangements used in this work. In a) an older uniform field IM-MS instrument is shown; in b) a traveling wave IM-MS instrument is shown; and in c) a uniform field IM-MS instrument is shown. Each of these instrument schematics provides unique possibilities for structural IM-MS studies.

shown in Figure 1.1b.^{5,6} This instrument contains interchangeable ESI and MALDI ion sources followed an ion mobility analyzer and a TOF mass analyzer. This instrument platform also contains ion fragmentation cells both before and after the drift cell. Agilent Technologies (Santa Clara, CA) released the second commercially available IM-MS in 2014 and is shown in Figure 1.1c.^{7,8} This instrument contains an ESI ion source followed by an ion mobility drift tube, and TOF mass analyzer. The experimental work in Chapter III was performed on the instrument in Figure 1.1a. The experimental work in Chapter II and Chapter IV was performed on the instruments in Figure 1.1b,c. There are a few differences between the instruments shown in Figure 1.1b,c that deserve special mention due to how they affect structural IM-MS measurements.

1.1.1.1. Fragmentation Capabilities

Tandem mass spectrometry (MS/MS) allows for fragmentation between consecutive mass spectrometry experiments. Fragmentation studies can elucidate two-dimensional structural information of molecular species as well as aid in identifying fragmentation mechanisms. The orientations of the IM-MS instruments described in the previous section provide different fragmentation capabilities. Both IM-MS instruments in Figure 1.1b,c allow for fragmentation after the ion mobility analyzer. This feature allows fragment ions to be traced back to precursor ions through alignment on m/z to drift time plots. This approach is useful for identifying fragments in complicated spectra where knowledge of the precursor ion is particularly useful. The instrument in Figure 1.1b also allows for fragmentation before the ion mobility analyzer. This arrangement allows for mobility data to be collected for the individual fragment ions. This provides mobility as

well as mass information to be collected for each fragment ion, which is also very helpful in identifying fragment species.

1.1.1.2. Ion Mobility Analyzers

There are two types of ion mobility analyzers used in the IM-MS instruments discussed above. A uniform field or an electrostatic drift tube is used in the instruments in Figure 1.1a,c thus terming these instruments as drift tube ion mobility (DTIM). A traveling wave or electrodynamic ion mobility analyzer is used in Figure 1.1b thus terming this instrument traveling wave ion mobility (TWIM). These IM analyzers differ in how the electric field is applied across the drift cell. In DTIM a constant electric field is applied that moves the ions through the drift cell. With TWIM, the electric field is applied in the form of waves that move the ions through the drift cell. While both of these methods provide separation of gas phase ions, CCS values can only be directly derived from DTIM measurements. This is because the kinetic theory of gases, which is discussed in the next section, requires that the drift times be obtained in a uniform electric field. While the kinetic theory of gases cannot be directly applied to TWIM measurements, CCS values can be obtained through the use of calibration standards.⁹

In addition to the nature of the electric field in each of these drift tubes, they also allow for different drift gases. Helium as a buffer gas will arguably provide the most accurate structural information due to its small size and small polarizability. The small size of helium allows it to sample more details on the conformational surface of the ion. The polarizability of the buffer gas is a concern because a larger polarizability will result

in inelastic interactions between the buffer gas and ion, which is not accounted for in the kinetic theory of gases. While nitrogen, argon, and carbon dioxide can provide different IM separations, they are not ideal for purely structural studies. DTIM can utilize any drift gas, while TWIM will not operate successfully with helium. The traveling wave that provides the separation requires a larger buffer gas for the traveling wave to push the ions through the drift tube. Structural information is still obtainable in different drift gases, but currently only helium and nitrogen can be compared to theoretically calculated CCS values for computationally generated conformations. It is important to remember the effects that polarizability may have on gas phase ions when correlating between the experimental and theoretical values.

1.2. Experimental Collision Cross Section Determination

In an ion mobility experiment, separation occurs as ions traverse the electric field and collide with neutral gas molecules based on the prevailing physical properties of ion charge state and ion surface area. The number of collisions with neutral gas molecules is proportional to the rotationally-averaged ion surface area (\AA^2), which is directly related to the ion's structure and termed the ion-neutral CCS. Under the assumptions that these ion-neutral collisions are brief and elastic, the kinetic theory of gases can be used to derive an equation relating the IM measurement and separation parameters to CCS.

The drift velocity (v_d) of an ion through the drift cell is defined by the length of the drift cell (L) and the drift time (t_d) of the ion. Under the condition that the electrostatic field is weak, the ion velocity through the neutral gas can also be defined in terms of the ion's mobility constant (K) and the electrostatic field strength (E):

$$v_d = \frac{L}{t_d} = KE \quad (1)$$

When the electrostatic field is sufficiently weak (*i.e.* low-field conditions) and a Maxwell distribution can be used to describe the thermodynamic equilibrium of ion velocities, the mean thermal velocity is:

$$v_{mean} = \left(\frac{8k_B T}{\pi M_r} \right)^{\frac{1}{2}} \quad (2)$$

where k_b is the Boltzmann constant, T is the temperature of the gas in Kelvins, and M_r is the molar mass of the drift gas. The remainder of the ion velocity is accounted for by a minimal component of velocity in the direction of the electrostatic field. Thus, IM is typically considered directed diffusion. It is convention to normalize K to standard temperature and pressure (STP) conditions of 0°C and 760 Torr, referred to as the reduced mobility, (K_0):

$$K_0 = K \frac{p}{760} \frac{273}{T} \quad (3)$$

The low-field condition is important as K is not constant at high field conditions. When K is constant, the ion-neutral collision cross section (Ω) and K_0 are inversely related through the following expression:

$$K_0 = \frac{(18\pi)^{1/2}}{16} \frac{ze}{(k_B T)^{1/2}} \left[\frac{1}{m_i} + \frac{1}{m_n} \right]^{1/2} \frac{760}{p} \frac{T}{273} \frac{1}{N_0} \frac{1}{\Omega} \quad (4)$$

where N_0 is the number density of the drift gas and at STP, m_i and m_n are the masses of the ion and neutral gas, respectively, in the form of the ion-neutral collision pair's reduced mass, and ze is the ion's charge.

To calculate Ω from the empirical measurement of an IM separation, Eqns. (1) and (3) are substituted for K_θ to incorporate t_d , and Eqn. (4) is rearranged into the form commonly referred to as the Mason-Schamp equation:

$$\Omega = \frac{(18\pi)^{1/2}}{16} \frac{ze}{(k_B T)^{1/2}} \left[\frac{1}{m_i} + \frac{1}{m_n} \right]^{1/2} \frac{t_d E}{L} \frac{760}{p} \frac{T}{273} \frac{1}{N_0} \quad (5)$$

Equation 5 holds under the assumption that the total translational energy does not change upon ion-neutral collisions in the IM drift cell, but there are limits to this approximation. Nevertheless, Eqn. (5) is generally accepted as that used for reporting CCSs in uniform field experiments unless otherwise noted by the particular study.

1.3. *Theoretical Collision Cross Section Determination*

Several computational approaches exist for calculating the theoretical collision cross section (CCS) of computationally generated conformations. These methods vary from approximations in just two dimensions to more accurate physical interpretations of the interactions in the drift cell. Experimentally, a drift time is converted into the CCS term using the method discussed in the previous section. Theoretically, the structure of the gas phase ion is used to determine the CCS or the orientationally average surface area. The methods that are used are depicted in Figure 1.2 and will be discussed in greater detail below.

The simplest approach is termed the projection approximation¹⁰. As the name suggests, the gas phase ion or molecule is projected onto a two-dimensional surface as illustrated in Figure 1.2a. While this image predates the computational algorithm, as well as the method for obtaining CCS values from IM-MS experiments, it depicts the idea of projecting an image of the molecule to get structural information. This image is from an

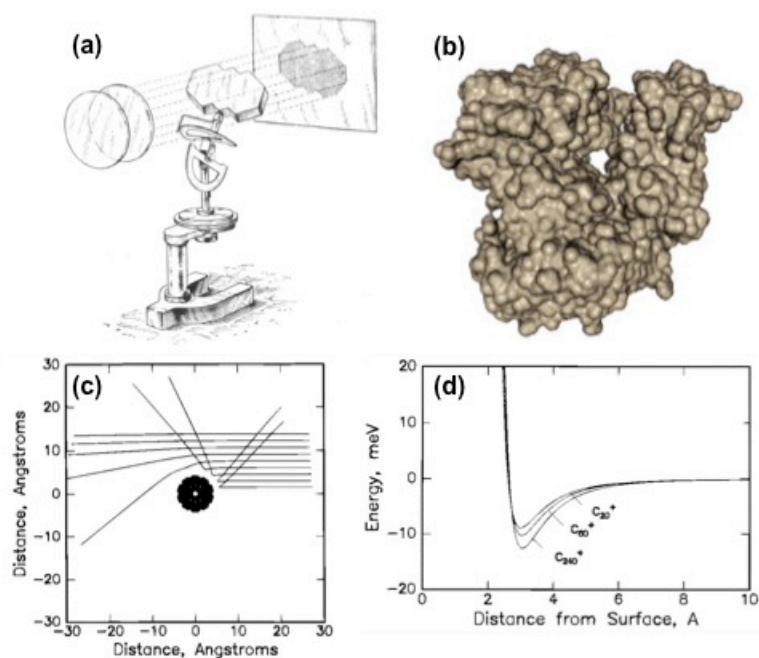


Figure 1.2 Illustrations of the four current approaches for calculating theoretical CCS values are shown here. The projection approximation is shown in a) and the projection superposition approximation is shown in b). Exact hard sphere scattering is shown in c) and trajectory method in d). Panel a) is adapted with permission from E. Mack Jr, *Journal of the American Chemical Society* **1925**, 47, 2468-2482, Fig. 5. Panel b) is adapted with permission from C. Bleiholder.; T. Wyttentbach; M.T. Bowers, *International Journal of Mass Spectrometry* **2011**, 308, 1-10, Fig. 5b. Panels c) and d) are adapted with permission from M.F. Mesleh; J.M. Hunter; A.A. Shvartsburg; C.G. Schatz; M.F. Jarrold, *The Journal of Physical Chemistry* **1996**, 100, 16082-16086 Fig. 2,3.

early work on calculating CCS values from beeswax models to gain more structural information concerning their size and shape.¹¹ The projection approximation uses a computer algorithm to project the molecule and then calculate the area of the box around the molecule on this surface. Random points are selected within this area and the ratio of points that fall on the projected molecule to the total number of random points selected is determined and then multiplied by the area of the box which results in a CCS term. This protocol is then repeated for several different projections of the molecule, and then all the CCS term are averaged to generate the CCS value for the molecule. While this approach is considered an approximation, it does a very good job of quickly predicting the CCS for experimental measurements obtained with helium as the buffer gas. This is due to helium's inert characteristic of having completely elastic collisions with the gas phase ion in the drift tube. Other larger drift gases such as nitrogen do have completely elastic collisions with the gas phase ion thus having a lengthening effect on drift time resulting in larger experimental CCS values. Consequently, the drift gas must be considered for theoretical determination of CCS terms in order to provide proper agreement with experimental measurements.

Recently, Bowers and colleagues have improved on the projection approximation with a new approach entitled projected superposition approximation (PSA)¹²⁻¹⁵. This method determines the projection approximation as mentioned above and the uses an addition shape factor (ρ) to obtain the PSA CCS value.

$$\Omega_{PSA} = \rho\Omega_{PA} \quad (6)$$

This shape factor is a measure of the molecules concavity and is depicted with the molecular surface shown in Figure 1.2b. A fully convex (spherical) molecule would have

a shape factor of 1, whereas molecules with concave areas on their surface would have a shape factor of >1 . This is because concave regions on the surface would generate more surface area. This approach still benefits from the faster computational characteristic of the projection approximation. It also has a preliminary nitrogen parameter set and therefore can generate nitrogen CCS values as well.

Two other methods exist; they are the exact hard sphere scattering¹⁶ and the trajectory method¹⁷, and they both determine the CCS value by measuring scattering angles between the incoming and departing trajectory of the buffer gas atom. The methods differ, however, in how they treat the atoms. Exact hard sphere scattering represents the atoms as hard spheres, as indicated in Figure 1.2c, while the trajectory method represents them with 12-6-4 Lennard-Jones potentials as shown in Figure 1.2d. In order to see how these methods are derived from the kinetic theory of gases, we will start with a slightly different form of Equation 4 from the previous section:

$$K = \frac{(18\pi)^{1/2}}{16} \left[\frac{1}{m} + \frac{1}{m_B} \right]^{1/2} \frac{ze}{(k_B T)^{1/2} \Omega_{avg}^{(1,1)}} \frac{1}{N} \quad (7)$$

Here, m is the mass of the ion and m_B is the mass of the buffer gas, ze is the charge of the gas phase ion, T is the temperature, Ω_{avg} is the orientationally averaged collision integral, and N is the number density of the buffer gas. This collision integral can be determined from the scattering angle of the incoming and departing trajectory of the buffer atom by averaging over the impact parameter and relative velocity of the buffer gas atom. The impact parameter (b) is the perpendicular distance between the path of the buffer gas and the center of the field created by the gas phase ion that the buffer gas is approaching. The trajectory method calculates the orientationally average CCS and is calculated using the following the equation:

$$\Omega_{avg}^{(1,1)} = \frac{1}{8\pi^2} \int_0^{2\pi} d\theta \int_0^\pi d\phi \sin\phi \int_0^{2\pi} d\gamma \frac{\pi}{8} \left(\frac{\mu}{k_B T} \right)^3 \int_0^\infty dg e^{-\mu g^2 / (2k_B T)} g^5 \int_0^\infty db 2b (1 - \cos \chi(\theta, \phi, \gamma, g, b)) \quad (8)$$

In this equation, θ , ϕ , and γ are the angles involved in the collision geometry of the buffer gas with the gas phase ion. The relative velocity of the gas phase ion is defined by g , and the impact parameter by b . The scattering angle is defined by $\chi(\theta, \phi, \gamma, g, b)$. This trajectory calculation is then run within a 12-6-4 Lennard-Jones potential described by the following equation:

$$\Phi(\theta, \phi, \gamma, b, r) = 4\varepsilon \sum_i^n \left[\left(\frac{\sigma}{r_i} \right)^{12} - \left(\frac{\sigma}{r_i} \right)^6 \right] - \frac{\alpha}{2} \left(\frac{ze}{n} \right)^2 \left[\left(\sum_i^n \frac{x_i}{r_i^3} \right)^2 + \left(\sum_i^n \frac{y_i}{r_i^3} \right)^2 + \left(\sum_i^n \frac{z_i}{r_i^3} \right)^2 \right] \quad (9)$$

In this equation the first term is the sum of a two-body 6-12 interaction. The second term represents the ion-induced dipole interaction. The Lennard-Jones parameters are defined by ε for the well depth and σ for the distance when the potential becomes positive. The polarizability of the buffer gas is defined by α . The effective potential is determined by averaging this Lennard-Jones potential across all the atoms in the gas phase ion. The exact hard sphere scattering method that was mentioned previously does not utilize this potential and is calculated according to the following equation:

$$\Omega_{avg}^{(1,1)} = \frac{1}{4\pi^2} \int_0^{2\pi} d\theta \int_0^\pi d\varphi \sin\varphi \int_0^{2\pi} d\gamma \int_0^\infty db 2b (1 - \cos \chi(\theta, \varphi, \gamma, b)) \quad (10)$$

This approach considers concave surfaces by allowing the trajectory to have multiple collisions (as does the trajectory method), but does not consider the Lennard-Jones potential. Additionally, it does not take into account the polarizability of the buffer gas and, consequently, is only suitable for measurements made in helium.

The above methods each have benefits and limitations. While the projection approximation method is just an approximation of the CCS value, it is by far the most

time efficient approach to generating large sets of CCS values. It provides a very good approximation especially for small gas phase ions with around 10-200 atoms. The exact hard sphere scattering method is also a very time efficient approach and works well for larger ions with approximately 1000 atoms where the concavity of the surface becomes more important. These two methods are only viable options if the buffer gas utilized is helium. Both PSA and the trajectory method allow for nitrogen buffer gas as well as helium, but these two methods require more user and computational effort. Currently, PSA is only available through a web interface that requires structure files to be uploaded independently, and for results to be pulled from individual e-mail files. Additionally, this method is currently only available for biological molecules with specific Carbon to Nitrogen to Oxygen ratios. The actual computational cost is similar to the projection approximation, even for the calculations including nitrogen parameters. Once this program is available for batch processing, it will become a more widely used tool. The trajectory method is by far the most rigorous method for calculating theoretical CCS values, but it has a very high computational cost.

1.4. Theoretical Structure Determination

The CCS term derived from experimental IM-MS measurements provides a rotationally averaged surface area of the analyte ion. However, this descriptor of ion size is relatively broad and does not offer detailed structural information. In order to obtain more detailed structural information consistent with the surface area that is measured, computational modeling methods are often used.

These computational modeling methods consist of generating a statistical ensemble of three-dimensional conformations of the ion followed by an *in silico* IM experiment to determine the corresponding CCS of each ion conformation. Quantum mechanical (QM), molecular dynamics (MD), systematic searching, and coarse-grain approaches are all used for theoretical conformational space sampling in support of CCS measurements. QM approaches, which model the molecule on an electron scale, are mostly used for small molecules due to the time required to run these calculations. Studies that have implemented these methods include small peptides^{18,19} and organometallic complexes²⁰. The level of theory employed in these studies includes Hartree Fock²¹, Density Functional Theory²²⁻³¹, Moller-Plesset³²⁻³⁴ and semi-empirical methods^{35,36}. These QM methods vary in how they treat electron correlation.

Systematic search protocols are also used to generate conformations. These approaches include Monte Carlo methods^{37,38}, stochastic searching³⁹, and de novo folding⁴⁰. These methods use random sampling of atom movements or dihedral angles to sample conformational space. Coarse grain approaches, which represent sections of the molecule rather than individual atoms or electrons, as well as simply using structures from databases are used for large molecules such as proteins⁴¹⁻⁵¹, protein complexes⁵²⁻⁵⁷ and viruses⁵⁸.

The most used method in support of IM-MS is MD where the molecules are represented as a collection of atoms and their behavior is described by a force field that has parameters for each atom type (element and connectivity) in the molecule. In particular, enhanced MD studies have been performed that sample more conformational space by using either elevated temperatures⁵⁹⁻⁶¹ or exchanging structures between parallel

simulations⁶²⁻⁶⁴. Simulated annealing cycles through heating the system and then slowing cooling the system to achieve low energy conformations.⁶⁵ The high temperature allows the molecule to traverse energy barriers more easily thus sampling more conformational space. Replica exchange MD runs parallel MD simulations and then exchanges coordinates of the molecule between the simulations, again traversing energy barriers more easily.⁶⁶ These methods are primarily used for small molecules^{67,68}, peptides⁶⁹⁻⁷⁴, and proteins⁷⁵⁻⁷⁸. Several studies that utilized computational modeling in support of structural IM-MS are listed in Table 1.1.

Structural biology studies have been of particular interest to the IM-MS community including reports on the amyloid β -protein and its connection to Alzheimer's disease.⁷⁹⁻⁸⁶ The structure of the amyloid β -protein has been investigated as well as mutants that may contribute to the disease.⁸⁷ Other small proteins including bradykinin⁸⁸, α -synuclein⁸⁹, ubiquitin^{90,91}, and tau^{92,93} have also been structurally characterized with IM-MS. Membrane proteins⁹⁴, including ion channels⁹⁵, have been investigated with structural IM-MS methods. Several model peptides have been used to gain insight into secondary structure⁹⁶⁻¹⁰⁶, isomer separations^{107,108}, and characterization with hydrogen deuterium exchange¹⁰⁹⁻¹¹¹. Other peptide studies include the gonadotropin-releasing hormone antagonist (GnRH)^{112,113} and tryptic peptides^{114,115}. The structure-function relationships of enzymes have also been explored with IM-MS.¹¹⁶⁻¹¹⁸

Oligonucleotides have been thoroughly investigated with these methods to gain more insight into their structure in the gas phase.¹¹⁹⁻¹²⁴ Specifically, DNA duplexes¹²⁵, triplexes¹²⁶, and quadruplexes¹²⁷⁻¹²⁹ have been investigated to better understand the binding efficiencies of these biological molecules that play a major role in gene

Table 1.1 Selected Studies of Metabolites Using Ion Mobility-Mass Spectrometry

Model Systems	References
<i>Quantum Mechanics</i>	
Peptides and Oligonucleotides	86,122
Metal Containing	20,22,23,28,33,36,124,141,152,158-160
Macrocycles	21,24,25,26,162,163,167
Other Small Molecules	27,29-32,34,35,145-148,151,153,154,156,157
<i>Molecular Dynamics</i>	
Peptides and Proteins	59-63,69,70,72-85,87-89,91-94,96-98,100-104, 106-112,114,115,119,120,138
Enzymes	117,118
Oligonucleotides	64,68,126-129
Non Biological	140,142-144,149,161,164-166,168,170-173,175
Small Biological Molecules	67,113,121,130-132,139
<i>Systematic Searching</i>	
Peptides and Proteins	37,38,40
Non Biological	169
Small Biological Molecules	39,136,137
<i>Coarse Grain</i>	
Peptides and Protines	41,42,44-57
Viruses	58
Enzymes	116
Oligonucleotides	43,99,123
Non Biological	176
Small Biological Molecules	135
<i>Combination of Methods</i>	
Peptides and Proteins	18,19,71,90,95,105,155
Oligonucleotides	125
Non Biological	150,174
Small Biological Molecules	133,134

regulation and transcription. Structural IM-MS has been useful in examining other classes of biomolecules such as carbohydrates^{130,131} and lipids¹³² where their set of structural building blocks result in many structural isomers. Small molecules such as natural products^{133,134}, drug molecules^{135,136}, and metabolites^{137,138} have also been investigated with IM-MS. The deviations of subclasses, such as cyclic peptide natural products, from peptide trend lines have been linked to structural characteristics that were identified by a combination of computational modeling and IM-MS experimental measurements.¹³⁹

IM-MS has also been used in structural studies of non-biological species such as dendrimers¹⁴⁰ and polymers including polyethylene glycol^{141,142}, polylactides¹⁴³, and polystyrene¹⁴⁴. Aromatic compounds in oil¹⁴⁵ as well as nitrate explosives¹⁴⁶ have also been studied with IM-MS and computational methods. Several studies have looked at benzene containing compounds including anilines¹⁴⁷⁻¹⁴⁹, benzene clusters¹⁵⁰ and derivatives¹⁵¹. Diastereomers have also benefited from IM-MS isomeric separations in conjunction with DFT optimized structures.¹⁵²⁻¹⁵⁵ The photophysical behavior of Schiff base^{156,157} as well as the structures of oxide clusters¹⁵⁸⁻¹⁶⁰ have been elucidated with IM-MS and theoretical calculations. Host-guest chemistry has also greatly benefited from IM-MS, as these species do not crystallize well and are often not present in large quantities, thus ruling out typical structural determination methods such as X-ray crystallography and NMR. The gas phase structures of cucurbit[n]urils¹⁶¹⁻¹⁶³, rotaxanes¹⁶⁴, metallomacrocyclics¹⁶⁵⁻¹⁷⁰, and polyhedral oligomeric silsesquioxanes¹⁷¹⁻¹⁷⁶ have been investigated to provide information on the size of the cage and its transport abilities. In addition to the journal articles previously mentioned, there are two articles

that describe the general protocols for coarse grain methods¹⁷⁷ and MD calculations¹⁷⁸ in support of structural IM-MS as well as several reviews on the subject¹⁷⁹⁻¹⁸⁴.

1.5 Applications of IM-MS and Computational Modeling

As evident by the extensive literature collection in the previous section, the combination of computational modeling with IM-MS has allowed for many structural IM-MS studies across a wide variety of applications. The ability to analyze complex samples and analyze different biological classes simultaneously as shown in Figure 1.3 has proven beneficial in biological studies. These three plots contain m/z data on the x-axis and collision cross section data on the y-axis. The data points representing oligonucleotides, carbohydrates, peptides, and lipids in Figure 1.3a show how different classes of biomolecules separate based on their gas phase packing efficiencies.¹²¹ Lipids that have more degrees of freedom in their fatty acyl tails inhabit a large drift time area whereas carbohydrates that form more compact structures by virtue of their sugar rings occupy a much shorter drift time space. Trend lines, as shown in Figure 1.3b, can then be derived from this experimental data. These trend lines can then guide future identification of biological species in complex samples. Figure 1.3c has the trend lines overlaid on arrival time distributions for a sample mixture with species from each biological class.

In addition to the numerous biological studies performed with IM-MS, the low sensitivity and the additional dimension of separation allow for small differences in polymer precursors to be detected. MS and MS/MS have long been used as a tool in polymer characterization, but the addition of IM allows more insight into polymer

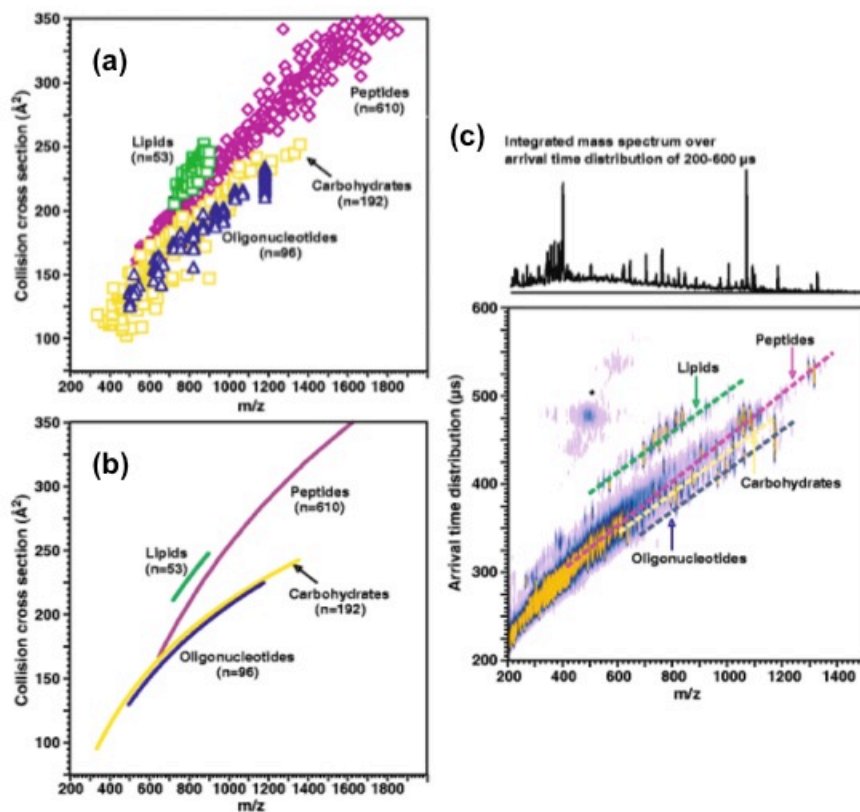


Figure 1.3. The plots above depict the ability of IM-MS to separate molecules based on biological class. Experimental CCS values are plotted in a) for lipids, peptides, carbohydrates, and oligonucleotides. b) Logarithmic regression trend lines are shown for each of these classes of biomolecules. These trend lines are then overlaid with a drift plot of m/z vs. arrival drift time in c). Adapted from L.S. Fenn, M. Kliman, A. Mahshutt, S.R. Zhao, and J.A. McLean, *Analytical and Bioanalytical Chemistry* **2009**, 394, 235-244, Fig. 1(a,b,c), with permission from Springer Science+Business Media.

structure. In this section, the applications that will be discussed later in this work are briefly described.

1.5.1. Polymers

The versatility and widespread applications of polymers make them incredibly useful materials. Polyurethanes in upholstered furniture and clothing provide comfort in our daily lives. We enjoy television, computers, and eyeglasses everyday that have various parts made with polycarbonate. Fireproof uniforms and body armor made from aramids protect us from natural and unnatural danger. In order to satisfy these and the many other demands for polymers, several companies make billions of dollars annually producing and selling millions of tons of polymers and polymer precursors.¹⁸⁵⁻¹⁸⁷ Whether we consider polyurethanes from Bayer, polycarbonates from SABIC, or aramids from DuPont, these companies greatly profit from supplying some of the world's most important materials. The versatility that polymers demonstrate reflects the varying structural possibilities that exist for synthetic polymer species. Although polymers are based on simple monomer units, the connectivity of these units to form complex molecules helps to determine the function of the polymer. While this structural diversity allows for a variety of applications for polymer species, characterization of these often-complex materials can be very challenging.

Mass spectrometry has long been used as a tool in polymer research.¹⁸⁸⁻¹⁹³ Its ability to provide accurate mass measurements and its low detection limits make it an excellent tool in polymer characterization. Accurate mass measurements are not only important for precursor ion species, but also for polymer fragments that result when

MS/MS experiments are performed, which provide insight into the smaller units that make up the polymer species. Low detection limits allow impurities to be detected in large-scale polymer production samples. Identifying polymer structure and sample impurities are both important to companies who make millions of tons of these products annually. Bayer MaterialScience, a major producer of polyurethanes, has expressed interest in gaining a better understanding of the hard block species they use in their polyurethane manufacturing. Polyurethanes are composed of varying amounts of soft block and hard block sections. Within this work, MS, MS/MS, IM-MS, and computational studies provide separation of isomeric species, structural details that contribute to these separations, and fragmentation pathways of 2-ring, 3-ring, and 4-ring polyurethane hard block MDA species.

1.5.2. Natural Products

Natural products are an interesting class of molecules due to their diverse biological activities. These diverse biological activities are representative of diverse structural characteristics, which align better than molecules synthesized in combinatorial libraries with current drug molecules as shown in Figure 1.4.¹⁹⁴ A challenge in natural product discovery is that these secondary metabolites are often present in significantly low abundance in complex biological samples. IM-MS has the ability to isolate analytes of low abundance (such as natural products) with very little sample preparation making it a very useful tool in natural product discovery. The diverse structural characteristics that allow IM-MS to separate natural products make them difficult to study with MD techniques due to the lack of a current force field that would accurately describe such a

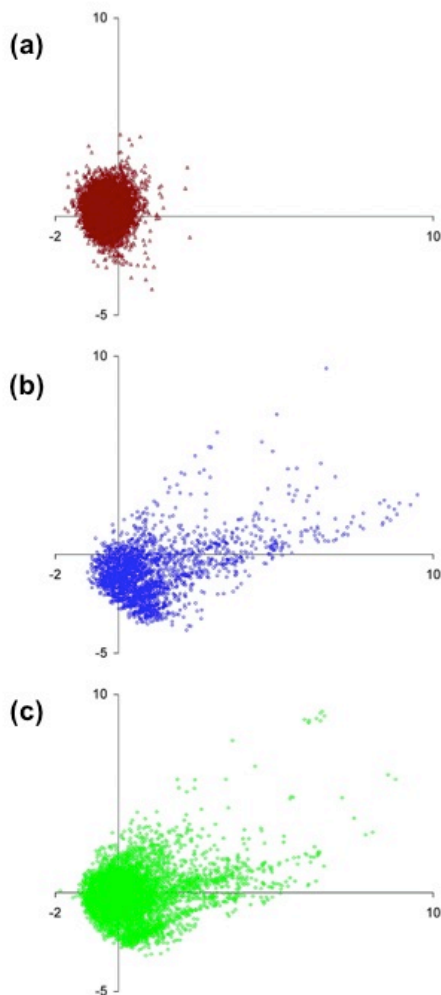


Figure 1.4. Principal component analysis plots for (a) combinatorially synthesized molecules, (b) natural products, and (c) current drug molecules. The principal components are based on structural characteristics of the chemical compounds such as fused ring systems, number of chiral centers and number of certain elements. Adapted from M. Feher, J.M. Schmidt, *Journal of Chemical Information and Computer Sciences* **2003**, 43 (1), 218-227.

dissimilar group of molecules. This notion led to the development of a distance geometry protocol to sample conformational space of natural product molecules in support of IM-MS. Distance geometry generates possible three-dimensional conformations based on sampling interatomic distances between the atoms in the molecule. This is a purely mathematical approach to sampling conformational space and is very time efficient.

1.5.3. Metabolites

Metabolic studies have proven difficult due to the size and complexity of the metabolome, which is comprised of thousands of metabolites having varied functional groups and chemical properties. A complicating factor for metabolite analysis by MS strategies is that they generally occur over a limited mass range (*ca.* 100-1000 Da) and thus the predicted frequency of nominally isobaric, but distinct, species can be quite high and difficult to distinguish without additional separation. The integration of IM with MS allows the separation of isobaric species, which is helpful in metabolic profiling within dense regions of conformational space occupied by multiple subclasses of metabolites. Table 1.2 lists a number of metabolomics studies which demonstrate the advantages of IM-MS for structurally diverse metabolite species. Profiling studies of blood, liver, lymph, and urinary metabolomes with IM-MS illustrate the separation of chemical noise while simultaneously monitoring metabolic changes.¹⁹⁵⁻¹⁹⁸ Studies utilizing IM-MS have also focused on metabolomics of prostate, skin, and colon cancer cell lines with the goal of identifying new diagnostic metabolic markers.^{199,200} Real-time temporal metabolic monitoring of Jurkat cells by IM-MS has been demonstrated.²⁰¹ Targeted pharmacokinetic analyses have benefitted significantly from IM-MS in the

Table 1.2 Selected Studies of Metabolites Using Ion Mobility-Mass Spectrometry

Model System	Type of Study	References
<i>Clinical</i>		
Urine	Characterization	195
Lymph	Metabolic Changes	196
Blood	Metabolic Profiling	197
HepG2 Cells	Role of Nonoxidative Metabolites	198
Colon Cancer	Detect and Analyze	199
Prostate Cancer	Detection and Metabolomics	200
Jurkat Cells	Changes in Metabolite Levels	201
<i>Pharmaceutical</i>		
Opiates	Identify and Separation	202
Cocaine	Structure and Mobility in Different Gases	203
Vinblastine	Separation	204
Leflunomide and Acetaminophen	Metabolic Changes	205
Carbamazepine	Structural Identification and Isomers	39
Cocaine	Metabolic Profiling	206
<i>Microorganisms</i>		
<i>E. coli</i>	Metabolic Profiling	20,208
<i>Aspergillus fumigatus</i> and <i>Candida</i>	Detection and Profiling	209

characterization of drugs and their metabolites.^{39,202-206} By including IM separations, Trim *et al.* demonstrated improved separation of isobaric MALDI matrix interferences from metabolites in whole body tissue sections,²⁰⁴ while others have utilized IM-MS to study common microorganisms such as *Aspergillus fumigatu*, *Candida* species, and *E. coli*.²⁰⁷⁻²⁰⁹ Collectively, these general metabolic studies have demonstrated great utility in the combination of IM with MS.

1.6. Conclusions and Objectives

My dissertation research has focused on selecting and developing appropriate strategies for computational modeling in support of structural IM-MS measurements. Chapter II demonstrates a project where molecular dynamic simulations were used in conjunction with a series of IM-MS and MS/MS techniques to fully characterize methylenedianiline (MDA), which serves as a precursor to hard block segments in polyurethanes. Due to the chemical simplicity of these polymer precursors, current MD methods were a suitable approach in these studies. Chapter III introduces a conformational sampling technique labeled distance geometry and discusses the development of a protocol for IM-MS research. The distance geometry approach proves to be a much more time efficient method for sampling conformational space. The distance geometry protocol is benchmarked against current MD methods on a set of natural product molecules. Chapter IV utilizes the distance geometry protocol to provide theoretical collision cross section ranges for a set of metabolites. The goal of this research is to offer another metric to utilize for IM-MS metabolite identification. Finally,

Chapter V contains conclusions and future directions for the aforementioned research endeavors.

1.7. Acknowledgments

This chapter contains sections of the book chapter for Natural Products Analysis: Instrumentation, Methods, and Applications: “Structural separations for natural product characterization by ion mobility-mass spectrometry: Fundamental theory to emerging applications,” by Sarah M. Stow, Nichole M. Lareau, Kelly M. Hines, C. Ruth McNeese, Cody R. Goodwin, Brian O. Bachmann, and John A. McLean. Vladimer Havlicek and John Spizek, Eds. Wiley-Blackwell, 2014.

Financial support for this work was provided by the National Institutes for Health (R01GM092218 and UH2TR00491), the Defense Threat Reduction Agency (HDTRA1-09-1-0013 and DE-001165), the Defense Advanced Research Projects Agency (DARPA-11-73-MPSys-FP-011), the Vanderbilt Institute of Chemical Biology, and the Vanderbilt Institute of Integrative Biosystems Research and Education.

1.8. References

1. Mason, E. A.; Schamp, H. W. Mobility of gaseous ions in weak electric fields. *Annals of Physics* 1958, 4 (3), 233-270.
2. McDaniel, E. W.; Mason, E. A. *Mobility and diffusion of ions in gases*. John Wiley and Sons: New York, 1973.
3. Mason, E. A.; McDaniel, E. W. *Transport properties of ions in gases*. John Wiley & Sons: New York, 1988; Vol. 891.
4. Sundarapandian, S.; May, J. C.; McLean, J. A. Dual source ion mobility-mass spectrometer for direct comparison of electrospray ionization and MALDI collision cross section measurements. *Analytical Chemistry* 2010, 82 (8), 3247-3254.
5. Giles, K.; Pringle, S. D.; Worthington, K. R.; Little, D.; Wildgoose, J. L.; Bateman, R. H. Applications of a travelling wave - based radio - frequency - only stacked ring ion guide. *Rapid Communications in Mass Spectrometry* 2004, 18 (20), 2401-2414.
6. Pringle, S. D.; Giles, K.; Wildgoose, J. L.; Williams, J. P.; Slade, S. E.; Thalassinos, K.; Bateman, R. H.; Bowers, M. T.; Scrivens, J. H. An investigation of the mobility separation of some peptide and protein ions using a new hybrid quadrupole/travelling wave IMS/oa-ToF instrument. *International Journal of Mass Spectrometry* 2007, 261 (1), 1-12.
7. Tang, K.; Shvartsburg, A. A.; Lee, H.-N.; Prior, D. C.; Buschbach, M. A.; Li, F.; Tolmachev, A. V.; Anderson, G. A.; Smith, R. D. High-sensitivity ion mobility spectrometry/mass spectrometry using electrodynamic ion funnel interfaces. *Analytical Chemistry* 2005, 77 (10), 3330-3339.
8. May, J. C.; Goodwin, C. R.; Lareau, N. M.; Leaptrot, K. L.; Morris, C. B.; Kurulugama, R. T.; Mordehai, A.; Klein, C.; Barry, W.; Darland, E. Conformational Ordering of Biomolecules in the Gas Phase: Nitrogen Collision Cross Sections Measured on a Prototype High Resolution Drift Tube Ion Mobility-Mass Spectrometer. *Analytical Chemistry* 2014, 86 (4), 2107-2116.
9. Ruotolo, B. T.; Benesch, J. L. P.; Sandercock, A. M.; Hyung, S. J.; Robinson, C. V. Ion mobility-mass spectrometry analysis of large protein complexes. *Nature Protocols* 2008, 3 (7), 1139-1152.
10. von Helden, G.; Hsu, M. T.; Gotts, N.; Bowers, M. T. Carbon cluster cations with up to 84 atoms: structures, formation mechanism, and reactivity. *The Journal of Physical Chemistry* 1993, 97 (31), 8182-8192.

11. Mack Jr, E. Average cross-sectional areas of molecules by gaseous diffusion methods. *Journal of the American Chemical Society* 1925, 47 (10), 2468-2482.
12. Bleiholder, C.; Wyttenbach, T.; Bowers, M. T. A novel projection approximation algorithm for the fast and accurate computation of molecular collision cross sections (I). *Method. International Journal of Mass Spectrometry* 2011, 308 (1), 1-10.
13. Bleiholder, C.; Contreras, S.; Do, T. D.; Bowers, M. T. A novel projection approximation algorithm for the fast and accurate computation of molecular collision cross sections (II). Model parameterization and definition of empirical shape factors for proteins. *International Journal of Mass Spectrometry* 2013, 345, 89-96.
14. Anderson, S. E.; Bleiholder, C.; Brocker, E. R.; Stang, P. J.; Bowers, M. T. A novel projection approximation algorithm for the fast and accurate computation of molecular collision cross sections (III): Application to supramolecular coordination-driven assemblies with complex shapes. *International Journal of Mass Spectrometry* 2012, 330-332, 78-84.
15. Bleiholder, C.; Contreras, S.; Bowers, M. T. A novel projection approximation algorithm for the fast and accurate computation of molecular collision cross sections (IV). Application to polypeptides. *International Journal of Mass Spectrometry* 2013, 354, 275-280.
16. Shvartsburg, A. A.; Jarrold, M. F. An exact hard-spheres scattering model for the mobilities of polyatomic ions. *Chemical Physics Letters* 1996, 261 (1), 86-91.
17. Mesleh, M. F.; Hunter, J. M.; Shvartsburg, A. A.; Schatz, G. C.; Jarrold, M. F. Structural information from ion mobility measurements: effects of the long-range potential. *The Journal of Physical Chemistry* 1996, 100 (40), 16082-16086.
18. Moss, C. L.; Chamot-Rooke, J.; Nicol, E.; Brown, J.; Campuzano, I.; Richardson, K.; Williams, J. P.; Bush, M. F.; Bythell, B.; Paizs, B. Assigning structures to gas-phase peptide cations and cation-radicals. An infrared multiphoton dissociation, ion mobility, electron transfer, and computational study of a histidine peptide ion. *The Journal of Physical Chemistry B* 2012, 116 (10), 3445-3456.
19. Schinle, F.; Jacob, C. R.; Wolk, A. B.; Greisch, J.-F.; Vonderach, M.; Weis, P.; Hampe, O.; Johnson, M. A.; Kappes, M. M. Ion Mobility Spectrometry, Infrared Dissociation Spectroscopy, and ab Initio Computations toward Structural Characterization of the Deprotonated Leucine-Enkephalin Peptide Anion in the Gas Phase. *The Journal of Physical Chemistry A* 2014, 118 (37), 8453-8463.
20. Baker, E. S.; Bushnell, J. E.; Wecksler, S. R.; Lim, M. D.; Manard, M. J.; Dupuis, N. F.; Ford, P. C.; Bowers, M. T. Probing shapes of bichromophoric metal-organic complexes using ion mobility mass spectrometry. *Journal of the American Chemical Society* 2005, 127 (51), 18222-18228.

21. Lee, T.-C.; Kalenius, E.; Lazar, A. I.; Assaf, K. I.; Kuhnert, N.; Grün, C. H.; Jänis, J.; Scherman, O. A.; Nau, W. M. Chemistry inside molecular containers in the gas phase. *Nature Chemistry* 2013, 5 (5), 376-382.
22. Joly, L.; Antoine, R.; Albrieux, F.; Ballivian, R.; Broyer, M.; Chirot, F.; Lemoine, J.; Dugourd, P.; Greco, C.; Mitric, R. Optical and Structural Properties of Copper– Oxytocin Dications in the Gas Phase. *The Journal of Physical Chemistry B* 2009, 113 (32), 11293-11300.
23. Ducháčková, L.; Roithová, J.; Milko, P.; Zabka, J.; Tsierkezos, N.; Schröder, D. Comparative Study of Mono-and Dinuclear Complexes of Late 3d-Metal Chlorides with N, N-Dimethylformamide in the Gas phase†. *Inorganic Chemistry* 2010, 50 (3), 771-782.
24. Hampe, O.; Karpuschkin, T.; Vonderach, M.; Weis, P.; Yu, Y.; Gan, L.; Kloppe, W.; Kappes, M. M. Heating a bowl of single-molecule-soup: structure and desorption energetics of water-encapsulated open-cage [60] fullerene anions in the gas-phase. *Physical Chemistry Chemical Physics* 2011, 13 (20), 9818-9823.
25. Fasciotti, M.; Gomes, A. F.; Gozzo, F. C.; Iglesias, B. A.; de Sá, G. F.; Daroda, R. J.; Toganoh, M.; Furuta, H.; Araki, K.; Eberlin, M. N. Corrole isomers: intrinsic gas-phase shapes via traveling wave ion mobility mass spectrometry and dissociation chemistries via tandem mass spectrometry. *Organic & Biomolecular Chemistry* 2012, 10 (42), 8396-8402.
26. Severa, L.; Jirásek, M.; Švec, P.; Teplý, F.; Révész, Á.; Schröder, D.; Koval, D.; Kašička, V.; Císařová, I.; Šaman, D. Counterion - Induced Inversion of Conformer Stability of a [5] Helquat Dication. *ChemPlusChem* 2012, 77 (8), 624-635.
27. Soliman, A.-R.; Hamid, A. M.; Momoh, P. O.; El-Shall, M. S.; Taylor, D.; Gallagher, L.; Abrash, S. A. Formation of Complex Organics in the Gas Phase by Sequential Reactions of Acetylene with the Phenylum Ion. *The Journal of Physical Chemistry A* 2012, 116 (36), 8925-8933.
28. Tsybizova, A.; Rulíšek, L.; Schröder, D.; Rokob, T. A. Coordination and Bond Activation in Complexes of Regioisomeric Phenylpyridines with the Nickel (II) Chloride Cation in the Gas Phase. *The Journal of Physical Chemistry A* 2012, 117 (6), 1171-1180.
29. Adamson, B. D.; Coughlan, N. J. A.; Continetti, R. E.; Bieske, E. J. Changing the shape of molecular ions: photoisomerization action spectroscopy in the gas phase. *Physical Chemistry Chemical Physics* 2013, 15 (24), 9540-9548.
30. Rijs, N. J.; Weiske, T.; Schlangen, M.; Schwarz, H. On divorcing isomers, dissecting reactivity, and resolving mechanisms of propane C H and aryl C X (X= halogen) bond activations mediated by a ligated copper (III) oxo complex. *Chemical Physics Letters* 2014, 608, 408-424.

31. Rogers, R. A.; Rodier, A. R.; Stanley, J. A.; Douglas, N. A.; Li, X.; Brittain, W. J. A study of the spiropyran–merocyanine system using ion mobility-mass spectrometry: experimental support for the cisoid conformation. *Chemical Communications* 2014, 50 (26), 3424-3426.
32. Bell, A. J.; Wright, T. G. Experimental and Theoretical Studies on the Complex Formed between H₂S and O₂. *The Journal of Physical Chemistry A* 2004, 108 (47), 10486-10490.
33. Fernandez-Lima, F. A.; Becker, C.; Gillig, K.; Russell, W. K.; Nascimento, M. A. C.; Russell, D. H. Experimental and theoretical studies of (CsI)_n Cs⁺ cluster ions produced by 355 nm laser desorption ionization. *The Journal of Physical Chemistry A* 2008, 112 (44), 11061-11066.
34. Momoh, P. O.; Xie, E.; Abrash, S. A.; Meot-Ner, M.; El-Shall, M. S. Gas Phase Reactions between Acetylene Radical Cation and Water. Energies, Structures and Formation Mechanism of C₂H₃O⁺ and C₂H₄O⁺ Ions. *The Journal of Physical Chemistry A* 2008, 112 (27), 6066-6073.
35. Zimnicka, M.; Troć, A.; Ceborska, M.; Jakubczak, M.; Koliński, M.; Danikiewicz, W. Structural Elucidation of Specific Noncovalent Association of Folic Acid with Native Cyclodextrins Using an Ion Mobility Mass Spectrometry and Theoretical Approach. *Analytical Chemistry* 2014, 86 (9), 4249-4255.
36. Schwarz, U.; Vonderach, M.; Armbruster, M. K.; Fink, K.; Kappes, M. M.; Weis, P. Cu (II)-and Mn (III)-Porphyrin-Derived Oligomeric Multianions: Structures and Photoelectron Spectra. *The Journal of Physical Chemistry A* 2013, 118 (2), 369-379.
37. Daly, S.; Poussigue, F.; Simon, A.-L.; MacAleese, L.; Bertorelle, F.; Chirot, F.; Antoine, R.; Dugourd, P. Action-Fret: Probing the Molecular Conformation of Mass-Selected Gas-Phase Peptides with Forster Resonance Energy Transfer Detected by Acceptor-Specific Fragmentation. *Analytical Chemistry* 2014, 86 (17), 8798-8804.
38. D'Urzo, A.; Konijnenberg, A.; Rossetti, G.; Habchi, J.; Li, J.; Carloni, P.; Sobott, F.; Longhi, S.; Grandori, R. Molecular Basis for Structural Heterogeneity of an Intrinsically Disordered Protein Bound to a Partner by Combined ESI-IM-MS and Modeling. *Journal of The American Society for Mass Spectrometry* 2014, 1-10.
39. Cuyckens, F.; Wassvik, C.; Mortishire-Smith, R. J.; Tresadern, G.; Campuzano, I.; Claereboudt, J. Product ion mobility as a promising tool for assignment of positional isomers of drug metabolites. *Rapid Communications in Mass Spectrometry* 2011, 25 (23), 3497-3503.
40. Al-Majdoub, M.; Opuni, K. F. M.; Koy, C.; Glocker, M. O. Facile fabrication and instant application of miniaturized antibody-decorated affinity columns for

higher-order structure and functional characterization of TRIM21 epitope peptides. *Analytical Chemistry* 2013, 85 (21), 10479-10487.

41. Scarff, C. A.; Patel, V. J.; Thalassinos, K.; Scrivens, J. H. Probing hemoglobin structure by means of traveling-wave ion mobility mass spectrometry. *Journal of the American Society for Mass Spectrometry* 2009, 20 (4), 625-631.
42. Wyttenbach, T.; Grabenauer, M.; Thalassinos, K.; Scrivens, J. H.; Bowers, M. T. The effect of calcium ions and peptide ligands on the relative stabilities of the calmodulin dumbbell and compact structures. *The Journal of Physical Chemistry B* 2009, 114 (1), 437-447.
43. Faull, P. A.; Florance, H. V.; Schmidt, C. Q.; Tomczyk, N.; Barlow, P. N.; Hupp, T. R.; Nikolova, P. V.; Barran, P. E. Utilising ion mobility-mass spectrometry to interrogate macromolecules: Factor H complement control protein modules 10–15 and 19–20 and the DNA-binding core domain of tumour suppressor p53. *International Journal of Mass Spectrometry* 2010, 298 (1), 99-110.
44. Baldwin, A. J.; Lioe, H.; Hilton, G. R.; Baker, L. A.; Rubinstein, J. L.; Kay, L. E.; Benesch, J. L. P. The Polydispersity of α B-Crystallin Is Rationalized by an Interconverting Polyhedral Architecture. *Structure* 2011, 19 (12), 1855-1863.
45. Zhou, M.; Dagan, S.; Wysocki, V. H. Protein subunits released by surface collisions of noncovalent complexes: natively compact structures revealed by ion mobility mass spectrometry. *Angewandte Chemie International Edition* 2012, 51 (18), 4336-4339.
46. Dykstra, A. B.; Sweeney, M. D.; Leary, J. A. Structural Evidence for the Tetrameric Assembly of Chemokine CCL11 and the Glycosaminoglycan Arixtra™. *Biomolecules* 2013, 3 (4), 905-922.
47. Calabrese, A. N.; Bowie, J. H.; Pukala, T. L. Structural Analysis of Calmodulin Binding by nNOS Inhibitory Amphibian Peptides. *Biochemistry* 2015, (54), 567-576.
48. Litwińczuk, A.; Ryu, S. R.; Nafie, L. A.; Lee, J. W.; Kim, H. I.; Jung, Y. M.; Czarnik-Matusiewicz, B. The transition from the native to the acid-state characterized by multi-spectroscopy approach: Study for the holo-form of bovine α -lactalbumin. *Biochimica et Biophysica Acta (BBA)-Proteins and Proteomics* 2014, 1844 (3), 593-606.
49. McCorvie, T. J.; Kopec, J.; Hyung, S.-J.; Fitzpatrick, F.; Feng, X.; Termine, D.; Strain-Damerell, C.; Vollmar, M.; Fleming, J.; Janz, J. M. Inter-domain Communication of Human Cystathionine β -Synthase STRUCTURAL BASIS OF S-ADENOSYL-L-METHIONINE ACTIVATION. *Journal of Biological Chemistry* 2014, 289 (52), 36018-36030.

50. Shepherd, D. A.; Marty, M. T.; Giles, K.; Baldwin, A. J.; Benesch, J. L. P. Combining tandem mass spectrometry with ion mobility separation to determine the architecture of polydisperse proteins. *International Journal of Mass Spectrometry* 2015, 377, 663-671.
51. Zhong, Y.; Han, L.; Ruotolo, B. T. Collisional and Coulombic Unfolding of Gas - Phase Proteins: High Correlation to Their Domain Structures in Solution. *Angewandte Chemie* 2014, 126 (35), 9363-9366.
52. Kaddis, C. S.; Lomeli, S. H.; Yin, S.; Berhane, B.; Apostol, M. I.; Kickhoefer, V. A.; Rome, L. H.; Loo, J. A. Sizing large proteins and protein complexes by electrospray ionization mass spectrometry and ion mobility. *Journal of the American Society for Mass Spectrometry* 2007, 18 (7), 1206-16.
53. Hogan, C. J., Jr.; Ruotolo, B. T.; Robinson, C. V.; Fernandez de la Mora, J. Tandem Differential Mobility Analysis-Mass Spectrometry Reveals Partial Gas-Phase Collapse of the GroEL Complex. *Journal of Physical Chemistry B* 2011, 115 (13), 3614-3621.
54. Freeke, J.; Bush, M. F.; Robinson, C. V.; Ruotolo, B. T. Gas-phase protein assemblies: Unfolding landscapes and preserving native-like structures using noncovalent adducts. *Chemical Physics Letters* 2012, 524, 1-9.
55. Hall, Z.; Politis, A.; Robinson, C. V. Structural Modeling of Heteromeric Protein Complexes from Disassembly Pathways and Ion Mobility-Mass Spectrometry. *Structure* 2012, 20 (9), 1596-1609.
56. Thomas, J. C.; Matak-Vinkovic, D.; Van Molle, I.; Ciulli, A. Multimeric Complexes among Ankyrin-Repeat and SOCS-box Protein 9 (ASB9), ElonginBC, and Cullin 5: Insights into the Structure and Assembly of ECS-type Cullin-RING E3 Ubiquitin Ligases. *Biochemistry* 2013, 52 (31), 5236-5246.
57. Zhong, Y.; Feng, J.; Ruotolo, B. T. Robotically assisted titration coupled to ion mobility-mass spectrometry reveals the interface structures and analysis parameters critical for multiprotein topology mapping. *Analytical Chemistry* 2013, 85 (23), 11360-11368.
58. Shoemaker, G. K.; van Duijn, E.; Crawford, S. E.; Uetrecht, C.; Baclayon, M.; Roos, W. H.; Wuite, G. J. L.; Estes, M. K.; Prasad, B. V. V.; Heck, A. J. R. Norwalk virus assembly and stability monitored by mass spectrometry. *Molecular & Cellular Proteomics* 2010, 9 (8), 1742-1751.
59. Bushnell, J. E.; Kemper, P. R.; Bazan, G. C.; Bowers, M. T. The Determination of Cis-Trans Conformations in Tetrahedral p-Phenylene Vinylene Oligomers. *Journal of Physical Chemistry A* 2004, 108 (38), 7730-7735.
60. Wong, R. L.; Williams, E. R.; Counterman, A. E.; Clemmer, D. E. Evaluation of ion mobility spectroscopy for determining charge-solvated versus salt-bridge

- structures of protonated trimers. *Journal of the American Society for Mass Spectrometry* 2005, 16 (7), 1009-1019.
61. Baker, E. S.; Dupuis, N. F.; Bowers, M. T. Aminoglycoside antibiotics: A-site specific binding to 16S. *International Journal of Mass Spectrometry* 2009, 283 (1), 105-111.
 62. Grabenauer, M.; Wu, C.; Soto, P.; Shea, J.-E.; Bowers, M. T. Oligomers of the prion protein fragment 106–126 are likely assembled from β -hairpins in solution, and methionine oxidation inhibits assembly without altering the peptide's monomeric conformation. *Journal of the American Chemical Society* 2010, 132 (2), 532-539.
 63. Le, T. N.; Pouilly, J. C.; Lecomte, F.; Nieuwjaer, N.; Manil, B.; Desfrancois, C.; Chirot, F.; Lemoine, J.; Dugourd, P.; van der Rest, G.; Gregoire, G. Gas-Phase Structure of Amyloid- β (12-28) Peptide Investigated by Infrared Spectroscopy, Electron Capture Dissociation and Ion Mobility Mass Spectrometry. *Journal of the American Society for Mass Spectrometry* 2013, 24 (12), 1937-1949.
 64. Arcella, A.; Dreyer, J.; Ippoliti, E.; Ivani, I.; Portella, G.; Gabelica, V.; Carloni, P.; Orozco, M. Structure and Dynamics of Oligonucleotides in the Gas Phase. *Angewandte Chemie* 2015, 127 (2), 477-481.
 65. Aarts, E.; Lenstra, J. K. Local search in combinatorial optimization. John Wiley & Sons, Inc. 1997.
 66. Cheng, X.; Cui, G.; Hornak, V.; Simmerling, C. Modified replica exchange simulation methods for local structure refinement. *The Journal of Physical Chemistry B* 2005, 109 (16), 8220-8230.
 67. Williams, J. P.; Bugarcic, T.; Habtemariam, A.; Giles, K.; Campuzano, I.; Rodger, P. M.; Sadler, P. J. Isomer Separation and Gas-Phase Configurations of Organoruthenium Anticancer Complexes: Ion Mobility Mass Spectrometry and Modeling. *Journal of the American Society for Mass Spectrometry* 2009, 20 (6), 1119-1122.
 68. Xie, T. Z.; Guo, K.; Huang, M.; Lu, X.; Liao, S. Y.; Sarkar, R.; Moorefield, C. N.; Cheng, S. Z. D.; Wesdemiotis, C.; Newkome, G. R. Towards Molecular Construction Platforms: Synthesis of a Metallotricyclic Spirane Based on Bis(2, 2'-6'-terpyridine) RuII Connectivity. *Chemistry-A European Journal* 2014, 20 (36), 11291-11294.
 69. Hilderbrand, A. E.; Clemmer, D. E. Determination of Sequence-Specific Intrinsic Size Parameters from Cross Sections for 162 Tripeptides. *Journal of Physical Chemistry B* 2005, 109 (23), 11802-11809.

70. Tao, L.; Dahl, D. B.; Pérez, L. M.; Russell, D. H. The contributions of molecular framework to IMS collision cross-sections of gas-phase peptide ions. *Journal of the American Society for Mass Spectrometry* 2009, 20 (9), 1593-1602.
71. Bellina, B.; Compagnon, I.; MacAleese, L.; Chirot, F.; Lemoine, J.; Maître, P.; Broyer, M.; Antoine, R.; Kulesza, A.; Mitrić, R. Binding motifs of silver in prion octarepeat model peptides: a joint ion mobility, IR and UV spectroscopies, and theoretical approach. *Physical Chemistry Chemical Physics* 2012, 14 (32), 11433-11440.
72. Harvey, S. R.; Porrini, M.; Stachl, C.; MacMillan, D.; Zinzalla, G.; Barran, P. E. Small-molecule inhibition of c-MYC: MAX leucine zipper formation is revealed by ion mobility mass spectrometry. *Journal of the American Chemical Society* 2012, 134 (47), 19384-19392.
73. Silveira, J. A.; Fort, K. L.; Kim, D.; Servage, K. A.; Pierson, N. A.; Clemmer, D. E.; Russell, D. H. From Solution to the Gas Phase: Stepwise Dehydration and Kinetic Trapping of Substance P Reveals the Origin of Peptide Conformations. *Journal of the American Chemical Society* 2013, 135 (51), 19147-19153.
74. Schenk, E. R.; Ridgeway, M. E.; Park, M. A.; Leng, F.; Fernandez-Lima, F. Isomerization kinetics of AT hook decapeptide solution structures. *Analytical Chemistry* 2014, 86 (2), 1210-1214.
75. McCullough, B. J.; Eastwood, H.; Clark, D. J.; Polfer, N. C.; Campopiano, D. J.; Dorin, J. A.; Maxwell, A.; Langley, R. J.; Govan, J. R. W.; Bernstein, S. L. Characterisation of DEFB107 by mass spectrometry: Lessons from an anti-antimicrobial defensin. *International Journal of Mass Spectrometry* 2006, 252 (2), 180-188.
76. McCullough, B. J.; Kalapothakis, J. M.; Chin, W.; Taylor, K.; Clarke, D. J.; Eastwood, H.; Campopiano, D.; MacMillan, D.; Dorin, J.; Barran, P. E. Binding a heparin derived disaccharide to defensin inspired peptides: insights to antimicrobial inhibition from gas-phase measurements. *Physical Chemistry Chemical Physics* 2010, 12 (14), 3589-3596.
77. Rozbesky, D.; Sovova, Z.; Marcoux, J.; Man, P.; Ettrich, R.; Robinson, C. V.; Novak, P. Structural Model of Lymphocyte Receptor NKR-P1C Revealed by Mass Spectrometry and Molecular Modeling. *Analytical Chemistry* 2013, 85 (3), 1597-1604.
78. Saikusa, K.; Fuchigami, S.; Takahashi, K.; Asano, Y.; Nagadoi, A.; Tachiwana, H.; Kurumizaka, H.; Ikeguchi, M.; Nishimura, Y.; Akashi, S. Gas-Phase Structure of the Histone Multimers Characterized by Ion Mobility Mass Spectrometry and Molecular Dynamics Simulation. *Analytical Chemistry* 2013, 85 (8), 4165-4171.
79. Dupuis, N. F.; Wu, C.; Shea, J.-E.; Bowers, M. T. Human Islet Amyloid Polypeptide Monomers Form Ordered β -hairpins: A Possible Direct

- Amyloidogenic Precursor. *Journal of the American Chemical Society* 2009, 131 (51), 18283-18292.
80. Wu, C.; Murray, M. M.; Bernstein, S. L.; Condrón, M. M.; Bitan, G.; Shea, J.-E.; Bowers, M. T. The Structure of A β 42 C-Terminal Fragments Probed by a Combined Experimental and Theoretical Study. *Journal of Molecular Biology* 2009, 387 (2), 492-501.
81. Klöniecki, M.; Jablonowska, A.; Poznanski, J.; Langridge, J.; Hughes, C.; Campuzano, I.; Giles, K.; Dadlez, M. Ion Mobility Separation Coupled with MS Detects Two Structural States of Alzheimer's Disease A β 1-40 Peptide Oligomers. *Journal of Molecular Biology* 2011, 407 (1), 110-124.
82. Do, T. D.; Economou, N. J.; LaPointe, N. E.; Kincannon, W. M.; Bleiholder, C.; Feinstein, S. C.; Teplow, D. B.; Buratto, S. K.; Bowers, M. T. Factors That Drive Peptide Assembly and Fibril Formation: Experimental and Theoretical Analysis of Sup35 NNQQNY Mutants. *Journal of Physical Chemistry B* 2013, 117 (28), 8436-8446.
83. Soper, M. T.; DeToma, A. S.; Hyung, S.-J.; Lim, M. H.; Ruotolo, B. T. Amyloid- β -neuropeptide interactions assessed by ion mobility-mass spectrometry. *Physical Chemistry Chemical Physics* 2013, 15 (23), 8952-8961.
84. Young, L.; Ndlovu, H.; Knapman, T. W.; Harris, S. A.; Radford, S. E.; Ashcroft, A. E. Monitoring oligomer formation from self-aggregating amylin peptides using ESI-IMS-MS. *International Journal for Ion Mobility Spectrometry* 2013, 16 (1), 29-39.
85. Zhang, T.; Zhang, J.; Derreumaux, P.; Mu, Y. Molecular mechanism of the inhibition of EGCG on the Alzheimer A β 1-42 dimer. *Journal of Physical Chemistry B* 2013, 117 (15), 3993-4002.
86. Sitkiewicz, E.; Klöniecki, M.; Poznański, J.; Bal, W.; Dadlez, M. Factors Influencing Compact-Extended Structure Equilibrium in Oligomers of A β 1-40 Peptide—An Ion Mobility Mass Spectrometry Study. *Journal of Molecular Biology* 2014, 426 (15), 2871-2885.
87. Murray, M. M.; Krone, M. G.; Bernstein, S. L.; Baumketner, A.; Condrón, M. M.; Lazo, N. D.; Teplow, D. B.; Wyttenbach, T.; Shea, J.-E.; Bowers, M. T. Amyloid β -Protein: Experiment and Theory on the 21-30 Fragment. *Journal of Physical Chemistry B* 2009, 113 (17), 6041-6046.
88. Sawyer, H. A.; Marini, J. T.; Stone, E. G.; Ruotolo, B. T.; Gillig, K. J.; Russell, D. H. The structure of gas-phase bradykinin fragment 1-5 (RPPGF) ions: an ion mobility spectrometry and H/D exchange ion-molecule reaction chemistry study. *Journal of the American Society for Mass Spectrometry* 2005, 16 (6), 893-905.

89. Bernstein, S. L.; Liu, D.; Wyttenbach, T.; Bowers, M. T.; Lee, J. C.; Gray, H. B.; Winkler, J. R. α -Synuclein: Stable compact and extended monomeric structures and pH dependence of dimer formation. *Journal of the American Society for Mass Spectrometry* 2004, 15 (10), 1435-1443.
90. Jung, J. E.; Pierson, N. A.; Marquardt, A.; Scheffner, M.; Przybylski, M.; Clemmer, D. E. Differentiation of compact and extended conformations of di-ubiquitin conjugates with lysine-specific isopeptide linkages by ion mobility-mass spectrometry. *Journal of the American Society for Mass Spectrometry* 2011, 22 (8), 1463-1471.
91. Warnke, S.; Baldauf, C.; Bowers, M. T.; Pagel, K.; von Helden, G. Photodissociation of conformer-selected ubiquitin ions reveals site-specific cis/trans isomerization of proline peptide bonds. *Journal of the American Chemical Society* 2014, 136 (29), 10308-10314.
92. Larini, L.; Gessel, M. M.; LaPointe, N. E.; Do, T. D.; Bowers, M. T.; Feinstein, S. C.; Shea, J.-E. Initiation of assembly of tau(273-284) and its Δ K280 mutant: an experimental and computational study. *Physical Chemistry Chemical Physics* 2013, 15 (23), 8916-8928.
93. Ganguly, P.; Do, T. D.; Larini, L.; LaPointe, N. E.; Feinstein, S. C.; Bowers, M. T.; Shea, J.-E. Tau Assembly: The Dominant Role of PHF6 (VQIVYK) in Microtubule Binding Region Repeat R3. *The Journal of Physical Chemistry B* 2015.
94. Laganowsky, A.; Reading, E.; Allison, T. M.; Ulmschneider, M. B.; Degiacomi, M. T.; Baldwin, A. J.; Robinson, C. V. Membrane proteins bind lipids selectively to modulate their structure and function. *Nature* 2014, 510 (7503), 172-175.
95. Konijnenberg, A.; Yilmaz, D.; Ingólfsson, H. I.; Dimitrova, A.; Marrink, S. J.; Li, Z.; Vénien-Bryan, C.; Sobott, F.; Koçer, A. Global structural changes of an ion channel during its gating are followed by ion mobility mass spectrometry. *Proceedings of the National Academy of Sciences* 2014, 111 (48), 17170-17175.
96. Counterman, A. E.; Clemmer, D. E. Anhydrous polyproline helices and globules. *The Journal of Physical Chemistry B* 2004, 108 (15), 4885-4898.
97. Sudha, R.; Jarrold, M. F. Left-handed and ambidextrous helices in the gas phase. *The Journal of Physical Chemistry B* 2005, 109 (23), 11777-11780.
98. Albrieux, F.; Calvo, F.; Chirot, F.; Vorobyev, A.; Tsybin, Y. O.; Lepere, V.; Antoine, R.; Lemoine, J.; Dugourd, P. Conformation of polyalanine and polyglycine dications in the gas phase: Insight from ion mobility spectrometry and replica-exchange molecular dynamics. *Journal of Physical Chemistry A* 2010, 114 (25), 6888-6896.

99. Atmanene, C. d.; Chaix, D.; Bessin, Y.; Declerck, N.; Van Dorsselaer, A.; Sanglier-Cianferani, S. Combination of noncovalent mass spectrometry and traveling wave ion mobility spectrometry reveals sugar-induced conformational changes of central glycolytic genes repressor/DNA complex. *Analytical Chemistry* 2010, 82 (9), 3597-3605.
100. McLean, J. R.; McLean, J. A.; Wu, Z.; Becker, C.; Perez, L. M.; Pace, C. N.; Scholtz, J. M.; Russell, D. H. Factors That Influence Helical Preferences for Singly Charged Gas-Phase Peptide Ions: The Effects of Multiple Potential Charge-Carrying Sites. *Journal of Physical Chemistry B* 2010, 114 (2), 809-816.
101. Chen, L.; Shao, Q.; Gao, Y.-Q.; Russell, D. H. Molecular Dynamics and Ion Mobility Spectrometry Study of Model β -Hairpin Peptide, Trpzip1. *Journal of Physical Chemistry A* 2011, 115 (17), 4427-4435.
102. Florance, H. V.; Stopford, A. P.; Kalapothakis, J. M.; McCullough, B. J.; Bretherick, A.; Barran, P. E. Evidence for α -helices in the gas phase: A case study using Melittin from honey bee venom. *Analyst* 2011, 136 (17), 3446-3452.
103. Ko, J. Y.; Heo, S. W.; Lee, J. H.; Oh, H. B.; Kim, H.; Kim, H. I. Host-Guest Chemistry in the Gas Phase: Complex Formation with 18-Crown-6 Enhances Helicity of Alanine-Based Peptides. *The Journal of Physical Chemistry A* 2011, 115 (49), 14215-14220.
104. Johnson, A. R.; Dilger, J. M.; Glover, M. S.; Clemmer, D. E.; Carlson, E. E. Negatively-charged helices in the gas phase. *Chemical Communications* 2014, 50 (64), 8849-8851.
105. Schubert, F.; Rossi, M.; Baldauf, C.; Pagel, K.; Warnke, S.; von Helden, G.; Filsinger, F.; Kupser, P.; Meijer, G.; Salwiczek, M. Exploring the conformational preferences of 20-residue peptides in isolation: Ac-Ala 19-Lys⁺ H⁺ vs. Ac-Lys-Ala 19⁺ H⁺ and the current reach of DFT. *Physical Chemistry Chemical Physics* 2015, 17 (11), 7373-7385.
106. Schubert, F.; Pagel, K.; Rossi, M.; Warnke, S.; Salwiczek, M.; Koksche, B.; von Helden, G.; Blum, V.; Baldauf, C.; Scheffler, M. Native like helices in a specially designed β peptide in the gas phase. *Physical Chemistry Chemical Physics* 2015, 17, 5376-5385.
107. Hill, H. H.; Hill, C. H.; Asbury, G. R.; Wu, C.; Matz, L. M.; Ichiye, T. Charge location on gas phase peptides. *International Journal of Mass Spectrometry* 2002, 219 (1), 23-37.
108. Shi, L.; Holliday, A. E.; Shi, H.; Zhu, F.; Ewing, M. A.; Russell, D. H.; Clemmer, D. E. Characterizing intermediates along the transition from polyproline I to polyproline II using ion mobility spectrometry-mass spectrometry. *Journal of the American Chemical Society* 2014, 136 (36), 12702-12711.

109. Wyttenbach, T.; Paizs, B.; Barran, P.; Brechi, L.; Liu, D.; Suhai, S.; Wysocki, V. H.; Bowers, M. T. The effect of the initial water of hydration on the energetics, structures, and H/D exchange mechanism of a family of pentapeptides: an experimental and theoretical study. *Journal of the American Chemical Society* 2003, 125 (45), 13768-13775.
110. Khakinejad, M.; Kondalaji, S. G.; Maleki, H.; Arndt, J. R.; Donohoe, G. C.; Valentine, S. J. Combining Ion Mobility Spectrometry with Hydrogen-Deuterium Exchange and Top-Down MS for Peptide Ion Structure Analysis. *Journal of The American Society for Mass Spectrometry* 2014, 25 (12), 2103-2115.
111. Schenk, E. R.; Almeida, R.; Miksovskaja, J.; Ridgeway, M. E.; Park, M. A.; Fernandez-Lima, F. Kinetic Intermediates of Holo-and Apo-Myoglobin Studied Using HDX-TIMS-MS and Molecular Dynamic Simulations. *Journal of The American Society for Mass Spectrometry* 2015, 26 (4), 555-563.
112. Barran, P. E.; Roeske, R. W.; Pawson, A. J.; Sellar, R.; Bowers, M. T.; Morgan, K.; Lu, Z.-L.; Tsuda, M.; Kusakabe, T.; Millar, R. P. Evolution of Constrained Gonadotropin-releasing Hormone Ligand Conformation and Receptor Selectivity. *Journal of Biological Chemistry* 2005, 280 (46), 38569-38575.
113. Barran, P. E.; Polfer, N. C.; Campopiano, D. J.; Clarke, D. J.; Langridge-Smith, P. R. R.; Langley, R. J.; Govan, J. R. W.; Maxwell, A.; Dorin, J. R.; Millar, R. P. Is it biologically relevant to measure the structures of small peptides in the gas-phase? *International Journal of Mass Spectrometry* 2005, 240 (3), 273-284.
114. Ruotolo, B. T.; Verbeck, G. F.; Thomson, L. M.; Gillig, K. J.; Russell, D. H. Observation of conserved solution-phase secondary structure in gas-phase tryptic peptides. *Journal of the American Chemical Society* 2002, 124 (16), 4214-4215.
115. Merenbloom, S. I.; Bohrer, B. C.; Koeniger, S. L.; Clemmer, D. E. Assessing the Peak Capacity of IMS-IMS Separations of Tryptic Peptide Ions in He at 300 K. *Analytical Chemistry* 2007, 79 (2), 515-522.
116. Cork, A. J.; Jergic, S.; Hammerschmidt, S.; Kobe, B.; Pancholi, V.; Benesch, J. L. P.; Robinson, C. V.; Dixon, N. E.; Aquilina, J. A.; Walker, M. J. Defining the structural basis of human plasminogen binding by streptococcal surface enolase. *Journal of Biological Chemistry* 2009, 284 (25), 17129-17137.
117. Zhou, M.; Politis, A.; Davies, R. B.; Liko, I.; Wu, K.-J.; Stewart, A. G.; Stock, D.; Robinson, C. V. Ion mobility-mass spectrometry of a rotary ATPase reveals ATP-induced reduction in conformational flexibility. *Nature Chemistry* 2014, 6 (3), 208-215.
118. Scott, D.; Layfield, R.; Oldham, N. J. Ion mobility - mass spectrometry reveals conformational flexibility in the deubiquitinating enzyme USP5. *Proteomics* 2015.

119. Gidden, J.; Bowers, M. T. Gas-phase conformational and energetic properties of deprotonated dinucleotides. *The European Physical Journal D-Atomic, Molecular, Optical and Plasma Physics* 2002, 20 (3), 409-419.
120. Baker, E. S.; Dupuis, N. F.; Bowers, M. T. DNA hairpin, pseudoknot, and cruciform stability in a solvent-free environment. *The Journal of Physical Chemistry B* 2009, 113 (6), 1722-1727.
121. Fenn, L. S.; Kliman, M.; Mahsut, A.; Zhao, S. R.; McLean, J. A. Characterizing ion mobility-mass spectrometry conformation space for the analysis of complex biological samples. *Analytical and Bioanalytical Chemistry* 2009, 394 (1), 235-244.
122. Rosu, F.; Gabelica, V.; De Pauw, E.; Antoine, R.; Broeyer, M.; Dugourd, P. UV Spectroscopy of DNA Duplex and Quadruplex Structures in the Gas Phase. *Journal of Physical Chemistry A* 2012, 116 (22), 5383-5391.
123. Ma, X.; Shah, S.; Zhou, M.; Park, C. K.; Wysocki, V. H.; Horton, N. C. Structural analysis of activated SgrAI-DNA oligomers using ion mobility mass spectrometry. *Biochemistry* 2013, 52 (25), 4373-4381.
124. Salpin, J.-Y.; MacAleese, L.; Chirof, F.; Dugourd, P. Structure of the Pb²⁺-deprotonated dGMP complex in the gas phase: a combined MS-MS/IRMPD spectroscopy/ion mobility study. *Physical Chemistry Chemical Physics* 2014, 16 (27), 14127-14138.
125. Gidden, J.; Baker, E. S.; Ferzoco, A.; Bowers, M. T. Structural motifs of DNA complexes in the gas phase. *International Journal of Mass Spectrometry* 2005, 240 (3), 183-193.
126. Arcella, A.; Portella, G.; Ruiz, M. L.; Eritja, R.; Vilaseca, M.; Gabelica, V.; Orozco, M. Structure of Triplex DNA in the Gas Phase. *Journal of the American Chemical Society* 2012, 134 (15), 6596-6606.
127. Baker, E. S.; Bernstein, S. L.; Bowers, M. T. Structural characterization of G-quadruplexes in deoxyguanosine clusters using ion mobility mass spectrometry. *Journal of the American Society for Mass Spectrometry* 2005, 16 (7), 989-997.
128. Baker, E. S.; Hong, J. W.; Gaylord, B. S.; Bazan, G. C.; Bowers, M. T. PNA/dsDNA complexes: site specific binding and dsDNA biosensor applications. *Journal of the American Chemical Society* 2006, 128 (26), 8484-8492.
129. Gabelica, V.; Shammel Baker, E.; Teulade-Fichou, M.-P.; De Pauw, E.; Bowers, M. T. Stabilization and structure of telomeric and c-myc region intramolecular G-quadruplexes: the role of central cations and small planar ligands. *Journal of the American Chemical Society* 2007, 129 (4), 895-904.

130. Plasencia, M. D.; Isailovic, D.; Merenbloom, S. I.; Mechref, Y.; Clemmer, D. E. Resolving and assigning N-linked glycan structural isomers from ovalbumin by IMS-MS. *Journal of the American Society for Mass Spectrometry* 2008, 19 (11), 1706-1715.
131. Yamaguchi, Y.; Nishima, W.; Re, S.; Sugita, Y. Confident identification of isomeric N-glycan structures by combined ion mobility mass spectrometry and hydrophilic interaction liquid chromatography. *Rapid Communications in Mass Spectrometry* 2012, 26 (24), 2877-2884, S2877/1-S2877/7.
132. Kim, H. I.; Kim, H.; Pang, E. S.; Ryu, E. K.; Beegle, L. W.; Loo, J. A.; Goddard, W. A.; Kanik, I. Structural characterization of unsaturated phosphatidylcholines using traveling wave ion mobility spectrometry. *Analytical Chemistry* 2009, 81 (20), 8289-8297.
133. Pouilly, J. C.; Lecomte, F.; Nieuwjaer, N.; Manil, B.; Schermann, J. P.; Desfrancois, C.; Grégoire, G.; Ballivian, R.; Chirot, F.; Lemoine, J. Combining ion mobility mass spectrometry and infrared multiphoton dissociation spectroscopy to probe the structure of gas-phase vancomycin–Ac 2 L K D A D A non-covalent complex. *International Journal of Mass Spectrometry* 2010, 297 (1), 28-35.
134. Stow, S. M.; Goodwin, C. R.; Kliman, M.; Bachmann, B. O.; McLean, J. A.; Lybrand, T. P. Distance Geometry Protocol to Generate Conformations of Natural Products to Structurally Interpret Ion Mobility-Mass Spectrometry Collision Cross Sections. *The Journal of Physical Chemistry B* 2014, 118 (48), 13812-13820.
135. Knapman, T. W.; Berryman, J. T.; Campuzano, I.; Harris, S. A.; Ashcroft, A. E. Considerations in experimental and theoretical collision cross-section measurements of small molecules using travelling wave ion mobility spectrometry-mass spectrometry. *International Journal of Mass Spectrometry* 2010, 298 (1), 17-23.
136. Campuzano, I.; Bush, M. F.; Robinson, C. V.; Beaumont, C.; Richardson, K.; Kim, H.; Kim, H. I. Structural characterization of drug-like compounds by ion mobility mass spectrometry: comparison of theoretical and experimentally derived nitrogen collision cross sections. *Analytical Chemistry* 2011, 84 (2), 1026-1033.
137. Dear, G. J.; Munoz - Muriedas, J.; Beaumont, C.; Roberts, A.; Kirk, J.; Williams, J. P.; Campuzano, I. Sites of metabolic substitution: investigating metabolite structures utilising ion mobility and molecular modelling. *Rapid Communications in Mass Spectrometry* 2010, 24 (21), 3157-3162.
138. Hyung, S.-J.; DeToma, A. S.; Brender, J. R.; Lee, S.; Vivekanandan, S.; Kochi, A.; Choi, J.-S.; Ramamoorthy, A.; Ruotolo, B. T.; Lim, M. H. Insights into

- antiamyloidogenic properties of the green tea extract (-)-epigallocatechin-3-gallate toward metal-associated amyloid- β species. *Proceedings of the National Academy of Sciences* 2013, 110 (10), 3743-8.
139. Goodwin, C. R.; Fenn, L. S.; Derewacz, D. K.; Bachmann, B. O.; McLean, J. A. Structural Mass Spectrometry: Rapid Methods for Separation and Analysis of Peptide Natural Products. *Journal of Natural Products* 2012, 75 (1), 48-53.
140. Tintaru, A.; Pricl, S.; Denbigh, L.; Liu, X.; Peng, L.; Charles, L. Conformational changes of small PAMAM dendrimers as a function of their charge state: A combined electrospray mass spectrometry, traveling-wave ion mobility and molecular modeling study. *International Journal of Mass Spectrometry* 2013, 354-355, 235-241.
141. Memboeuf, A.; Vékey, K.; Lendvay, G. Structure and energetics of poly (ethylene glycol) cationized by Li⁺, Na⁺, K⁺ and Cs⁺: a first-principles study. *European Journal of Mass Spectrometry* 2011, 17 (1), 33-46.
142. Larriba, C.; Fernandez de la Mora, J. The Gas Phase Structure of Coulombically Stretched Polyethylene Glycol Ions. *Journal of Physical Chemistry B* 2012, 116 (1), 593-598.
143. De Winter, J.; Lemaire, V.; Ballivian, R.; Chirot, F.; Coulembier, O.; Antoine, R.; Lemoine, J.; Cornil, J.; Dubois, P.; Dugourd, P.; Gerbaux, P. Size Dependence of the Folding of Multiply Charged Sodium Cationized Polylactides Revealed by Ion Mobility Mass Spectrometry and Molecular Modelling. *Chemistry - A European Journal* 2011, 17 (35), 9738-9745, S9738/1-S9738/4.
144. Gidden, J.; Bowers, M. T.; Jackson, A. T.; Scrivens, J. H. Gas-phase conformations of cationized poly (styrene) oligomers. *Journal of the American Society for Mass Spectrometry* 2002, 13 (5), 499-505.
145. Ahmed, A.; Cho, Y.; Giles, K.; Riches, E.; Lee, J. W.; Kim, H. I.; Choi, C. H.; Kim, S. Elucidating Molecular Structures of Nonalkylated and Short-Chain Alkyl ($n < 5, (\text{CH}_2)_n$) Aromatic Compounds in Crude Oils by a Combination of Ion Mobility and Ultrahigh-Resolution Mass Spectrometries and Theoretical Collisional Cross-Section Calculations. *Analytical Chemistry* 2014, 86 (7), 3300-3307.
146. Kozole, J.; Tomlinson-Phillips, J.; Stairs, J. R.; Harper, J. D.; Lukow, S. R.; Lareau, R. T.; Boudries, H.; Lai, H.; Brauer, C. S. Characterizing the gas phase ion chemistry of an ion trap mobility spectrometry based explosive trace detector using a tandem mass spectrometer. *Talanta* 2012, 99, 799-810.
147. Benassi, M.; Corilo, Y. E.; Uria, D.; Augusti, R.; Eberlin, M. N. Recognition and resolution of isomeric alkyl anilines by mass spectrometry. *Journal of the American Society for Mass Spectrometry* 2009, 20 (2), 269-277.

148. Borsdorf, H.; Neitsch, K.; Eiceman, G. A.; Stone, J. A. A comparison of the ion chemistry for mono-substituted toluenes and anilines by three methods of atmospheric pressure ionization with ion mobility spectrometry. *Talanta* 2009, 78 (4), 1464-1475.
149. Forsythe, J. G.; Stow, S. M.; Nefzger, H.; Kwiecien, N. W.; May, J. C.; McLean, J. A.; Hercules, D. M. Structural Characterization of Methylenedianiline Regioisomers by Ion Mobility-Mass Spectrometry, Tandem Mass Spectrometry, and Computational Strategies: I. Electrospray Spectra of 2-Ring Isomers. *Analytical Chemistry* 2014, 86, 4362-4370.
150. Rusyniak, M. J.; Ibrahim, Y. M.; Wright, D. L.; Khanna, S. N.; El-Shall, M. S. Gas-Phase Ion Mobilities and Structures of Benzene Cluster Cations (C₆H₆)ⁿ⁺, n= 2-6. *Journal of the American Chemical Society* 2003, 125 (39), 12001-12013.
151. Attah, I. K.; Hamid, A. M.; Meot-Ner, M.; El-Shall, M. S.; Aziz, S. G.; Alyoubi, A. O. Substituent effects on noncovalent bonds: complexes of ionized benzene derivatives with hydrogen cyanide. *The Journal of Physical Chemistry A* 2013, 117 (41), 10588-10597.
152. Leavell, M. D.; Gaucher, S. P.; Leary, J. A.; Taraszka, J. A.; Clemmer, D. E. Conformational studies of Zn-ligand-hexose diastereomers using ion mobility measurements and density functional theory calculations. *Journal of the American Society for Mass Spectrometry* 2002, 13 (3), 284-293.
153. Baker, E. S.; Hong, J. W.; Gidden, J.; Bartholomew, G. P.; Bazan, G. C.; Bowers, M. T. Diastereomer assignment of an olefin-linked bis-paracyclophane by ion mobility mass spectrometry. *Journal of the American Chemical Society* 2004, 126 (20), 6255-6257.
154. Révész, Á.; Schröder, D.; Rokob, T. A.; Havlík, M.; Dolenský, B. Identification and interconversion of diastereomeric oligo-Tröger bases probed by ion mobility mass spectrometry. *Physical Chemistry Chemical Physics* 2012, 14 (19), 6987-6995.
155. Flick, T. G.; Campuzano, I. D. G.; Bartberger, M. D. Structural Resolution of 4-Substituted Proline Diastereomers with Ion Mobility Spectrometry via Alkali Metal Ion Cationization. *Analytical Chemistry* 2015, 87 (6), 3300-3307.
156. Coughlan, N. J. A.; Catani, K. J.; Adamson, B. D.; Wille, U.; Bieske, E. J. Photoisomerization action spectrum of retinal protonated Schiff base in the gas phase. *The Journal of Chemical Physics* 2014, 140 (16), 164307.
157. Coughlan, N. J. A.; Adamson, B. D.; Catani, K. J.; Wille, U.; Bieske, E. J. Ion Mobility Unlocks the Photofragmentation Mechanism of Retinal Protonated Schiff Base. *The Journal of Physical Chemistry Letters* 2014, 5 (18), 3195-3199.

158. Koyasu, K.; Komatsu, K.; Misaizu, F. Structural transition of zinc oxide cluster cations: Smallest tube like structure at (ZnO)⁶⁺. *The Journal of Chemical Physics* 2013, 139 (16), 164308.
159. Ota, K.; Koyasu, K.; Ohshimo, K.; Misaizu, F. Structures of cobalt oxide cluster cations studied by ion mobility mass spectrometry. *Chemical Physics Letters* 2013, 588, 63-67.
160. Keijiro Ohshimo, S. A., Tatsuya Komukai, Ryoichi Moriyama, and; Misaizu, F. Structures and CO-Adsorption Reactivities of Nickel Oxide Cluster Cations Studied by Ion Mobility Mass Spectrometry. *The Journal of Physical Chemistry C* 2014.
161. Lee, S. J. C.; Lee, J. W.; Lee, H. H.; Seo, J.; Noh, D. H.; Ko, Y. H.; Kim, K.; Kim, H. I. Host-guest chemistry from solution to the gas phase: an essential role of direct interaction with water for high-affinity binding of cucurbit [n] urils. *The Journal of Physical Chemistry B* 2013, 117 (29), 8855-8864.
162. Öeren, M.; Shmatova, E.; Tamm, T.; Aav, R. Computational and ion mobility MS study of (all-S)-cyclohexylhemicucurbit [6] uril structure and complexes. *Physical Chemistry Chemical Physics* 2014, 16 (36), 19198-19205.
163. Noh, D. H.; Lee, S. J. C.; Lee, J. W.; Kim, H. I. Host-Guest Chemistry in the Gas Phase: Complex Formation of Cucurbit [6] uril with Proton-bound Water Dimer. *Journal of The American Society for Mass Spectrometry* 2014, 25 (3), 410-421.
164. Belowich, M. E.; Valente, C.; Smaldone, R. A.; Friedman, D. C.; Thiel, J.; Cronin, L.; Stoddart, J. F. Positive Cooperativity in the Template-Directed Synthesis of Monodisperse Macromolecules. *Journal of the American Chemical Society* 2012, 134 (11), 5243-5261.
165. Perera, S.; Li, X.; Soler, M.; Schultz, A.; Wesdemiotis, C.; Moorefield, C. N.; Newkome, G. R. Hexameric Palladium (II) Terpyridyl Metallomacrocycles: Assembly with 4, 4' - Bipyridine and Characterization by TWIM Mass Spectrometry. *Angewandte Chemie International Edition* 2010, 49 (37), 6539-6544.
166. Chan, Y.-T.; Li, X.-P.; Moorefield, C. N.; Wesdemiotis, C.; Newkome, G. R. Towards larger polygonal architectures: synthesis and characterization of iron(II)- and ruthenium(II)-bis(terpyridine) metallomacrocycles. *Chemistry - A European Journal* 2011, 17 (28), 7750-7754, S7750/1-S7750/23.
167. Heo, S. W.; Choi, T. S.; Park, K. M.; Ko, Y. H.; Kim, S. B.; Kim, K.; Kim, H. I. Host-guest chemistry in the gas phase: selected fragmentations of CB [6]-peptide complexes at lysine residues and its utility to probe the structures of small proteins. *Analytical Chemistry* 2011, 83 (20), 7916-7923.

168. Wang, J. L.; Li, X.; Lu, X.; Chan, Y. T.; Moorefield, C. N.; Wesdemiotis, C.; Newkome, G. R. Dendron - Functionalized Bis (terpyridine)-Iron (II) or - Cadmium (II) Metallomacrocycles: Synthesis, Traveling - Wave Ion - Mobility Mass Spectrometry, and Photophysical Properties. *Chemistry-A European Journal* 2011, 17 (17), 4830-4838.
169. Schultz, A.; Li, X.; Moorefield, C. N.; Wesdemiotis, C.; Newkome, G. R. Self-Assembly and Characterization of 3D Metallamacrocycles: A Study of Supramolecular Constitutional Isomers. *European Journal of Inorganic Chemistry* 2013, 2013 (14), 2492-2497.
170. Wang, M.; Wang, C.; Hao, X.-Q.; Li, X.; Vaughn, T. J.; Zhang, Y.-Y.; Yu, Y.; Li, Z.-Y.; Song, M.-P.; Yang, H.-B. From trigonal bipyramidal to platonic solids: self-assembly and self-sorting study of terpyridine-based 3D architectures. *Journal of the American Chemical Society* 2014, 136 (29), 10499-10507.
171. Gidden, J.; Kemper, P. R.; Shammel, E.; Fee, D. P.; Anderson, S.; Bowers, M. T. Application of ion mobility to the gas-phase conformational analysis of polyhedral oligomeric silsesquioxanes (POSS). *International Journal of Mass Spectrometry* 2003, 222 (1-3), 63-73.
172. Anderson, S. E.; Baker, E. S.; Mitchell, C.; Haddad, T. S.; Bowers, M. T. Structure of Hybrid Polyhedral Oligomeric Silsesquioxane Propyl Methacrylate Oligomers Using Ion Mobility Mass Spectrometry and Molecular Mechanics. *Chemistry of Materials* 2005, 17 (10), 2537-2545.
173. Anderson, S. E.; Mitchell, C.; Haddad, T. S.; Vij, A.; Schwab, J. J.; Bowers, M. T. Structural Characterization of POSS Siloxane Dimer and Trimer. *Chemistry of Materials* 2006, 18 (6), 1490-1497.
174. Anderson, S. E.; Bodzin, D. J.; Haddad, T. S.; Boatz, J. A.; Mabry, J. M.; Mitchell, C.; Bowers, M. T. Structural Investigation of Encapsulated Fluoride in Polyhedral Oligomeric Silsesquioxane Cages Using Ion Mobility Mass Spectrometry and Molecular Mechanics. *Chemistry of Materials* 2008, 20 (13), 4299-4309.
175. Brocker, E. R.; Anderson, S. E.; Northrop, B. H.; Stang, P. J.; Bowers, M. T. Structures of Metallosupramolecular Coordination Assemblies Can Be Obtained by Ion Mobility Spectrometry-Mass Spectrometry. *Journal of the American Chemical Society* 2010, 132 (38), 13486-13494.
176. Ren, X.; Sun, B.; Tsai, C.-C.; Tu, Y.; Leng, S.; Li, K.; Kang, Z.; Horn, R. M. V.; Li, X.; Zhu, M. Synthesis, self-assembly, and crystal structure of a shape-persistent polyhedral-oligosilsesquioxane-nanoparticle-tethered perylene diimide. *The Journal of Physical Chemistry B* 2010, 114 (14), 4802-4810.

177. Politis, A.; Park, A. Y.; Hyung, S.-J.; Barsky, D.; Ruotolo, B. T.; Robinson, C. V. Integrating ion mobility mass spectrometry with molecular modelling to determine the architecture of multiprotein complexes. *PLoS One* 2010, 5 (8), e12080.
178. Fernandez-Lima, F. A.; Wei, H.; Gao, Y. Q.; Russell, D. H. On the Structure Elucidation Using Ion Mobility Spectrometry and Molecular Dynamics. *Journal of Physical Chemistry A* 2009, 113 (29), 8221-8234.
179. Wyttenbach, T.; Bowers, M. T. *Modern Mass Spectrometry, Topics in Current Chemistry*; Schalley, C. A., Ed.; Springer: Berlin, 2003; 225, pp 207-232.
180. McLean, J. A.; Ruotolo, B. T.; Gillig, K. J.; Russell, D. H. Ion mobility-mass spectrometry: a new paradigm for proteomics. *International Journal of Mass Spectrometry* 2005, 240 (3), 301-315.
181. Uetrecht, C.; Rose, R. J.; van Duijn, E.; Lorenzen, K.; Heck, A. J. R. Ion mobility mass spectrometry of proteins and protein assemblies. *Chemical Society Reviews* 2010, 39 (5), 1633-1655.
182. Park, A. Y.; Robinson, C. V. Protein-nucleic acid complexes and the role of mass spectrometry in their structure determination. *Critical Reviews in Biochemistry and Molecular Biology* 2011, 46 (2), 152-164.
183. van der Spoel, D.; Marklund, E. G.; Larsson, D. S. D.; Caleman, C. Proteins, lipids, and water in the gas phase. *Macromolecular Bioscience* 2011, 11 (1), 50-59.
184. Laphorn, C.; Pullen, F.; Chowdhry, B. Z. Ion mobility spectrometry - mass spectrometry (IMS - MS) of small molecules: Separating and assigning structures to ions. *Mass Spectrometry Reviews* 2013, 32 (1), 43-71.
185. Bayer. 2013 Annual Report. 2013.
<http://www.annualreport2013.bayer.com/en/bayer-annual-report-augmented-version-2013.pdf> (accessed December 22, 2014).
186. SABIC. Annual Report 2013. 2013.
http://www.sabic.com/corporate/en/newsandmediarelations/publications/overview_annual_report.
187. DuPont. Non-GAAP Reconciliations 2008-2013. 2014.
[http://investors.dupont.com/files/doc_downloads/IR-Webcharts-Yearly-2008-2013-Revised-10-28-\(2\)_v001_t2z8i6.pdf](http://investors.dupont.com/files/doc_downloads/IR-Webcharts-Yearly-2008-2013-Revised-10-28-(2)_v001_t2z8i6.pdf) (accessed December 22, 2014).
188. Nielen, M. W. F. MALDI time-of-flight mass spectrometry of synthetic polymers. *Mass Spectrometry Reviews* 1999, 18 (5), 309-344.

189. Scrivens, J. H.; Jackson, A. T. Characterisation of synthetic polymer systems. *International Journal of Mass Spectrometry* 2000, 200 (1), 261-276.
190. Murgasova, R.; Hercules, D. M. MALDI of synthetic polymers—an update. *International Journal of Mass Spectrometry* 2003, 226 (1), 151-162.
191. Crecelius, A. C.; Baumgaertel, A.; Schubert, U. S. Tandem mass spectrometry of synthetic polymers. *Journal of Mass Spectrometry* 2009, 44 (9), 1277-1286.
192. Wesdemiotis, C.; Solak, N.; Polce, M. J.; Dabney, D. E.; Chaicharoen, K.; Katzenmeyer, B. C. Fragmentation pathways of polymer ions. *Mass Spectrometry Reviews* 2011, 30 (4), 523-559.
193. Aminlashgari, N.; Hakkarainen, M. *Mass Spectrometry of Polymers – New Techniques*, Advances in Polymer Science; Hakkarainen, M., Ed.; Springer: Berlin, 2012; 248, pp 1-38.
194. Feher, M.; Schmidt, J. M. Property distributions: differences between drugs, natural products, and molecules from combinatorial chemistry. *Journal of Chemical Information and Computer Sciences* 2003, 43 (1), 218-227.
195. Harry, E. L.; Weston, D. J.; Bristow, A. W. T.; Wilson, I. D.; Creaser, C. S. An approach to enhancing coverage of the urinary metabolome using liquid chromatography-ion mobility-mass spectrometry. *Journal of Chromatography B* 2008, 871 (2), 357-361.
196. Kaplan, K.; Dwivedi, P.; Davidson, S.; Yang, Q.; Tso, P.; Siems, W.; Hill, H. H. Monitoring Dynamic Changes in Lymph Metabolome of Fasting and Fed Rats by Electrospray Ionization-Ion Mobility Mass Spectrometry (ESI-IMMS). *Analytical Chemistry* 2009, 81 (19), 7944-7953.
197. Dwivedi, P.; Schultz, A. J.; Hill, H. H. Metabolic profiling of human blood by high-resolution ion mobility mass spectrometry (IM-MS). *International Journal of Mass Spectrometry* 2010, 298 (1-3), 78-90.
198. Castaneda, F.; Zimmermann, D.; Nolte, J.; Baumbach, J. I. Role of undecan-2-one on ethanol-induced apoptosis in HepG2 cells. *Cell Biology and Toxicology* 2007, 23 (6), 477-485.
199. Zimmermann, D.; Hartmann, M.; Nolte, J.; Baumbach, J. I. First detection of metabolites of the colon cancer cell line SW 480 using MCC/IMS and GC/MS. *International Journal of Ion Mobility Spectrometry* 2005, 8 (2), 3-6.
200. Kaplan, K.; Liu, X.; Fu, Y.-M.; Lin, H.; Meadows, G. G.; Siems, W.; Hill, H. H., Jr. Metabolic differences among melanoma and two prostate cancer cell lines by electrospray ion mobility mass spectrometry. *International Journal of Ion Mobility Spectrometry* 2011, 14 (4), 151-158.

201. Enders, J. R.; Marasco, C. C.; Kole, A.; Nguyen, B.; Sevugarajan, S.; Seale, K. T.; Wikswo, J. P.; McLean, J. A. Towards monitoring real-time cellular response using an integrated microfluidics-matrix assisted laser desorption ionisation/nanoelectrospray ionisation-ion mobility-mass spectrometry platform. *Iet Systems Biology* 2010, 4 (6), 416-427.
202. Matz, L. M.; Hill Jr, H. H. Evaluation of opiate separation by high-resolution electropray ionization-ion mobility spectrometry/mass spectrometry. *Analytical Chemistry* 2001, 73 (8), 1664-1669.
203. Matz, L. M.; Hill, H. H.; Beegle, L. W.; Kanik, I. Investigation of drift gas selectivity in high resolution ion mobility spectrometry with mass spectrometry detection. *Journal of the American Society for Mass Spectrometry* 2002, 13 (4), 300-307.
204. Trim, P. J.; Henson, C. M.; Avery, J. L.; McEwen, A.; Snel, M. F.; Claude, E.; Marshall, P. S.; West, A.; Princivalle, A. P.; Clench, M. R. Matrix-assisted laser desorption/ionization-ion mobility separation-mass spectrometry imaging of vinblastine in whole body tissue sections. *Analytical Chemistry* 2008, 80 (22), 8628-8634.
205. Chan, E. C. Y.; New, L. S.; Yap, C. W.; Goh, L. T. Pharmaceutical metabolite profiling using quadrupole/ion mobility spectrometry/time-of-flight mass spectrometry. *Rapid Communications in Mass Spectrometry* 2009, 23 (3), 384-394.
206. Kaplan, K. A.; Chiu, V. M.; Lukus, P. A.; Zhang, X.; Siems, W. F.; Schenk, J. O.; Hill, H. H., Jr. Neuronal metabolomics by ion mobility mass spectrometry: cocaine effects on glucose and selected biogenic amine metabolites in the frontal cortex, striatum, and thalamus of the rat. *Analytical Bioanalytical Chemistry* 2013.
207. Dwivedi, P.; Wu, P.; Klopsch, S. J.; Puzon, G. J.; Xun, L.; Hill, H. H. Metabolic profiling by ion mobility mass spectrometry (IMMS). *Metabolomics* 2008, 4 (1), 63-80.
208. Dwivedi, P.; Puzon, G.; Tam, M.; Langlais, D.; Jackson, S.; Kaplan, K.; Siems, W. F.; Schultz, A. J.; Xun, L. Y.; Woodsd, A.; Hill, H. H. Metabolic profiling of *Escherichia coli* by ion mobility-mass spectrometry with MALDI ion source. *Journal of Mass Spectrometry* 2010, 45 (12), 1383-1393.
209. Perl, T.; Juenger, M.; Vautz, W.; Nolte, J.; Kuhns, M.; Borg-von, Z. M.; Quintel, M. Detection of characteristic metabolites of *Aspergillus fumigatus* and *Candida* species using ion mobility spectrometry - metabolic profiling by volatile organic compounds. *Mycoses* 2011, 54 (6), e828-e837.

CHAPTER 2

STRUCTURAL CHARACTERIZATION OF METHYLENEDIANILINE REGIOISOMERS BY ION MOBILITY-MASS SPECTROMETRY, TANDEM MASS SPECTROMETRY, AND COMPUTATIONAL STRATEGIES

2.1. Introduction

Polyurethanes are inherently complex and thus structural characterization of these polymers can be challenging. Intrinsic distributions of molecular size and cross-linking produce structural heterogeneity,¹ even amongst purified samples. Additional heterogeneity can arise from varying amounts of hard and soft block segments and structural variations within the segments themselves.

Methylenedianiline (MDA) is used to synthesize methylene diphenyl diisocyanate (MDI), a major hard block component of polyurethanes. Most formulations of industrial grade MDA primarily contain 4,4'-MDA, along with a number of structural isomers and multimers.²⁻⁴ The purpose of this research is to fully characterize structural variations within MDA mixtures and eventually MDI mixtures. However, in order to better understand complex mixtures of MDA and MDI, it is first necessary to study 2-ring MDA regioisomers that differ only by the position of amine functional groups, as shown in Figure 2.1a (asterisks indicate unique protonation sites). By characterizing specific 2-ring species, we can gain insight into the behavior of more complex multimeric structures, and eventually determine relative abundances in complex MDA mixtures. Here, we also aim to characterize purified 3-ring and 4-ring MDA multimeric regioisomers. Possible protonation sites on the 3-ring and 4-ring MDA species are also

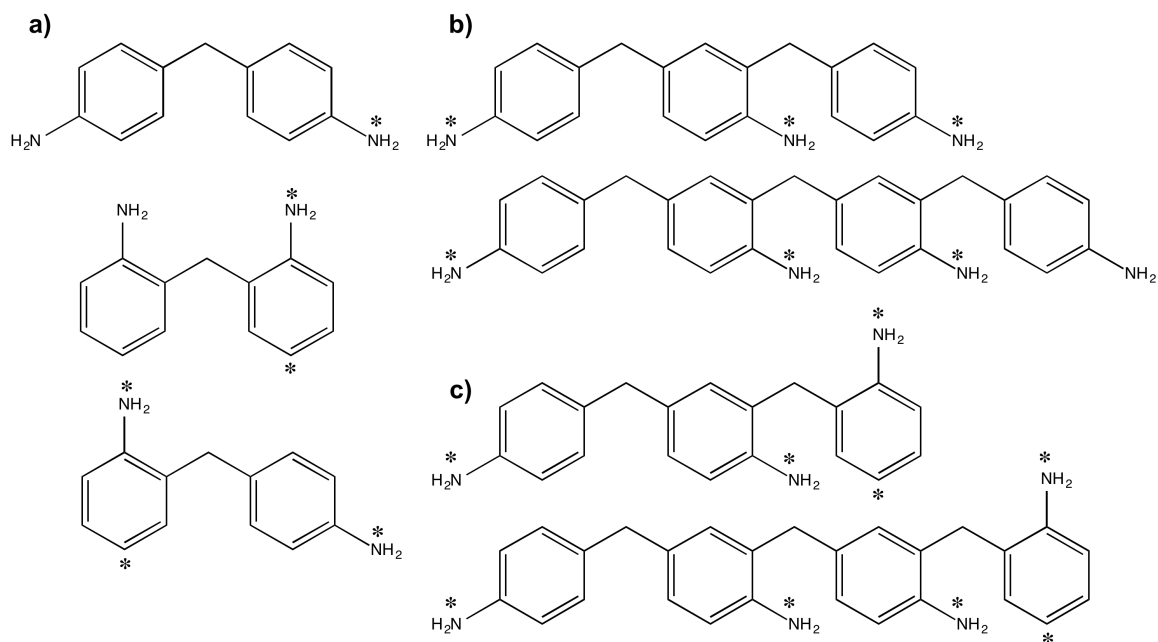


Figure 2.1. Structures of MDA positional isomers for a) 2-ring MDA (*theo.* neutral molecule monoisotopic mass =198.12 Da). The positional isomers will be referred to as 4,4'-MDA, 2,2'-MDA, and 2,4'-MDA. In b) and c) 3-ring MDA (303.17 Da) and 4-ring MDA (408.23 Da). In b) each additional aniline ring is attached in the para position while in c) the final aniline ring has its amine group in the ortho position. Potential protonation sites are labeled with an asterisk.

illustrated in Figure 2.1. In Figure 2.1b, each aniline ring is attached with its amine group in the para position for both 3-ring and 4-ring MDA, which represents the primary solution-phase conformation based on NMR studies (Appendix B, Figures B.1-6,26,27). Due to the location of the amine groups and bridging carbons, protonation in Figure 2.1b is possible only on the amine group and not the aniline ring. The structures shown in Figure 2.1c have one terminal aniline ring with its amine group attached in the ortho position (this structure is only representative of < 5% of the NMR signals for both the 3-ring and 4-ring MDA). Thus, while it is possible for both 3-ring and 4-ring MDA species to have the last aniline ring attached with an amine group in the ortho position (Figure 2.1c), this isomer is not preferred. As a result, this thesis will focus on the structures and protonation sites shown in Figure 2.1b.

Previous MDA studies in the literature were typically done in a workplace exposure context, and utilized gas chromatography - mass spectrometry (GC-MS),⁴⁻⁶ or more recently liquid chromatography - mass spectrometry (LC-MS) detection.⁷⁻¹² Limitations of these methods for MDA characterization include the necessity for sample derivatization (GC-MS), and an inability to detect and differentiate low abundance isomers such as 2,4'-MDA and 2,2'-MDA (both GC-MS and LC-MS). In contrast, techniques, which probe gas-phase structural conformations, may provide insight into the characterization and discrimination of even low-abundance isomers without requiring sample pre-treatment.

Ion mobility - mass spectrometry (IM-MS) is a gas-phase electrophoretic separation technique coupled to a mass measurement technique and thus is capable of differentiating isomeric species and characterizing these species by ion size and mass. In

IM, ions are subject to low energy collisions with a neutral buffer gas, and subsequently separated by their effective gas-phase size.¹³⁻¹⁶ Ions which possess a large cross-sectional area experience a high number of collisions and are impeded, whereas ions which possess a smaller cross-sectional area experience fewer collisions and traverse the IM drift region more rapidly. Gas-phase ion size and shape are described by the molecular collision cross section (CCS), which can be calculated directly using the elution time from an electrostatic drift tube (typically on the order of milliseconds). Coupled with molecular modeling studies, CCS data can be used to investigate three-dimensional gas-phase structures. A more detailed explanation of IM-MS methodology as well as potential applications for polymer analysis can be found elsewhere in the literature.¹⁷⁻²⁴

The additional dimension of separation based on the size and shape of gas-phase ions allows for the differentiation of isobaric species based on CCS. IM characterization of low-molecular-weight structural isomers was first studied by Hagen over two decades ago using a stand-alone (no MS) ambient pressure drift tube instrument.^{25,26} Small but reproducible CCS differences were observed for isomers due to factors such as the position of unique atoms (*e.g.* nitrogen in a carbon ring system), location of functional groups, and connectivity of aromatic ring systems. For example, a consistent trend was observed for substituted toluene isomers, where substitution at the *meta* position led to higher CCS values than substitutions at *para* or *ortho* positions.²⁵ Nevertheless, at the time Hagen was limited in his ability to fully interpret the data due to the lack of robust MS detection.

Inspired by Hagen's as well as other previous work, we used MS/MS, IM-MS, and IM-MS/MS methods to fully characterize and differentiate 2-ring, 3-ring, and 4-ring

MDA standards.^{23, 27-29} Two IM-MS instruments are utilized in this study: a commercial traveling wave instrument which supports multiple stages of fragmentation and a commercial drift tube instrument which supports direct CCS measurements in a variety of drift gases. CCS values were obtained for each isomer, which provides significant insight into isomeric gas-phase conformation(s) and their respective stabilities. Moreover, we utilize computational modeling to assist our interpretation of IM-MS data, and to facilitate connecting isomeric differences in CCS with molecular structures.

2.2 Experimental Section

Materials

4,4'-MDA, 2,4'-MDA, and 2,2'-MDA 2-ring MDA samples as well as 3-ring and 4-ring MDA samples were provided by Dr. Stefan Wershofen, Bayer MaterialScience AG, 47812 Uerdingen, Germany. Their authenticity was established by ¹³C and ¹H NMR as shown in Appendix B (Figures B.1-B.6, B.26, and B.27). Tetraalkylammonium salts and solvents were purchased from Sigma-Aldrich (St. Louis, MO). These included tetraalkylammonium bromides (TAA 1-8) and HPLC grade methanol. Water blended with 0.1% formic acid (optima grade) was obtained from Thermo Fisher Scientific (Waltham, MA).

Instrumentation

Traveling-wave ESI-IM-TOF/MS

MS, MS/MS, and traveling-wave (TWIM) IM-MS data were obtained on interchangeable Synapt G2 and G2-S (Waters Corporation, Milford, MA) mass spectrometers. The TWIM (traveling wave ion mobility) platform differs from traditional drift-tube ion mobility (DTIM) in that it utilizes electrodynamic rather than electrostatic

fields. As the exact quantitative nature of the TWIM electrodynamic field is unknown, collision cross section (CCS) values cannot be obtained directly from the kinetic theory of gasses using TWIM experimental drift time values. Nevertheless, TWIM CCS values can be determined when measurements are calibrated using DTIM CCS values from the literature.¹⁷ In order to obtain CCS values from TWIM measurements, we used a series of quaternary ammonium salts as calibration standards in conjunction with their literature DTIM CCS values.³⁰

All samples were analyzed as positive ions with electrospray ionization (ESI). The TWIM drift cell was operated with a pressure of 3 mbar (2.25 Torr), an electrodynamic wave height of 35 V and velocity of 700 m/s, and the TOF resolution ($m/\Delta m$) was approximately 20,000. MDA samples were dissolved at a concentration of 0.10 mg/mL in 9:1 methanol:water containing 0.1% formic acid (v/v). When metal salts were used, each was at a final concentration of 0.050 mg/mL. A direct infusion flow rate of 6.00 $\mu\text{L}/\text{min}$ was used for all samples. Other instrument settings were as follows: 3.00 kV capillary voltage, 80 °C source temperature, 150 °C desolvation temperature, 10 V sampling cone, 2 V extraction cone, 20 L/hr cone gas flow, 1 mL/min trap gas flow, 90 mL/min IMS gas flow. All collision-induced dissociation (CID) experiments were performed prior to TWIM mobility separation. The TOF calibration was performed using sodium formate clusters.

Center-of-mass (COM) collision energies were converted from lab-frame collision energies using the following equation:

$$E_{COM} = E_{LAB} * \frac{m_{gas}}{m_{gas} + m_{ion}}.$$

Lab-frame energies are the voltages applied in the tandem MS instrumentation, while COM energy is essentially the available energy for molecular rearrangement or fragmentation.³¹ Therefore, COM energy typically has more useful interpretation power across various instrument platforms.³² The MS/MS capabilities of these instruments enable fragmentation experiments to be conducted both before and after the IM region providing a wider variety of fragmentation information.

Electrostatic drift-tube ESI-IM-TOF/MS

DTIM measurements using nitrogen and helium buffer gas were performed on a prototype and commercial ESI-IM-QTOF mass spectrometer (Agilent Technologies, Santa Clara, CA).³³ The prototype instrument was used for 2-ring MDA data while the commercial instrument was used for 3-ring and 4-ring MDA data due to availability for the respective instruments at the time of the experiment. Details of this instrumentation are provided elsewhere, but briefly the IM-MS consists of a 78 cm uniform-field drift tube coupled to a high resolution QTOFMS ($m/\Delta m$ 40,000). The buffer gas was maintained at a pressure of *ca.* 4 Torr and drift voltages were varied in order to correct for the non-IM flight time of ions through the interfacing ion optics. CCS values were calculated from drift times using the Mason-Schamp equation. MDA samples were at a concentration of 0.095 mg/mL in 9:1 methanol:water containing 0.1% formic acid (*v/v*); also, LiCl and NaCl were added to the solution so that each had a final concentration of 0.025 mg/mL. A direct infusion flow rate of 6.00 $\mu\text{L}/\text{min}$ was used. Nitrogen-based CCS measurements were obtained for direct comparison with TWIM CCS measurements while helium-based CCS values were measured for comparison with computational CCS calculations.

Computational and modeling data

As IM provides a general structural description, IM-MS results are often supplemented with computational studies to gain further insight into the gas phase conformations of the molecules of interest.³⁴ These studies generally include two steps: 1) computationally sampling the conformational space and 2) theoretical determination of CCS values for the generated conformations. More detailed structural information can then be inferred from closer inspection of generated conformations that align with experimental CCS values. Although different methods exist for both conformational sampling and theoretical determination of CCS values, the following protocol was used in this study. A geometry optimization at the Hartree-Fock level with a 6-31G* basis set was performed with Gaussian 09³⁵ for all of the possible protonation sites on each isomer (2,2'-MDA: 2 sites, 2,4'-MDA: 3 sites, and 4,4'-MDA: 1 site). Partial charges for each molecule were derived from *ab initio* electrostatic potential calculations using a 6-31G* basis set. These partial charges were then fitted using the restrained electrostatic potential (RESP) program in AMBER.³⁶⁻³⁸ For each of the protonated, isomers, a short energy minimization was performed in AMBER followed by a 10 ps molecular dynamic simulation to heat the molecule to 1200K. Then, a long molecular dynamic simulation was run at 1200K for 9,000 ps. Structural snapshots were saved every 16,667 steps during the simulation, resulting in 3,000 structural snapshots. These high-energy structural snapshots were then cooled to 300K during a 15 ps molecular dynamic simulation.

MOBCAL software was used to theoretically determine the collision cross section of the resulting conformations.³⁹⁻⁴¹ First, the projection approximation was used to

generate helium collision cross section values. For comparison with the nitrogen experimental values, nitrogen trajectory method values were determined for a set of conformations spanning the entire collision cross section range. These values were used to create a linear function to convert the remaining projection approximation values to nitrogen trajectory method values. The computational conformational space plots were then aligned with the experimental data to give structural insight to the MDA isomers.⁴² Alignment of theoretically generated conformations with experimental CCS values for 3-ring and 4-ring MDA is shown in Appendix B, Figures B.28 and B.29.

2.3 Results and Discussion for 2-Ring MDA

I. Characterization by MS and Tandem MS

Previously, underivatized 4,4'-MDA has been studied using LC-MS/MS instrumentation.⁷⁻¹² In these studies, the fragmentation of the 4,4'-MDA parent ion ($[M+H]^+ = 199$ Da) was monitored by means of a transition characteristic signal at 106 Da. However, to the best of our knowledge, no research has been reported for 2,2'-MDA and 2,4'-MDA structural isomers using modern LC-MS techniques.

In the present study, we observed both of these signals (199 Da, 106 Da) in the 4,4'-MDA, 2,2'-MDA and 2,4'-MDA direct infusion ESI mass spectra as shown in Figure 2.2a-c. In this thesis, we use the spectra resulting from ESI rather than the more complex spectra resulting from MALDI, which will be the focus in later works. The base peak of the 4,4'-MDA spectrum is the $[M+H]^+$ signal at 199 Da, but for 2,2'-MDA and 2,4'-MDA the 106 Da fragment is the base peak. An additional signal, although low in

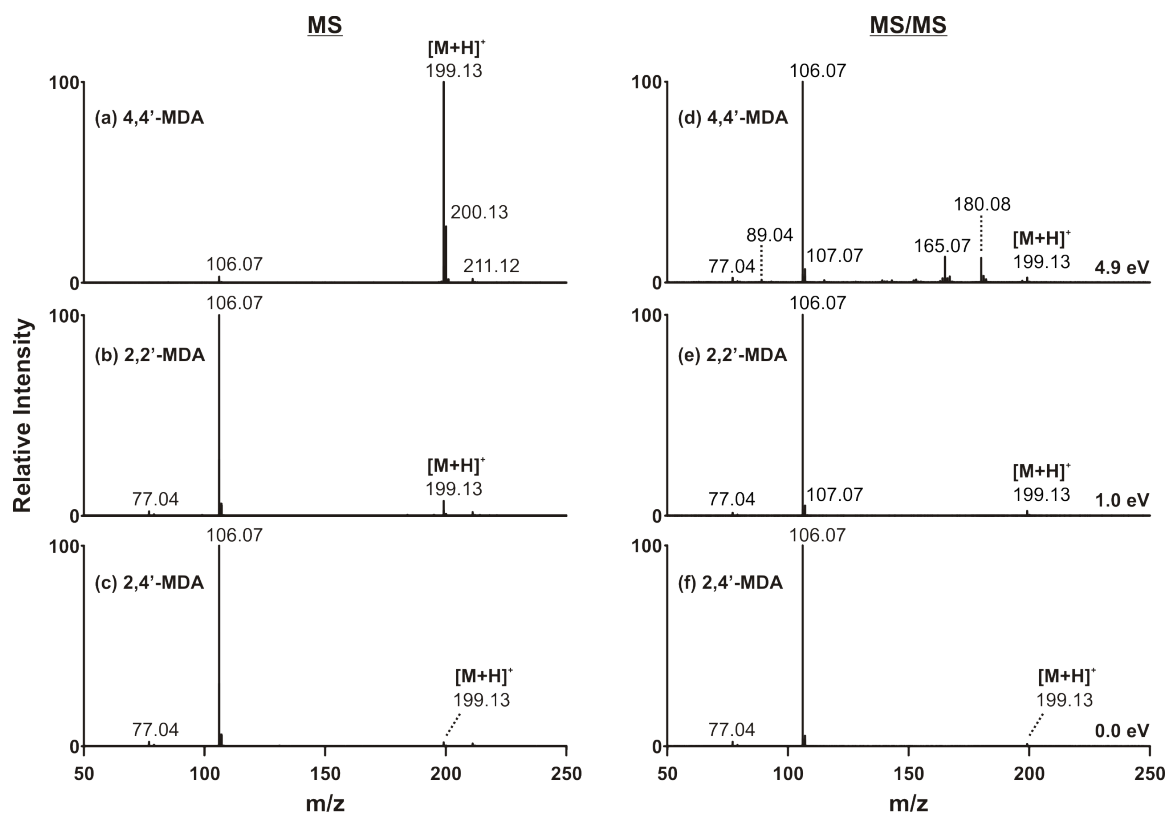


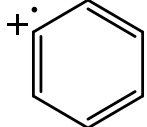
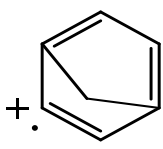
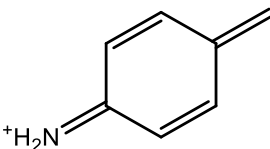
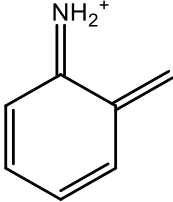
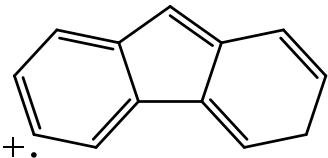
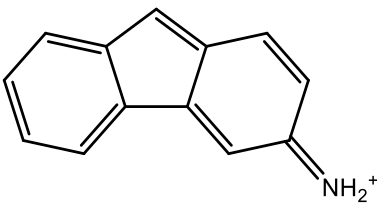
Figure 2.2. (*left*) Mass spectra of MDA isomers using direct infusion ESI-TOFMS for (a) 4,4'-MDA, (b) 2,2'-MDA, and (c) 2,4'-MDA. (*right*) Tandem mass spectra for parent ions ($[M+H]^+ = 199.13$ Da) of (a) 4,4'-MDA, (b) 2,2'-MDA, and (c) 2,4'-MDA. Center-of-mass collision energies are shown at right; corresponding lab-frame collision energies are 40 eV, 8 eV, and 0 eV, respectively. For 2,4'-MDA, no collision energy was required for dissociation.

abundance, is observed at 211 Da. The base peak for the 4,4'-MDA at 199 Da is representative of the higher stability of the 4,4'-MDA than that of the 2,2'-MDA and 2,4'-MDA. The difference in stability is due to location of protonation site and will be discussed in more detail later in the thesis.

Tandem mass spectra of protonated 4,4'-MDA, 2,2'-MDA and 2,4'-MDA are presented in Figure 2.2d-f, and potential corresponding structures of fragment signals are shown in Table 2.1. Unsurprisingly, the fragmentation spectra of all the isomers are similar in nature. However, while 4,4'-MDA required high collision energy to generate fragments (Figure 2.2d), 2,2'-MDA and 2,4'-MDA required minimal or no additional energy to induce dissociation (Figure 2.2e, f). Because of the high collision energy required to fragment 4,4'-MDA, additional signals of 165 Da and 180 Da are observed which are not present in 2,2'-MDA and 2,4'-MDA tandem mass spectra. Additional fragmentation data and discussion concerning the low-intensity 211 Da signal is provided in the Appendix B (Figure B.7).

In order to compare the gas-phase stabilities of the three isomers, we monitored the conversion from 199 Da to 106 Da as a function of applied collision energy for all three isomers as shown in Figure 2.3. Both lab-frame and center-of-mass (COM) collision energies are displayed. It is clear that 4,4'-MDA (double *para*-substitution) is significantly more stable than either 2,2'-MDA (double *ortho*-substitution) or 2,4'-MDA (combined *ortho*- and *para*-substitution). For example, when 2.0 eV (COM) are applied to the 4,4'-MDA isomer, over 95% of the normalized signal remains in the 199 Da parent ion. However, at that same energy, the 199 Da parent ions for both 2,2'-MDA and 2,4'-

Table 2.1. Possible structures of commonly observed MDA fragment ions.

Theoretical	Observed	Proposed Structure(s)
<i>m/z</i>	<i>m/z</i>	
77.04	77.04	
89.04	89.04	
106.07	106.07	 
165.07	165.07	
180.08	180.08	

MDA are entirely depleted. The underlying cause of this key difference as well as minor differences in the gas-phase behavior of 2,2'-MDA and 2,4'-MDA will be discussed later in the thesis, as these observations were corroborated by other methods of structural analysis. A potential complicating factor in MS-based analysis of these compounds is the uncertain location of the additional proton that creates the $[M+H]^+$ ions. Literature on aniline suggests two potential protonation sites in the gas-phase, one on the amine and one on the aromatic ring *para* to the amine.⁴³⁻⁴⁷ Recently, Eberlin and coworkers demonstrated that aniline molecules protonated at the amine group can be resolved from those protonated on the ring using TWIM separation.⁴⁸ Because MDA isomers are essentially two aniline molecules connected by a methylene bridge, it is probable this behavior applies to MDA as well. Therefore, as tandem MS alone was unable to provide clarity about how protonation sites affect gas-phase structures, structural analysis by IM and computational methods were required.

II. Structural analysis using IM-MS and computational methods

Using both TWIM and DTIM instrumentation, CCS values were obtained for the $[M+H]^+$ ions of the three isomers as shown in Table 2. Due to inherent differences in instrumentation and data analysis between TWIM and DTIM methodology, small differences for CCS values between platforms were expected, as observed in Table 2. In order to obtain CCS values from TWIM instrumentation, the use of calibration standards is required; in contrast, DTIM CCS values can be directly calculated from the kinetic theory of gases using the Mason-Schamp equation.¹³⁻¹⁵ Therefore, it is expected that the

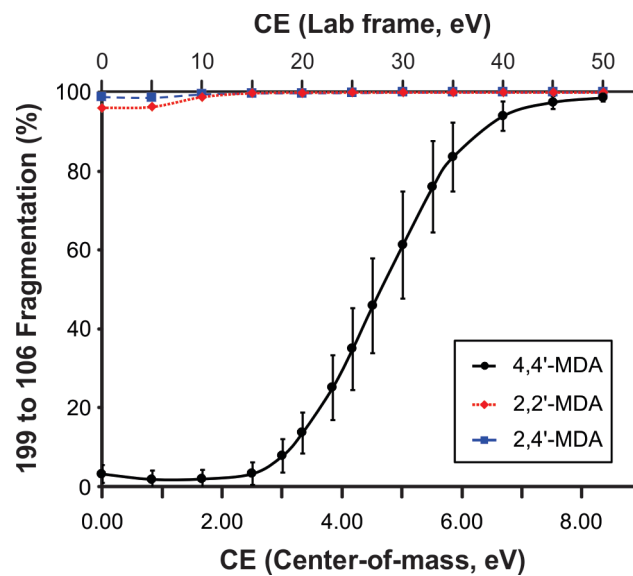


Figure 2.3. Collision-induced dissociation curves monitoring the transition of respective 199 Da parent ions to 106 Da fragment ions. Individual curves for 4,4'-MDA (*solid line; black circles*), 2,2'-MDA (*short dash, red squares*), and 2,4'-MDA (*long dash; blue triangles*) are superimposed. Both center-of-mass and lab-frame collision energies are shown.

Table 2.2. Collision cross-section values of various MDA ions obtained on T-wave and drift tube IM-MS instrumentation. Errors shown represent the respective standard deviations.

MDA Species (Ion)	T-wave N₂ (Å²)	DTIM N₂ (Å²)
4,4' [M+H] ⁺	156.0 ± 0.7	162.7 ± 0.3
2,2' [M+H] ⁺	139.9 ± 1.8	145.0 ± 0.2
2,4' [M+H] ⁺ (1)	139.9 ± 1.1	145.4 ± 0.4
2,4' [M+H] ⁺ (2)	155.9 ± 0.5	N/A

DTIM CCS values are more accurate than the TWIM CCS values. In this study, DTIM CCS values were systematically higher than TWIM CCS values by $3.4 \pm 0.5\% \text{ \AA}^2 (\text{N}_2)$. We hypothesize that this systematic difference between TWIM and DTIM CCS values results from the calibration of the former and from the exposure of the charge on the MDA molecules. For the tetraalkylammonium ions used for TWIM CCS calibration, the charge resides in the center of the molecule and is surrounded by hydrocarbon tails. These tails essentially shield the charged region from the polarizable N_2 drift gas. As a result, only weak inelastic collisions occur between the tetraalkylammonium calibrants and N_2 . However, in our MDA system, the charge is not shielded, and thus the MDA ions are expected to experience stronger inelastic interactions with N_2 which are not accounted for using the current calibration strategy.

Significant differences in CCS for the $[\text{M}+\text{H}]^+$ ions were observed between 4,4'-MDA and 2,2'-MDA, suggesting the protonation site is not centrally located in the structure. For 2,4'-MDA, we observed two CCS values in TWIM and only one corresponding CCS value for DTIM. This will be discussed later, as further analysis of the role of protonation on gas-phase stability was necessary to explain this observation.

While only one type of protonation site is available for 4,4'-MDA, the *para*-amino groups (*p*- NH_2), two potential sites exist for 2,2'-MDA and three for 2,4'-MDA, as shown by the asterisks in Figure 2.1. For 2,2'-MDA, protonation can occur at either the *ortho*-amino groups (*o*- NH_2) or the aromatic ring opposite the *ortho*-amino group (*ring*). On 2,4'-MDA, *p*- NH_2 , *o*- NH_2 and *ring* sites are all present, and any one of these may be protonated.

While CCS measurements were obtained using both TWIM and DTIM platforms, the majority of IM-MS and IM-MS/MS data was obtained using the TWIM platform and will therefore be the focus of this thesis. Extracted CCS profiles of the protonated isomers (199 Da) obtained using IM-MS are shown in Figure 2.4a. One conformation of 4,4'-MDA was generated with a CCS of 156 \AA^2 while 2,2'-MDA generated one conformation with a CCS of 140 \AA^2 . In contrast, 2,4'-MDA generated two conformations having CCS values of 156 \AA^2 and 140 \AA^2 . The alignment of these two values with the 4,4'-MDA and 2,2'-MDA CCS values in Figure 2.4a (dotted line) indicate similar respective conformations.

Additionally, an IM-MS/MS structural depletion study was performed to connect the gas-phase stabilities of these conformations with potential protonation sites. In Figure 2.5, IM profiles were obtained for the protonated isomers using different collision energies and corresponding drift times were converted to CCS values. Consistent with earlier tandem MS data, 4,4'-MDA has one primary conformation (156 \AA^2) which begins to deplete when high collision energy (3.1 eV) is applied as shown in Figure 2.5a. We can assign this CCS value to a conformation which is *p*-NH₂ protonated, as 4,4'-MDA cannot be protonated at other positions. Because 2,4'-MDA contains one *p*-NH₂ site as well, we also assign its CCS value of 156 \AA^2 to *p*-NH₂ protonation. Evidence for this is shown in Figure 2.5c, where the ~45% depletion rate of the larger 2,4'-MDA conformation for 3.1 eV matches that of 4,4'-MDA shown in Figure 2.5a. Because both of these conformations are rather resistant to collisionally-induced depletion and fragmentation, we conclude that *p*-NH₂ protonation generates species that are relatively stable in the gas-phase.

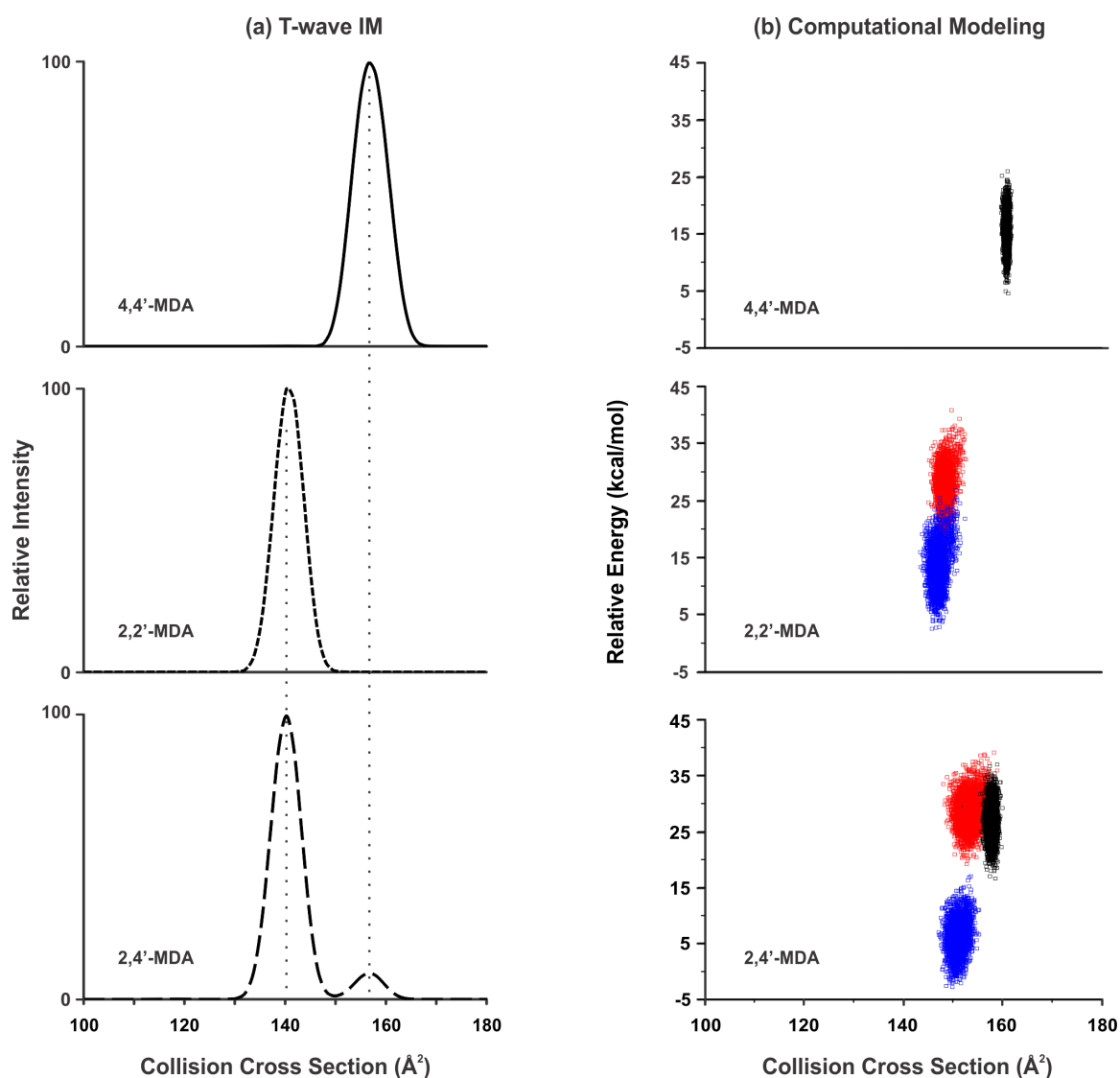


Figure 2.4. (a) CCS profiles of 4,4'-MDA (*solid line*), 2,2'-MDA (*short dash*), and 2,4'-MDA (*long dash*) $[M+H]^+$ ions extracted from T-wave data. Vertical lines are added for visual alignment. (b) Conformations for the possible protonation sites for the (a) 4,4'-MDA, (b) 2,2'-MDA, and (c) 2,4'-MDA were generated using computational conformational search methods. The theoretical nitrogen CCS is plotted against the relative energy for each computationally generated conformation. Conformations for the *p*-NH₂ protonated isomers are shown in black, the *o*-NH₂ protonated isomers are shown in red and the *ring* protonated isomers in blue.

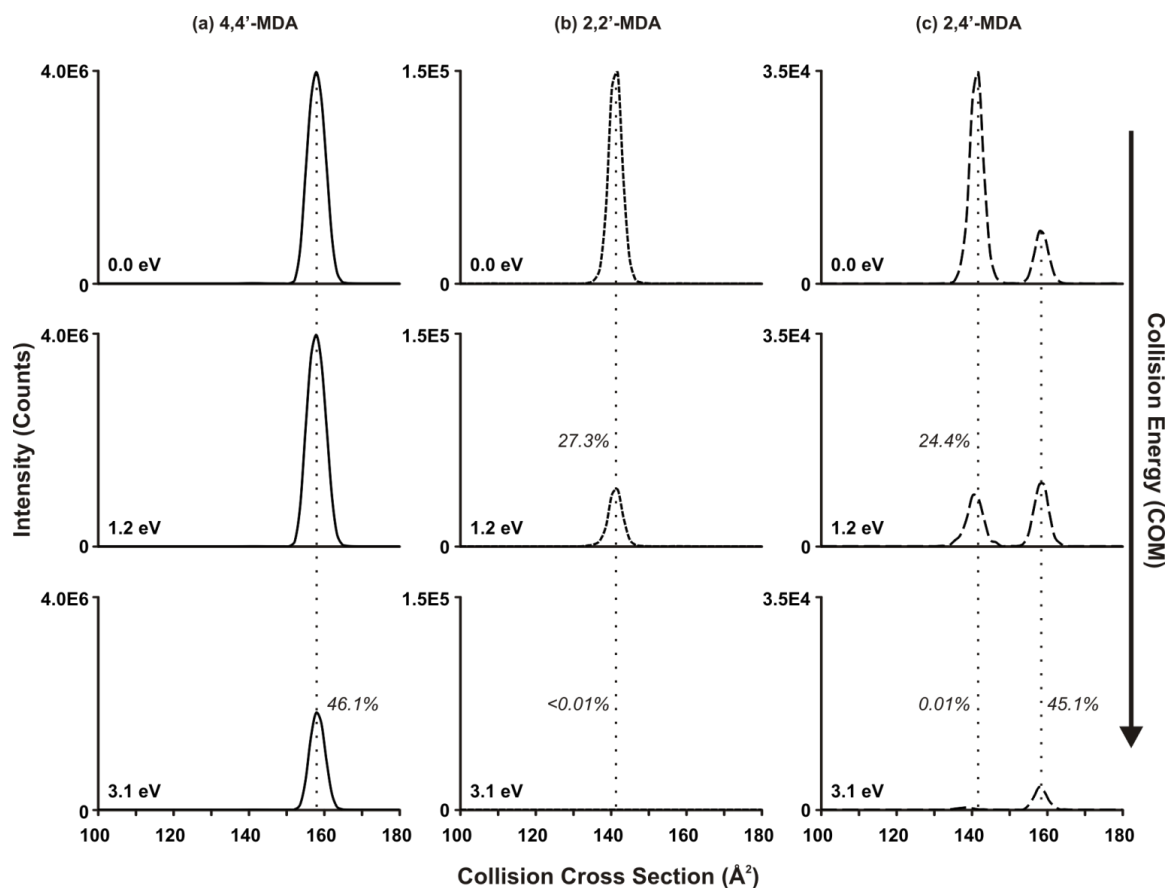


Figure 2.5. Collisionally-activated CCS profiles of $[M+H]^+$ ions for (a) 4,4'-MDA, (b) 2,2'-MDA, and (c) 2,4'-MDA. Center-of-mass energies are shown; corresponding lab-frame energies are 0 eV, 10 eV, and 25 eV, respectively. Note the difference in scales of the y-axes for (a) - (c). Inset relative percentages represent signal intensities compared to those without collisional activation. Vertical lines are added for visual alignment.

In contrast, the less intense conformations for 2,2'-MDA and 2,4'-MDA of 140 Å² were less stable, leading to significant depletion upon collisional activation (Figure 2.5b-c). Both of these conformations were entirely depleted when 3.1 eV of energy was applied. These are more difficult to assign structurally, as two remaining protonation sites exist for the isomers (*o*-NH₂ and *ring*). Conformations of all the possible protonation sites for the three isomers were generated using theoretical conformational search methods to provide further structural insight. For each of the six protonation sites 3,000 conformations were generated and the theoretical CCS value and energy was determined and plotted for each conformation in Figure 2.4b. The protonation sites are indicated by the following colors: the *p*-NH₂ conformations are shown in black, the *o*-NH₂ conformations are shown in red, and the *ring* conformations are shown in blue. The *p*-NH₂ conformations for both the 2,4'-MDA isomer and the 4,4'-MDA isomer demonstrate close theoretical CCS alignment and thus support the assignment of the larger observed CCS value. For *o*-NH₂ and *ring* protonation sites in 2,2'-MDA and 2,4'-MDA, theoretical CCS values are similar, which makes it difficult to differentiate these protonation sites by CCS. However, the 2,2'-MDA and 2,4'-MDA maps shown in Figure 2.4b do suggest that protonation at the *o*-NH₂ position creates higher energy conformations than those with *ring* protonation. High-energy conformations likely correspond to species that undergo metastable fragmentation in the mass spectrometer, which was observed for 2,2'-MDA and 2,4'-MDA as noted earlier in Figures 2.2 and 2.3. Therefore, it is likely that *o*-NH₂ protonation leads to metastable fragmentation into 106 Da, whereas *ring* protonation is somewhat more stable and allows detection of (at least some of) these ions as intact 199 Da species.

Although the stability of the MDA isomers is related to protonation site, it should be noted that small differences in energy can change the relative abundances of each site. As shown in Table 2.2, we did not observe the *p*-NH₂ protonation site for 2,4'-MDA using DTIM instrumentation, while this protonation site was observed in low abundance using TWIM instrumentation (*e.g.* Figure 2.4a). This is likely due to the different ion sources for the two platforms, which results in different voltages, ion transmission efficiencies, *etc.* As mentioned earlier, previous studies on aniline protonation in the gas-phase suggest that the two protonation sites (-NH₂ or *ring*) are relatively close in energy. Therefore, the relative abundances of aniline protonation sites can fluctuate due to of small changes in experimental conditions.⁴³ Likewise, MDA protonation sites appear to be close in energy, and the relative abundances of the protonation sites can change as well. This explains why the *p*-NH₂ conformation of 2,4'-MDA is observed in low abundance using TWIM instrumentation but not using DTIM instrumentation. However, once the MDA compounds are protonated, the relative order of stability across both platforms is consistent as shown in Appendix B (Table B.1).

A closer look at the computationally generated conformations gives further insight into the metastable nature of the *o*-NH₂ protonated isomers. The computationally generated conformations were structurally clustered based on RMSD resulting in ten representative structures. These structures for the possible protonation sites for the three isomers can be found in Appendix B (Figures B.8-B.25), but the most populated conformations are shown in Figure 2.6. The most populated conformation for 4,4'-MDA is shown in Figure 2.6a. This molecule exhibits an extended structure, consistent with

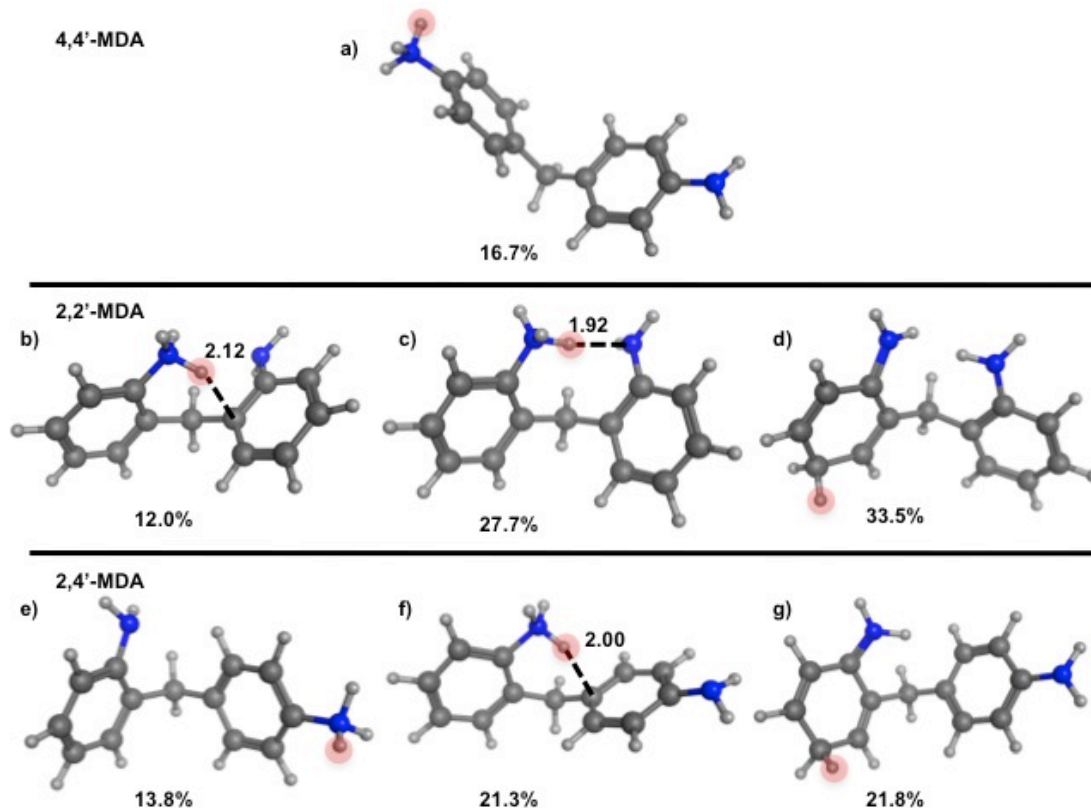


Figure 2.6. RMSD clustering representatives from computational conformational sampling are shown for each of the protonation sites. (a) 4,4'-MDA *p*-NH₂ protonated, (b) 2,2'-MDA *o*-NH₂ protonated, (c) 2,2'-MDA *o*-NH₂ protonated, (d) 2,2'-MDA *ring* protonated, (e) 2,4'-MDA *p*-NH₂ protonated, (f) 2,4'-MDA *o*-NH₂ protonated, and (g) 2,4'-MDA *ring* protonated. Red circles indicate the additional proton. Labeled bond distances are used to show the proximity of the additional proton to the bridging carbon that would lead to a 1,5-hydrogen shift fragmentation of the 2-ring MDA. A percentage is shown below each conformation to show how many conformations the selected one represents, as a result of RMSD clustering. Two conformations are shown for the 2,2'-MDA *o*-NH₂ protonated 2-ring MDA due to two favorable conformations that result from this protonation.

experimental CCS data shown in Table 2.2. Conformations for 2,2'-MDA are shown in Figure 2.6b-d. The conformations in Figure 2.6b-c show *o*-NH₂ protonated 2,2'-MDA, where as the conformation in Figure 2.6d shows *ring* protonation. Two *o*-NH₂ protonated isomers are needed here to explain two of our experimental observations. Figure 2.6b is represented by metastable *o*-NH₂ protonation, while Figure 2.6c is representative of a slightly more stable and highly populated *o*-NH₂ protonation. When the proton resides between the two amine groups, a more stable conformation is achieved, which may explain why we see a slightly more stable 2,2'-MDA isomer in Figure 2.3 compared to the 2,4'-MDA isomer. These three conformations are all representative of a smaller structure, which is consistent with the experimental CCS data shown in Table 2.2. Conformations for 2,4'-MDA are shown in Figure 2.6e-g. Figure 2.6e shows the *p*-NH₂ protonation whereas Figure 2.6f shows *o*-NH₂ protonation and Figure 2.6g shows *ring* protonation. The conformation in Figure 2.6e is representative of the extended structure similar to the conformation shown in Figure 2.6a, which supports the experimental CCS alignment for both 4,4'-MDA and the larger 2,4'-MDA conformation. The conformations shown in Figure 2.6f-g are representative of a smaller structure, which is also consistent with the experimental CCS data in Table 2.2. The smaller structures observed for the *o*-NH₂ protonation and *ring* protonation for 2,2'-MDA and 2,4'-MDA support the alignment of their experimental CCS values.

III. Mechanism for protonation and fragmentation of MDA isomers

Combining tandem MS, IM-MS, IM-MS/MS, and computational modeling data, we propose mechanisms for protonation and fragmentation of MDA structural isomers in Figure 2.7 The gas-phase stability of each isomer is inherently related to both the position

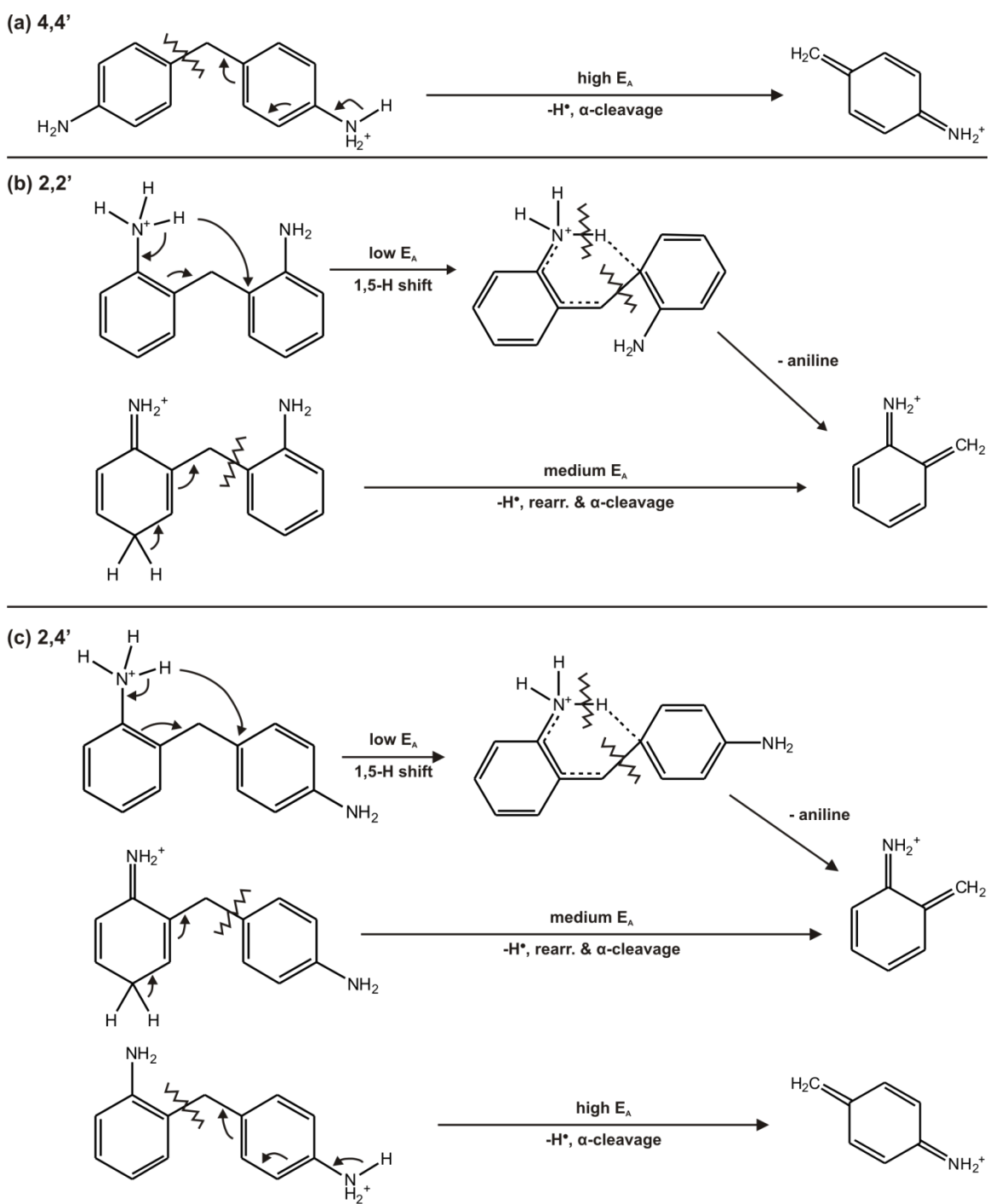


Figure 2.7. Proposed protonated structures and 199 Da \rightarrow 106 Da fragmentation pathways for MDA isomers. Activation energy is abbreviated E_A .

of the amine groups and the location of the additional proton. The 4,4'-MDA isomer can only be protonated at *p*-NH₂ groups and is the most stable gas-phase ion we observed. When a large collision energy is applied to the 4,4'-MDA parent ion, a loss of a hydrogen radical occurs, leading to *alpha* cleavage and formation of the 106 Da fragment. As collision energy continues to increase, other pathways also emerge, forming other fragments (Figure 2.2d). On the other hand, 2,2'-MDA can be protonated at either the *o*-NH₂ or *ring* position. When 2,2'-MDA is protonated on an *o*-NH₂ group, even without applied collision energy, it readily undergoes a 1,5-hydrogen shift, due to the proximity of the amine hydrogen to the bridging carbon on the opposite aromatic ring (Figure 2.6b), which leads to formation of the 106 Da fragment and neutral aniline. The driving force for this process is likely the stability of the products: aniline can either remain neutral or further decompose to 77 Da as shown in Figure 2.2e-f, and the 106 Da fragment can further rearrange to a tropylium-like ion of the same mass.^{7,43} This mechanism describes the metastable behavior of these ions; therefore, detection of *o*-NH₂ protonated 2,4'-MDA or 2,2'-MDA is minimal. As a result, the primary conformation observed for the 2,2'-MDA [M+H]⁺ ion (199 Da) is composed of *ring* protonated species. When a moderate collision energy is applied to ring protonated 2,2'-MDA, loss of a hydrogen radical on the ring leads to rearrangement and formation of the 106 Da fragment as well. Finally, 2,4'-MDA may be protonated at all three sites. Protonation at the *o*-NH₂ leads to significant metastable fragmentation due to a 1,5-hydrogen shift (Figure 2.6f) as in 2,2'-MDA, and protonation at the *ring* position leads to hydrogen radical loss and rearrangement upon collisional activation. In contrast, protonation at the *p*-NH₂ results in a more stable conformation which fragments through a mechanism similar to that of 4,4'-

MDA. This fragmentation mechanism observed for the 2-ring isomers should play a major role in the characterization of the larger industrial MDA sample mixtures.

2.4 Results and Discussion for 3-Ring and 4-Ring MDA

I. Characterization by MS and Tandem MS

ESI spectra were obtained for the protonated 3-ring ($[M+H^+] = 304$ Da) and 4-ring ($[M+H^+] = 409$ Da) MDA species and are shown in Figure 2.8a. In addition to the protonated precursor ions, significant peaks are observed at 211 Da and 106 Da for the 3-ring MDA species and peaks at 316 Da, 211 Da and 106 Da are observed for the 4-ring MDA. These peaks correspond to fragments of the precursor ion and become more intense in the tandem mass spectra as shown in Figure 2.8b. Even before collision energy is applied to induce fragmentation, the peak at 211 Da for the 3-ring and 316 Da for the 4-ring MDA correspond to the base peaks of the spectra, signifying that the corresponding precursor ions are readily dissociated. It is also interesting to note that the mass difference of 93 Da between the precursor ion and its most abundant fragment present in the spectra is the same mass difference that was observed for the 2-ring MDA species between the 199 Da precursor ion and its major fragment at 106 Da, corresponding to the loss of a terminal neutral aniline.

In addition to the fragment peaks, additional signals are observed at m/z 152.6 and m/z 158.6, respectively, for both the 3-ring and 4-ring spectra. These masses correspond to doubly charged ions for the 3-ring and the 4-ring isomers based on isotope spacing.

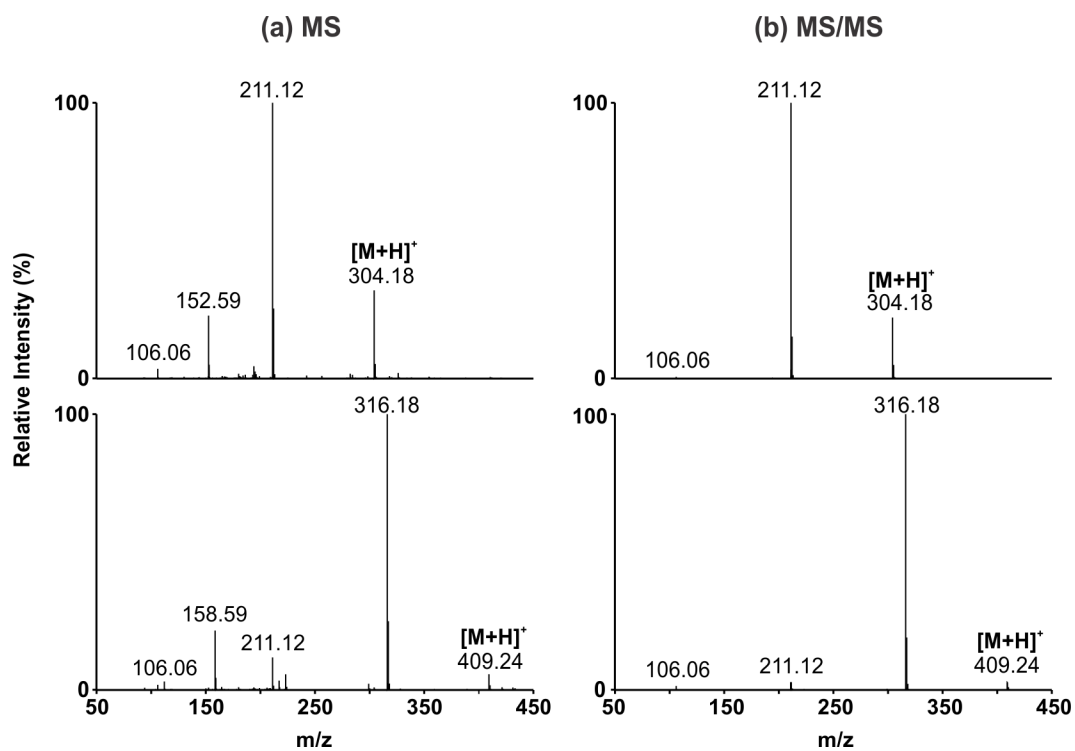


Figure 2.8. (a) Mass spectra of 3-ring and 4-ring MDA using direct infusion ESI-TOFMS. (b) Tandem mass spectra for 3-ring and 4-ring MDA parent ions ($[M + H]^+ = 304.18$ Da and $[M + H]^+ = 409.24$ Da, respectively).

When these ions were mass selected and fragmented via an MS/MS experiment, singly charged ions at higher m/z values were produced further indicating that these peaks correspond to doubly-charged species (Appendix B, Figures B.30 and B.31). The conversion from precursor ion to fragment ions was monitored as a function of applied collision energy for both the 3-ring and 4-ring MDA as shown in Figure 2.9. The IM-MS/MS structural depletion of the precursor ion is shown in Figure 2.9a,b and the breakdown curves for the fragment ions are shown in Figure 2.9c,d. These breakdown curves show the percentage of precursor ion to fragment conversion observed in the spectra at various collision energies, and were obtained by taking the intensity of the indicated fragment ion and dividing by the intensity of its corresponding precursor ion. In Figure 2.9c, 3-ring MDA has two breakdown curves, representative of the 106 and 211 fragments. The precursor ion breaks down into the 211 fragment at a significantly lower energy threshold than the 106 fragment. Figure 2.9d corresponds to 4-ring MDA, which has three curves, representative of the 106, 211, and 316 fragments. Again the 316 and 211 fragments form at lower collision energies than the 106 fragment. This observation is further discussed later in this chapter in the context of IM and computational results.

In Section 2.3, the 106 fragment formed readily from the 2-ring MDA when external amines were located ortho to the bridging carbon (2,2'-MDA and 2,4'-MDA) but not readily for the 4,4'-MDA. The observation that the 106 fragment requires higher collision energy than the other isomers to form from both the 3-ring and 4-ring MDA species suggests that the external amines are located in para positions to the bridging carbon in a similar manner as the 2-ring 4,4'-MDA. The observation of the 106 fragment

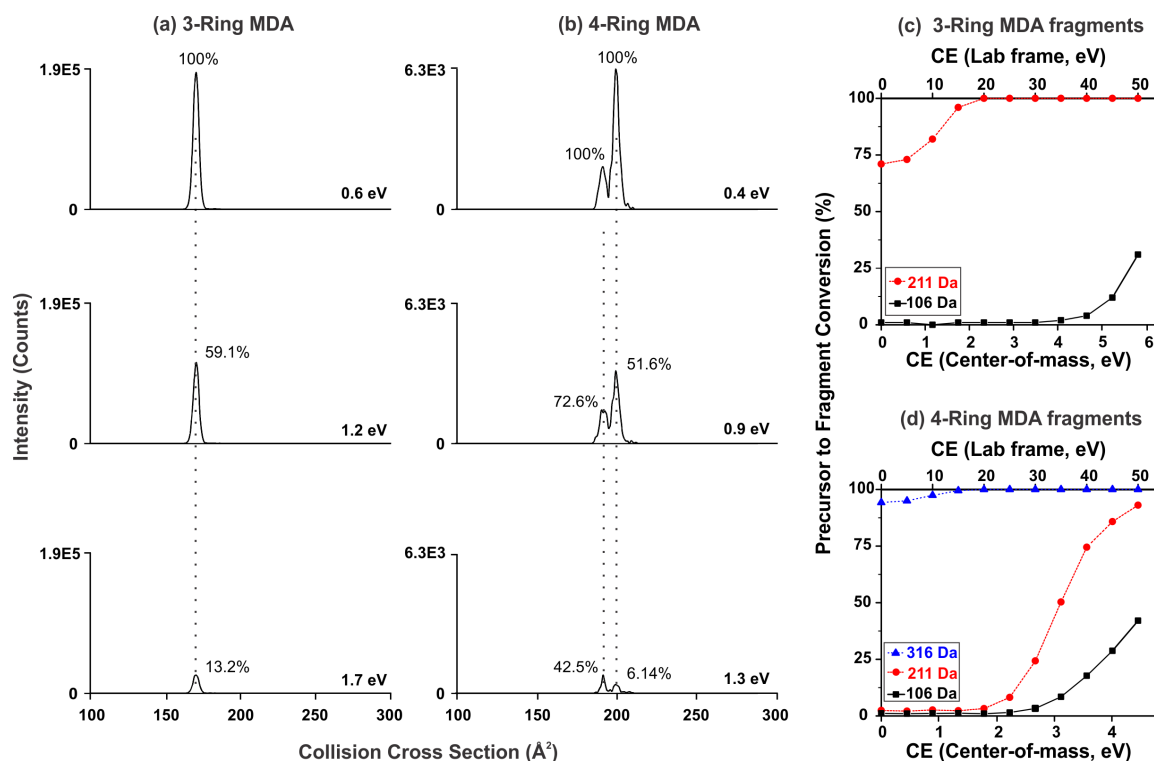


Figure 2.9. Collisionally activated CCS profiles of $[M+H]^+$ ions for (a) 3-ring MDA and (b) 4-ring MDA. Center of mass energies are shown. The inset relative percentages represent signal intensities compared to those without collisional activation. Vertical lines are added for visual alignment. Collision-induced dissociation curves monitoring the transition of precursor ions to fragment ions for (c) 3-ring MDA and for (d) 4-ring MDA. Center of mass collision energies (CE) are shown on the lower axis. (See text for details).

ion forming at higher collision energies further indicates that the structures shown in Figure 1a are accurate structural depictions of the 3-ring and 4-ring isomers. However, when comparing the Figure 2.9c,d with the 2-ring MDA breakdown curves in Figure 2.3 there is a notable difference between the 3-ring and 4-ring isomers, relative to the 2-ring isomers. Specifically, the 2-ring isomers showed ~30% fragmentation at a center-of-mass (COM) of 4.0 eV, and the 4-ring isomer in this work shows essentially the same behavior in Figure 2.9d. On the other hand, the 3-ring isomer requires a collision energy of 5.8 eV to reach a similar 30% fragmentation yield. This indicates that there must be a significant structural difference between the 3-ring and 4-ring isomers, making production of 106 Da ions a higher energy pathway in the 3-ring isomer system, *vide infra*.

II. Structural analysis using IM-MS and computational methods

Collision cross section (CCS) values were measured for the $[M+H]^+$ ions using both TWIM and DTIM instrumentation and are provided in Table 2.3. The number of measurements for each CCS value is shown in parentheses. Slight differences were observed for the N_2 CCS values between the two instrument platforms most likely reflecting the chemical mismatch of the TAA calibration standards used for TWIM CCS measurements. As discussed in Section 2.3, these differences likely reflect the exposure of the proton charge on the MDA molecules, which would result in stronger inelastic interactions with the N_2 buffer gas, as compared to the charge-shielded tetraalkylammonium salts used for calibration. Of particular note is the second conformation observed in the mobility spectrum for 4-ring MDA using the TWIM (199.5\AA^2), but not observed in the DTIM analysis. This is reflective of the gas phase

Table 2.3. Collision cross section values for 3-ring and 4-ring MDA ions obtained on TWIM and drift tube IM-MS instrumentation. Errors shown represent the respective standard deviations. The number of measurements on which each CCS value is based are shown in parentheses.

MDA Species (Ion)	TWIM N₂ (Å²)	DTIM N₂ (Å²)	DTIM He (Å²)
3-ring [M+H] ⁺	171.3 ± 0.1 (n=6)	178.7 ± 0.6 (n=14)	105.5 ± 0.6 (n=18)
4-ring [M+H] ⁺ (1)	191.2 ± 0.7 (n=6)	202.1 ± 1.0 (n=14)	132.7 ± 1.1 (n=19)
4-ring [M+H] ⁺ (2)	199.5 ± 1.0 (n=6)	N/A	N/A

stability of these ions and will be discussed in greater detail later. CCS values were also obtained in helium in order to provide better comparison with the theoretical CCS values calculated for the computationally generated conformations. Alignment of theoretical and experimental data in both helium and nitrogen drift gases is available in the Appendix B, Figures B.28 and B.29.

The TWIM, IM traces obtained in nitrogen shown in Figure 2.10a indicate two conformations for both the 3-ring and 4-ring MDA species. The larger CCS conformation observed for the 3-ring MDA species is much less abundant than the smaller CCS conformation, accounting for ~2%. For the 4-ring MDA, the larger CCS conformation is more abundant than the smaller CCS conformation, the latter accounting for ~8% of the intensity. The IM-MS/MS structural depletion study in Figure 2.9 shows the stability of these conformations at varying collision energies. The mobility profiles were obtained at increasing collision energies to compare the depletion rates of the precursor ions. Only the smaller CCS 3-ring MDA conformation appears once collision energy is applied (Figure 2.9a) compared to the IM trace with no collision energy (Figure 2.10a). The two conformations for the 4-ring MDA are visible for all collision energies used. Figure 2.9b also shows that the larger CCS conformation of the 4-ring MDA decreases at a much faster rate (100% to 52% to 6%) than the smaller CCS conformation (100% to 73% to 43%) indicating that the species having the larger CCS conformation is less stable than species represented by the smaller CCS.

In order to facilitate direct comparison between the 3-ring and 4-ring MDA structures, the COM collision energies are considered. Using COM energies, the 1.2 eV in the middle panel for the 3-ring MDA can be compared with the 1.3 eV in the bottom

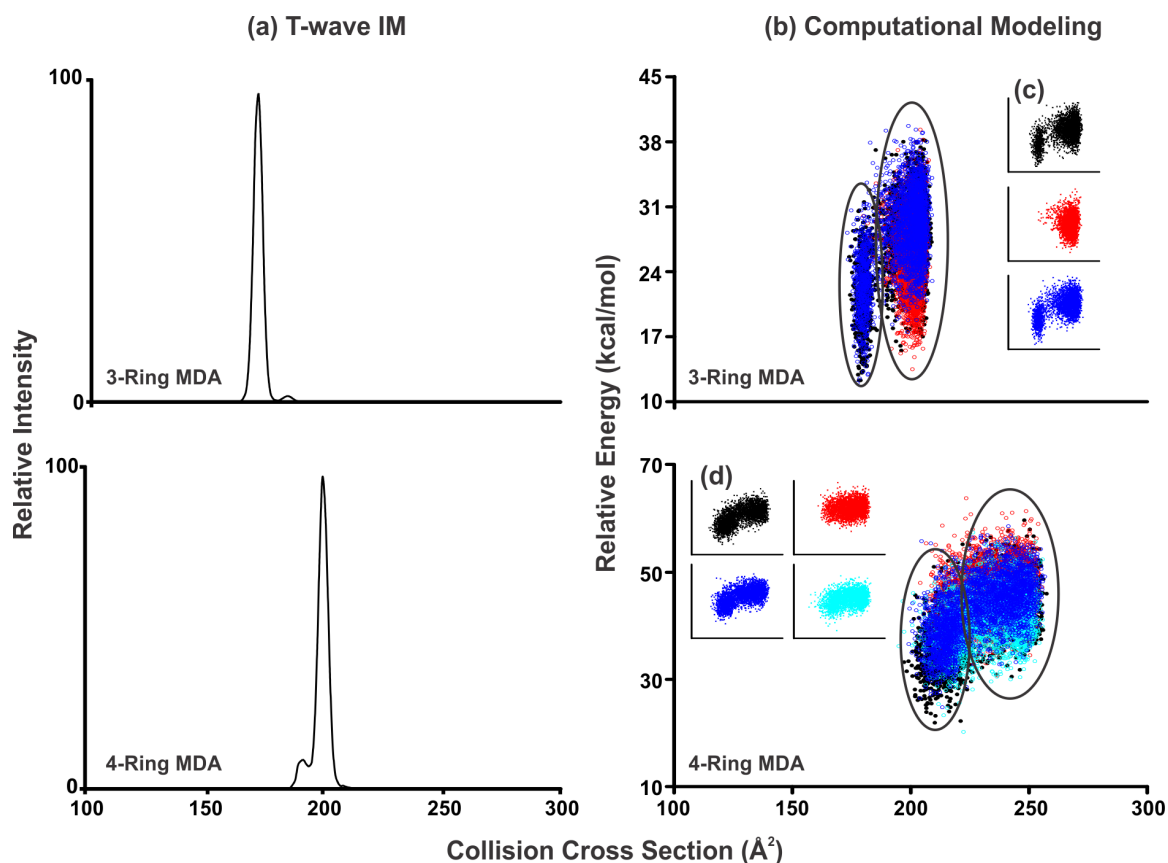


Figure 2.10. (a) CCS profiles for 3-ring MDA (top) and 4-ring MDA (bottom) extracted from TWIM data. (b) Conformational space plots for the possible protonation sites of 3-ring MDA (top) and 4-ring MDA (bottom) generated using computational conformational search methods. The theoretical helium CCS is plotted against the relative energy for each conformation. Theoretical conformations for each protonation site are black, red, and blue respectively across the structure depicted in Figure 1 for the 3-ring MDA and black, red, cyan, and blue respectively across the structure for the 4-ring MDA. Insets of the conformations resulting from individual protonation species are shown in (c) and (d) to clarify the conformational clusters present on each plot.

panel for the 4-ring MDA, showing that the 3-ring and smaller 4-ring MDA CCS conformations decrease at similar percentages (~50%) which suggests that the two have similar structural conformations. It is also worth noting that the depletion rates do not mimic those observed for the 4,4', 2,2', or 2,4' 2-ring MDA isomers in Figure 2.5. This observation suggests two differences between the 2-ring MDA isomers and 3-ring and 4-ring MDA. First, in Figure 2.5, the 4,4'-MDA 2-ring isomer has the same $[M+H]^+$ intensity at 0.0 and 1.7 eV, and decreased only to 46.2% at 4.2 eV. In this work the 3-ring isomer $[M+H]^+$ intensity in Figure 2.9a is reduced to 13.2% at 1.7 eV, while the major 4-ring isomer peak shows only 6.1% at 1.3 eV in Figure 2.9b. This suggests that, although the 4,4'-MDA 2-ring, the 3-ring, and the 4-ring isomers all have terminal para-amino groups, different processes dominate fragmentation for the higher order multimers which are characterized by the m/z 211 and 106 fragments. Second, the behavior of the lower abundance peak in Figure 2.9b extrapolates to a value of about 25% intensity for the energy of 1.7 eV, a behavior comparable to that of the 2,2' and 2,4'-MDA 2-ring isomers from our earlier study. These observations indicate that fragmentation of the 3-ring and 4-ring isomers must be dominated by the internal amine group(s), leading to lower energy pathways, *vide infra*.

Computational modeling generates theoretical structures that can be aligned with the experimental data according to their CCS values. This gives insight into the conformations that were observed experimentally and why a difference in stability is observed. For both 3-ring and 4-ring MDA, the structures shown in Figure 1a were modeled separately with an additional proton for each possible protonation site. This

resulted in 3 unique starting structures for the 3-ring MDA and 4 unique starting structures for the 4-ring MDA. The conformational space plots based on the molecular dynamics conformational space sampling simulations are shown in Figure 2.10b. The overlaid colors on the conformational space plots represent independently modeled protonation sites, with the color scheme following protonation on the amine nitrogen from left to right across the structures shown in Figure 1a. For the 3-ring MDA, the protonation sites are indicated in black, red, and blue respectively across the structure and for the 4-ring MDA the protonation sites are indicated in black, red, cyan, and blue respectively across the structure. Figure 2.10c,d show the results from each independently modeled protonation site that are combined in Figure 2.10b. Conformation space plots for each protonation site for both helium and nitrogen exhibit similar distributions as seen in Appendix B, Figures B.28 and B.29. The plots in Figure 2.10b show two distinct conformational clouds indicated with the black circles for both the 3-ring and 4-ring MDA, which agrees with the experimental bimodal IM traces in Figure 2.10a.

Figure 2.11 shows selected conformations based on root mean squared deviation (RMSD) clustering and alignment with experimental CCS values. Each conformation is labeled with its theoretical CCS value along with the percentage of conformations that the structure represents based on RMSD clustering analysis. Each conformation shown represents a different protonation site and thus a separately modeled set of conformations. The percentage indicates how representative the conformation shown is of the independently modeled protonation sites and therefore do not show relations between the conformations in Figure 2.11 since each of these protonated species was modeled

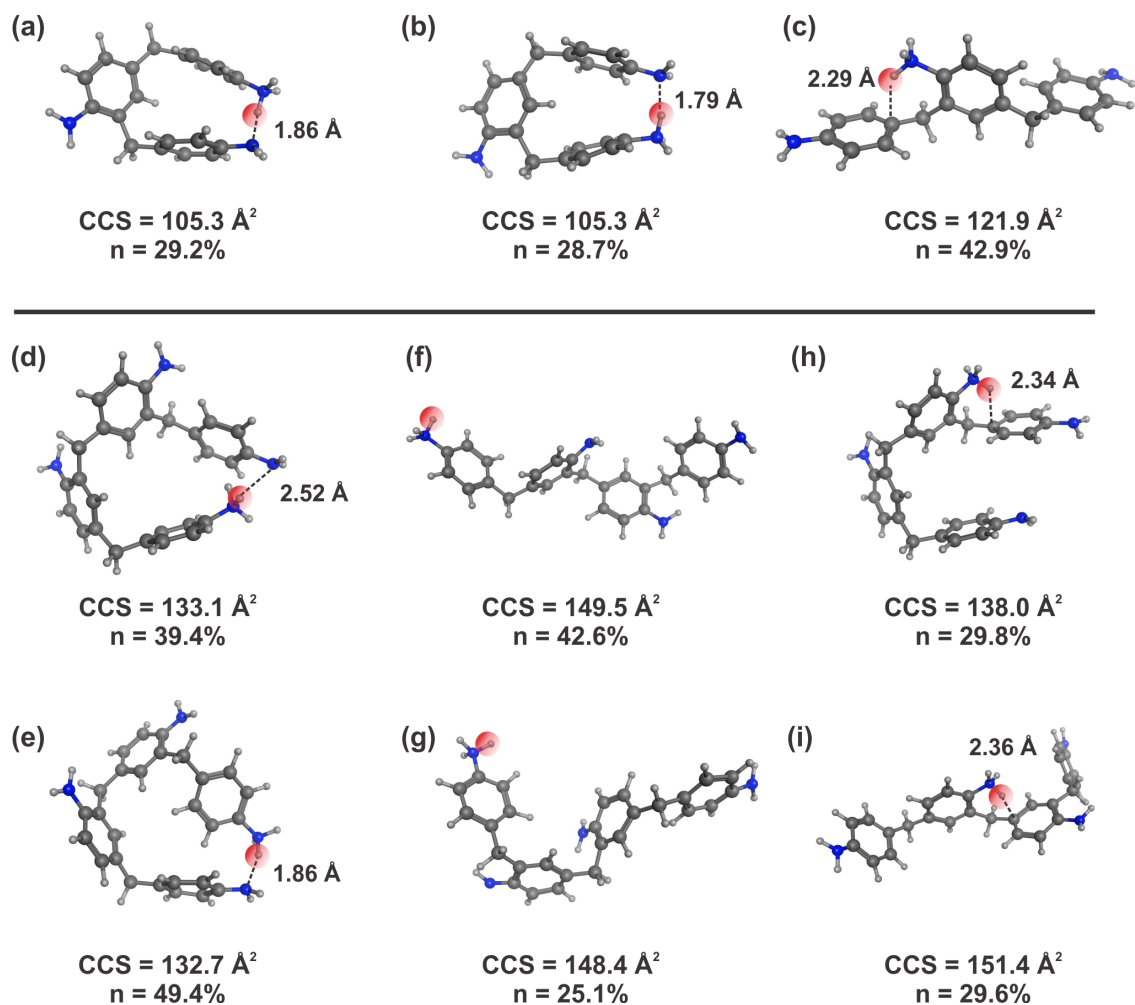


Figure 2.11. RMSD clustering representatives from computational conformational sampling are shown for each of the protonation sites for the 3-ring MDA (a-c) and for the 4-ring MDA (d-i). Labeled bond distances are used to show the proximity of the additional proton to the terminal nitrogen or bridging carbon that would lead to a 1,5-hydrogen shift fragmentation.

separately. A comprehensive set of representative conformations that were generated for each protonation site can be found in Appendix B, Figures B.30-B.56.

Conformations for the 3-ring MDA are shown in Figure 2.11a-c. The conformations in Figure 2.11a,b represent the smaller CCS conformational space cluster and are the result obtained when protonation occurs at the amines on the terminal rings. These conformations agree with experimental CCS helium values obtained on the DTIM instrument (Table 2.3) and are the most representative structures based on RMSD clustering analysis. The smaller CCS, and more stable conformation of the 3-ring MDA, reflects the structure in which the two external amine groups share the additional proton. Likewise, the conformation in Figure 2.11c is representative of protonation on the internal amine and aligns with the larger CCS conformational space cluster for the 3-ring MDA (Figure 2.10b). This conformation is a cluster representative structure, but due to gas-phase stability does not have a corresponding experimental CCS value from the DTIM instrument. Given that the CCS value we observe experimentally for the 3-ring MDA aligns with the smaller CCS conformational cluster, we surmise that the larger experimental CCS value corresponds to the larger CCS conformational space cloud. The position of the proton on the internal amine is very similar to that of protonation on both the 2,2' and 2,4' 2-ring MDA species when protonation occurs on the ortho amine. It is also important to note that this additional proton on the amine is aligned in an energetically favorable position with the most basic region of the adjacent aniline ring.

For the 4-ring MDA, two conformational clusters exist in Figure 2.10b with representative structures shown in Figure 2.11d-i. The conformations in Figure 2.11d,e are representative of the smaller CCS cluster, in agreement with Table 2.3, and represent

conformations that are protonated on the external amines. Protonation at the periphery of the molecule form smaller CCS conformations, similar to the 3-ring MDA, that wrap around and share the proton between the two external amine groups. The conformations in Figure 2.11f-i are representative of the larger CCS cluster, for which there are two possibilities. The first is shown in Figure 2.11f,g where protonation occurs on the external amines, similar to the conformations in Figure 2.11d,e, but here the conformation remains in an extended form rather than forming a cyclic species to share the proton. Figure 2.11h,i shows the other possibility where protonation occurs on one of the two internal amines. Again, this position of the proton on the internal amine is very similar to that of protonation on both the 2,2'- and 2,4'- 2-ring MDA species when protonated on the ortho amine. This similarity suggests the 3-ring and 4-ring MDA should fragment via a similar mechanism to that of the 2-ring MDA.

There is an interesting difference in the IM intensities shown in Figure 2.9a,b for both the 3-ring and 4-ring MDA. As indicated above, the 3-ring MDA peak corresponding to the lower CCS structures (Figure 2.11a,b) is intense, whereas the lower CCS peak for the 4-ring MDA spectra (Figure 2.11d,e) is much lower in abundance. Also, the onset of the 106 Da fragment peak is accessed at higher collision energies for the 3-ring isomer, as seen in Figure 2.9c. These observations correlate well with the known behavior of macrocyclic structures. Specifically, there is an optimum size for the formation of large cyclic structures, the most stable in the range of 15 atoms in the ring.⁴⁹ The cyclic 3-ring MDA structures in Figure 2.11a,b have 16 atoms while the cyclic 4-ring MDA structures in Figure 2.11d,e are composed of 20 atoms, and thus the former should be more stable than the latter. Compatible with this, the non-cyclic structures in Figure

2.11f,g are prominent for the 4-ring MDA, but not for the 3-ring isomer. Because of the shared hydrogen in Figure 2.11a,b this stability is reflected in the higher fragmentation energy required for dissociation of the 3-ring MDA. A similar effect has been noted previously for hydrogen transfer reactions in the MS/MS fragmentation of aramids.⁵⁰

III. Mechanism for protonation and fragmentation of MDA isomers

Based on the conformational observations from both IM and theoretical simulations and the results from tandem MS studies, fragmentation mechanisms can be suggested for both the 3-ring and 4-ring MDA species. These mechanisms are shown in Figure 2.12. For the 3-ring MDA, there are two fragments in the MS/MS spectra in Figure 2.8b at 106 and 211 Da compared to the 2-ring MDA isomers which only yielded a single fragment at 106 Da. Figure 2.12a shows how both of these fragments are formed from the 304 Da precursor ion. Here, the 106 Da fragment forms via an α -cleavage reaction of the 304 Da ion that also results in the loss of a neutral 198 Da fragment that mimics the 2,4' 2-ring MDA. The conformation of the 304 Da precursor ion for this reaction is shown in Figure 2.11a,b and has a theoretical He CCS of 105.3 \AA^2 which is very similar to the He experimental value in Table 1 of 105.5 \AA^2 . As previously mentioned, the 15-member ring present in these conformations is energetically favorable and must therefore be opened before the α -cleavage reaction can occur. This explains why there is not significant formation of the 106 Da fragment in Figure 2.9c until ca. 4 eV. Figure 2.9c also shows that at 0 eV the 304 Da fragment is already converted to the 211 Da fragment over 70%, suggesting that this fragmentation pathway is readily accessible. This low energy 1,5 hydrogen shift mechanism was previously observed for the 2,2' and 2,4' 2-ring MDA

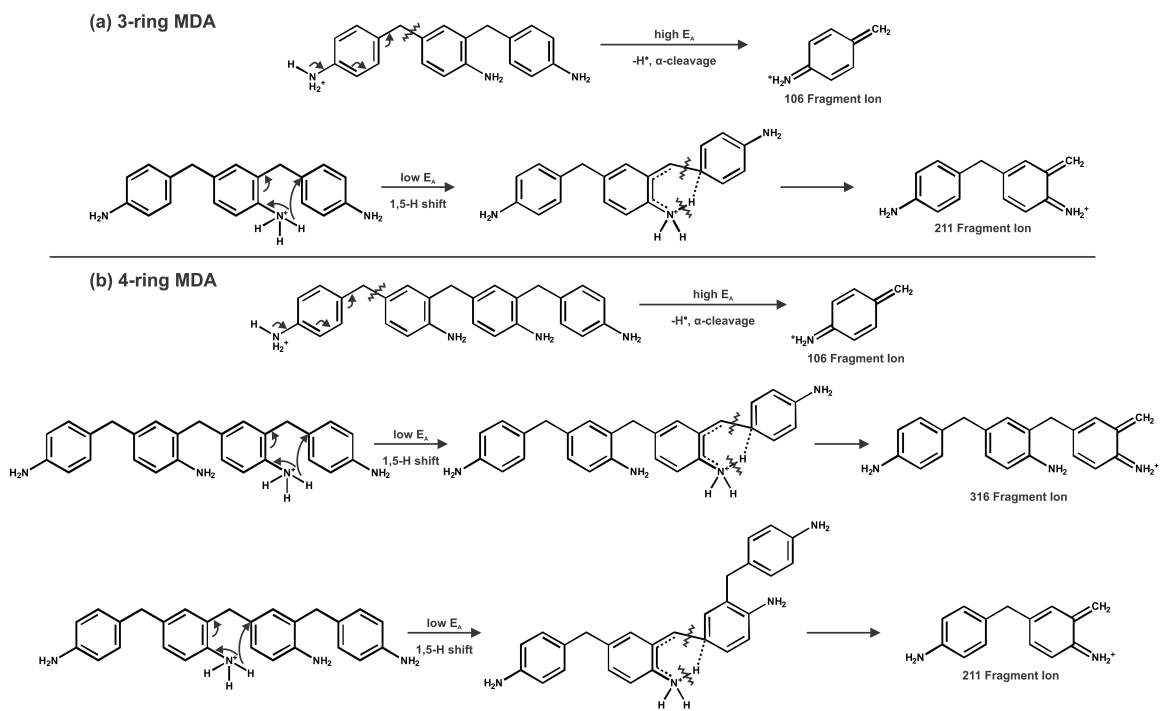


Figure 2.12. Proposed fragmentation pathways for 3-ring and 4-ring MDA structures.

isomers, but not with protonation on an internal amine as show here in Figure 2.12a with the 3-ring MDA. Although the larger 3-ring conformation shown in Figure 2.11c does not have a corresponding experimental He CCS value, this conformation is assigned to the 304 Da precursor ion for the 1,5 hydrogen shift fragmentation pathway due to the location of the additional proton near the most basic site on the adjacent aniline ring. This 1,5 hydrogen shift fragmentation results in loss of neutral aniline as well as the 211 Da fragment.

For the 4-ring MDA there are three fragments present in the MS/MS spectra in Figure 2.8b at 106, 211, and 316 Da. Figure 2.12b shows how these three fragment ions are formed from the 409 Da precursor ion. Similar to the 3-ring MDA, the 106 Da fragment forms via a high-energy α -cleavage reaction. Also similar to the 3-ring MDA, the 4-ring MDA forms a cyclic conformation as seen in Figure 2.11d,e with theoretical He CCS values of 133.1 and 132.7 \AA^2 respectively. These conformations exhibit the best agreement with the experimental He CCS value of 132.7 \AA^2 in Table 2.3. At 20 atoms though, these cyclic structures are no longer as energetically favored as the 3-ring MDA and therefore the extended conformations shown in Figure 2.11f,g are also possible. The proposed favorability of this extended conformation is further validated by the observation that significant production of the 106 Da fragment occurs at 2.75 eV in Figure 2.9d compared to the 4 eV for the 3-ring MDA. Additionally, the larger CCS conformation for the 4-ring MDA is more abundant than the smaller CCS conformation in Figure 2.10a. Figure 2.9d also shows that the 409 Da precursor ion has converted to the 316 Da fragment at 94% at 0 eV. Similar to the 3-ring MDA, the low energy 1,5 hydrogen shift fragmentation mechanism is initiated by protonation on an internal amine,

which is represented by the conformation in Figure 2.11h. This fragmentation reaction results in loss of neutral aniline as well as the 316 Da ion fragment. The 211 Da fragment of the 4-ring MDA also occurs via a 1,5 hydrogen shift initiated by protonation on an internal amine, but instead of the protonated amine being located adjacent to an external aniline this internal amine is located directly in the middle of the 4-ring MDA structure with two 2-ring MDA units on each side as shown in the conformation in Figure 2.11i. In order for the fragmentation mechanism to occur, a larger portion of the structure must be orientated such that the additional proton is in proximity to the most basic site on the adjacent aniline ring. This explains why significant formation of the 211 Da fragment does not occur until 2.25 eV in Figure 2.9d. These fragmentation mechanisms observed for the 3-ring and 4-ring MDA, which mimic the α -cleavage and 1,5 hydrogen shift observed for the 2-ring MDA isomers, will serve as the basis for characterizing larger MDA sample mixtures possessing additional internal amines which can serve as possible protonation sites.

2.5 Conclusions

In this study, 2-ring MDA structural isomers have been characterized and differentiated by their gas-phase stabilities and potential protonation sites using a combination of MS, IM, and structural insights guided by theoretical modeling. Our results confirm that, similar to aniline, MDA may be protonated at either amine positions or at ring positions in the gas-phase. Structural differences between positional isomers play a large role in determining the gas-phase stability, as does the site of protonation. The collective use of tandem MS, IM-MS, IM-MS/MS, and computational methods

allowed us to gain significant structural understanding of this system and suggests that a holistic approach to studying positional isomers is of great utility.

Industrial grade MDA, which is used to synthesize polyurethanes, is comprised primarily of 4,4'-MDA but also 2,2'-MDA, 2,4'-MDA, and larger multimers. Based on the data presented in this paper, we hypothesize that previous studies on MDA mixtures which focused primarily on 4,4'-MDA did so due to the large difference in gas-phase stability between 4,4'-MDA and the other two isomers, 2,2'-MDA and 2,4'-MDA. These isomers were likely in low abundance in MDA samples; however, due to metastable fragmentation, the researchers were likely unable to detect them.

In this study, 3-ring and 4-ring MDA species were also characterized using an MS-based analytical approach. We conclude that the protonation sites for the 3-ring and 4-ring MDA regioisomers are only at the amine group. Additionally we determined that protonation on either external or internal amine groups greatly influences the gas-phase stability of these species. The use of MS/MS, IM-MS, and computational modeling allowed for the structural characterization of these gas-phase ions and further promotes the benefit of combining several different MS-based technologies for comprehensive characterization studies.

These larger MDA units are composed primarily of linking anilines with the amine group in the para position to the bridging carbon, but do not maintain the gas-phase stability of the 4,4'-MDA due to possible protonation on internal amine groups, leading to charge-directed fragmentation of the 3-ring and 4-ring MDA. A thorough understanding of the fragmentation mechanisms initiated by internally protonated amines for both the 3-ring and 4-ring MDA will greatly facilitate the interpretation of

fragmentation spectra of the larger MDA units which are expected to dissociate via similar mechanisms. Further studies on larger MDA units will allow us to observe if this trend continues as chain length increases or if other, more stable attachment patterns form. Understanding that these chains fragment easily when protonated on internal amines will prove helpful when identifying the structures of precursor and fragment ions with MS. Tandem MS studies will provide fragmentation titration curves that can be compared to those for the 2-, 3-, and 4-ring MDA to determine if ions formed from the larger MDA units fragment via similar pathways. IM and theoretical simulations have been demonstrated to separate different protonation sites for the 2-, 3-, and 4-ring isomers and should help to identify different conformers in mixtures of larger MDA species, where the structural heterogeneity is more diverse.

A more thorough understanding of MDA behavior in the gas-phase will lead to a more comprehensive characterization of industrial MDA mixtures and better understanding of polyurethane fragmentation in mass spectrometry. In future studies, we look to structurally characterize larger MDA oligomers, complex MDA, and complex MDI mixtures using not only ESI-IM-MS but also MALDI-IM-MS. Our results on the 2-ring MDA compounds suggest IM-MS methods of characterizing larger multimers and MDA mixtures will prove beneficial to fully understand not only the molecular composition of the sample but also the structural differences between isobaric species within the sample. These differences, invisible to most polymer characterization methods, likely play a role in the resulting gas-phase structures of the polyurethanes.

2.6 Acknowledgements

I would like to thank Dr. Stefan Wershofen for providing 4,4'-, 2,4'-, and 2,2'-2-ring, 3-ring and 4-ring MDA samples. I also acknowledge the characterization support of Dr. Don Stec and the Vanderbilt NMR facilities, which is supported by the National Institute of Health (NIH, grant award number S10 RR019022). Additionally, I acknowledge the Vanderbilt Center for Structural Biology and Dr. Terry Lybrand for computational support and the Searle Systems Biology and Bioengineering Undergraduate Research Experience (SyBBURE) Program for summer support for Nicholas W. Kwiecien and Tiffany M. Onifer for experimental work. This research was funded by the Defense Threat Reduction Agency under Grants HDTRA1-09-1-00-13 and DTRA100271 A-5196; and the Defense Advanced Research Projects Agency under Grant W911NF-12-2-0036; and the National Institutes of Health UH2RT000491.

2.7 References

1. Chattopadhyay, D. K.; Raju, K. Structural engineering of polyurethane coatings for high performance applications. *Progress in Polymer Science* 2007, 32 (3), 352-418.
2. Eifler, W.; Ick, J. U.S. Patent 4,189,443, February 19, 1980.
3. van den Berg, H.; van der Ham, L.; Gutierrez, H.; Odu, S.; Roelofs, T.; de Weerd, J. Phosgene free route to Methyl Diphenyl Diisocyanate (MDI): A technical and economical evaluation. *Chemical Engineering Journal* 2012, 207-208, 254-257.
4. Skarping, G.; Dalene, M. Determination of 4, 4' -methylenediphenyldianiline (MDA) and identification of isomers in technical-grade MDA in hydrolysed plasma and urine from workers exposed to methylene diphenyldiisocyanate by gas chromatography-mass spectrometry. *Journal of Chromatography B: Biomedical Sciences and Applications* 1995, 663 (2), 209-216.
5. Cocker, J.; Brown, L. C.; Wilson, H. K.; Rollins, K. A GC/MS method for the determination of 4, 4' -diaminodiphenylmethane and substituted analogues in urine. *Journal of Analytical Toxicology* 1988, 12 (1), 9-14.
6. Bailey, E.; Brooks, A. G.; Bird, I.; Farmer, P. B.; Street, B. Monitoring exposure to 4, 4' -methylenedianiline by the gas chromatography-mass spectrometry determination of adducts to hemoglobin. *Analytical Biochemistry* 1990, 190 (2), 175-181.
7. Chen, K.; Dugas, T. R.; Cole, R. B. Identification of metabolites of 4, 4' -methylenedianiline in vascular smooth muscle cells by liquid chromatography - electrospray tandem mass spectrometry. *Journal of Mass Spectrometry* 2006, 41 (6), 728-734.
8. Chen, K.; Dugas, T. R.; Cole, R. B. Liquid chromatography-electrospray tandem mass spectrometry investigations of fragmentation pathways of biliary 4, 4' -methylenedianiline conjugates produced in rats. *Analytical and Bioanalytical Chemistry* 2008, 391 (1), 271-278.
9. Chen, K.; Cole, R. B.; Santa Cruz, V.; Blakeney, E. W.; Kanz, M. F.; Dugas, T. R. Characterization of biliary conjugates of 4, 4' -methylenedianiline in male versus female rats. *Toxicology and Applied Pharmacology* 2008, 232 (2), 190-202.
10. Johnson, J. R.; Karlsson, D.; Dalene, M.; Skarping, G. Determination of aromatic amines in aqueous extracts of polyurethane foam using hydrophilic interaction

- liquid chromatography and mass spectrometry. *Analytica Chimica Acta* 2010, 678 (1), 117-123.
11. Pezo, D.; Fedeli, M.; Bosetti, O.; Nerín, C. Aromatic amines from polyurethane adhesives in food packaging: the challenge of identification and pattern recognition using quadrupole-time of flight-mass spectrometry. *Analytica Chimica Acta* 2012, 756, 49-59.
 12. Wang, C. Y.; Li, H. Q.; Wang, L. G.; Cao, Y.; Liu, H. T.; Zhang, Y. Insights on the mechanism for synthesis of methylenedianiline from aniline and formaldehyde through HPLC-MS and isotope tracer studies. *Chinese Chemical Letters* 2012, 23 (11), 1254-1258.
 13. McDaniel, E. W. *Collision phenomena in ionized gases*. Wiley: New York, 1964.
 14. McDaniel, E. W.; Mason, E. A. *Mobility and diffusion of ions in gases*. John Wiley and Sons: New York, 1973.
 15. Mason, E. A. *Ion mobility: its role in plasma chromatography*. In *Plasma Chromatography*, 1984.
 16. Eiceman, G. A.; Karpas, Z. *Ion Mobility Spectrometry, Second Edition*. CRC Press: Boca Raton, FL, 2005; p 360 pp.
 17. Ruotolo, B. T.; Benesch, J. L. P.; Sandercock, A. M.; Hyung, S.-J.; Robinson, C. V. Ion mobility-mass spectrometry analysis of large protein complexes. *Nature Protocols* 2008, 3 (7), 1139-1152.
 18. Wilkins, C. L.; Trimpin, S. *Ion Mobility Spectrometry-Mass Spectrometry: Theory and Applications*. CRC Press: Boca Raton, FL, 2011.
 19. Hines, K. M.; Enders, J. R.; McLean, J. A. *Multidimensional Separations by Ion Mobility - Mass Spectrometry*. John Wiley & Sons: New York.
 20. Hilton, G. R.; Jackson, A. T.; Thalassinos, K.; Scrivens, J. H. Structural analysis of synthetic polymer mixtures using ion mobility and tandem mass spectrometry. *Analytical Chemistry* 2008, 80 (24), 9720-9725.
 21. Gies, A. P.; Kliman, M.; McLean, J. A.; Hercules, D. M. Characterization of branching in aramid polymers studied by MALDI- ion mobility/mass spectrometry. *Macromolecules* 2008, 41 (22), 8299-8301.
 22. Trimpin, S.; Clemmer, D. E. Ion mobility spectrometry/mass spectrometry snapshots for assessing the molecular compositions of complex polymeric systems. *Analytical Chemistry* 2008, 80 (23), 9073-83.

23. Li, X.; Guo, L.; Casiano-Maldonado, M.; Zhang, D.; Wesdemiotis, C. Top-down multidimensional mass spectrometry methods for synthetic polymer analysis. *Macromolecules* 2011, 44 (12), 4555-4564.
24. Hoskins, J. N.; Trimpin, S.; Grayson, S. M. Architectural differentiation of linear and cyclic polymeric isomers by ion mobility spectrometry-mass spectrometry. *Macromolecules* 2011, 44 (17), 6915-6918.
25. Hagen, D. F. Characterization of isomeric compounds by gas and plasma chromatography. *Analytical Chemistry* 1979, 51 (7), 870-874.
26. Hagen, D. F.; Carr, T. W. *Characterization of Isomers by Plasma Chromatography*. Plenum Press: New York: 1984.
27. Wesdemiotis, C.; Solak, N.; Polce, M. J.; Dabney, D. E.; Chaicharoen, K.; Katzenmeyer, B. C. Fragmentation pathways of polymer ions. *Mass Spectrometry Reviews* 2011, 30 (4), 523-559.
28. Laphorn, C.; Dines, T. J.; Chowdhry, B. Z.; Perkins, G. L.; Pullen, F. S. Can ion mobility mass spectrometry and density functional theory help elucidate protonation sites in 'small' molecules? *Rapid Communications in Mass Spectrometry* 2013, 27 (21), 2399-2410.
29. Tintaru, A.; Chendo, C.; Wang, Q.; Viel, S.; Quéléver, G.; Peng, L.; Posocco, P.; Pricl, S.; Charles, L. Conformational sensitivity of conjugated poly (ethylene oxide)-poly (amidoamine) molecules to cations adducted upon electrospray ionization—A mass spectrometry, ion mobility and molecular modeling study. *Analytica Chimica Acta* 2014, 808, 163-174.
30. Campuzano, I.; Bush, M. F.; Robinson, C. V.; Beaumont, C.; Richardson, K.; Kim, H.; Kim, H. I. Structural characterization of drug-like compounds by ion mobility mass spectrometry: comparison of theoretical and experimentally derived nitrogen collision cross sections. *Analytical Chemistry* 2011, 84 (2), 1026-1033.
31. Sleno, L.; Volmer, D. A. Ion activation methods for tandem mass spectrometry. *Journal of Mass Spectrometry* 2004, 39 (10), 1091-1112.
32. Rodgers, M. T.; Armentrout, P. B. Noncovalent metal-ligand bond energies as studied by threshold collision - induced dissociation. *Mass Spectrometry Reviews* 2000, 19 (4), 215-247.
33. May, J. C.; Goodwin, C. R.; Lareau, N. M.; Leaptrot, K. L.; Morris, C. B.; Kurulugama, R. T.; Mordehai, A.; Klein, C.; Barry, W.; Darland, E. *Conformational Ordering of Biomolecules in the Gas Phase: Nitrogen Collision*

Cross Sections Measured on a Prototype High Resolution Drift Tube Ion Mobility-Mass Spectrometer. *Analytical Chemistry* 2014, 86 (4), 2107-2116.

34. Wyttenbach, T.; Bowers, M. T. Gas-phase conformations: The ion mobility / Ion Chromatography Method. In *Modern Mass Spectrometry*, Springer: 2003; pp 207-232.
35. Frisch, M. J.; Trucks, G. W.; Schlegel, H. B.; Scuseria, G. E.; Robb, M. A.; Cheeseman, J. R.; Scalmani, G.; Barone, V.; Mennucci, B.; Petersson, G. A. et. al. Gaussian 09, Revision A. 02, Gaussian. Inc., Wallingford, CT 2009, 2 (3), 4.
36. Case, D. A.; Darden, T. A.; Cheatham Iii, T. E.; Simmerling, C. L.; Wang, J.; Duke, R. E.; Luo, R.; Walker, R. C.; Zhang, W.; Merz, K. M. AMBER 11. University of California, San Francisco 2010, 142.
37. Case, D. A.; Babin, V.; Berryman, J.; Betz, R. M.; Cai, Q.; Cerutti, D. S.; Cheatham Iii, T. E.; Darden, T. A.; Duke, R. E.; Gohlke, H. Amber 14 2014.
38. Bayly, C. I.; Cieplak, P.; Cornell, W.; Kollman, P. A. A well-behaved electrostatic potential based method using charge restraints for deriving atomic charges: the RESP model. *The Journal of Physical Chemistry* 1993, 97 (40), 10269-10280.
39. Wyttenbach, T.; Helden, G. v.; Batka Jr, J. J.; Carlat, D.; Bowers, M. T. Effect of the long-range potential on ion mobility measurements. *Journal of the American Society for Mass Spectrometry* 1997, 8 (3), 275-282.
40. Mesleh, M. F.; Hunter, J. M.; Shvartsburg, A. A.; Schatz, G. C.; Jarrold, M. F. Structural information from ion mobility measurements: effects of the long-range potential. *The Journal of Physical Chemistry* 1996, 100 (40), 16082-16086.
41. Shvartsburg, A. A.; Jarrold, M. F. An exact hard-spheres scattering model for the mobilities of polyatomic ions. *Chemical Physics Letters* 1996, 261 (1), 86-91.
42. Bush, M. F.; Campuzano, I. D. G.; Robinson, C. V. Ion Mobility Mass Spectrometry of Peptide Ions: Effects of Drift Gas and Calibration Strategies. *Analytical Chemistry* 2012, 84 (16), 7124-7130.
43. Rappoport, Z. *The chemistry of anilines*. John Wiley & Sons: 2007; Vol. 169.
44. Lau, Y. K.; Kebarle, P. Substituent effects on the intrinsic basicity of benzene: proton affinities of substituted benzenes. *Journal of the American Chemical Society* 1976, 98 (23), 7452-7453.

45. Karpas, Z.; Berant, Z.; Stimac, R. M. An ion mobility spectrometry/mass spectrometry (IMS/MS) study of the site of protonation in anilines. *Structural Chemistry* 1990, 1 (2-3), 201-204.
46. Roy, R. K.; De Proft, F.; Geerlings, P. Site of protonation in aniline and substituted anilines in the gas phase: a study via the local hard and soft acids and bases concept. *The Journal of Physical Chemistry A* 1998, 102 (35), 7035-7040.
47. Russo, N.; Toscano, M.; Grand, A.; Mineva, T. Proton affinity and protonation sites of aniline. Energetic behavior and density functional reactivity indices. *The Journal of Physical Chemistry A* 2000, 104 (17), 4017-4021.
48. Lalli, P. M.; Iglesias, B. A.; Toma, H. E.; Sa, G. F.; Daroda, R. J.; Silva Filho, J. C.; Szulejko, J. E.; Araki, K.; Eberlin, M. N. Protomers: formation, separation and characterization via travelling wave ion mobility mass spectrometry. *Journal of Mass Spectrometry* 2012, 47 (6), 712-719.
49. Wilen, S. H.; Mander, L. N.; Eliel, E. L. *Stereochemistry of organic compounds*. John Wiley: 1994.
50. Gies, A. P.; Ellison, S. T.; Stow, S. M.; Hercules, D. M. Matrix-assisted laser desorption/ionization-time-of-flight/time-of-flight collision-induced dissociation study of poly(*p*-phenylenediamine terephthalamide) fragmentation reactions. *Analytica Chimica Acta* 2014, 808, 124-143.

CHAPTER 3

DISTANCE GEOMETRY PROTOCOL TO GENERATE CONFORMATIONS OF NATURAL PRODUCTS AND METABOLITES TO STRUCTURALLY INTERPRET ION MOBILITY-MASS SPECTROMETRY COLLISION CROSS SECTIONS

3.1. Introduction

Ion mobility-mass spectrometry (IM-MS) is an analytical technique used to separate gas-phase ions based on their structural properties such as size and shape as well as their mass, in the IM and MS dimensions, respectively. The structural properties affect the ion's collision cross section (CCS), or rotationally averaged surface area.¹⁻³ Ongoing efforts in our laboratories utilize IM-MS to aid in natural product discovery from bacterial colonies.^{4,5} IM-MS is often able to structurally separate the low-abundance secondary metabolites from the complex biological background, a key challenge in natural product discovery by MS.

In an effort to help elucidate the structural information derived from CCS data, computational methods are often used to interpret IM-MS experiments.⁶⁻⁹ A computational algorithm is used to generate conformations of the molecule, defining its conformational space. Then, a theoretical CCS is calculated for each of the conformations. Conformations that fall within the experimental CCS range can then be further interrogated to provide a more detailed understanding of the molecular conformation(s) that are consistent with experiment. Table 3.1 lists methods commonly used for generating conformations in support of IM-MS experimental data. For large

Table 3.1. Representative IM-MS structural studies of different model systems.

Computational Methods	Model System
Coarse-grained Modeling	Protein Complexes ¹⁰⁻¹³ Virus ^{14,15}
Molecular Dynamics (Simulated Annealing, Replica Exchange, etc.)	Peptides ^{17,18} Carbohydrates ^{19,20} Natural Products ^{4,21}

systems such as protein complexes¹⁰⁻¹³ and virus assemblies^{14,15} coarse-grained methods are used to obtain the cross-sectional area. For smaller systems (peptides¹⁶⁻¹⁸, carbohydrates^{19,20}, smaller molecules^{4,21}, etc.), some form of molecular dynamics (MD) is the current method of choice.

Long MD simulations with an appropriate force field for the molecule(s) of interest are typically required to obtain a thorough and useful conformational analysis. While the IM-MS experimental data can be generated rapidly (on the order of ms (IM) and μ s (MS)), MD simulations for conformational analysis are quite time consuming (days to weeks depending on the modeled structures). Furthermore, natural products are a very structurally diverse group of molecules, and this can make appropriate force field selection difficult. Although force fields exist that can describe many natural product molecules realistically, it is not clear that any current force field is appropriate for all members of this diverse class of molecules. If an inappropriate force field is used in the MD simulation, the resulting molecular conformations might be chemically unreasonable. One possible solution is to generate new potential function parameters for each molecule of interest, but this can be a time-consuming process if large numbers of molecules need to be studied. An alternative solution is to use computational techniques that do not rely on a force field for conformational sampling.

Distance geometry generates molecular conformations by sampling different possible inter-atomic distances between all pairs of atoms in the molecule.^{22,23} Upper and lower distance limits, or bounds, are defined for each pair of atoms in the molecule and then a distance within these bounds is selected randomly for each pair. Lower bounds are typically adjusted to avoid atomic overlaps (*i.e.*, the lower bound may be set as the sum

of the van der Waals radii of the atom pair), while upper bounds can be set at an arbitrarily large value to increase the number of possible conformations that are generated. Note that as the upper bound is increased, a larger number of chemically unreasonable conformations will be generated. To limit the number of chemically unreasonable conformations generated, bounds for covalently bonded atom pairs are normally restricted to values quite close to the corresponding equilibrium bond lengths. Pair distances for atoms involved in bond angles at sp²- and sp³-hybridized atoms can also be restricted to produce chemically reasonable angle values, and additional restraints are routinely imposed to preserve stereochemistry at chiral centers. The set of selected atom-pair distances is then converted to the corresponding set of Cartesian coordinates that define the unique molecular conformation. By selecting different random distances for each pair of atoms in subsequent iterations, a collection of unique molecular conformations is generated. Since IM-MS experiments are conducted with ionized molecules, a cation is then added to each generated conformer, based on the minimum of the calculated molecular electrostatic potential grid. The cation-associated conformations generated with this computational protocol typically require brief geometry optimization to relieve any residual, small geometrical distortions (*e.g.*, slightly distorted bond lengths, bond angles, etc.) and to optimize the cation position. These geometry optimization calculations can be performed with either a quantum mechanical (QM) method or molecular mechanics energy minimization with an appropriate force field.

3.2. Experimental Section

The steps for the suggested distance geometry protocol as well as the MD-based method are shown in Figure 3.1 with a more detailed discussion below.

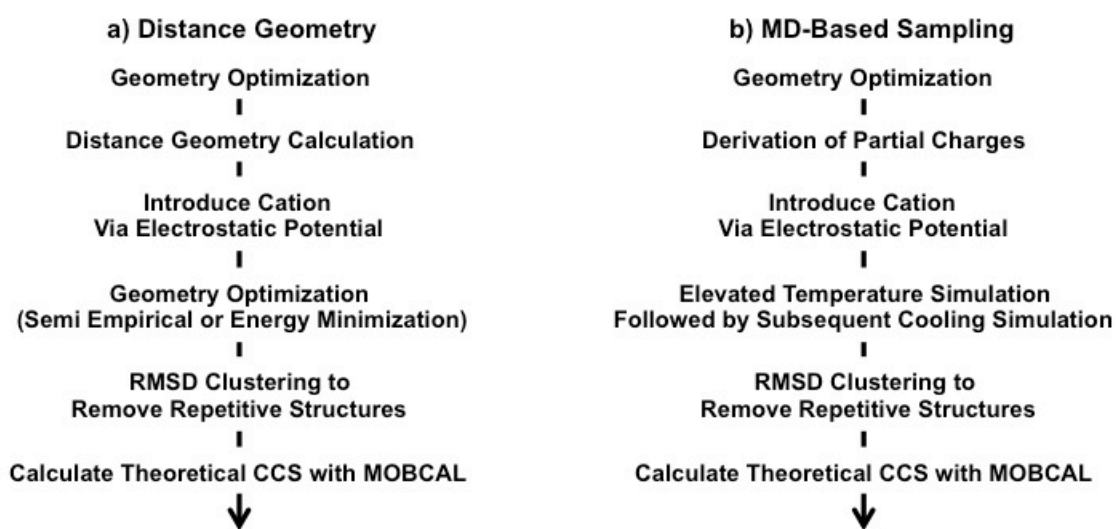


Figure 3.1. A schematic workflow for conformational analyses using the distance geometry protocol and the MD-based protocol.

Molecular Dynamics Method

An MD-based sampling protocol has been implemented where the system undergoes a single heating and cooling cycle during the calculation. One of the following two methods was used depending on which force field (GAFF²⁴ or MMFF94x²⁵) better described the molecule of interest.

For an MD simulation performed with the GAFF force field, a geometry optimization at the Hartree-Fock level with a 6-31G* basis set was performed with Gaussian09²⁶ for each test molecule. Partial charges for each molecule were derived from an *ab initio* electrostatic potential calculation using a 6-31G* basis set, and fitted using the RESP²⁷ program in AMBER²⁸. XLEaP was then used to generate the molecule-sodium complex. Chirality constraints were applied in the form of improper torsion angles and a distance restraint was placed on the sodium ion to keep it near the molecule during the simulation. Next, 1000 steps of steepest descent/ conjugate gradient energy minimization was performed with the sander module followed by a 10 ps MD simulation to heat the molecule to 1000 K. Then, a long MD simulation was run at 1000 K for 9000 ps where structural snapshots were saved every 3ps during the simulation. Each snapshot was then cooled to 300 K during a 15 ps MD simulation followed by a short energy minimization. The MOBCAL implementation of the projection approximation, exact hard sphere scattering, or calibrated trajectory methods (depending on the size of the molecule) were used to calculate the CCS of each sodium-coordinated complex.²⁹⁻³¹ Specifically, for molecules containing less than 100 atoms, the projection approximation was used. For molecules containing more than 100 atoms, the exact hard sphere scattering method was used with one exception. For erythromycin, which has several

oxygen atoms and a concave region between the two sugar rings a correlated trajectory method was used to achieve better alignment with the experimental data.

An MD-based sampling method was also performed in the Molecular Operating Environment (MOE)³² program with the MMFF94x force field. The sodium-coordinated complexes generated for the AMBER MD simulations were used as starting structures. Chiral centers were fixed and a distance restraint was used to retain the sodium cation near the molecule during the simulation. Each sodium-coordinated complex was first energy minimized, and then heated to 800-1000 K over a 10 ps MD simulation. Next, a long MD simulation was run at that elevated temperature (800-1000 K) for 9000 ps where structural snapshots were saved every 3 ps during the simulation. These snapshots were then cooled to 300 K during a 15 ps MD simulation followed by a short energy minimization. As described above, MOBCAL was used to calculate the CCS of each sodium-coordinated complex.

Distance Geometry

All distance geometry calculations were performed with the DGEOM95 program.³³ Initial input structures for the DG calculations were obtained from structural databases or generated with a model building program (*e.g.*, MOE), followed by geometry optimization in Gaussian09. DGEOM95 assigns connectivity and bond types based on input coordinates if connectivity information is not provided explicitly in the starting structure file. This information is used to assign distance restraints to actual bond lengths for covalently attached atoms and to detect non- and partially-rotatable bonds within the molecule. Torsions, or 1-4 distance restraints, are utilized for atoms in certain structural relationships. Atoms attached to double bonds and atoms within aromatic rings

are set coplanar, while amide and ester torsion angles are set to 0 ± 15 degrees. For all other torsion angles, lower bounds are set to $+60$ or -60 degrees (gauche orientations) for acyclic bonds and to eclipsed conformations for cyclic bonds or bonds adjacent to double bonds or aromatic rings by default. All other torsion angle upper bounds are set to 180 degrees (trans conformations). Distance restraints for all other atom pairs are defined so that the lower distance bound is set to the sum of their van der Waals radii, while upper distance bounds are set to the length of the longest chain between the two atoms (*i.e.*, the largest possible distance permitted by the series of bonds that connect the two atoms). In addition to these distance restraints, chiral centers are maintained by calculating the vector cross product of the tetrahedron enclosed by the four atoms attached to the chiral center and then ensuring the sign of the vector cross product remains the same in generated structures.

Once these distance restraints are generated, the triangle inequality theorem is used to verify that all distances are geometrically consistent. The triangle inequality theorem simply states that for any set of three atoms A, B, and C, the distance between atoms A-B cannot be longer than the sum of the distances between atoms A-C and B-C. Random pairwise distances that fall within the defined bounds are then selected through a partial metrization method that ensures that the majority of the random pairwise distances satisfy the triangle inequality.³⁴ The set of distances are then converted to discrete Cartesian coordinates, generating a unique conformation. These steps of selecting random pairwise distances and then converting them to Cartesian coordinates are repeated until the desired number of conformations is generated. Finally, a clustering step is performed so that degenerate conformations (pairwise RMSD < 1.0 Å) are removed. For the

molecules in this test set, we generated between 2,000 – 20,000 conformations to assess how thoroughly the distance geometry calculations sample conformational space.

Many empirically derived mobility measurements are determined with sodium-coordination of the cationizing species, in particular for natural products that can often contain oxygen-rich carbohydrate moieties and the high oxyphilicity of alkali metals. The initial conformations from distance geometry require connectivity for all atoms, which does not allow for easy incorporation of a coordinated cation. We used the XLEaP module in AMBER to coordinate a sodium cation with each conformer generated by the distance geometry program, placing the ion at the minimum of the molecular electrostatic potential computed from the partial charges. Then, we tested both a semi-empirical QM technique and molecular mechanics energy minimization for the geometry optimization step. For the QM geometry optimization we used the PDDG/PM3 Hamiltonian³⁵ with Gaussian09²⁶. A QM geometry optimization calculation is somewhat more CPU-intensive than molecular mechanics energy minimization, but may be the only practical option when suitable force fields are not available. We also used molecular mechanics energy minimization calculations, with either the MMFF94x force field²⁵ in MOE³² or the GAFF force field²⁴ in AMBER²⁸. For the GAFF force field calculations, we used atomic partial charge parameters developed for the MD simulations described above. Otherwise, we used default parameter values from each force field for all molecules.

Suppose³⁶ and OC³⁷ programs were used to cluster low-energy structures generated by each computational protocol into conformational families to achieve data reduction and facilitate structural analysis. The Suppose program superimposes all possible pairs of conformations and computes the root mean squared difference (RMSD)

in structure for each pair. The OC program then sorts the structures into clusters based on structural similarities as determined by a threshold RMSD cutoff value. For comparison purposes an RMSD cutoff value of 1.0 Å was chosen for both distance geometry and MD calculations. The OC program was used to select a molecular conformation that most closely represents the mean structure for each cluster. MOBCAL was then used to calculate the theoretical CCS for each cluster representative.

Experimental CCS Measurements

All 10 natural products were obtained from Sigma Chemical Company (St. Louis, MO). MALDI ionization was performed for 200:1 molar ratios of the analytes with either 2,5-dihydroxybenzoic acid or α -cyano-4-hydroxycinnamic acid matrix. The MALDI-IM-TOFMS has a 13.9 cm IM drift cell that is maintained at a pressure of *ca.* 3 Torr helium and an orthogonal reflection TOFMS with a 1 m flight path maintained at a pressure of 5×10^{-8} Torr. The temperature of the drift tube was ~ 293 K and the electrostatic-field strength ranged from ~ 90 -120 V cm⁻¹. Further experimental and instrumentation details have been presented previously in the literature.^{4,38}

3.3 Results and Discussion

The ten natural products studied here are shown in Figure 3.2. They range in size from 44 atoms ($[M+Na]^+$: 303.0 m/z) to 268 atoms ($[M+Na]^+$: 1133.6 m/z) and represent different subclasses of natural product molecules. Representatives from macrolides (brefeldin, erythromycin, josamycin), cyclic peptides (valinomycin), aromatic polyketides (doxorubicin), aminoglycoside antibiotics (neomycin), and other classes (capsaicin, lincomycin, antimycin, and ampicillin) were chosen to determine how distance geometry would perform across a wide range of natural product molecules.

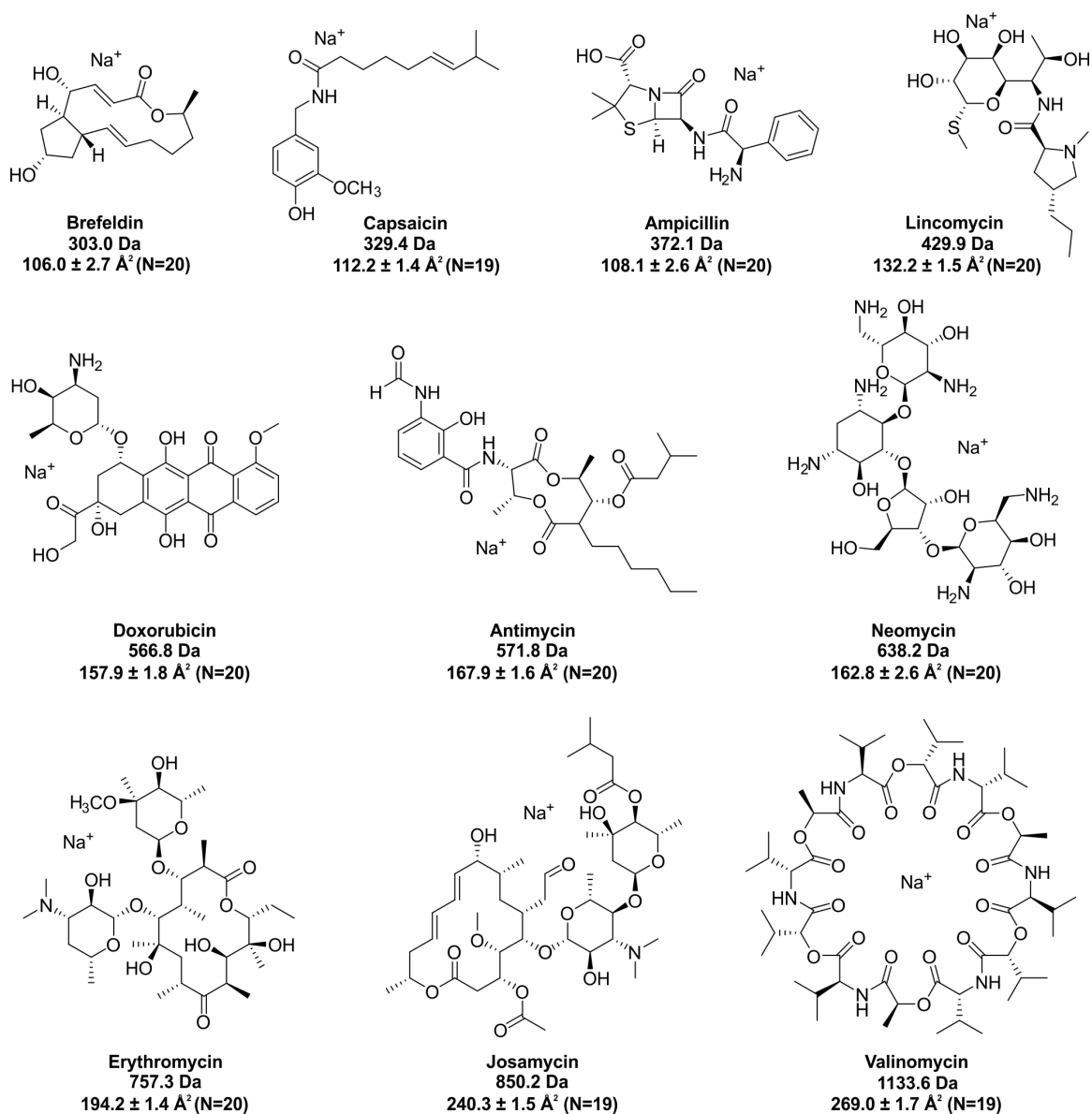


Figure 3.2. Two-dimensional structure representations of the ten natural products tested in the present study. Each natural product is labeled with corresponding m/z , experimental CCS, and number of experimental CCS measurements.

These different classes further emphasize the difficulty of trying to select a force field that would accurately describe such a diverse group of molecules.

The computational cost for both the MD-based method and the distance geometry calculations is presented for all ten molecules in the histogram in Figure 3.3. The computational cost for the MD method is typically at least an order of magnitude greater than the distance geometry protocol. These time values reflect calculations that were run on a single processor except for calculations performed in Gaussian09, which were run on four processors. Note that the calculated times do not incorporate the theoretical CCS calculation, only the time required to generate the conformations, to better compare the DG and MD strategies. Although the computational cost for the QM geometry optimization with distance geometry is not much smaller than that for the MD-based sampling protocol, without an appropriate force field for the molecule, this may be the best option. Also, since distance geometry calculations scale O^n and molecular dynamics calculations scale $O(n)$, the computational advantage for the DG protocol decreases for extremely large, flexible molecules (E.g., large peptides or small proteins).

To better ascertain the robustness and reliability of the distance geometry computational protocol, we performed a detailed analysis of results as a function of total number of requested conformations. Conformational space plots are shown in Figure 3.4 for four of the ten natural products (lincomycin (Figure 3.4a and 3.4b), neomycin (Figure 3.4c and 3.4d), josamycin (Figure 3.4e and 3.4f), and valinomycin (Figure 3.4g and 3.4h)), with detailed results for the remaining six presented in Appendix C (Figures C.11 and C.12). In the left panel of Figure 3.4, conformational space plots are shown that

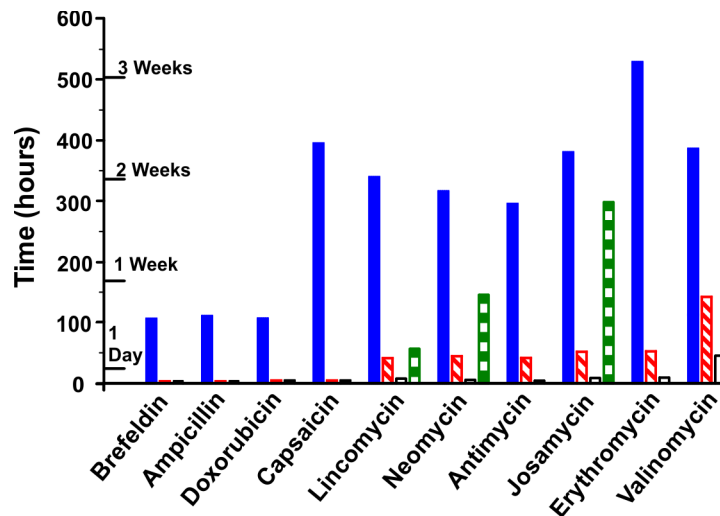


Figure 3.3. Histogram summarizing the computational cost of the distance geometry protocol compared to MD-based sampling. MD results are shown in solid blue and distance geometry results are shown in dashed red and open black depending upon how many initial conformations are requested (red for 20,000 conformations and black for 8,000 conformations). Results from the semi-empirical geometry optimization are shown in boxed green.

compare the results when either 8,000 or 20,000 conformations are generated by distance geometry. The theoretical CCS value is plotted against the computed energy for each conformation. The vertical grey bar indicates the experimental CCS range. When only 8,000 structures are requested a similar conformational space is covered compared to the 20,000-conformation sample for all test molecules, but at a much reduced total computation time. While comparable results are obtained for some of the test molecules when only 2,000 conformations are requested (data shown in Appendix C (Figure C.15)), this is not always the case with some of the larger and/or more flexible molecules. Thus, we conclude that for molecules of this size and molecular complexity, 8,000-10,000 generated conformations should sample conformational space adequately. In the right panel of Figure 3.4, the distance geometry results and MD conformational sampling results are plotted for comparison. There is a noticeable energy difference between the two methods that is reflective of the approaches these calculations take when sampling conformational space. The MD-based conformational sampling method tends to generate predominantly low-energy conformations, since MD preferentially samples low-energy regions of the energy surface. By contrast, DG is designed to explore all geometrically possible conformations (within the limits of the defined distance upper bounds), so it should always generate some slightly higher energy conformations as compared with MD-based sampling. While MD-based conformational sampling does generate lower energy conformations (due to the extensive cooling step in the calculation), nevertheless similar conformations are generated with each method. Clustering data as well as

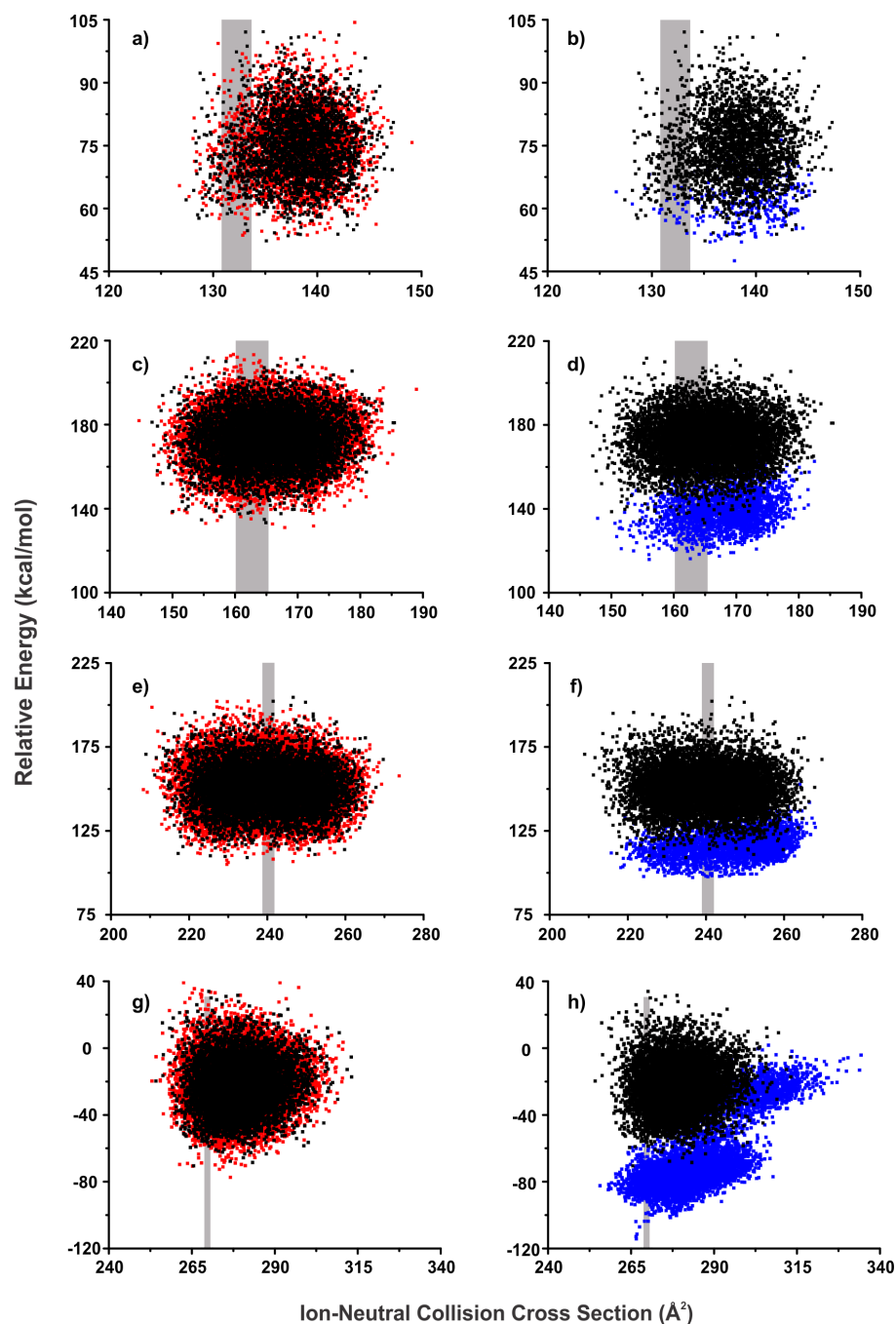


Figure 3.4. Scatter plots for four representative natural products to show where the generated conformations occur in relative energy versus theoretical CCS. The IM-MS measured CCS range (mean value and standard error) indicated by the vertical grey bar. In panels (a), (c), (e), and (g), the comparison for 8,000 (black) versus 20,000 (red) conformations generated by distance geometry is shown. In panels (b), (d), (f), and (h), the comparison for 8,000 (black) conformers from distance geometry versus MD-based conformational sampling (blue) is displayed. Results are shown for lincomycin (a & b), neomycin (c & d), josamycin (e & f), and valinomycin (g & h).

representative structures that illustrate these similarities are presented in Appendix C (Figures C.16 – C.44).

For lincomycin in Figure 3.4b, neomycin in Figure 3.4d, and josamycin in Figure 3.4f the distance geometry and MD methods perform comparably, generating a similar number of conformations within the experimental CCS range. For valinomycin in Figure 3.4h, the MD sampling method generates more conformations that agree with the accepted experimental gas-phase conformation of valinomycin.³⁹ This is almost certainly because valinomycin complexes the sodium cation within the cyclic peptide structure, and its low-energy conformations are thus influenced strongly by the presence of the cation. In the absence of the sodium ion, a dramatically different conformational ensemble is sampled. By contrast, the presence or absence of sodium coordination has little or no influence on the overall ensemble of conformations obtained for the other test molecules.

To illustrate the interpretation of experimental ion mobility conformation, ion mobility traces for the representative natural products are shown in Figure 3.5 along with sample conformations generated with the distance geometry protocol for the four natural products discussed above (results for all other molecules are in Appendix C (Figure C.13)). A conformation that agrees with the experimental data is shown near the mobility peak to the left, while a conformation that does not show agreement is also displayed for comparative purposes to the right. For conformations that fall within the experimental CCS range, sodium is typically coordinated with multiple atoms, generally leading to conformational contraction. By comparison when the sodium cation is coordinated with

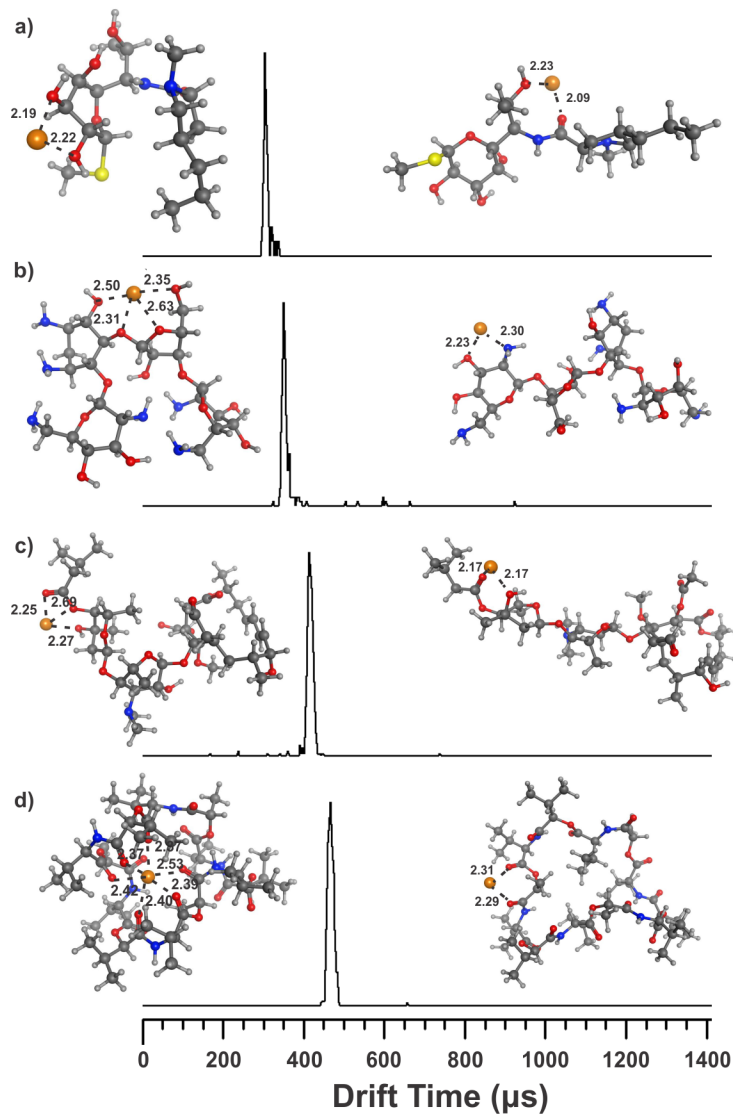


Figure 3.5. IM traces for the representative natural products shown in Figure 3.4, namely (a) lincomycin, (b) neomycin, (c) josamycin, and (d) valinomycin. The most representative conformation generated with distance geometry from within the experimental range is shown for each natural product to the left of the mobility peak and a conformation that does not agree with the experimental measurement is shown on the right of the mobility peak to illustrate the coordination of computation with experiment for interpretation of structure.

only one or two atoms, the conformations tend to be more open and extended. While there is modest conformational contraction observed for lincomycin (Figure 3.5a), neomycin (Figure 3.5b), and josamycin (Figure 3.5c), the effect is far more dramatic for valinomycin (Figure 3.5d). The valinomycin conformation that agrees best with the experimental data has the sodium ion localized in the center of the cyclic peptide ring where it coordinates with multiple oxygen atoms. The valinomycin conformation that is inconsistent with the experimental CCS data has the sodium ion coordinated on the periphery to only two oxygen atoms, resulting in a more elongated peptide conformation. Additional representative conformations from RMSD clustering for all ten of the natural products generated with both distance geometry and the MD sampling method can be found in Appendix C (Figures C.16 – C.36).

Advantages and Challenges for both Distance Geometry and Molecular Dynamics Sampling

As summarized in Table 3.2, both distance geometry and MD sampling methods have potential advantages and limitations for the conformational sampling task. It is important to first consider how each method is sampling conformational space. An MD calculation samples conformational space by generating trajectories on an energy hypersurface. This surface is defined by a force field, which describes all covalent and non-covalent interactions for the molecule(s) of interest. A suitable force field is crucial for effective use of an MD-based method; a force field that is not properly parameterized for the molecules of interest is not likely to yield relevant conformational information.

Distance geometry uses only inter-atomic distance data to generate a collection of conformations. The distance information is typically defined as “bounds”, *i.e.*, upper and

Table 3.2. Advantages and challenges associated with distance geometry and MD-based strategies.

Distance Geometry	MD-Based Sampling
Advantages	
<ul style="list-style-type: none"> • Sample the entire conformational space • Calculation does not depend on a force field • Time efficient 	<ul style="list-style-type: none"> • Preferentially samples low(er) energy conformations • Ion interacts with the molecule throughout the entire simulation
Challenges	
<ul style="list-style-type: none"> • Ions not included explicitly during DG calculations 	<ul style="list-style-type: none"> • Time consuming • Simulation is based on force fields which are not parameterized for all molecules • No easy way to determine when sufficient conformational sampling has been achieved

lower distance limits, rather than a fixed value, and these bounds are defined by chemical properties such as equilibrium bond lengths and bond angle values, van der Waals radii, etc. Thus, distance geometry methods can be used for conformational sampling even when suitable force fields are not available for the molecules of interest. This situation is exacerbated when molecules contain many different and non-uniform chemical functional groups and connectivity as encountered with natural products.

Clearly, it is important to ensure that conformational space is sampled adequately. Molecular dynamics simulations preferentially sample low energy regions of conformational space while distance geometry can generate all geometrically possible conformations allowed by the imposed bounds. Therefore, distance geometry can sample all conformational space if sufficiently loose distance bounds are set and if enough conformations are generated. In principle, MD-based methods can also sample all conformational space if a sufficiently long simulation is run. In practice, the computation time required to achieve any specified degree of “conformational space coverage” for molecules like those examined in this study will be much greater for MD-based sampling methods compared to distance geometry protocols, as our results clearly demonstrate.

Nevertheless, both of these methods can generate chemically unreasonable conformations. While distance geometry can create distorted, or strained, molecular conformations when loose bounds are used, a short energy minimization calculation can usually relax the distorted conformation. When distance bounds are defined more tightly, few, if any, distorted conformations are generated. MD-based conformational sampling strategies will typically generate relatively few strained, or high-energy, conformations. However, if elevated temperatures are used to increase conformational sampling

efficiency by facilitating transitions from one low-energy region to another on the energy surface, significantly more distorted, high-energy conformations may be generated, and subsequent energy minimization performed at the end of the calculation may not always relax the distorted conformations. The unique structural motifs (*e.g.* heterocyclization, macrocyclization) typical of the natural products investigated in this study make them particularly susceptible to conformational distortion during high-temperature MD simulations. Thus, while both methods can produce chemically unreasonable structures in the final solution dataset, this issue impacts the MD sampling protocol efficiency more dramatically due to the greater computational cost for the MD calculations.

In order to generate structures that are relevant for interpretation of the experimental data, conformations that represent the cation-molecule complex explicitly must be generated. In an MD simulation, the ion can be present throughout the simulation to facilitate this task. In cases where the cation may exert a significant influence on molecular conformation, *e.g.*, valinomycin, the MD sampling strategy may generate a larger number of chemically reasonable conformations that agree well with experimental CCS data. While it is possible to include the cation explicitly in the distance geometry calculation protocol, it is generally much easier to introduce the cation after the initial conformations have been generated. In cases where the cation has significant impact on the preferred conformations, it is quite possible that the distance geometry protocol will produce far fewer structures that agree well with experimental CCS data. This tradeoff between computational cost or explicit inclusion of the cation during all stages of the conformational sampling procedure (*e.g.*, MD-based methods) clearly favors distance

geometry when the site of cationization is well understood and can be fixed prior to calculation.

3.4 Conclusions

These results clearly show that the distance geometry plus geometry optimization protocol can be an effective and computationally efficient conformational sampling strategy for analysis of IM-MS data for natural products. In all but one case, the distance geometry protocol performed at least as well as the MD sampling method, but at a fraction of the computational expense. The MD method appears superior only for valinomycin, a cyclic peptide. There are two major factors that contribute to this observation for valinomycin. First, it is much larger than the other molecules in the test set, with many more degrees of freedom. As a result, many more conformations would have to be generated during a distance geometry calculation to get reasonable conformational sampling. More significantly, low-energy conformations for valinomycin are strongly influenced by the presence and position of the sodium cation. Therefore, explicit inclusion of the sodium ion during the conformational sampling process is important, but this cannot be done efficiently with our distance geometry protocol at present.

Computational analysis of the conformational space for natural products in support of structural IM-MS provides further insight into the structural motifs that cause gas phase separation of these species from primary metabolites. Incorporating computational methods with further IM-MS studies will provide additional structural information, which could aid identification of these natural products, because of

structural uniqueness compared to primary metabolites, from complex biological samples. Additionally, IM-MS is currently showing great promise as an analytical method in the fields of systems, synthetic, and chemical biology. This is due to its ability to separate and analyze complex samples containing a wide array of biological molecules such as peptides, carbohydrates, and metabolites. A computational method, such as distance geometry, that can efficiently sample the conformational space of all of these structurally different biomolecules could potentially facilitate structural interpretation of IM-MS signals on a timescale more commensurate with the experiment itself.

3.5 Acknowledgements

We would like to thank the Vanderbilt Center for Structural Biology for computational support and Dr. Larissa S. Fenn for experimental support. Financial support for this research was funded by the Defense Threat Reduction Agency (HDTRA1-09-1-00-13), the National Institutes of Health (RO1GM092218), the Vanderbilt Institute of Chemical Biology, and the Vanderbilt Institute for Integrative Biosystems Research and Education.

3.6 References

1. McDaniel, E. W.; Mason, E. A. *The Mobility and Diffusion of Ions in Gases*; Wiley: New York, 1973.
2. Mason, E. A.; McDaniel, E. W. *Transport Properties of Ions in Gases*; Wiley: New York, 1988.
3. McLean, J. A. The Mass-Mobility Correlation Redux: The Conformational Landscape of Anhydrous Biomolecules. *Journal of the American Society of Mass Spectrometry* 2009, 20, 1775-1781.
4. Goodwin, C. R.; Fenn, L. S.; Derewacz, D. K.; Bachmann, B. O.; McLean, J. A. Structural Mass Spectrometry: Rapid Methods for Separation and Analysis of Peptide Natural Products. *Journal of Natural Products* 2012, 75, 48-53.
5. Derewacz, D. K.; Goodwin, C. R.; McNeese, C. R.; McLean, J. A.; Bachmann, B. O. Antimicrobial Drug Resistance Affects Broad Changes in Metabolomic Phenotype in Addition to Secondary Metabolism. *Proceedings of the National Academy of Science U.S.A.* 2013, 110, 2336-2341.
6. Clemmer, D. E.; Jarrold, M. F. Ion Mobility Measurements and Their Applications to Clusters and Biomolecules. *Journal of Mass Spectrometry* 1997, 32, 577-592.
7. Wyttenbach, T.; Bowers, M. T. *Modern Mass Spectrometry, Topics in Current Chemistry*; Schalley, C. A., Ed.; Springer: Berlin, 2003; 225, pp 207-232.
8. Zakharova, N. L.; Crawford, C. L.; Hauck, B. C.; Quinton, J. K.; Seims, W. F.; Hill Jr, H. H.; Clark, A. E. An Assessment of Computational Methods for Obtaining Structural Information of Moderately Flexible Biomolecules from Ion Mobility Spectrometry. *Journal of the American Society for Mass Spectrometry* 2012, 23, 792-805.
9. Hall, Z.; Politis, A.; Bush, M. F.; Smith, L. J.; Robinson, C. V. Charge-State Dependent Compaction and Dissociation of Protein Complexes: Insights from Ion Mobility and Molecular Dynamics. *Journal of the American Chemical Society* 2012, 134, 3429-3438.
10. Pukala, T. L.; Ruotolo, B. T.; Zhou, M.; Politis, A.; Stefanescu, R.; Leary, J. A.; Robinson, C. V. Subunit Architecture of Multiprotein Assemblies Determined Using Restraints from Gas-Phase Measurements. *Structure* 17, 1235-1243.
11. Politis, A.; Park, A. Y.; Hyung, S.-J.; Barsky, D.; Ruotolo, B. T.; Robinson, C. V. Integrating Ion Mobility Mass Spectrometry with Molecular Modelling to

- Determine the Architecture of Multiprotein Complexes. *PLoS One* 2010, 5, e12080.
12. Wang, S. C.; Politis, A.; Di, B. N.; Bavro, V. N.; Tucker, S. J.; Booth, P. J.; Barrera, N. P.; Robinson, C. V. Ion Mobility Mass Spectrometry of Two Tetrameric Membrane Protein Complexes Reveals Compact Structures and Differences in Stability and Packing. *Journal of the American Chemical Society* 2010, 132, 15468-15470.
 13. Bernstein, S. L.; Liu, D.; Wyttenbach, T.; Bowers, M. T.; Lee, J. C.; Gray, H. B.; Winkler, J. R. α -Synuclein: Stable Compact and Extended Monomeric Structures and pH Dependence of Dimer Formation. *Journal of the American Society for Mass Spectrometry* 2004, 15, 1435-1443.
 14. Knapman, T. W.; Morton, V. L.; Stonehouse, N. J.; Stockley, P. G.; Ashcroft, A. E. Determining the Topology of Virus Assembly Intermediates Using Ion Mobility Spectrometry-Mass Spectrometry. *Rapid Communications in Mass Spectrometry* 2010, 24, 3033-3042.
 15. Uetrecht, C.; Rose, R. J.; van, D. E.; Lorenzen, K.; Heck, A. J. R. Ion Mobility Mass Spectrometry of Proteins and Protein Assemblies. *Chemical Society Reviews* 2010, 39, 1633-1655.
 16. Ruotolo, B. T.; Verbeck, G. F.; Thomson, L. M.; Gillig, K. J.; Russell, D. H. Observation of Conserved Solution-Phase Secondary Structure in Gas-Phase Tryptic Peptides. *Journal of the American Chemical Society* 2002, 124, 4214-4215.
 17. Albrieux, F.; Calvo, F.; Chirot, F.; Vorobyev, A.; Tsybin, Y. O.; Lepere, V.; Antoine, R.; Lemoine, J.; Dugourd, P. Conformation of Polyalanine and Polyglycine Dications in the Gas Phase: Insight from Ion Mobility Spectrometry and Replica-Exchange Molecular Dynamics. *Journal of Physical Chemistry A* 2010, 114, 6888-6896.
 18. Dupuis, N. F.; Wu, C.; Shea, J.-E.; Bowers, M. T. Human Islet Amyloid Polypeptide Monomers Form Ordered β -hairpins: A Possible Direct Amyloidogenic Precursor. *Journal of the American Chemical Society* 2009, 131, 18283-18292.
 19. Plasencia, M. D.; Isailovic, D.; Merenbloom, S. I.; Mechref, Y.; Clemmer, D. E. Resolving and Assigning N-linked Glycan Structural Isomers from Ovalbumin by IMS-MS. *Journal of the American Society for Mass Spectrometry* 2008, 19, 1706-1715.
 20. Yamaguchi, Y.; Nishima, W.; Re, S.; Sugita, Y. Confident Identification of Isomeric N-glycan Structures by Combined Ion Mobility Mass Spectrometry and

Hydrophilic Interaction Liquid Chromatography. *Rapid Communications in Mass Spectrometry* 2012, 26, 2877-2884, S2877/1-S2877/7.

21. Pouilly, J. C.; Lecomte, F.; Nieuwjaer, N.; Manil, B.; Schermann, J. P.; Desfrancois, C.; Gregoire, G.; Ballivian, R.; Chirot, F.; Lemoine, J.; et al.. Combining Ion Mobility Mass Spectrometry and Infrared Multiphoton Dissociation Spectroscopy to Probe the Structure of Gas-Phase Vancomycin-Ac2 LKDADA Non-Covalent Complex. *International Journal of Mass Spectrometry* 2010, 297, 28-35.
22. Crippen, G. M. *Distance Geometry and Conformational Calculations*, Chemometrics Research Studies Series 1; Wiley: New York, 1981.
23. Blaney, J. M.; Dixon, J. S. *Distance Geometry in Molecular Modeling*. In *Reviews in Computational Chemistry*, John Wiley & Sons, Inc.: 1994; pp 299-335.
24. Wang, J.; Wolf, R. M.; Caldwell, J. W.; Kollman, P. A.; Case, D. A. Development and Testing of a General Amber Force Field. *Journal of Computational Chemistry* 2004, 25, 1157-1174.
25. Halgren, T. A. Merck molecular force field. I. Basis, Form, Scope, Parameterization, and Performance of MMFF94. *Journal of Computational Chemistry* 1998, 17, 490-519.
26. Frisch, M. J.; Trucks, G. W.; Schlegel, H. B.; Scuseria, G. E.; Robb, M. A.; Cheeseman, J. R.; Scalmani, G.; Barone, V.; Mennucci, B.; Petersson, G. A.; et al. *Gaussian 09, Revision A. 01*; Gaussian, Inc.: Wallingford, CT 2009.
27. Bayly, C. I.; Cieplak, P.; Cornell, W.; Kollman, P. A. A Well-Behaved Electrostatic Potential Based Method Using Charge Restraints for Deriving Atomic Charges: the RESP model. *Journal of Physical Chemistry* 1993, 97, 10269-10280.
28. Case, D. A.; Darden, T. A.; Cheatham Iii, T. E.; Simmerling, C. L.; Wang, J.; Duke, R. E.; Luo, R.; Walker, R. C.; Zhang, W.; Merz, K. M. *AMBER 11*. University of California, San Francisco 2010, 142.
29. Mesleh, M. F.; Hunter, J. M.; Shvartsburg, A. A.; Schatz, G. C.; Jarrold, M. F. Structural Information from Ion Mobility Measurements: Effects of the Long-Range Potential. *Journal of Physical Chemistry* 1996, 100, 16082-16086.
30. Shvartsburg, A. A.; Jarrold, M. F. An Exact Hard-Spheres Scattering Model for the Mobilities of Polyatomic Ions. *Chemical Physics Letters* 1996, 261, 86-91.

31. Bush, M. F.; Campuzano, I. D. G.; Robinson, C. V. Ion Mobility Mass Spectrometry of Peptide Ions: Effects of Drift Gas & Calibration Strategies. *Analytical Chemistry* 2012, 84, 7124-7130.
32. Molecular Operating Environment (MOE), 2012.10; Chemical Computing Group Inc.: 1010 Sherbooke St. West, Suite #910, Montreal, QC, Canada, H3A 2R7, 2012.
33. Blaney, J. M.; Crippen, G. M.; Dearing, A.; Dixon, S.; Spellmeyer, D. C. DGEOM95, Chiron Corporation, 1984-1995.
34. Kuszewski, J.; Nilges, M.; Brünger, A. T. Sampling and Efficiency of Metric Matrix Distance Geometry: A Novel Partial Metrization Algorithm. *Journal of Biomolecular NMR* 1992, 2, 33-56.
35. Repasky, M. P.; Chandrasekhar, J.; Jorgensen, W. L. PDDG/PM3 and PDDG/MNDO: Improved Semiempirical Methods. *Journal of Computational Chemistry* 2002, 23, 1601-1622.
36. Smith, J. A. Suppose - superposition software, 2006; Vanderbilt University: Nashville, TN, 2006.
37. Barton, G. J. OC - A Cluster Analysis Program, 2002; University of Dundee, Scotland, UK, 2002.
38. Sundarapandian, S.; May, J. C.; McLean, J. A. Dual Source Ion Mobility-Mass Spectrometer for Direct Comparison of Electrospray Ionization and MALDI Collision Cross Section Measurements. *Analytical Chemistry* 2010, 82, 3247-3254.
39. Wyttenbach, T.; Batka Jr, J. J.; Gidden, J.; Bowers, M. T. Host/Guest Conformations of Biological Systems: Valinomycin/Alkali Ions. *International Journal of Mass Spectrometry* 1999, 193, 143-152.

CHAPTER 4

OBTAINING THEORETICAL COLLISION CROSS SECTION RANGES FOR LARGE SETS OF METABOLITES TO AID IN IDENTIFICATION BY ION MOBILITY-MASS SPECTROMETRY

4.1. Introduction

Metabolomics is a rapidly emerging field in chemical biology due to its ability to provide information concerning the physiological state of an organism.^{1,2} Biomarker discovery, a goal in metabolomics, is proving key to diagnosing diseases at early stages in patients. In order to perform these studies, analytical techniques are required that can analyze complex biological samples. While LC-MS techniques provide retention time and mass-to-charge ratio (m/z) information that can be compared with databases to aid in identification³⁻⁵, database searching does not always yield an unambiguous metabolite identity. Ion mobility-mass spectrometry (IM-MS) allows for the separation of ionized molecules based on their size and shape, in addition to their m/z . Drift time data obtained from IM-MS can be used to determine the collision cross section (CCS) of these ions. This additional feature of the metabolite ion allows for more accurate identifications to be made in complex biological samples.

In addition to experimental CCS values, theoretical CCS values can also be obtained by computationally sampling the conformational space of the molecule of interest. Typically, these theoretical studies include a method for obtaining a theoretical structure by sampling the conformational space followed by an *in silico* CCS calculation for each conformation. The theoretical CCS value that most closely agrees with the

experimental value is then selected for further structural investigations. Additional approaches consider one low energy structure either from experiment (X-ray crystallography and NMR) or theoretical calculation and determine a theoretical CCS value for the individual structure. Rather than attempting to calculate a specific CCS value, we are proposing the generation and use of theoretical CCS ranges that result from sampling all the conformational space of the molecule. Developing a comprehensive database of these theoretical CCS ranges for typical metabolite molecules will facilitate the identification process.

In order to generate theoretical ranges for large sets of metabolites, a computational approach is needed that can perform this task in a time efficient manner. Current metabolomics databases contain thousands of metabolites, which, regardless of the size of the chemical compounds, is a daunting task for an extensive conformational sampling study. Many conformational sampling techniques utilize molecular dynamics (MD) methods which rely on force fields to describe molecular classes. The various classes of molecular compounds that are represented in the metabolome make it difficult, if not impossible, to find one force field that would accurately describe every metabolite. These challenges suggest that the protocol utilizing distance geometry methods developed in the previous chapter should prove useful in this study. Distance geometry, which samples conformational space based solely on interatomic distances within the molecule, does not rely on a force field to sample conformational space and is a very time efficient computational technique.

Before a database of theoretical CCS values can be assembled, theoretical ranges must be compared to experimental CCS values of metabolite standards. In this work,

nitrogen theoretical CCS ranges will be calculated for 50 metabolites. Standards of these 50 metabolites will then be used to obtain experimental nitrogen CCS values. CCS values from both a drift tube (DTIM) and a traveling wave (TWIM) instrument will be compared to the theoretical ranges. DTIM CCS measurements are useful because they are obtained directly using the kinetic theory of gases and can arguably generate CCS values that show better agreement with theoretical CCS values based on current theoretical approaches. TWIM CCS measurements conversely, cannot be obtained directly with the kinetic theory of gases, but can generate accurate CCS values with appropriate calibration standards. Additionally, many metabolomics studies are currently performed on TWIM instruments and, therefore, there is great merit in comparing the theoretical CCS ranges with these values. Comparison between theoretical CCS ranges and TWIM CCS values will also benchmark calibration approaches on these platforms in regards to metabolomics workflows.

While the long-term goal of this work is to aid in identification of unknown metabolites through database generation of theoretical CCS ranges, there is also an additional benefit to finding these ranges. They can serve as a guide when determining experimental CCS values for metabolite standards. Metabolites generally occupy a low-mass region of the spectra, which suffers from complexity due to endogenous noise from the sample and exogenous noise from the instrument at that mass region. This makes feature selection and identification a challenge for these compounds. Benchmarking experimental CCS values against the theoretical ranges that result from sampling all conformational space of the metabolite can provide extra validation for the CCS value. The work presented here shows that good agreement can be found between experimental

and theoretical CCS values for metabolite standards and serves as an early step in generating databases of theoretical CCS ranges for metabolomics research.

4.2. Experimental Section

Materials

The 50 Metabolite samples, HPLC grade methanol, and tetraalkylammonium bromides (TAA 1-8) were purchased from Sigma-Aldrich (St. Louis, MO). Tune mix was provided from Agilent Technologies (Santa Clara, CA). Water blended with 0.1% formic acid (optima) grade was obtained from Thermo Fisher Scientific (Waltham, MA). Metabolite samples were at a concentration of 10mmol in 1:1 methanol:water containing 0.1% formic acid.

Instrumentation

Experimental CCS values were obtained on a commercial ESI-IM-QTOF mass spectrometer (Agilent Technologies, Santa Clara, CA). Details of the instrumentation are provided elsewhere,^{6,7} but, briefly, the IM-MS consists of a 78 cm uniform-field drift tube coupled to a high resolution QTOFMS ($m/\Delta m$ 40,000). The buffer gas (nitrogen) was maintained at a pressure of *ca.* 4 Torr and the drift voltages were varied in order to correct for the non-IM flight time of ions through the interfacing ion optics. The collision cross section calculator available with the IM-MS Browser software employs the Mason-Schamp equation to determine experimental CCS values for the metabolites. The experimental methods for CCS values from a TWIM mass spectrometer can be found in the literature.⁸

Theoretical Collision Cross Section Calculations

Starting structures for all 50 metabolites were obtained from PubChem. These neutral structures initially underwent a geometry optimization at the Hartree Fock level of theory with a 6-31G* basis set in the Gaussian 09 software.⁹ These structures were used to generate the cation coordinating structures for the remainder of the calculation. Each of the neutral structures was also protonated based on pKa values and known protonation sites found in the literature.¹⁰ These protonated structures also underwent a geometry optimization at the Hartree Fock level of theory with a 6-31G* basis set. The structures of the 50 metabolites with their site of protonation identified can be found in Appendix D. (Figures D.3-D.8). The geometry optimization not only provides a good starting structure, but it also provides the electrostatic potential needed for partial charge derivation for introducing cations and later energy minimization steps. After the initial geometry optimization, both the protonated and neutral structures underwent a distance geometry calculation with DGEOM95¹¹ to generate all possible three-dimensional conformations of the metabolite. The distance restraints utilized in this program are described elsewhere in the literature,¹² but a brief description will be provided below. This program provides an RMSD cutoff to reject generated conformations that are too similar to other generated conformations. The set of metabolites spans a mass range of 90 – 828 Da and the number of rotatable bonds ranges from 0 – 25. This suggests that different RMSD cutoffs may be needed across this range. Values of 0.5, 0.75, and 1.00 RMSD were used for mass ranges of 90-199 Da, 200-399 Da, and 400-828 Da, respectively. These values were determined based on conformational sampling

capabilities and their effects on resulting CCS ranges. This data can be found in Appendix D (Figure D.1).

Once the conformations were generated from distance geometry, a sodium cation was added to each of the neutral metabolites with the xLeap software found in AMBER14¹³. The cation is placed with the neutral molecule according to the electrostatic potential grid. The cationized metabolites, as well as the protonated metabolites, then underwent a short energy minimization with the sander module in AMBER to generate low energy conformations.¹⁴ A theoretical CCS value was then determined for each conformer, or for a subset of conformers (depending on the size of data set), using either MOBCAL¹⁵⁻¹⁷ or PSA¹⁸⁻²¹. Details on the subsets of conformers used for this calculation can be found in Appendix D (Figure D.2).

4.3. Results and Discussion

The 50 metabolites investigated in this study are listed in Table 4.1 with their m/z values. An abbreviation is also included for each metabolite that will be used in the figures in this thesis. These metabolites span an m/z range of 90.03 Da to 828.27 Da and represent different subclasses of metabolites including organic acids, nucleotides, vitamins, and other classes.

Table 4.1. The metabolites examined in this study are listed in the table below with their *m/z* values.

Metabolite (Abbreviation)	<i>m/z</i> (M+H)⁺[M+Na]⁺	Metabolite (Abbreviation)	<i>m/z</i> (M+H)⁺[M+Na]⁺
Lactic Acid (LA)	(91.04) [113.02]	Biotin (BIO)	(245.10) [267.08]
Choline (CHO)	104.11 [M] ⁺	2'deoxyadenosine (2DE)	(252.11) [274.09]
Nicotinic Acid (NIC)	(124.04) [146.02]	Thiamine (THI)	265.11 [M] ⁺
5-Fluorouracil (SFL)	(131.03) [153.01]	Adenosine (ADO)	(268.10) [290.09]
Leucine (LEU)	(132.10) [154.08]	Guanosine (GUA)	(284.10) [306.08]
Amphetamine (APH)	(136.11) [158.09]	Ondansetron (OND)	(294.16) [316.14]
Salicylic Acid (SAL)	(139.04) [161.02]	Cocaine (COC)	(304.15) [326.14]
Fucose (FUC)	(165.08) [187.06]	Glutathione (GTA)	(308.09) [330.07]
Quinolinic Acid (QUN)	(168.03) [190.01]	NANA (NAN)	(310.11) [332.10]
Uric Acid (URC)	(169.04) [191.02]	CMP (CMP)	(324.06) [346.04]
Glucose (GLU)	(181.07) [203.05]	UMP (UMP)	(325.04) [347.03]
Mannose (MAN)	(181.07) [203.05]	Sucrose (SUC)	(343.12) [365.11]
Tyrosine (TYR)	(182.08) [204.06]	Melibiose (MEB)	(343.12) [365.11]
Sorbitol (SOR)	(183.09) [205.07]	AMP (AMP)	(348.07) [370.05]
Kynurenate (KYN)	(190.05) [212.03]	LacNAc (LAC)	(370.13) [392.12]
Citric Acid (CIT)	(193.03) [215.02]	Colchicine (COL)	(400.18) [422.16]
MDMA (MDM)	(194.12) [216.10]	ADP (ADP)	(428.04) [450.02]
Caffeine (CAF)	(195.09) [217.07]	Folate (FOL)	(442.15) [464.13]
ADMA (ADM)	(203.15) [225.13]	Glycodeoxycholate (GLY)	(450.32) [472.30]
Pantothenic Acid (PAN)	(220.12) [242.10]	Verapamil (VER)	(455.29) [477.27]
GlcNAc (GLC)	(222.10) [244.08]	Raffinose (RAF)	(505.18) [527.16]
GalNAc (GAL)	(222.10) [244.08]	Glutathione Oxidized (GOX)	(613.16) [635.14]
Melatonin (MLT)	(233.13) [255.11]	Stachyose (STA)	(667.23) [689.21]
Thymidine (THY)	(243.10) [265.08]	Acetyl coenzyme A (ACA)	(810.13) [832.11]
Cytidine (CYT)	(244.09) [266.07]	Maltopentose (MLP)	(829.28) [851.26]

Comparison with Drift Tube Experimental CCS Values

Experimental CCS values were obtained on the DTIM-MS for several of the metabolites in Table 4.1. These values were then plotted with the theoretical CCS ranges in Figure 4.1. The CCS values are plotted on the x-axis and the metabolites are listed on the y-axis. Several of the metabolites, indicated with red circles, show agreement with the theoretical ranges (indicated with the horizontal gray bars). Many of these metabolites tend to fall toward the lower end of the theoretical ranges. This observation is due to the fact that all possible three-dimensional conformations are generated with the distance geometry approach producing larger theoretical CCS values than observed experimentally. The addition of the cation, and to some degree the proton, causes the metabolites to form more densely packed conformations which correspond to smaller CCS values. More thorough experimental investigation may be needed for metabolites that fall towards the upper end of the theoretical CCS range. The experimental DTIM CCS values are based on 7-8 voltage measurements and would benefit from more values.

The green triangles in Figure 4.1 correspond to metabolites that did not agree with their theoretical CCS range. Depending on whether the experimental value fell above or below the theoretical range, there are differing reasons why this discrepancy occurs. If the experimental value is below the theoretical range, the error is likely correlated to inaccurate sampling of conformational space. If the experimental value is above the theoretical range, the error is likely correlated to either failure in assumptions for the kinetic theory of gases or incorrect assignment of peaks from the IM-MS experimental data. The kinetic theory of gases, on which CCS calculations are based, assumes completely elastic interactions between the drift gas and the molecular ion. For the

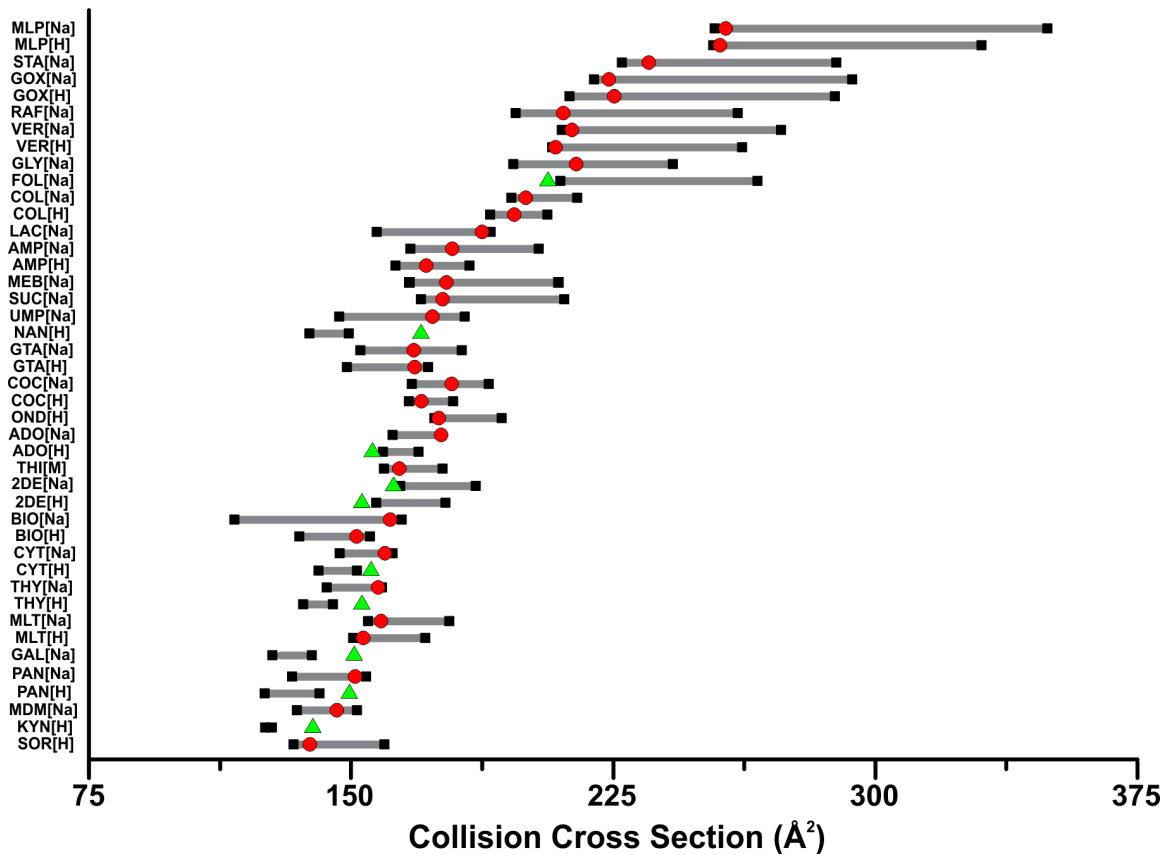


Figure 4.1. The experimental CCS values for the DTIM instrument are compared with the theoretical CCS ranges in this plot. The nitrogen CCS values are plotted on the x-axis and the metabolites are listed on the y-axis in order of increasing m/z value. The theoretical ranges are represented with grey rectangles with black squares on each end. The experimental values are represented with either red circles or green triangles depending on whether they agree or disagree with the theoretical ranges.

smaller metabolites, the polarizability effect of nitrogen is stronger. This corresponds to more inelastic interaction that results in longer drift times and larger CCS values. This trend is observed when the experimental CCS values falling above the theoretical CCS ranges for the smallest metabolite values. Experimental values could also be incorrect due to the false identification of peaks in the IM-MS experiment. Endogenous and exogenous noise in the low mass region of the spectra makes feature selection and identification a challenge for these compounds. Deviations between the theoretical and experimental CCS values will be discussed in further detail later in the thesis.

Comparison with Traveling Wave Experimental CCS Values

Many IM-MS metabolomics experiments occur on instruments that utilize traveling wave IM drift cells and, therefore, it would be useful to see if the theoretical CCS ranges show good alignment with experimental values from these types of instruments. A recent study compared CCS values from TWIM instruments with theoretical CCS values rather than ranges. Figure 4.2 displays CCS values from this study aligned with our theoretical CCS ranges. Experimental values that agree with the theoretical range are indicated with blue circles, where values that disagree are indicated with cyan triangles. The low mass species that show poor agreement between experiment and theory are not concerning as it has been shown previously that the polarizability of nitrogen in TWIM experiments has a greater affect on these species.^{22,23} For the higher mass species, both folate and adenosine fall below the theoretical range which is similar to the observation with the DTIM data. This deviation will be discussed in the next section in the light of more structural detail.

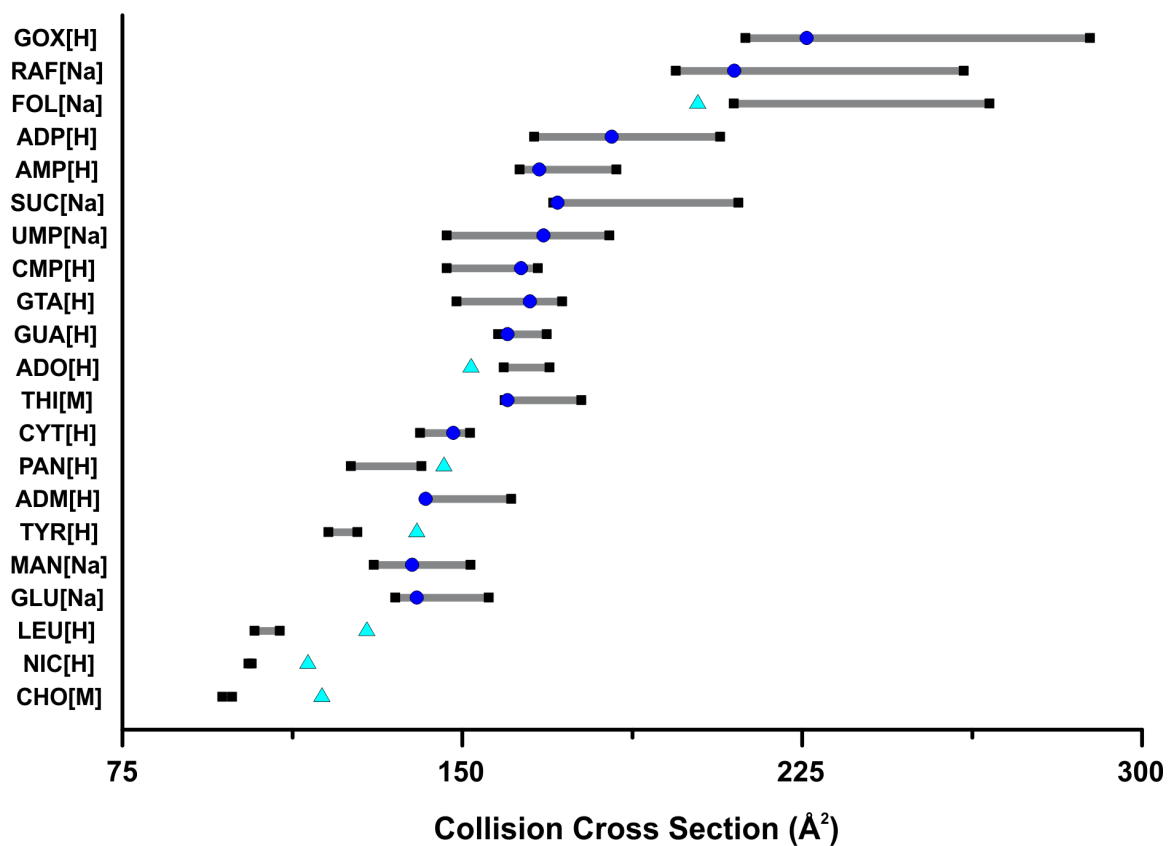


Figure 4.2. Literature TWIM experimental CCS values are compared with the theoretical CCS ranges in this plot. The nitrogen CCS values are plotted on the x-axis and the metabolites are listed on the y-axis in order of increasing m/z value. The theoretical ranges are represented with grey rectangles with black squares on each end. The experimental values are represented with either blue circles or cyan triangles depending on whether they agree or disagree with the theoretical ranges.

Incongruences Between Theoretical Ranges and Experimental Values

Of the 40 metabolites for which experimental and theoretical CCS calculations were compared, 13 failed to show agreement between the two values. Six sample conformations that were closest to the experimental CCS value are displayed in Figure 4.2 and will provide insight into why these deviations occurred. For the conformations shown in Figure 4.2a-c, the experimental values were determined to be lower than the theoretical ranges. For folate in Figure 4.2a, distance geometry failed to generate a conformation where folate coordinated the sodium cation completely within the structure. Folate, with 10 rotatable bonds, has a structure that would be influenced by the presence of a cation. This is similar to the challenge we previously encountered with the cyclic peptide failing to coordinate the sodium cation within their structure.¹² This is a current challenge with distance geometry methods as the additional cation is not present for the entire simulation but rather only relaxed with the structure through a short energy minimization. While the influence of the cation on structure is not as dramatic for 2'-deoxyadenosine in Figure 4.2b, we can attribute the deviation between theory and experiment to inaccurate sampling, but further experimental measurements are needed to verify that the experimental CCS value is correct. The error associated with protonated adenosine in Figure 4.2c, which also falls below the theoretical range, may result from inaccurate placement of the proton. Due to the lack of parameters for a free proton in the general AMBER force field (GAFF)¹⁴ used for the energy minimization step and the inability to incorporate a free proton during the distance geometry step, the proton was attached to a specific site on the metabolite species. While it is unlikely that the location of the proton would change the theoretical CCS range of adenosine (based on its size and

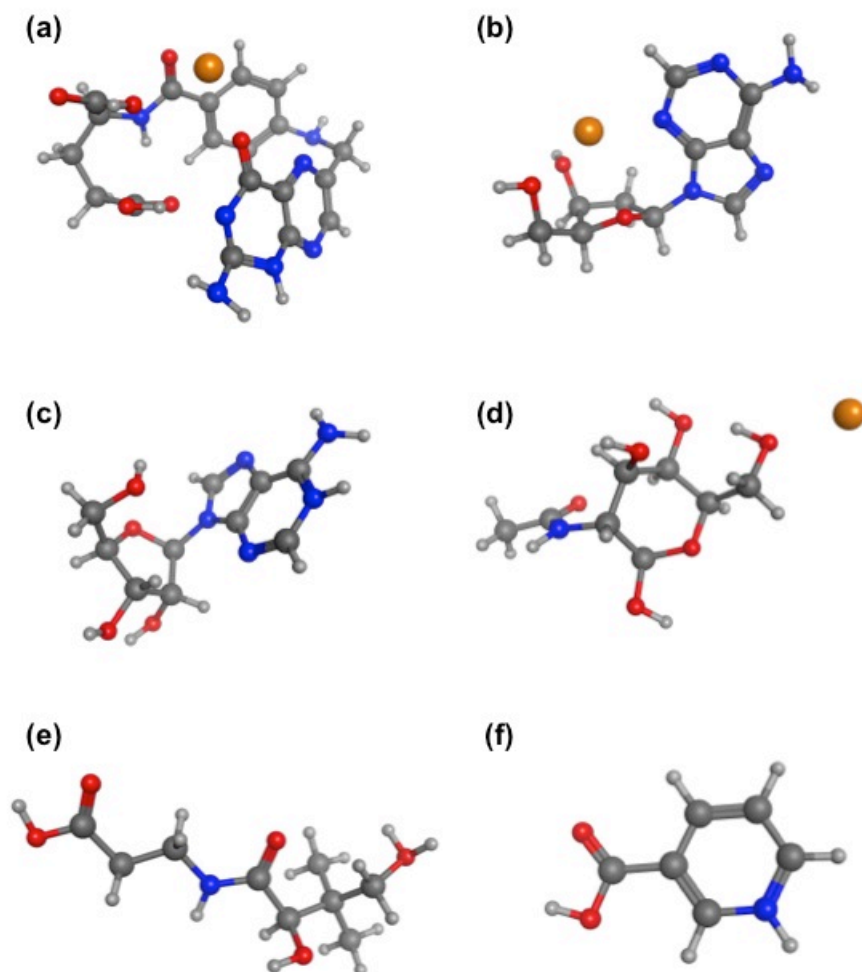


Figure 4.3. Conformations for six metabolites are presented that do not show agreement between their experimental CCS values and their theoretical CCS ranges. The conformation that comes closest the experimental CCS value is shown for a) folate, b) 2'-deoxyadenosine, c) adenosine, d) N-Acetyl, D-Galactosamine, e) pantothenic acid, and f) nicotinic acid.

number of rotatable bonds) it is possible considering we observed the deviation from both the DTIM and TWIM instrument platforms.

The metabolites in Figure 4.3d-f deviated to larger experimental CCS values from the theoretical range. For these three species, it is hard to visualize a conformation that would result in a large CCS value. For N-Acetyl, D-Galactosamine in Figure 4.3d, the sodium cation is already 2.3 Å from the closest oxygen. Pantothenic acid in Figure 4.3e is stretched out linearly and nicotinic acid in Figure 4.3f has very little conformational space to sample. These structural observations suggest that the deviation between the theoretical ranges and experimental CCS values is more likely related to the failed assumptions with the kinetic theory of gases or inaccurate peak identifications. In order to further investigate if the polarizability of nitrogen is causing these disparities, experimental CCS values in helium would need to be obtained to see if there is still a deviation in the values. Additionally, more experimental measurements will offer more confidence in the experimental CCS values.

At this point it is important to mention possible sources of error for both experimental CCS measurements and theoretical CCS calculations. These sources of error likely contribute to disagreement between the two CCS values and are summarized in Table 4.2 below. First, the experimental errors will be discussed. Although instrument capabilities are constantly improving, poor mobility resolution for the mass range of the metabolite samples could result in misidentified metabolite ions. Faint sample peaks or endogenous sample noise can make identification difficult for certain species. The remaining sources of error that will be discussed for experimental CCS measurements

Table 4.2. Sources of error for both experimental and theoretical CCS calculations.

Sources for Error in CCS Calculations	
Experiment	Theory
<ul style="list-style-type: none">• Poor resolution• Small size of the ion• Ion and drift gas interaction	<ul style="list-style-type: none">• Cation sampling• Approximation based calculations• Scattering angle calculations

concern the ion-neutral interaction between the metabolite ion and the neutral drift gas molecules. The Mason-Schamp equation assumes elastic interactions between the ion and neutral buffer gas. Previous work has shown that this assumption holds for measurements made in helium, which is a small (4 Da), monoatomic atom. The assumption no longer holds for the larger (28 Da) diatomic nitrogen gas molecule.^{24,25} The inelastic interaction between the gas phase ion and nitrogen drift gas results from momentum transfer during the collision, which corresponds to a longer drift time and thus larger CCS values.²⁶ This momentum transfer will have a greater effect on these small metabolite ions and therefore altering their experimental CCS values to differ from a purely structural measurement. In addition to their size difference, helium and nitrogen have considerably different polarizability values, 0.205\AA^3 and 1.641\AA^3 respectively.¹⁷ While it has been suggested that polarizability of different drift gases does not effect CCS measurements for larger gas phase ions, it may play a role for the smaller metabolites examined in this work.

There are also sources of error for the theoretical CCS calculations. Distance geometry arguably samples all possible conformations space making it difficult to claim that certain experimentally observed conformations may not have been generated. Achieving appropriate coordination of the cation is more difficult with distance geometry methods and therefore the modeling could fail to generate the observed experimental structures. The remaining sources of error result from the theoretical CCS calculations methods. Both the projection superposition approximation (PSA) and the trajectory method (TM) were used in this work to calculate theoretical CCS values. The PSA calculation starts the projection approximation, which calculates the area of two-

dimensional projected images of the molecule. The calculation then uses a shape factor, which is a measure of the concavity of the molecular surface of the ion, to adjust the projection approximation CCS value. In order to obtain nitrogen CCS values a set of “preliminary parameters” are used. It is speculated that these parameters are based on previous measurements and theory. The authors of PSA admit that there is room for improvement in these parameters and thus this could contribute to error in these calculated CCS values. This approximation approach only considered the structure of the ion and therefore does not directly incorporate ion-neutral interactions that are known to have an influence on CCS for drift gases other than helium. With the exception of the twelve metabolites that do not contain the appropriate ratio of carbon, oxygen, and nitrogen, the PSA method was used to determine theoretical CCS values. The TM is a more rigorous approach to determining theoretical CCS values and was used for the twelve remaining metabolites. It integrates over scattering angles to obtain the rotationally averaged surface area or CCS of the ion. This approach incorporates Lennard-Jones potentials in an attempt to accurately describe the ion-neutral interaction. Although this is a theoretically rigorous approach, it can fail to accurately generate CCS values that agree with experimental CCS values. This is most likely due to the method not completely accounting for the polarizability and momentum transfer that both affect the CCS measurement. Modifications to the original calculation attempt to more accurately model nitrogen as a diatomic atom¹⁷ but for small molecules where polarizability and momentum transfer play a larger role in CCS determination there is still a deviation between experiment and theory.

In order to obtain a clearer picture of ion-neutral interactions in the gas phase, a MD simulation could be performed that would mimic the environment of a drift tube used in an IM experiment. This would allow for the actual interactions between the sample ion and the neutral buffer gas to be observed under the pressure and temperature conditions that occur experimentally. While this approach would provide very helpful insight into the ion-neutral interactions that influence CCS measurements, it is outside the scope of the present work.

Time Advantage with the Distance Geometry Modeling Method

One major drawback that has hindered computational modeling of large sets of molecules in support of IM-MS research is the time that is required for many of these calculations. If each metabolite requires weeks or months of computational time to produce theoretical CCS ranges, creating databases of these ranges would take much too long to prove useful. Distance geometry circumvents this issue because it generates these CCS ranges on the time scale of hours or days, not weeks or months. The histograms in Figure 4.4 show the time required for generating the set of conformations for the metabolites used in this study. Data for protonated species is shown in Figure 4.4a and for sodiated species in Figure 4.4b. The time required for sampling the conformational space of metabolites in the study ranges from minutes to hours, which is a very favorable time scale for the generation of theoretical CCS values. Additional time is required to obtain an initial starting structure for the distance geometry calculation and for the theoretical CCS calculation for the resulting conformation. The time requirements for various approaches are tabulated in Appendix D (Table D.1). Calculation of the

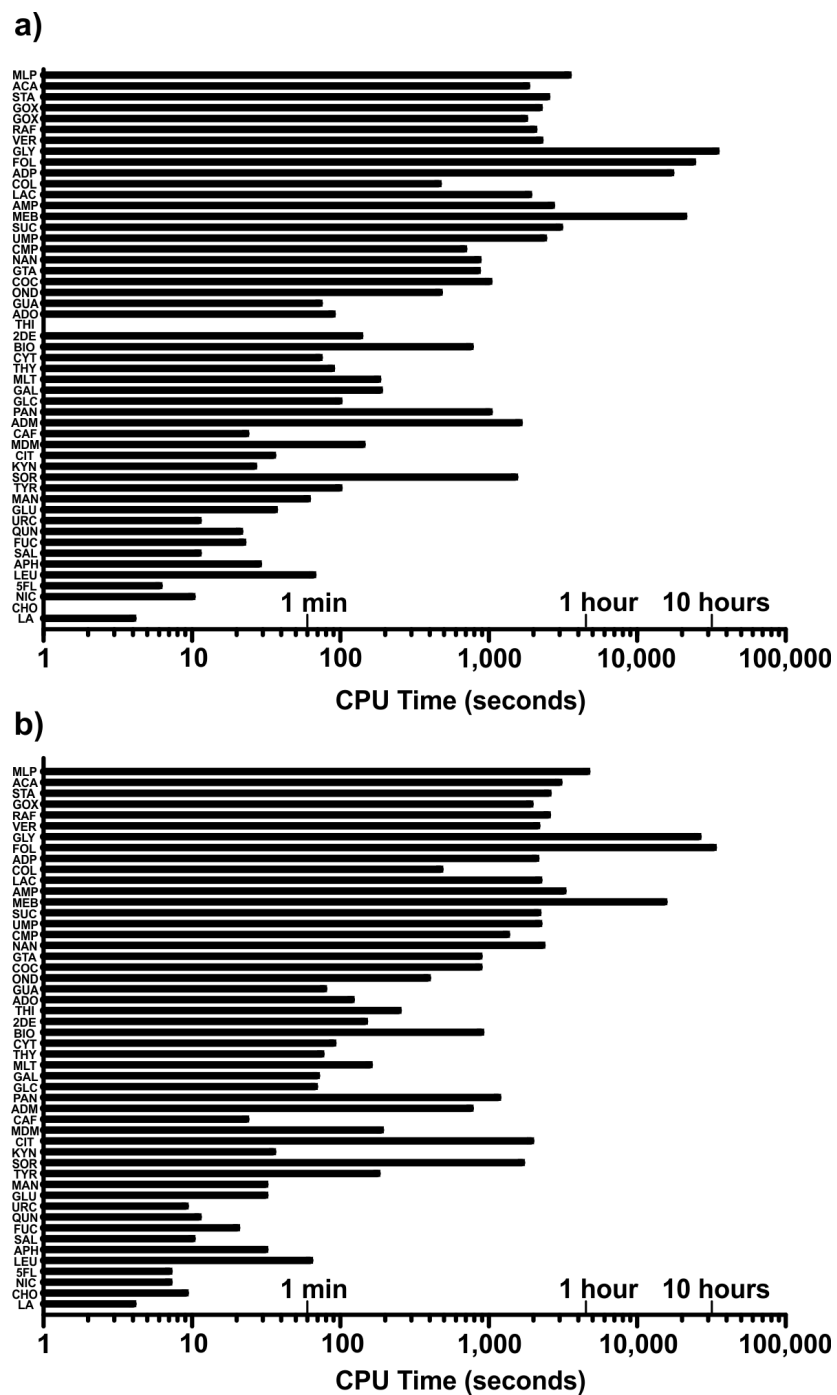


Figure 4.4. The CPU time required for sampling the conformational space with the distance geometry protocol is shown in these plots for the a) protonated species and b) sodiated species. The CPU time is presented on the x-axis in log scale and the metabolites are listed on the y-axis. The $[M]^+$ species are shown with the sodiated data.

theoretical CCS depends greatly on the drift gas and the level of theory used. Although the time plotted in Figure 4.4 is not fully encompassing, it more clearly reflects the time required for conformational sampling with distance geometry methods. These additional time requirements may add anywhere from two hours to two days to the calculation. While this increases the time required, initial structure parameterization and *in silico* theoretical CCS measurements are required for any conformational sampling approach in support of IM-MS measurements.

4.4. Conclusions

Applying the distance geometry conformational sampling protocol to metabolite compounds proves to be a time efficient method for generating accurate theoretical CCS ranges. There are still several considerations for constructing these database ranges. First, experimental helium values need to be compared to the theoretical CCS ranges. This will help identify whether some of the incongruences we observe are a result of the polarizability of the nitrogen drift gas or rather a result of the modeling approach. Additionally, more replicates of the nitrogen CCS measurement will provide more confidence in the values.

Ten of the metabolites in the initial data set were not compared to theoretical CCS values due to their preference to form negative ions. Future work will aim to generate theoretical conformations for the negative ions as well as for larger sets of metabolites. Distance geometry should prove useful for the negative ions because the challenge of an additional proton or cation will no longer be a concern.

These theoretical CCS ranges will benefit future generation of CCS values as they provide a benchmark for the experimental measurement. Once the deviations between the theoretical ranges and experimental values are fully understood, corrected databases of theoretical CCS ranges can be constructed. These databases will then offer an additional feature for identifying metabolites in future metabolomics studies.

4.5. Acknowledgments

I would like to thank the Center for Structural Biology for computational support and Nichole M. Lareau for extensive experimental support. Additionally, I would like to thank Dr. Ruwan Kurulugama from Agilent Technologies for experimental support. Financial support for this research was funded by the Defense Threat Reduction Agency (HDTRA 1-09-1-00-13), the National Institutes of Health (R01GM092218), the Vanderbilt Institute of Chemical Biology, and the Vanderbilt Institute for Integrative Biosystems Research and Education.

4.6. References

1. Derewacz, D. K.; Goodwin, C. R.; McNeese, C. R.; McLean, J. A.; Bachmann, B. O. Antimicrobial drug resistance affects broad changes in metabolomic phenotype in addition to secondary metabolism. *Proceedings of the National Academy of Sciences* 2013, 110 (6), 2336-2341.
2. Dwivedi, P.; Wu, P.; Klopsch, S. J.; Puzon, G. J.; Xun, L.; Hill Jr, H. H. Metabolic profiling by ion mobility mass spectrometry (IMMS). *Metabolomics* 2008, 4 (1), 63-80.
3. Guan, W.; Zhou, M.; Hampton, C. Y.; Benigno, B. B.; Walker, L. D.; Gray, A.; McDonald, J. F.; Fernández, F. M. Ovarian cancer detection from metabolomic liquid chromatography/mass spectrometry data by support vector machines. *BMC Bioinformatics* 2009, 10 (1), 259.
4. Bruce, S. J.; Tavazzi, I.; Parisod, V.; Rezzi, S.; Kochhar, S.; Guy, P. A. Investigation of human blood plasma sample preparation for performing metabolomics using ultrahigh performance liquid chromatography/mass spectrometry. *Analytical Chemistry* 2009, 81 (9), 3285-3296.
5. Vuckovic, D. Current trends and challenges in sample preparation for global metabolomics using liquid chromatography–mass spectrometry. *Analytical and Bioanalytical Chemistry* 2012, 403 (6), 1523-1548.
6. Tang, K.; Shvartsburg, A. A.; Lee, H.-N.; Prior, D. C.; Buschbach, M. A.; Li, F.; Tolmachev, A. V.; Anderson, G. A.; Smith, R. D. High-sensitivity ion mobility spectrometry/mass spectrometry using electrodynamic ion funnel interfaces. *Analytical Chemistry* 2005, 77 (10), 3330-3339.
7. May, J. C.; Goodwin, C. R.; Lareau, N. M.; Leaptrot, K. L.; Morris, C. B.; Kurulugama, R. T.; Mordehai, A.; Klein, C.; Barry, W.; Darland, E. Conformational Ordering of Biomolecules in the Gas Phase: Nitrogen Collision Cross Sections Measured on a Prototype High Resolution Drift Tube Ion Mobility-Mass Spectrometer. *Analytical chemistry* 2014, 86 (4), 2107-2116.
8. Paglia, G.; Williams, J. P.; Menikarachchi, L.; Thompson, J. W.; Tyldesley-Worster, R.; Halldórsson, S. d.; Rolfsson, O.; Moseley, A.; Grant, D.; Langridge, J. Ion mobility derived collision cross sections to support metabolomics applications. *Analytical Chemistry* 2014, 86 (8), 3985-3993.
9. Frisch, M. J.; Trucks, G. W.; Schlegel, H. B.; Scuseria, G. E.; Robb, M. A.; Cheeseman, J. R.; Scalmani, G.; Barone, V.; Mennucci, B.; Petersson, G. A. *Gaussian 09, Revision A. 02*, Gaussian, Inc., Wallingford, CT 2009, 2 (3), 4.
10. Tang, C. L.; Alexov, E.; Pyle, A. M.; Honig, B. Calculation of pK_as in RNA: On the structural origins and functional roles of protonated nucleotides. *Journal of Molecular Biology* 2007, 366 (5), 1475-1496.

11. Blaney, J. M.; Crippen, G. M.; Dearing, A.; Dixon, S.; Spellmeyer, D. C. DGEOM95, Chiron Corporation, 1984-1995.
12. Stow, S. M.; Goodwin, C. R.; Kliman, M.; Bachmann, B. O.; McLean, J. A.; Lybrand, T. P. Distance Geometry Protocol to Generate Conformations of Natural Products to Structurally Interpret Ion Mobility-Mass Spectrometry Collision Cross Sections. *The Journal of Physical Chemistry B* 2014, 118 (48), 13812-13820.
13. Case, D. A.; Babin, V.; Berryman, J.; Betz, R. M.; Cai, Q.; Cerutti, D. S.; Cheatham Iii, T. E.; Darden, T. A.; Duke, R. E.; Gohlke, H. Amber 142014.
14. Wang, J.; Wolf, R. M.; Caldwell, J. W.; Kollman, P. A.; Case, D. A. Development and testing of a general amber force field. *Journal of Computational Chemistry* 2004, 25 (9), 1157-1174.
15. von Helden, G.; Hsu, M. T.; Gotts, N.; Bowers, M. T. Carbon cluster cations with up to 84 atoms: structures, formation mechanism, and reactivity. *The Journal of Physical Chemistry* 1993, 97 (31), 8182-8192.
16. Mesleh, M. F.; Hunter, J. M.; Shvartsburg, A. A.; Schatz, G. C.; Jarrold, M. F. Structural information from ion mobility measurements: effects of the long-range potential. *The Journal of Physical Chemistry* 1996, 100 (40), 16082-16086.
17. Campuzano, I.; Bush, M. F.; Robinson, C. V.; Beaumont, C.; Richardson, K.; Kim, H.; Kim, H. I. Structural characterization of drug-like compounds by ion mobility mass spectrometry: comparison of theoretical and experimentally derived nitrogen collision cross sections. *Analytical Chemistry* 2011, 84 (2), 1026-1033.
18. Bleiholder, C.; Wyttenbach, T.; Bowers, M. T. A novel projection approximation algorithm for the fast and accurate computation of molecular collision cross sections (I). *Method. International Journal of Mass Spectrometry* 2011, 308 (1), 1-10.
19. Bleiholder, C.; Contreras, S.; Do, T. D.; Bowers, M. T. A novel projection approximation algorithm for the fast and accurate computation of molecular collision cross sections (II). Model parameterization and definition of empirical shape factors for proteins. *International Journal of Mass Spectrometry* 2013, 345, 89-96.
20. Anderson, S. E.; Bleiholder, C.; Brocker, E. R.; Stang, P. J.; Bowers, M. T. A novel projection approximation algorithm for the fast and accurate computation of molecular collision cross sections (III): Application to supramolecular coordination-driven assemblies with complex shapes. *International Journal of Mass Spectrometry* 2012, 330-332, 78-84.

21. Bleiholder, C.; Contreras, S.; Bowers, M. T. A novel projection approximation algorithm for the fast and accurate computation of molecular collision cross sections (IV). Application to polypeptides. *International Journal of Mass Spectrometry* 2013, 354, 275-280.
22. Knapman, T. W.; Berryman, J. T.; Campuzano, I.; Harris, S. A.; Ashcroft, A. E. Considerations in experimental and theoretical collision cross-section measurements of small molecules using travelling wave ion mobility spectrometry-mass spectrometry. *International Journal of Mass Spectrometry* 2010, 298 (1), 17-23.
23. Forsythe, J. G.; Stow, S. M.; Nefzger, H.; Kwiecien, N. W.; May, J. C.; McLean, J. A.; Hercules, D. M. Structural Characterization of Methylenedianiline Regioisomers by Ion Mobility-Mass Spectrometry, Tandem Mass Spectrometry, and Computational Strategies: I. Electrospray Spectra of 2-Ring Isomers. *Analytical Chemistry* 2014, 86, 4362-4370.
24. Beegle, L. W.; Kanik, I.; Matz, L.; Hill Jr., H. H. Effects of Drift-Gas Polarizability on Glycine Peptides in Ion Mobility Spectrometry. *International Journal of Mass Spectrometry*, 2002, 216, 257-268.
25. Hill Jr., H. H.; Hill, C. H., Asbury, G. R.; Wu, C.; Matz, L. M.; Ichiye, T. Charge Location on Gas Phase Peptides. *International Journal of Mass Spectrometry*, 2002, 219, 23-27.
26. Larriba-Andaluz, C.; Fernandex-Garcia, J.; Ewing, M. A.; Hogan Jr., C. J.; Clemmer, D. E. Gas Molecule Scattering and Ion Mobility Measurements for Organic Macro-ions in He versus N₂ Environments. *Physical Chemistry Chemical Physics*, 2015.

CHAPTER 5

CONCLUSIONS AND FUTURE DIRECTIONS

5.1. Summary

Computational methods have proven to be incredibly useful supplemental tools in structural IM-MS experimental studies. Alone, IM-MS studies can provide insight into gas phase separations and general structural information in the form of a CCS value. When complemented with conformational space studies, actual three-dimensional structures can be aligned with these experimental numerical values.

Polyurethane hard block precursors were successfully characterized by combining MS/MS, IM-MS, and computational strategies. Each of these techniques offered unique insight into the behavior of these gas phase ions. Fragments were identified, as well as fragmentation mechanisms that produce these ions. Conformational differences that led to separations in the gas phase were also elucidated from these methods. The approach of utilizing these techniques in conjunction with one another should prove useful for many future structural characterization studies of polymers and their precursors.

While MD methods are primarily used to sample conformational space in support of structural IM-MS, there are limitations to this approach. The need for unique force fields for specific molecular classes makes MD studies appear in stark contrast to the complex biological samples that are often analyzed with IM-MS. Additionally, MD calculations can be quite time consuming when we want to ensure that all conformational space is sampled. This is also in contrast to the millisecond time scale of IM-MS experiments. These incongruences suggested that a different computational approach

might be more appropriate for conformational space sampling in support of IM-MS studies. Distance geometry proved to be an alternate approach by efficiently sampling conformational space utilizing only interatomic distances within the molecule. This purely mathematical approach is very time efficient and can be applied to any molecular species as it does not require class specific force field information.

The distance geometry protocol was initially benchmarked against a set of natural product molecules. These molecules were ideal for the distance geometry study because the unique structural motifs they contain not only make them excellent drug precursors, but also make them difficult to model with traditional MD approaches. With the exception of cyclic peptides whose three-dimensional conformation is greatly influenced by the presence of an additional cation, the distance geometry protocol proved accurate in sampling conformational space in support of IM-MS natural product research.

Distance geometry was then used to generate theoretical CCS ranges for a set of metabolite standards. These ranges were compared to experimental CCS values from both DTIM and TWIM mass spectrometers. The agreement between theory and experimental is an important first step toward reaching the ultimate goal of this project which is to generate theoretical CCS ranges for metabolite database searching. This additional feature will help in identification of metabolites in complex biological samples.

5.2. *Future Directions*

5.2.1. *MDA Characterization*

The extensive characterization studies of MDA in Chapter II were performed with electrospray ionization. It is common in MS polymer studies to also utilize matrix

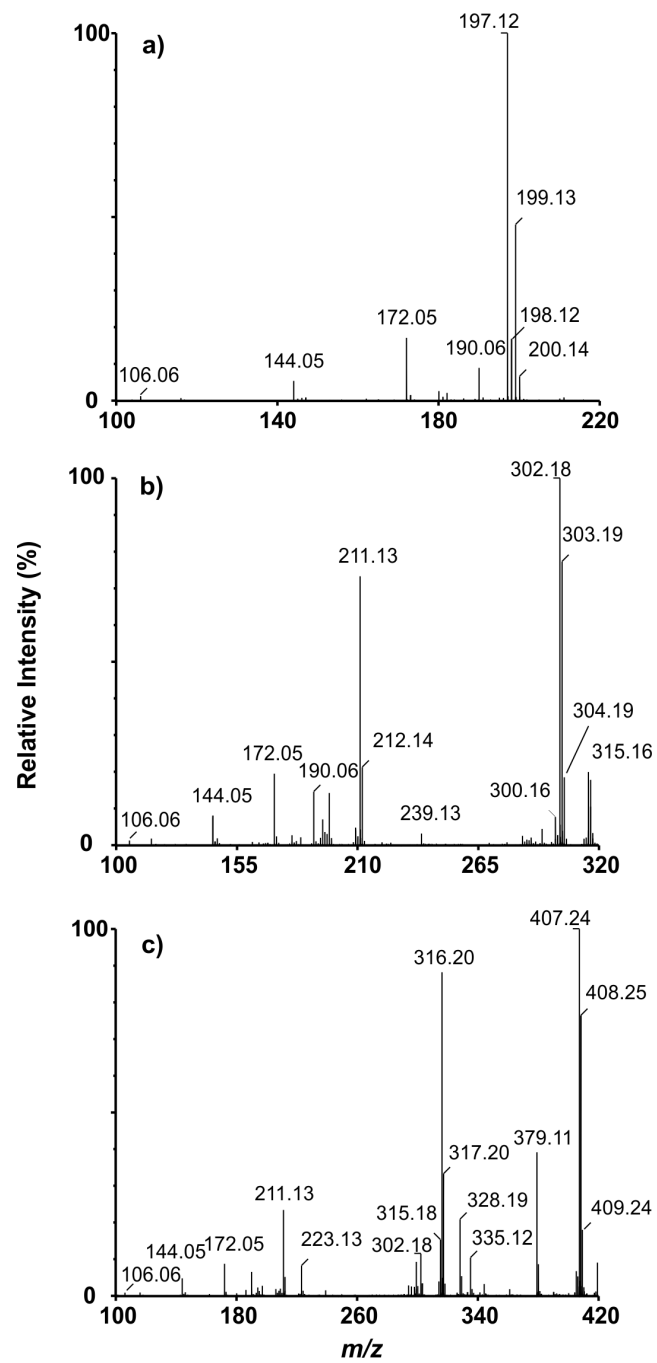


Figure 5.1. MALDI-MS data is shown for a) 4,4'-MDA, b) 3-ring MDA, and c) 4-ring MDA.

assisted laser desorption ionization (MALDI) to aid in characterization studies. Different ions are produced with this method as shown in Figure 5.1 and should provide further insight in the gas phase behavior of MDA. These future characterization studies will also include the effects of cation coordination on MDA. Additionally, mixtures of larger MDA ring species (5-ring, 6-ring, and 7-ring) will be analyzed with the combined IM-MS, MS/MS, and computational method. The work in Chapter II should prove useful for identifying fragments and fragmentation mechanisms for these large MDA species.

5.2.2. Distance Geometry

Distance geometry has proved to accurately sample the conformational space of natural products and metabolites in support of IM-MS CCS measurements. One drawback of this method was its ability to generate conformations that coordinate the cation extensively since it cannot be present during the entire simulation. This drawback suggests that this method may prove more useful for negative ion conformational space sampling. Preliminary results shown in Figure 5.2 for a set of bile acids show that distance geometry can generate theoretical conformations that agree with experimental measurements. The bile acids analyzed here are as follows: chendeoxycholic acid (CHE), hydoxycholic acid (HYO), ursodeoxycholic acid (URS), lithocholic acid (LIT), deoxycholic acid (DEO), cholic acid (CHO), taurochenodeoxycholic acid (TCH), taurocholic acid (TCO), taurodeoxycholic acid (TDE), tauroolithocholic acid (TLI), glycocholic acid (GCO), glycodeoxycholic acid (GDE), and glycochenodeoxycholic acid (GCH). For all thirteen of these negative ion species, distance geometry was able to generate ranges that agreed with the experimental data.

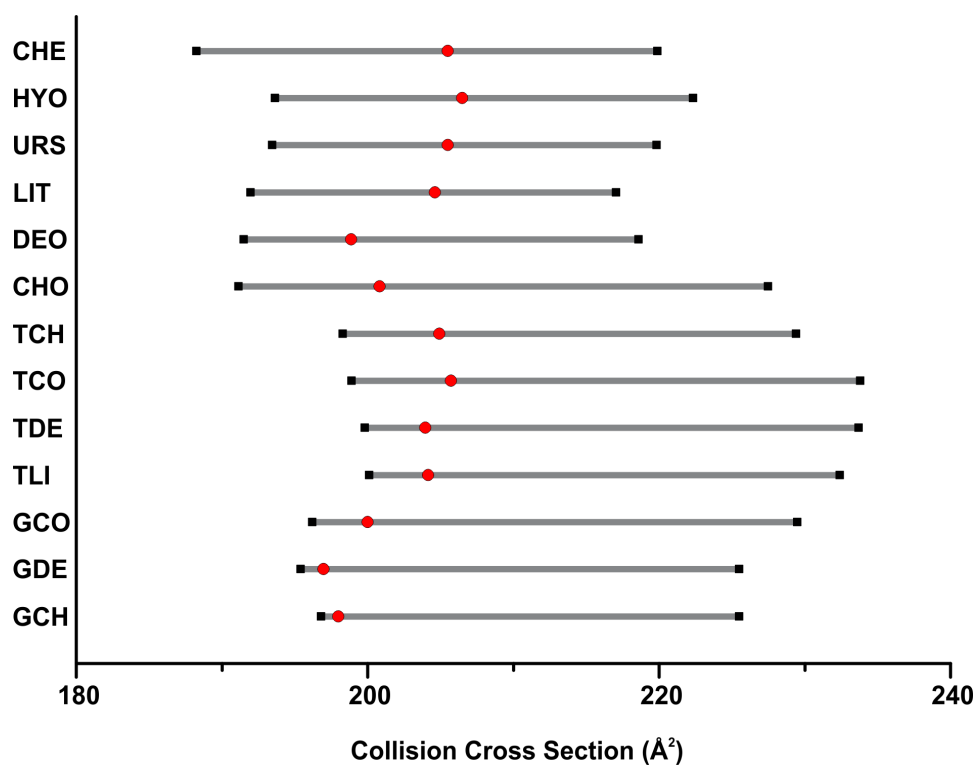


Figure 5.2. Theoretical CCS ranges and experimental TWIM CCS data for a set of negative ion bile acids. The ranges are represented with the gray bars and the experimental values are represented with the red circles. All CCS data is obtained in nitrogen.

5.3. *Conclusions*

The benefits of incorporating computational modeling in support of structural IM-MS studies have been thoroughly discussed throughout this dissertation research. While the CCS values determined from experimental drift time measurements provide a general shape for the molecular ion, additional computational modeling can generate theoretical conformations that provide detailed structural information. Selecting the appropriate conformational sampling technique and method to theoretically calculate CCS for the generated conformers is key in successful structural IM-MS studies. As seen in Chapter II, for studies where the molecules are well defined by current force fields, MD approaches work well for structural characterization. Here the generated structures were also used to help suggest fragmentation mechanisms. When the molecules of interest contain unique structural motifs or when there are large sets of molecules to be analyzed, MD methods may not be the best approach. By sampling interatomic distances to generate possible three-dimensional conformations, distance geometry successfully predicted theoretical CCS values or ranges for natural products and metabolites in Chapters III and IV. Distance geometry also proved to be a time efficient approach for sampling conformational space in support of structural IM-MS studies.

Selecting the appropriate method for the theoretical CCS calculation is also necessary to obtain accurate results. The experimental drift gas and size of the molecule are both important factors to consider when selecting the method. Obtaining experimental helium CCS values for MDA in Chapter II resulted in better alignment between theory and experiment for these small molecules. Future work to obtain experimental CCS values in helium drift gas for metabolite compounds should offer better agreement for the

smaller species. In addition to the experimental concerns with nitrogen as a drift gas, these theoretical CCS calculations are very time consuming. Future work to improve on the software and software accessibility should propel these methods forward as considerable CCS data is obtained in nitrogen drift gas.

Despite the challenges of selecting appropriate strategies for both generating conformations and obtaining their theoretical CCS, computational studies offer important structural insight for IM-MS CCS measurements. Methods, such as distance geometry for sampling conformational space and PSA for calculating theoretical CCS values, operate on time scales more similar to experimental IM-MS measurements. This makes these strategies more alluring than traditional methods that are much more computationally expensive. Conformational space sampling methods will not only provide detailed structural information for future IM-MS studies, but they may also guide identification of species in complex sample analysis. This work has provided both an example of how encompassing IM-MS methods can be when combined with MS/MS and conformational sampling studies and a new, time efficient approach for sampling conformational space in support of IM-MS CCS measurements. Integrating the time efficient, computational protocol developed here with future IM-MS studies will provide an additional metric for determining CCS values, aid in identification of unknowns in complex sample analysis, and offer more comprehensive structural information.

APPENDIX A

REPRINT PERMISSIONS FOR CHAPTERS

- Chapter I. **S. M. Stow**, N. M. Lareau, K. M. Hines, C. R. McNeese, C. R. Goodwin, B. O. Bachmann, and J. A. McLean, *Classification of Natural Product Classes by Ion Mobility-Mass Spectrometry in **Natural Product Analysis: Instrumentation, Methods, and Applications***. Wiley-Blackwell (2014). **Book Chapter**
- Chapter II. J. G. Forsythe, **S. M. Stow**, H. Nefzger, N. W. Kwiecien, J. C. May, J. A. McLean, and D. M. Hercules, *Structural Characterization of Methylenedianiline Regioisomers by Ion Mobility-Mass Spectrometry, Tandem Mass Spectrometry, and Computational Strategies: I. Electrospray Spectra of 2-Ring Isomers*, *Analytical Chemistry* 86 (2014) 4362-4370.
- S. M. Stow**, T. M. Onifer, J. G. Forsythe, H. Nefzger, N. W. Kwiecien, J. C. May, J. A. McLean, and D. M. Hercules, *Structural Characterization of Methylenedianiline Regioisomers by Ion Mobility-Mass Spectrometry, Tandem Mass Spectrometry, and Computational Strategies: II. Electrospray Spectra of 3-Ring and 4-Ring Isomers*, Submitted to *Analytical Chemistry*.
- Chapter III. **S. M. Stow**, C. R. Goodwin, M. Kliman, B. O. Bachmann, J. A. McLean, and T. P. Lybrand, *A Distance Geometry Protocol to Generate Conformations of Natural Products to Structurally Interpret Ion Mobility-Mass Spectrometry Collision Cross Sections*, *Journal of Physical Chemistry B* 118 (2014) 13812-13820.

APPENDIX B

SUPPLEMENTARY MATERIALS FOR CHAPTER II

B.1. Supplemental Materials for 2-Ring MDA Isomers

NMR Spectroscopy Protocol for Purified MDA Isomers

NMR experiments were acquired using a 14.0 T Bruker magnet equipped with a Bruker AV-III console operating at 600.13 MHz. All spectra were acquired in 5mm NMR tubes using a Bruker 5 mm TCI cryogenically cooled NMR probe. Chemical shifts were referenced internally to DMSO (2.49 ppm) which also served as the ^2H lock solvents. For 1D ^1H NMR, typical experimental conditions included 32K data points, 13 ppm sweep width, a recycle delay of 1.5 seconds and 64 scans. For 1D ^{13}C NMR, typical experimental conditions included 32K data points, 250 ppm sweep width, 20° excitation pulse, a recycle delay of 2 seconds and 512 scans. Multiplicity-edited HSQC experiments were acquired using a 1024 x 256 data matrix, a J(C-H) value of 145 Hz which resulted in a multiplicity selection delay of 34 ms, a recycle delay of 1.5 seconds and 64 scans per increment along with GARP decoupling on ^{13}C during the acquisition time (150 ms). The data was processed using a p/2 shifted squared sine window function and displayed with CH/CH₃ signals phased positive and CH₂ signals phased negative.

^1H NMR of 4,4'-MDA in DMSO

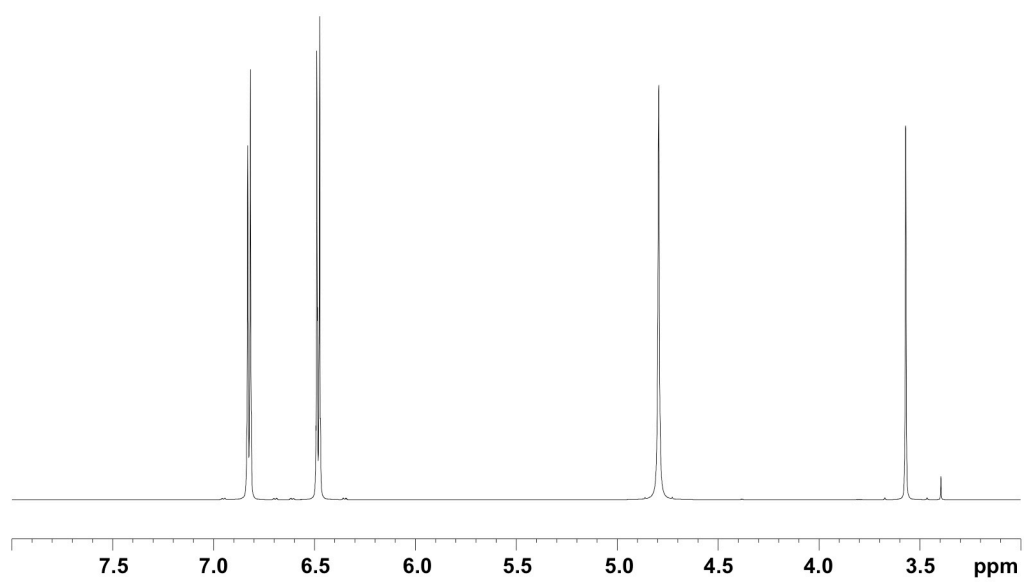


Figure B.1. ^1H NMR of 4,4'-MDA.

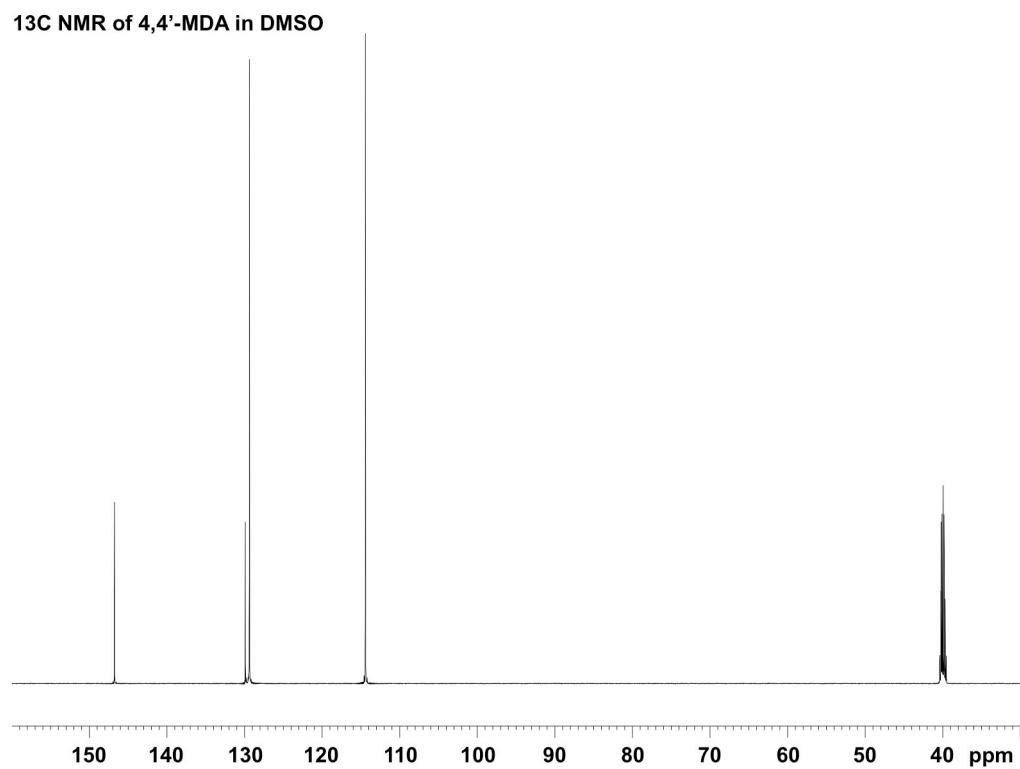


Figure B.2. ^{13}C NMR of 4,4'-MDA.

^1H NMR of 2,2'-MDA in DMSO

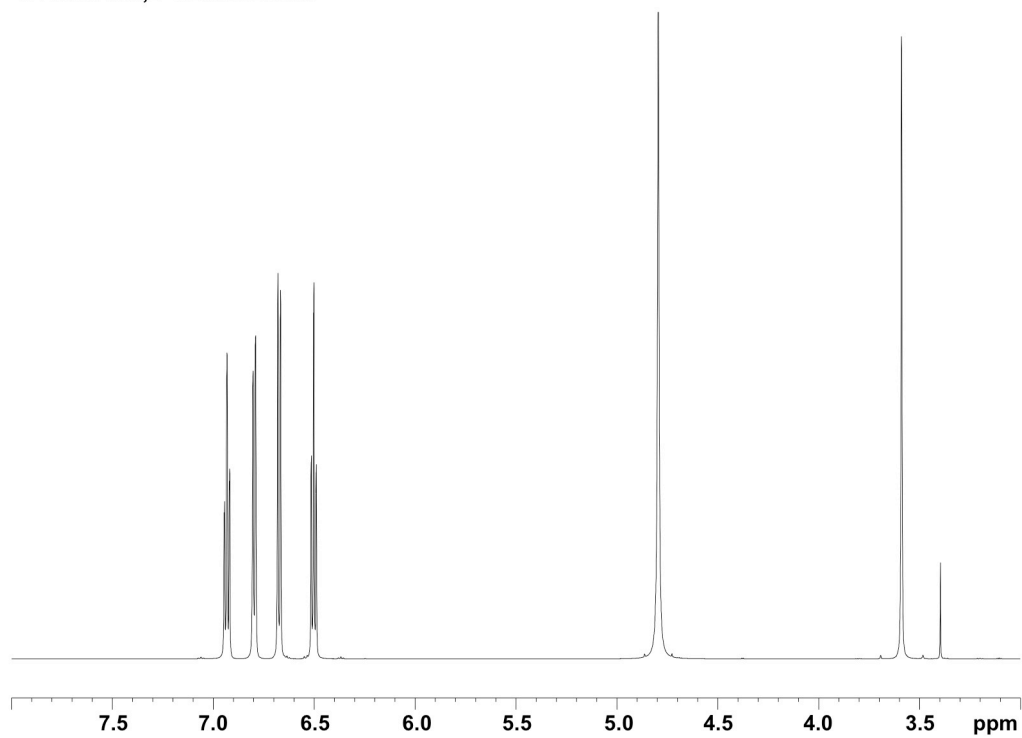


Figure B.3. ^1H NMR of 2,2'-MDA.

¹³C NMR of 2,2'-MDA in DMSO

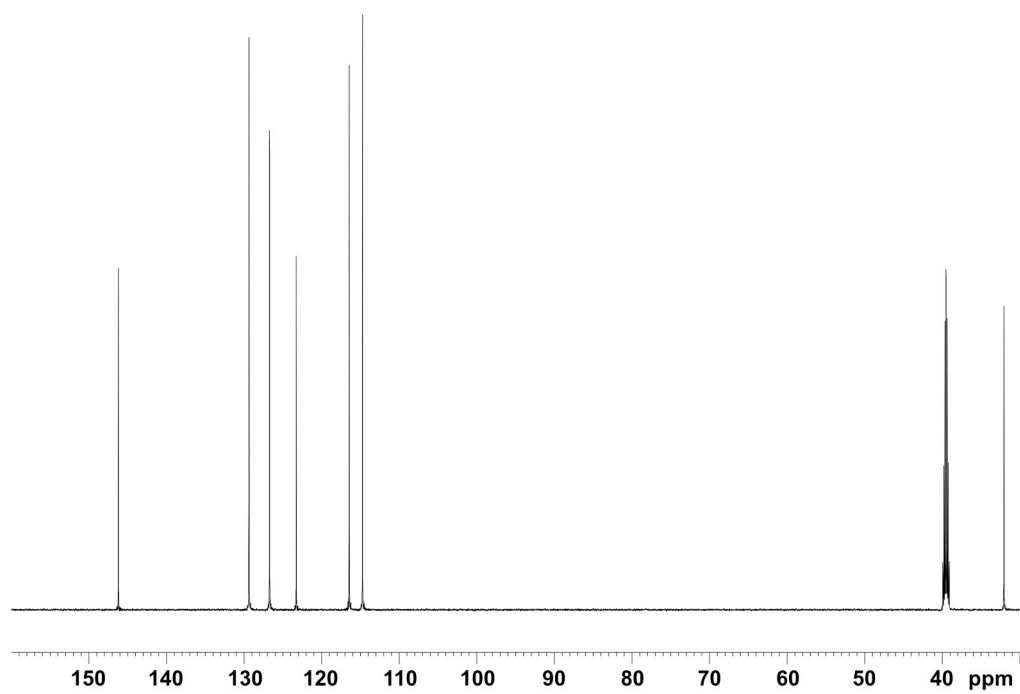


Figure B.4. ¹³C NMR of 2,2'-MDA.

^1H NMR of 2,4'-MDA in DMSO

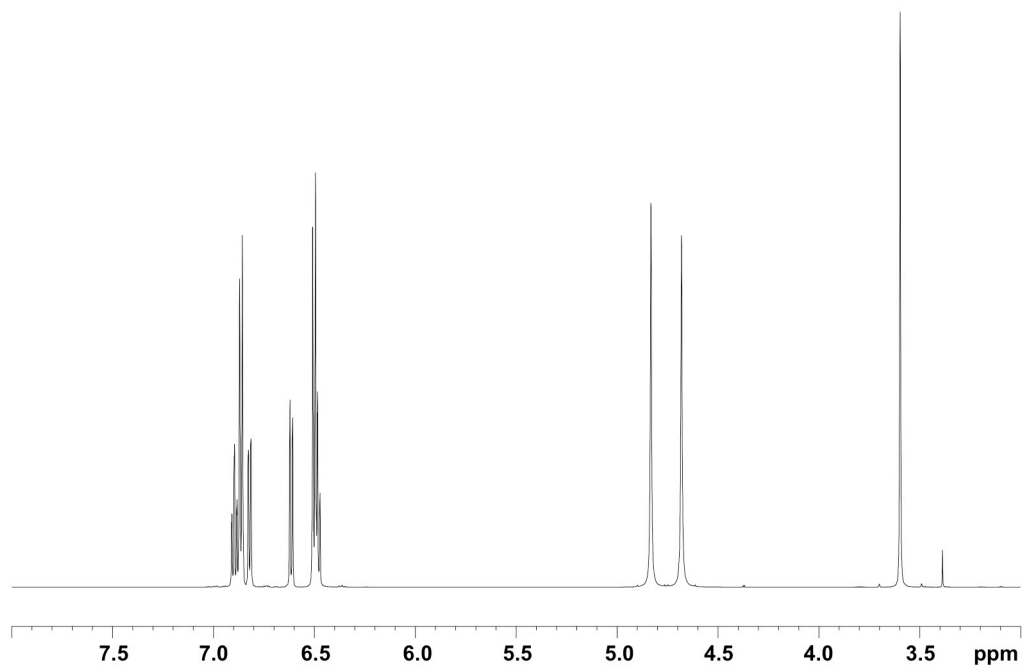


Figure B.5. ^1H NMR of 2,4'-MDA.

^{13}C NMR of 2,4'-MDA in DMSO

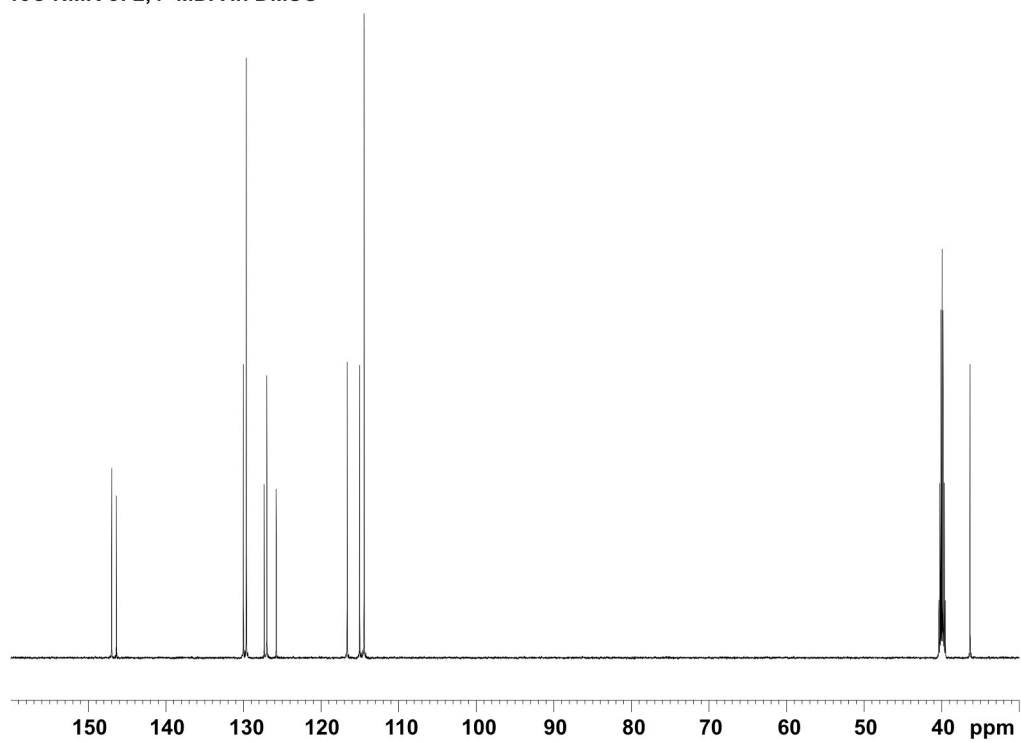


Figure B.6. ^{13}C NMR of 2,4'-MDA.

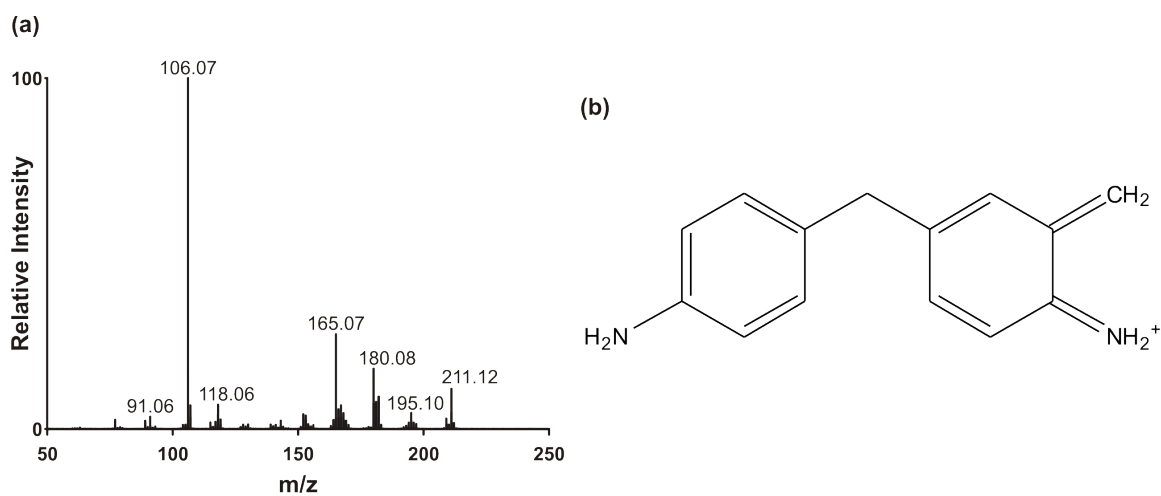


Figure B.7. (a) Tandem mass spectrum for 211 Da observed in the 4,4'-MDA sample. ESI ionization was used. A center-of-mass collision energy of 4.9 eV was applied (40 eV lab-frame). (b) Proposed structure for the 211 Da species. Most fragment signals for 211 Da match the 199 Da fragments shown in **Table 1** in the main text. The likely source of this ion is a very low abundance multimer which fragments into the 211 Da structure.

Table B.1. Comparison of relative gas-phase stabilities between traveling-wave IM and DTIM instrument platforms. Values reflect the percent abundance of the 199 Da parent ion relative to the 106 Da fragment. $n = 3$ for each value. For both instrument platforms, 4,4'-MDA is significantly more stable than 2,2'-MDA and 2,4'-MDA. However, in both cases 2,2'-MDA is slightly more stable than 2,4'-MDA.

[M+H]⁺ Species	T-wave IM	DTIM
4,4'-MDA	$97 \pm 2\%$	$99.89 \pm 0.01\%$
2,2'-MDA	$3.9 \pm 0.1\%$	$47.1 \pm 0.2\%$
2,4'-MDA	$0.9 \pm 0.4\%$	$37.6 \pm 0.6\%$

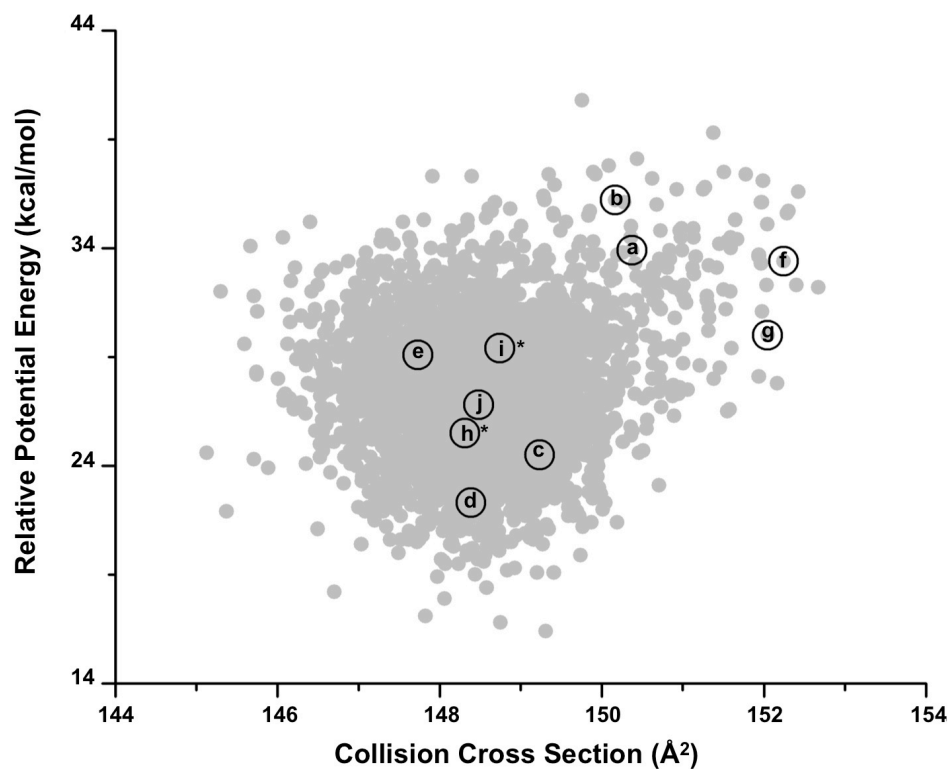


Figure B.8. Conformational space plot for the ortho amine protonated 2,2'-MDA. The 3,000 generated conformations are represented in grey, the clustering representative conformation are labeled with letters that correspond to the structures in Figures **B.9** and **B.10**. The asterisk indicates the structures that are shown in the manuscript.

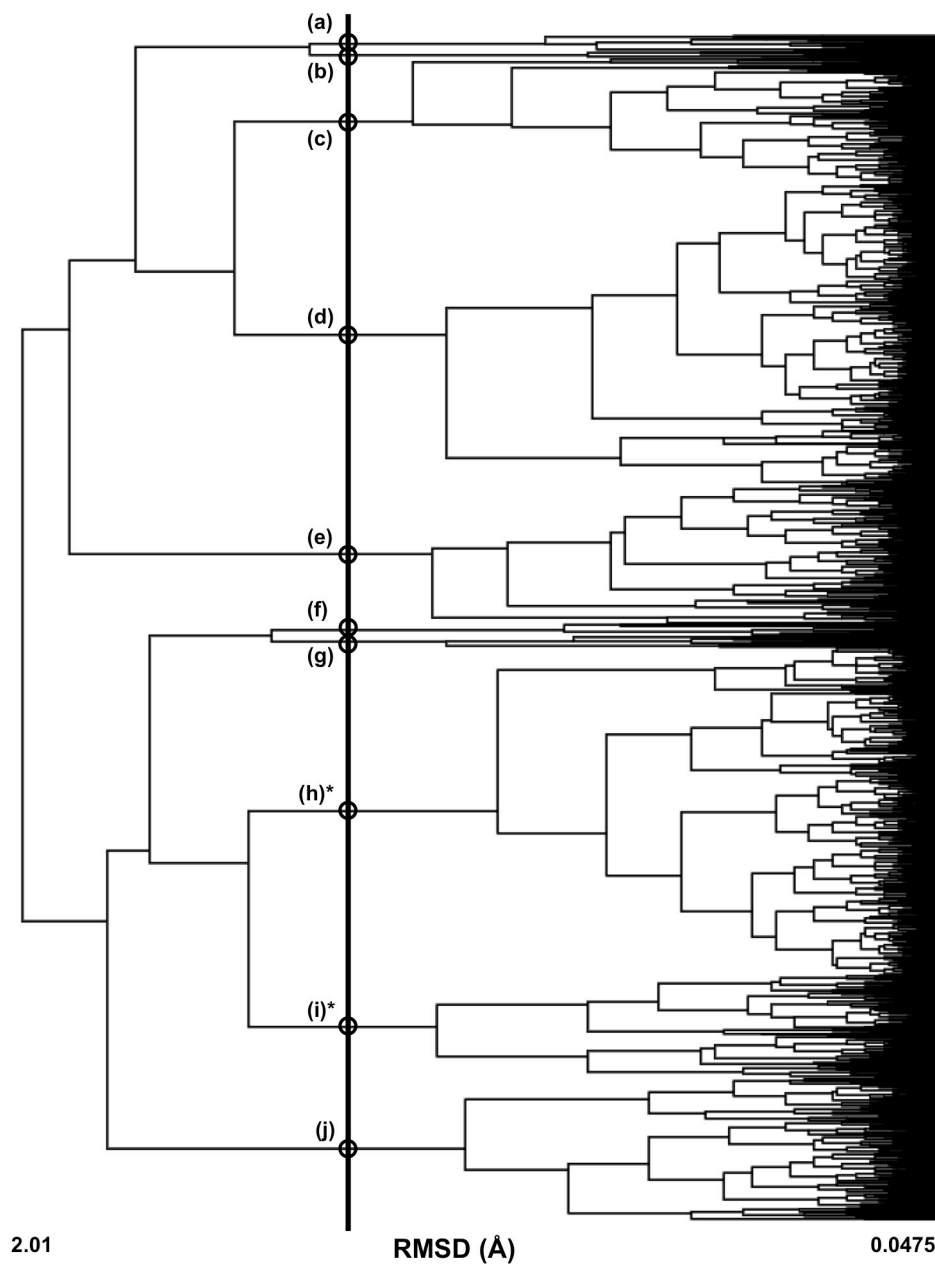


Figure B.9. Clustering analysis of 3,000 conformations of the ortho amine protonated 2,2'-MDA. Clustering is based on root mean square distance of atoms of superimposed structures. The vertical black bar indicates the RMSD cutoff (1.20 Å) used to select the conformations (circled) for further analysis. The asterisk represents the structures shown in the paper.

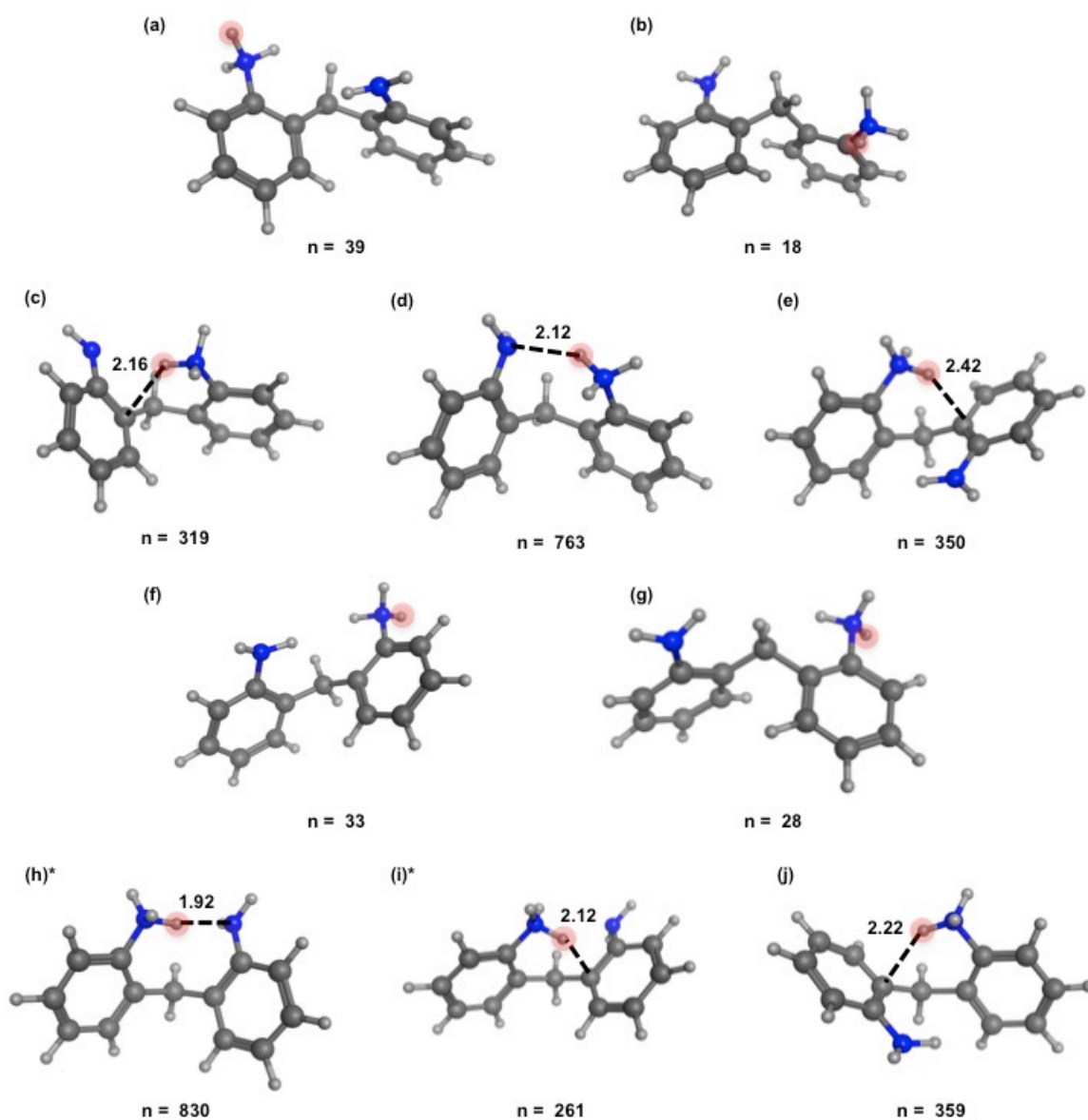


Figure B.10. Representative conformations of the ortho amine protonated 2,2'-MDA generated from an elevated temperature molecular dynamic protocol. Carbon atoms are shown in dark grey, hydrogen in light grey, and nitrogen in blue. The asterisk represents the structures shown in the paper. The number of conformations each of these represents from clustering is shown below the conformation.

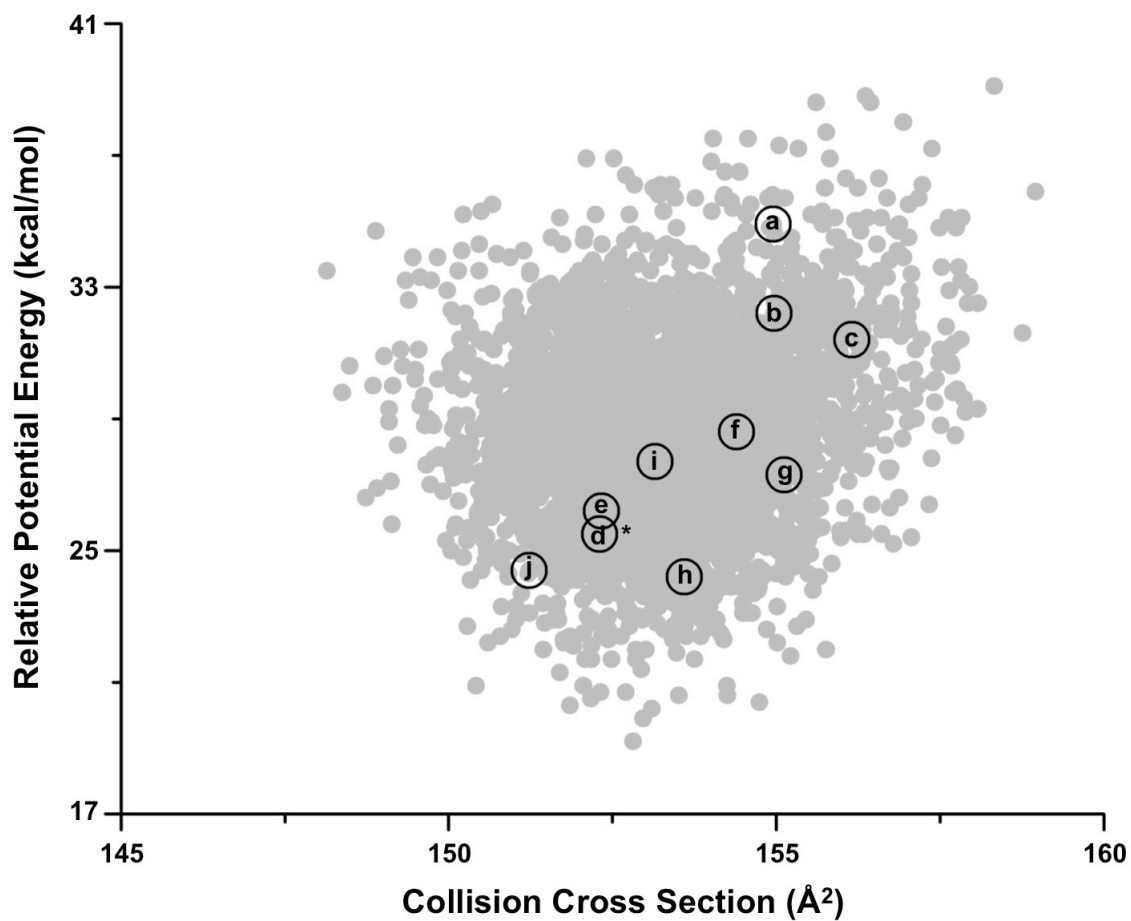


Figure B.11. Conformational space plot for ortho amine protonated 2,4'-MDA. The 3,000 generated conformations are represented in grey, the clustering representative conformation are labeled with letters that correspond to the structures in Figures B.12 and B.13. The asterisk indicates the structures that are shown in the manuscript.

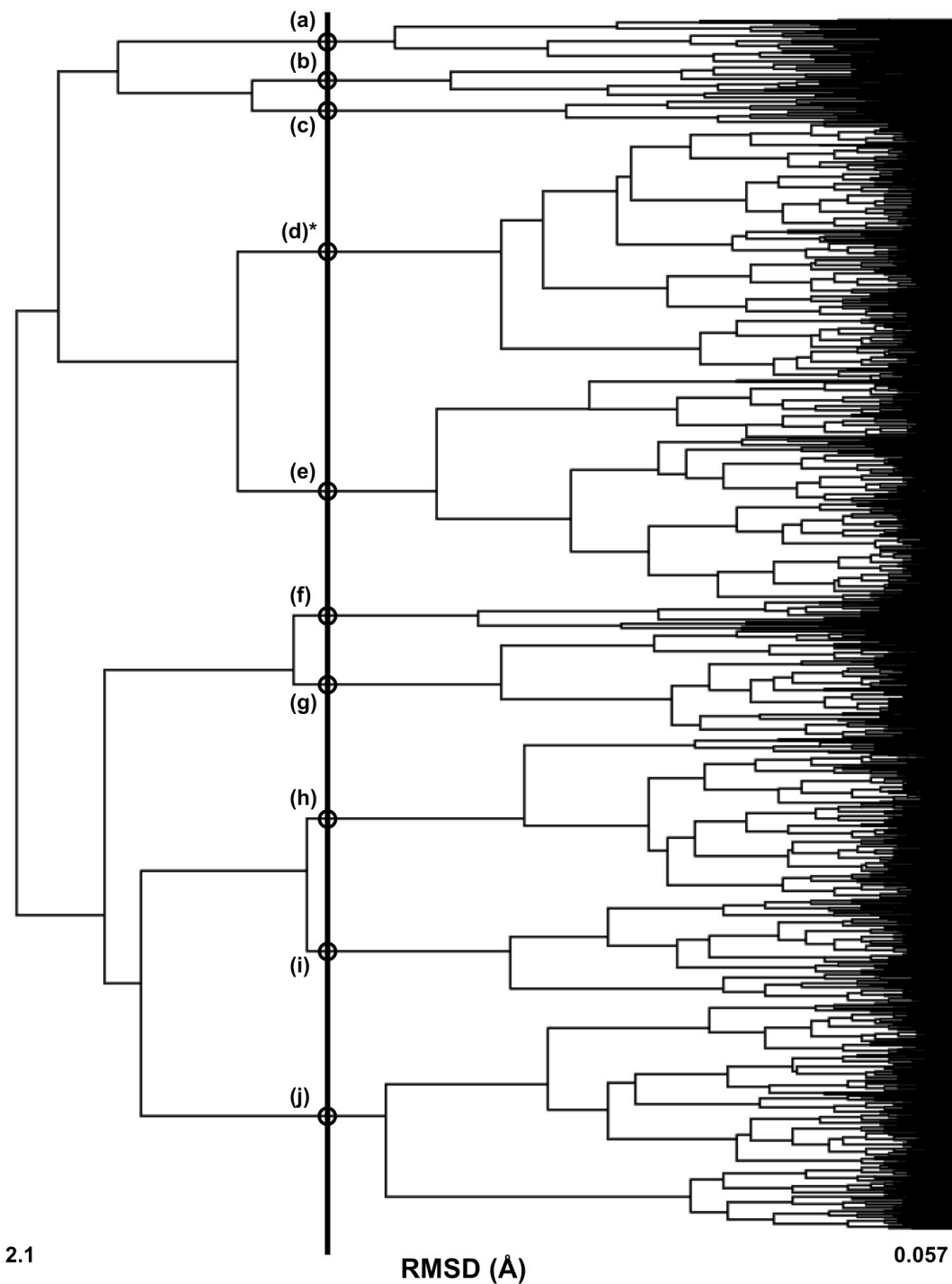


Figure B.12. Clustering analysis of 3,000 conformations of the ortho amine protonated 2,4'-MDA. Clustering is based on root mean square distance of atoms of superimposed structures. The vertical black bar indicates the RMSD cutoff (1.35 Å) used to select the conformations (circled) for further analysis. The asterisk represents the structures shown in the paper.

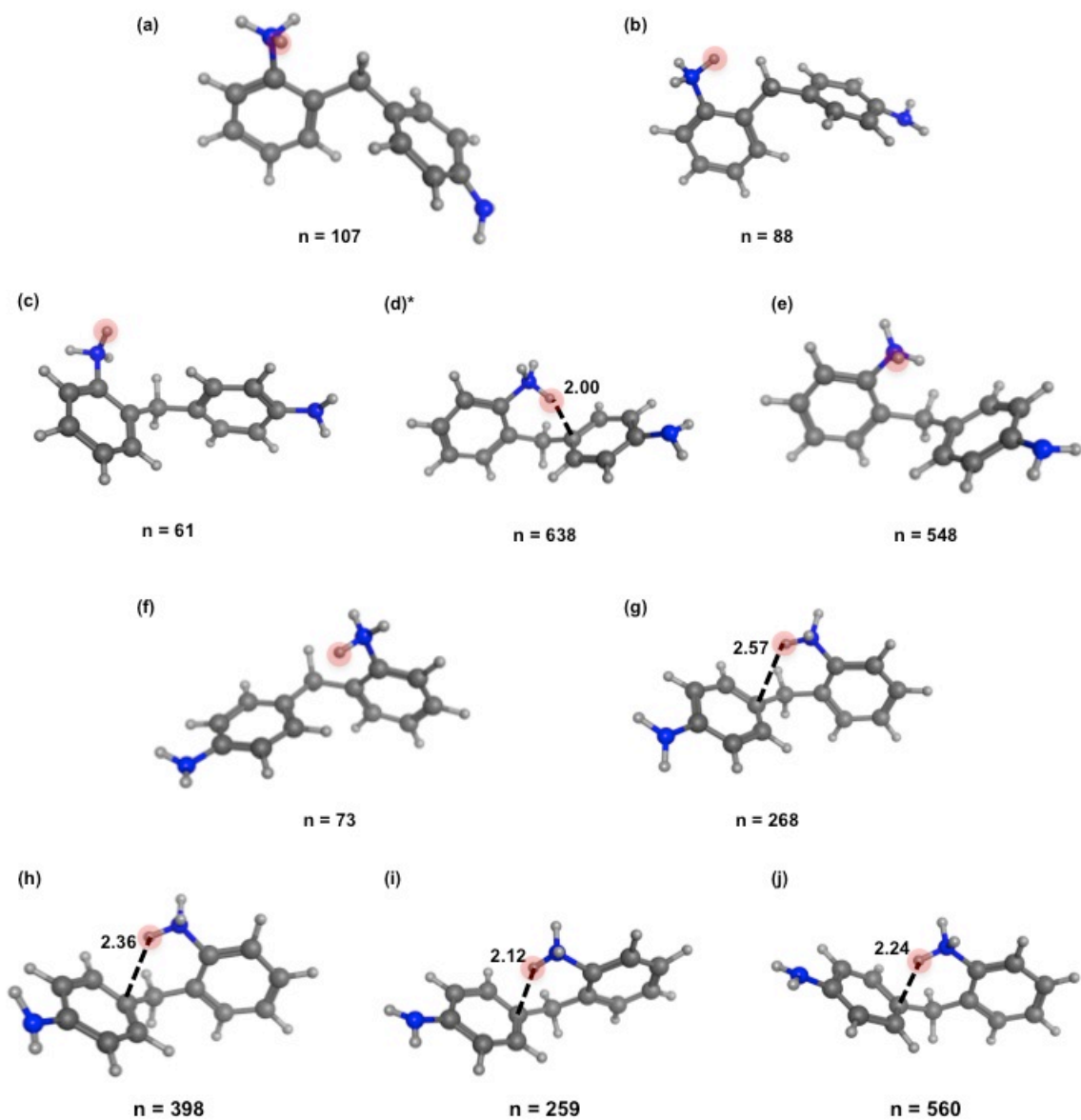


Figure B.13. Representative conformations of the ortho amine protonated 2,4'-MDA generated from an elevated temperature molecular dynamic protocol. Carbon atoms are shown in dark grey, hydrogen in light grey, and nitrogen in blue. The asterisk represents the structures shown in the paper. The number of conformations each of these represents from clustering is shown below the conformation.

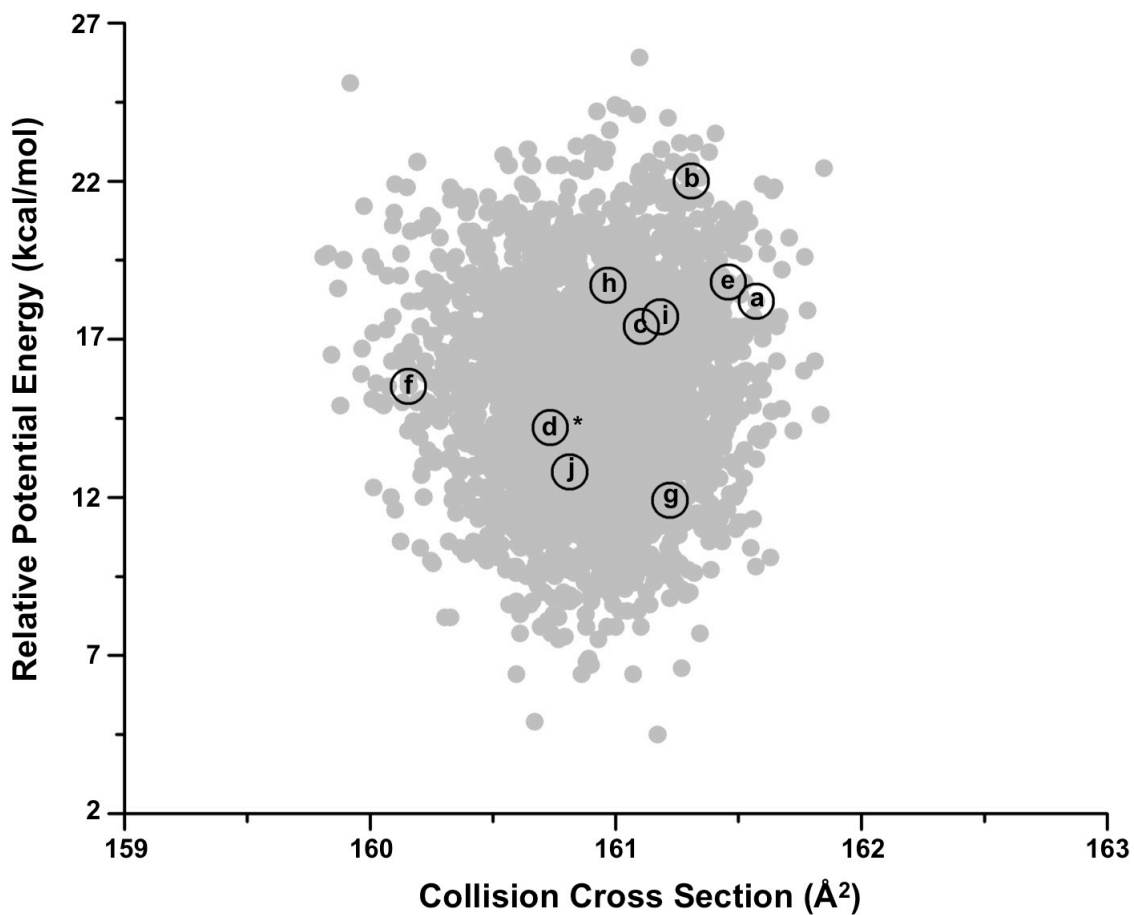


Figure B.14. Conformational space plot for the para amine protonated 4,4'-MDA. The 3,000 generated conformations are represented in grey, the clustering representative conformation are labeled with letters that correspond to the structures in Figures B.15 and B.16. The asterisk indicates the structures that are shown in the manuscript.

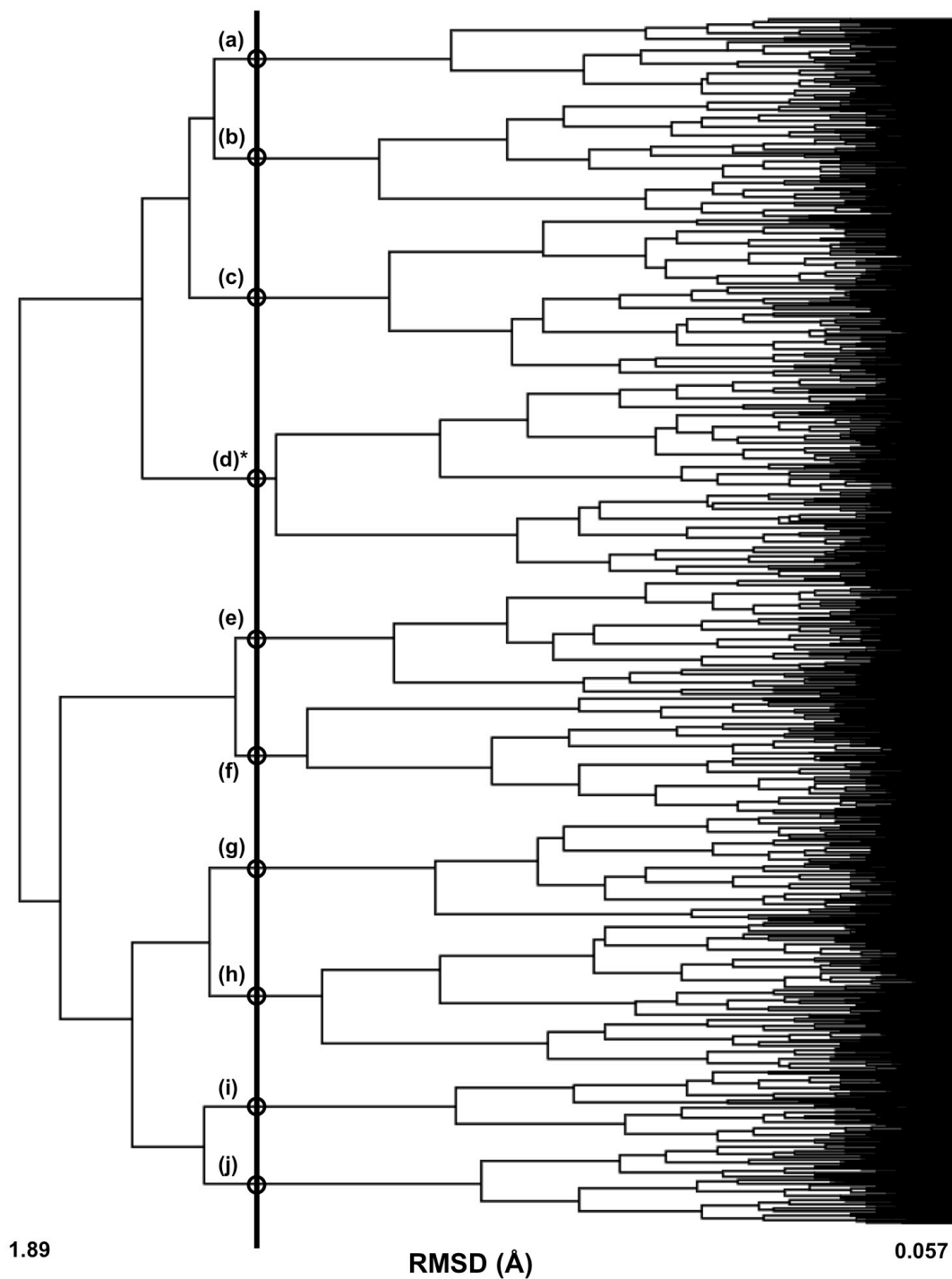


Figure B.15. Clustering analysis of 3,000 conformations of the para amine protonated 4,4'-MDA. Clustering is based on root mean square distance of atoms of superimposed structures. The vertical black bar indicates the RMSD cutoff (1.40 Å) used to select the conformations (circled) for further analysis. The asterisk represents the structures shown in the paper.

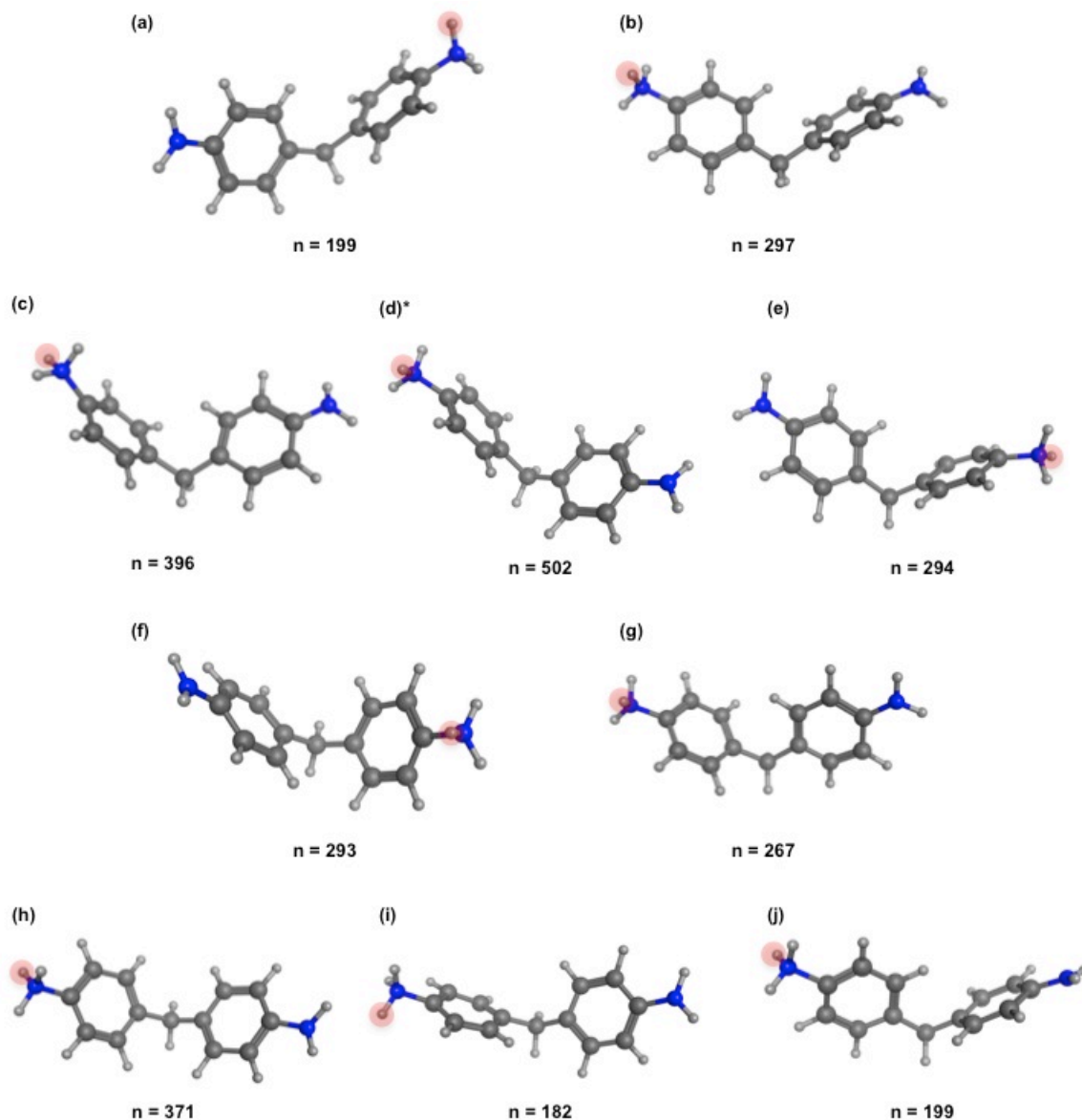


Figure B.16. Representative conformations of the para amine protonated 4,4'-MDA generated from an elevated temperature molecular dynamic protocol. Carbon atoms are shown in dark grey, hydrogen in light grey, and nitrogen in blue. The asterisk represents the structures shown in the paper. The number of conformations each of these represents from clustering is shown below the conformation.

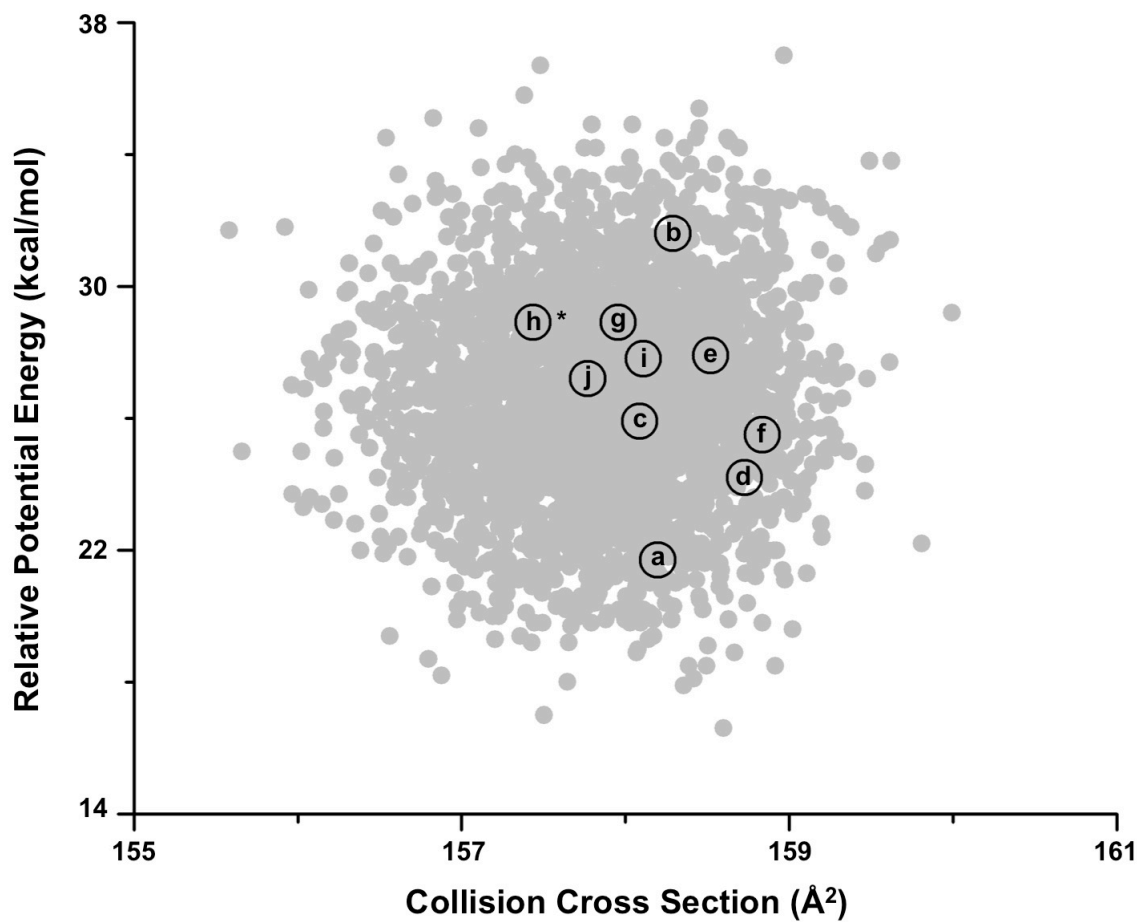


Figure B.17. Conformational space plot for the para amine protonated 2,4'-MDA. The 3,000 generated conformations are represented in grey, the clustering representative conformation are labeled with letters that correspond to the structures in Figures B.18 and B.19. The asterisk indicates the structures that are shown in the manuscript.

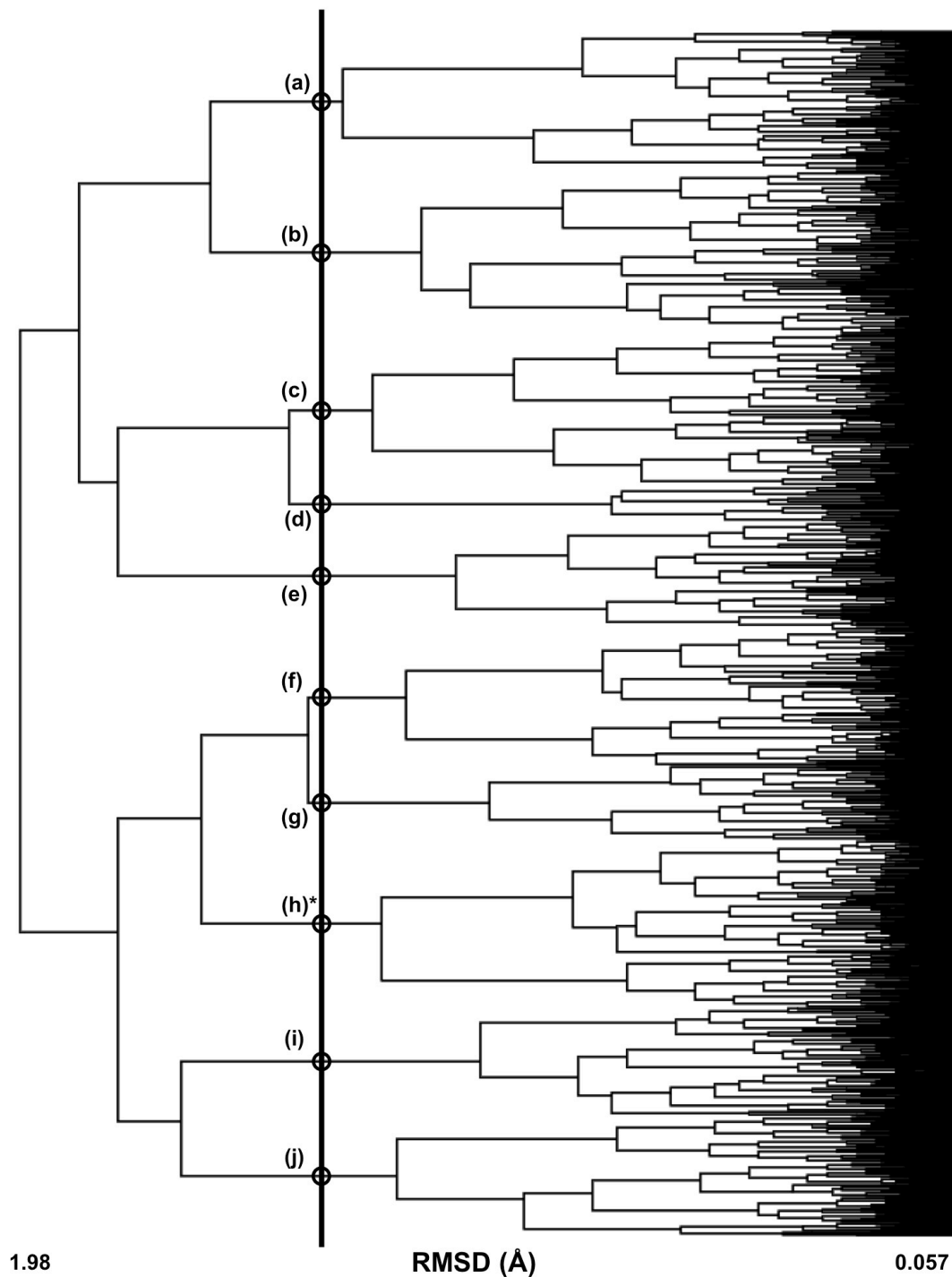


Figure B.18. Clustering analysis of 3,000 conformations of the para amine protonated 2,4'-MDA. Clustering is based on root mean square distance of atoms of superimposed structures. The vertical black bar indicates the RMSD cutoff (1.35 Å) used to select the conformations (circled) for further analysis. The asterisk represents the structures shown in the paper.

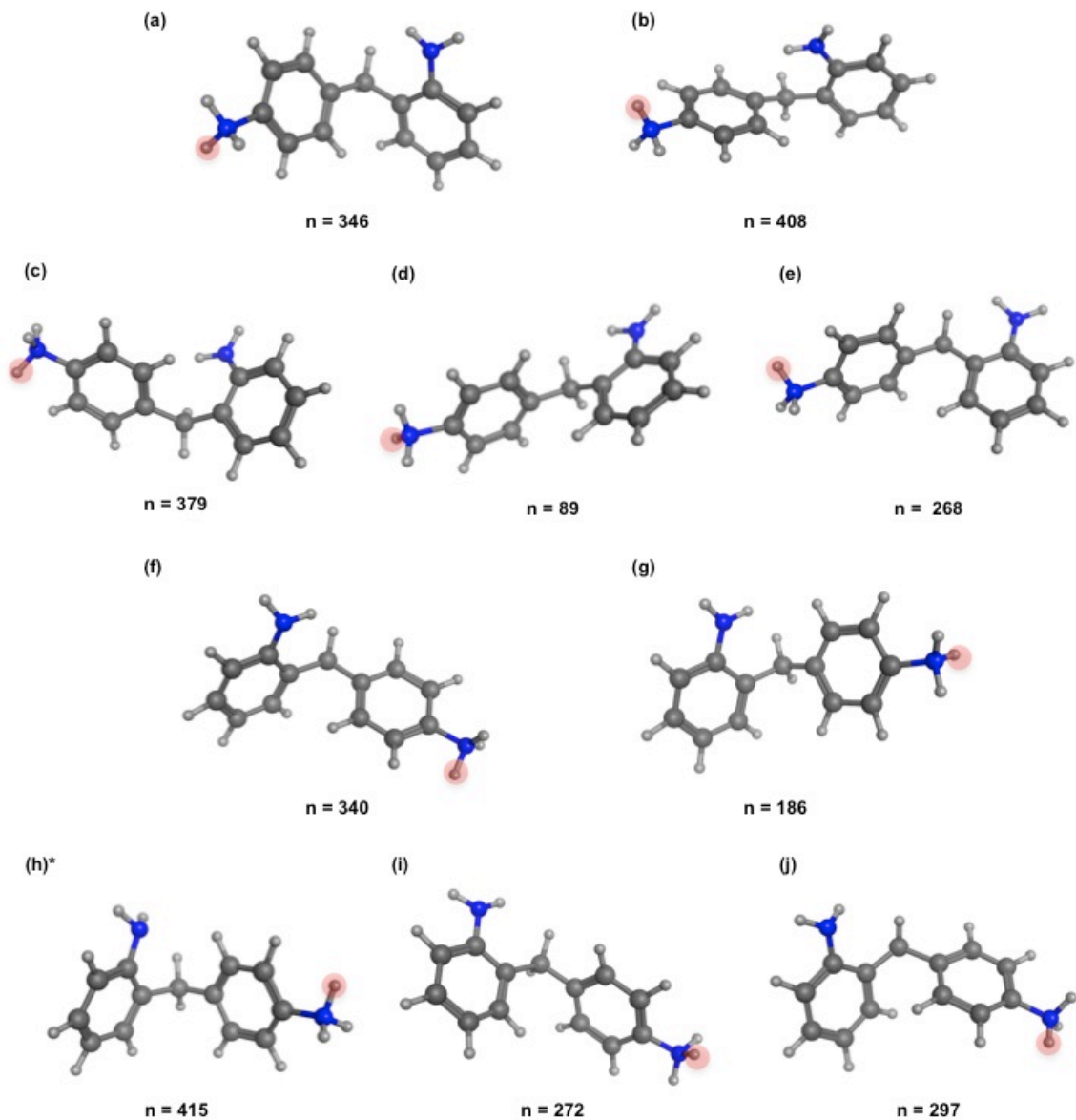


Figure B.19. Representative conformations of the para amine protonated 2,4'-MDA generated from an elevated temperature molecular dynamic protocol. Carbon atoms are shown in dark grey, hydrogen in light grey, and nitrogen in blue. The asterisk represents the structures shown in the paper. The number of conformations each of these represents from clustering is shown below the conformation.

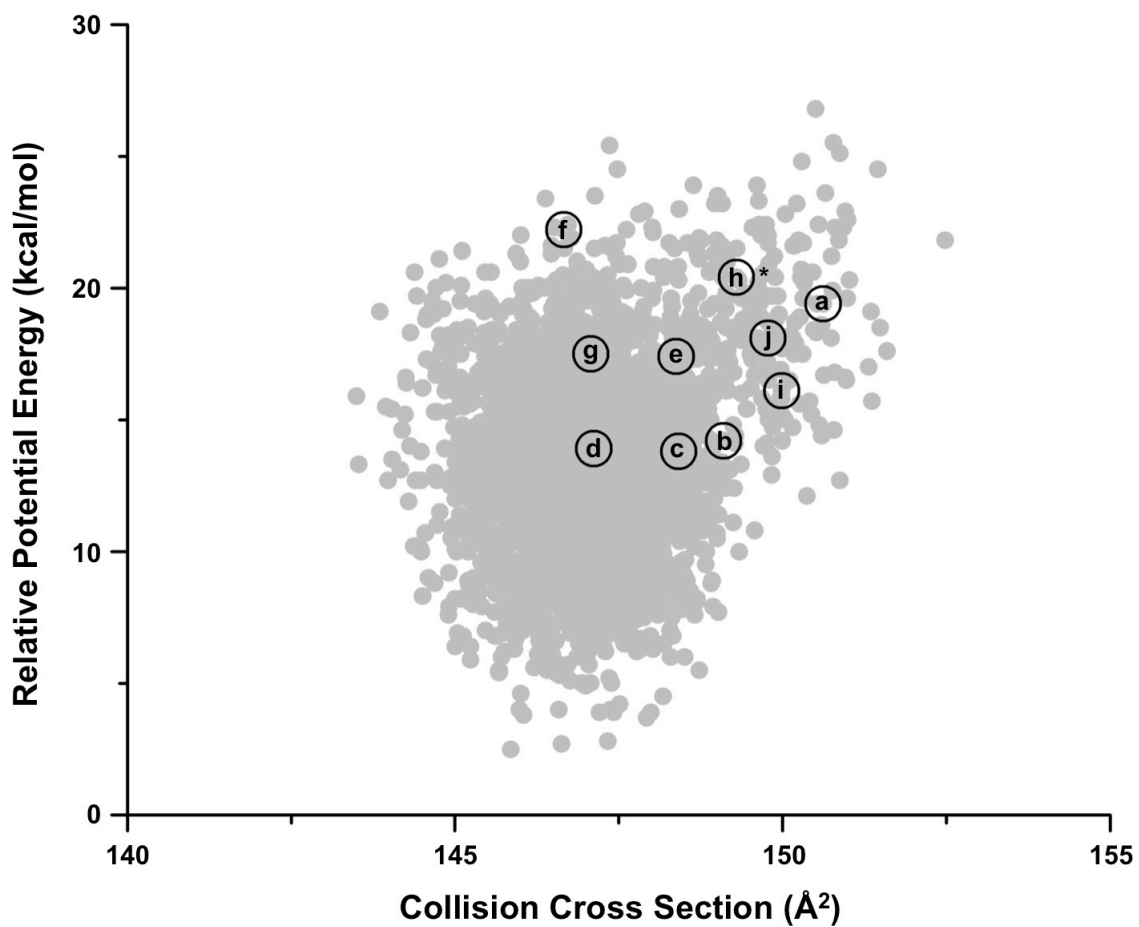


Figure B.20. Conformational space plot for the ring protonated 2,2'-MDA. The 3,000 generated conformations are represented in grey, the clustering representative conformation are labeled with letters that correspond to the structures in Figures B.21 and B.22. The asterisk indicates the structures that are shown in the manuscript.

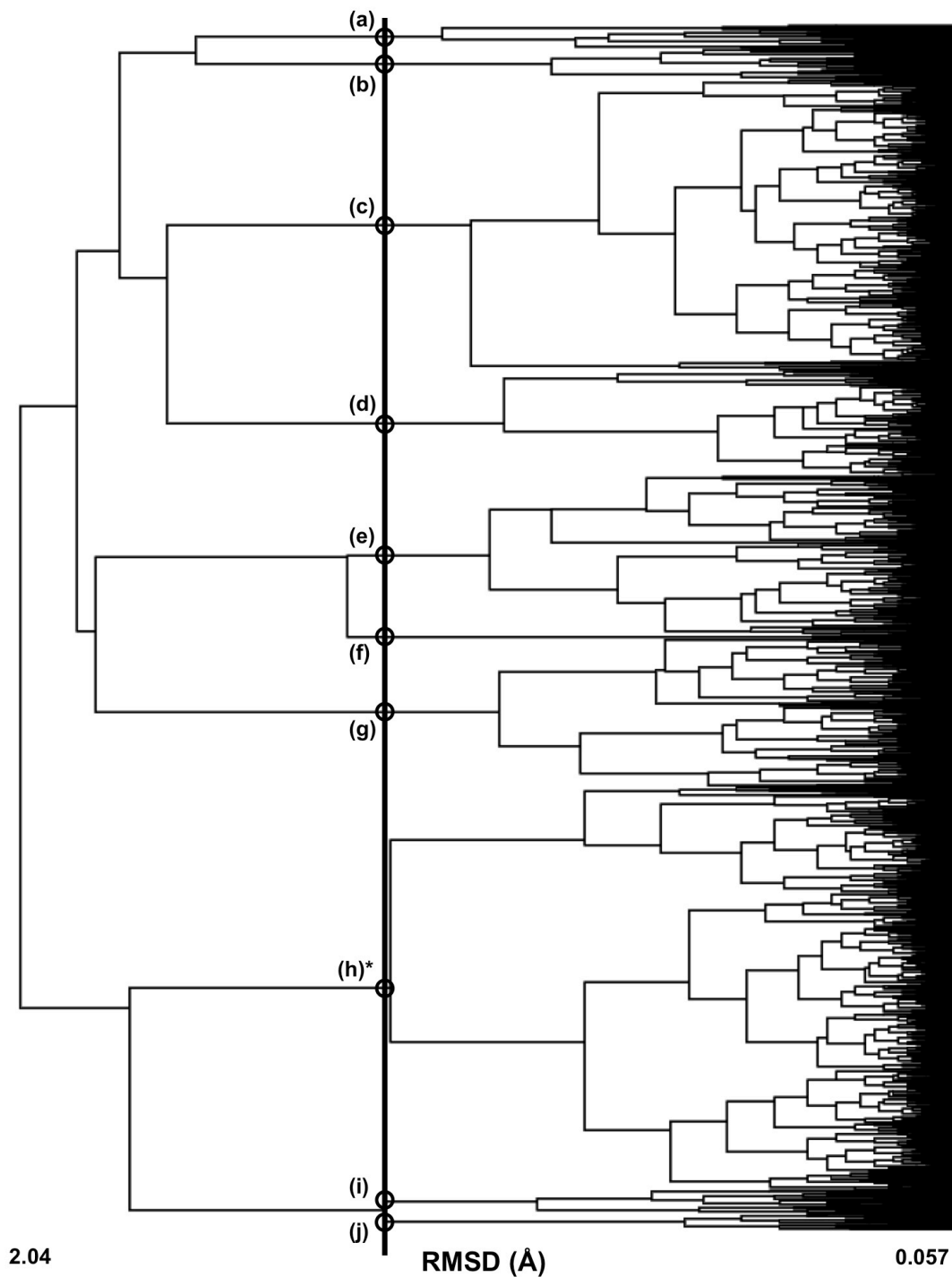


Figure B.21. Clustering analysis of 3,000 conformations of the ring protonated 2,2'-MDA. Clustering is based on root mean square distance of atoms of superimposed structures. The vertical black bar indicates the RMSD cutoff (1.26 Å) used to select the conformations (circled) for further analysis. The asterisk represents the structures shown in the paper.

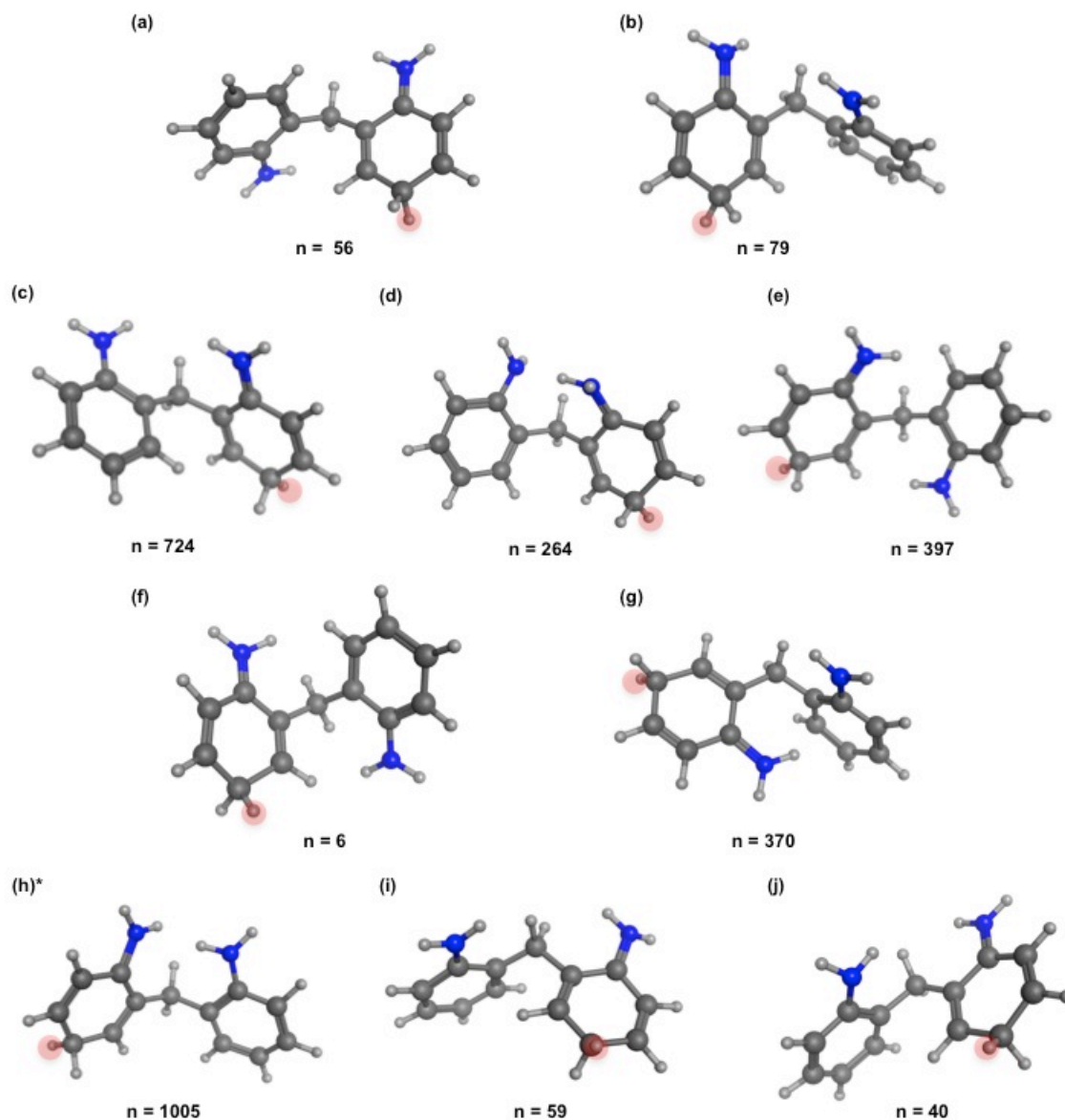


Figure B.22. Representative conformations of the ring protonated 2,2'-MDA generated from an elevated temperature molecular dynamic protocol. Carbon atoms are shown in dark grey, hydrogen in light grey, and nitrogen in blue. The asterisk represents the structures shown in the paper. The number of conformations each of these represents from clustering is shown below the conformation.

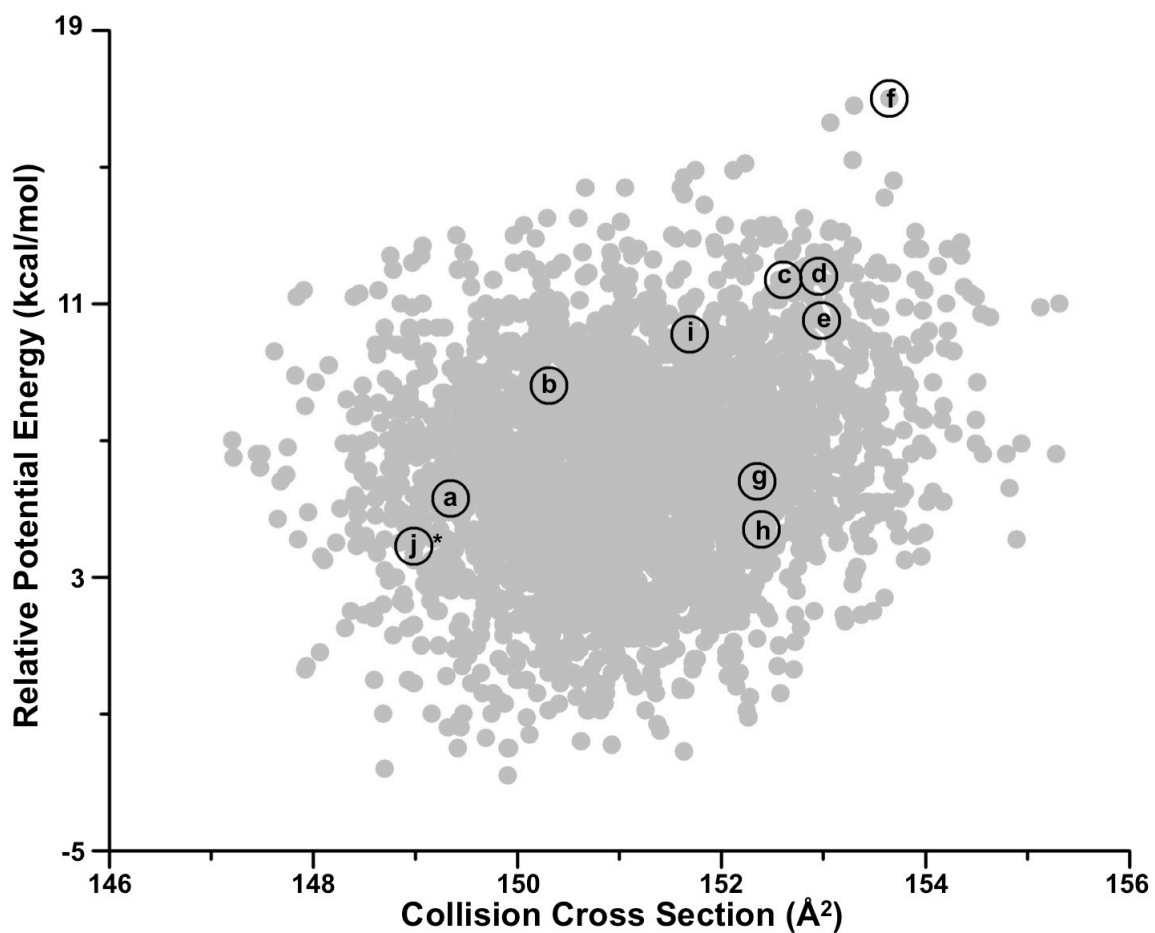


Figure B.23. Conformational space plot for the ring protonated 2,4'-MDA. The 3,000 generated conformations are represented in grey, the clustering representative conformation are labeled with letters that correspond to the structures in Figures B.24 and B.25. The asterisk indicates the structures that are shown in the manuscript.

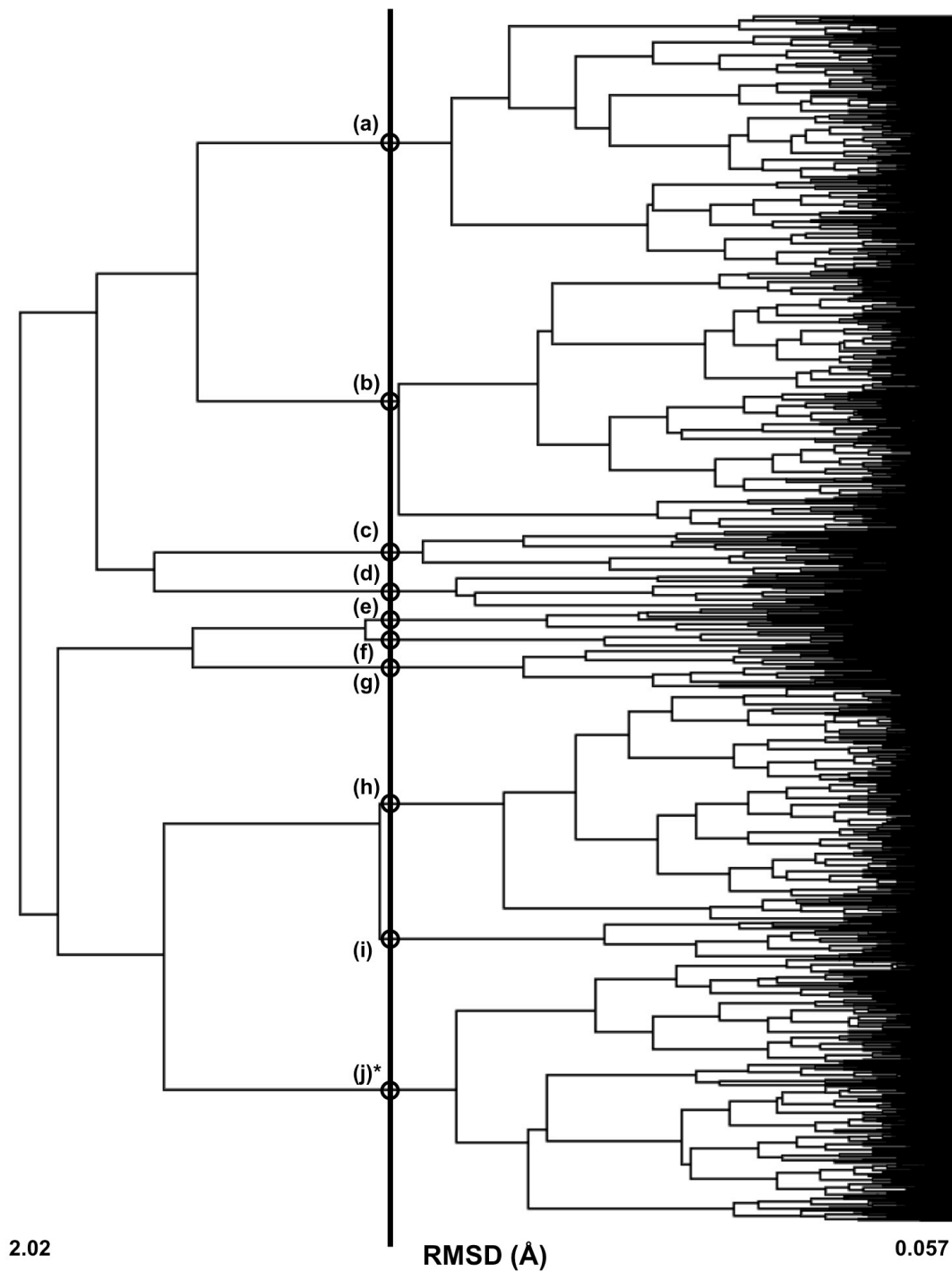


Figure B.24. Clustering analysis of 3,000 conformations of the ring protonated 2,4'-MDA. Clustering is based on root mean square distance of atoms of superimposed structures. The vertical black bar indicates the RMSD cutoff (1.25 Å) used to select the conformations (circled) for further analysis. The asterisk represents the structures shown in the paper.

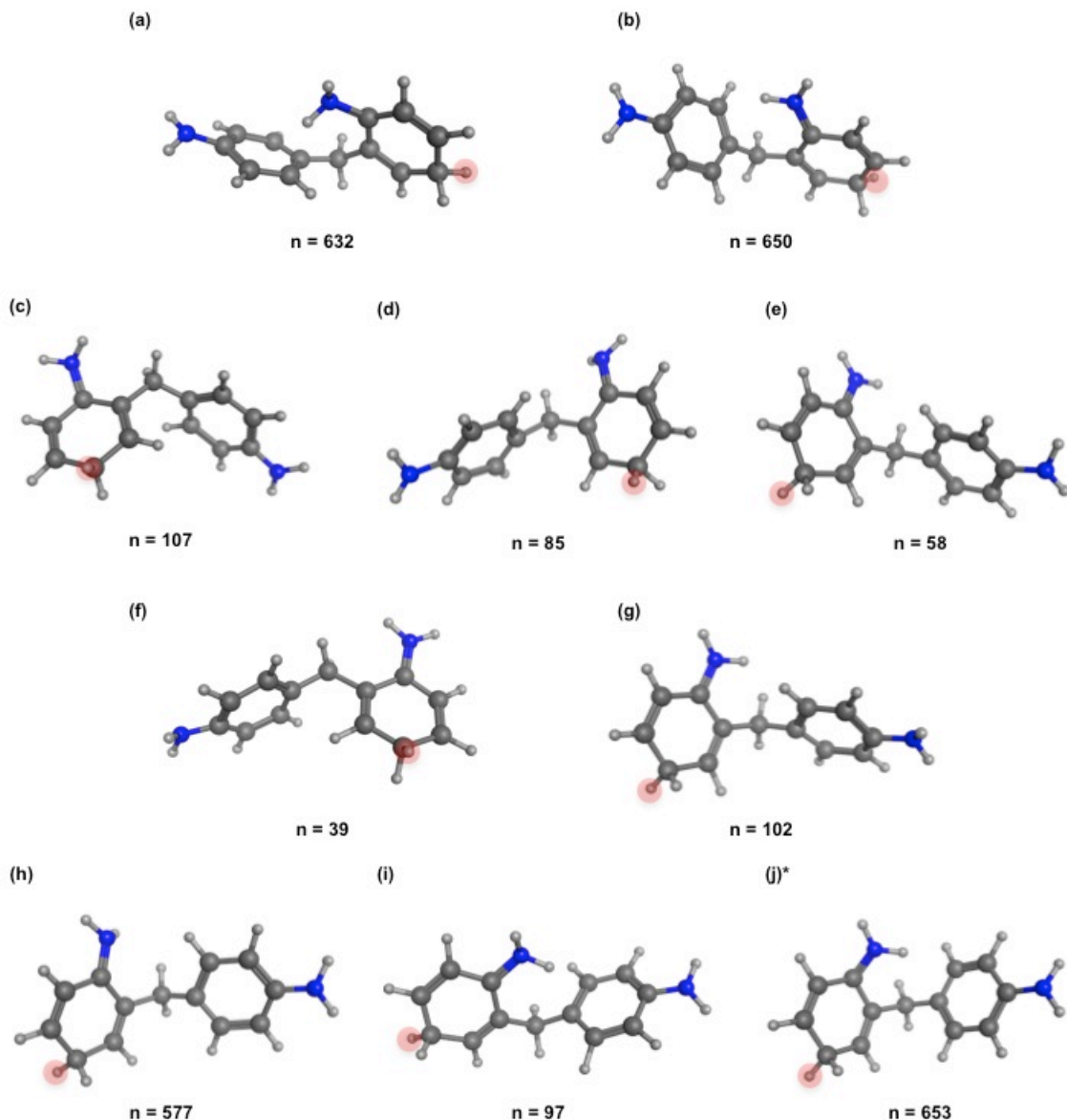


Figure B.25. Representative conformations of the ring protonated 2,4'-MDA generated from an elevated temperate molecular dynamic protocol. Carbon atoms are shown in dark grey, hydrogen in light grey, and nitrogen in blue. The asterisk represents the structures shown in the paper. The number of conformations each of these represents from clustering is shown below the conformation.

B.2. Supplemental Materials for 3-Ring and 4-Ring MDA Isomers

NMR Spectroscopy of Purified MDA Isomers

NMR experiments were acquired using a 14.0 T Bruker magnet equipped with a Bruker AV-III console operating at 600.13 MHz. All spectra were acquired in 5mm NMR tubes using a Bruker 5 mm TCI cryogenically cooled NMR probe. Chemical shifts were referenced internally to DMSO (2.49 ppm) which also served as the ^2H lock solvents. For 1D ^1H NMR, typical experimental conditions included 32K data points, 13 ppm sweep width, a recycle delay of 1.5 seconds and 64 scans.

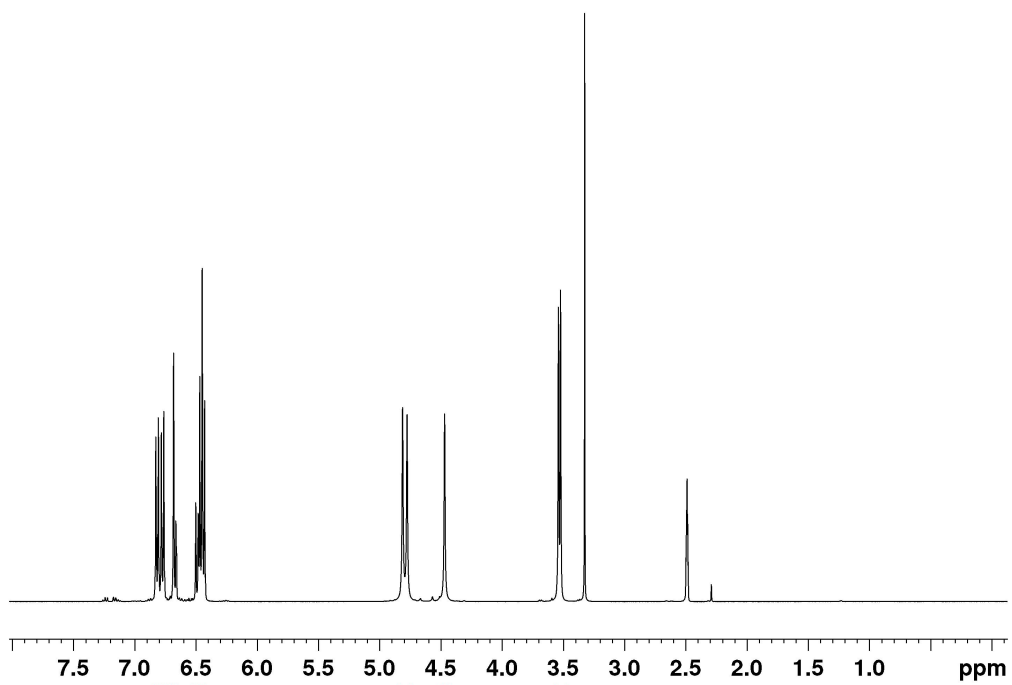


Figure B.26. ¹H NMR of 3-ring MDA

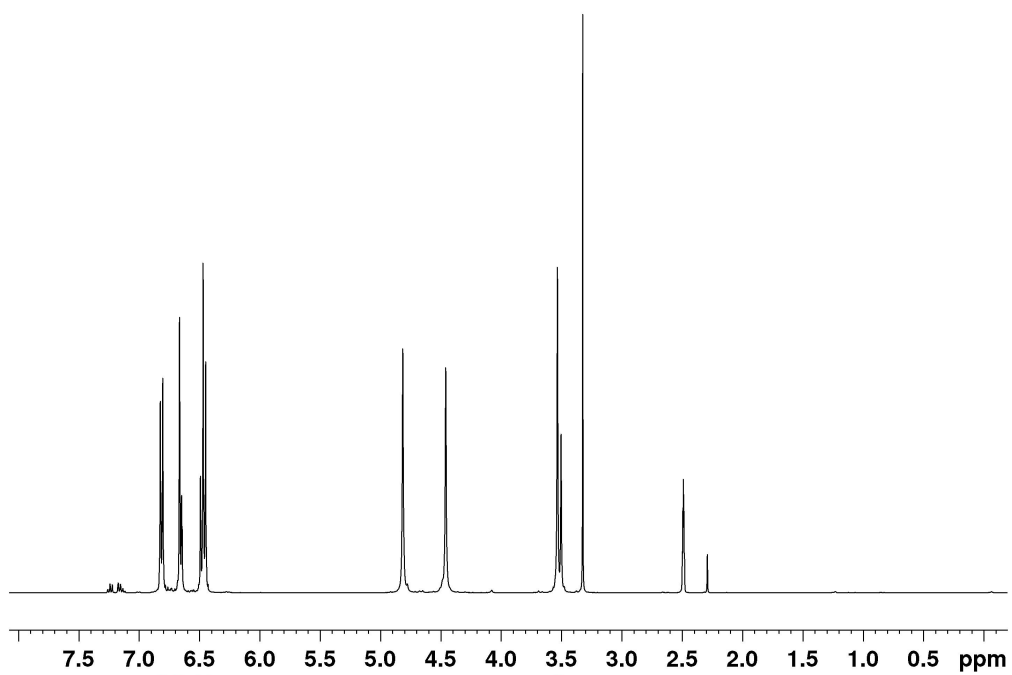


Figure B.27. 1H NMR of 4-ring MDA

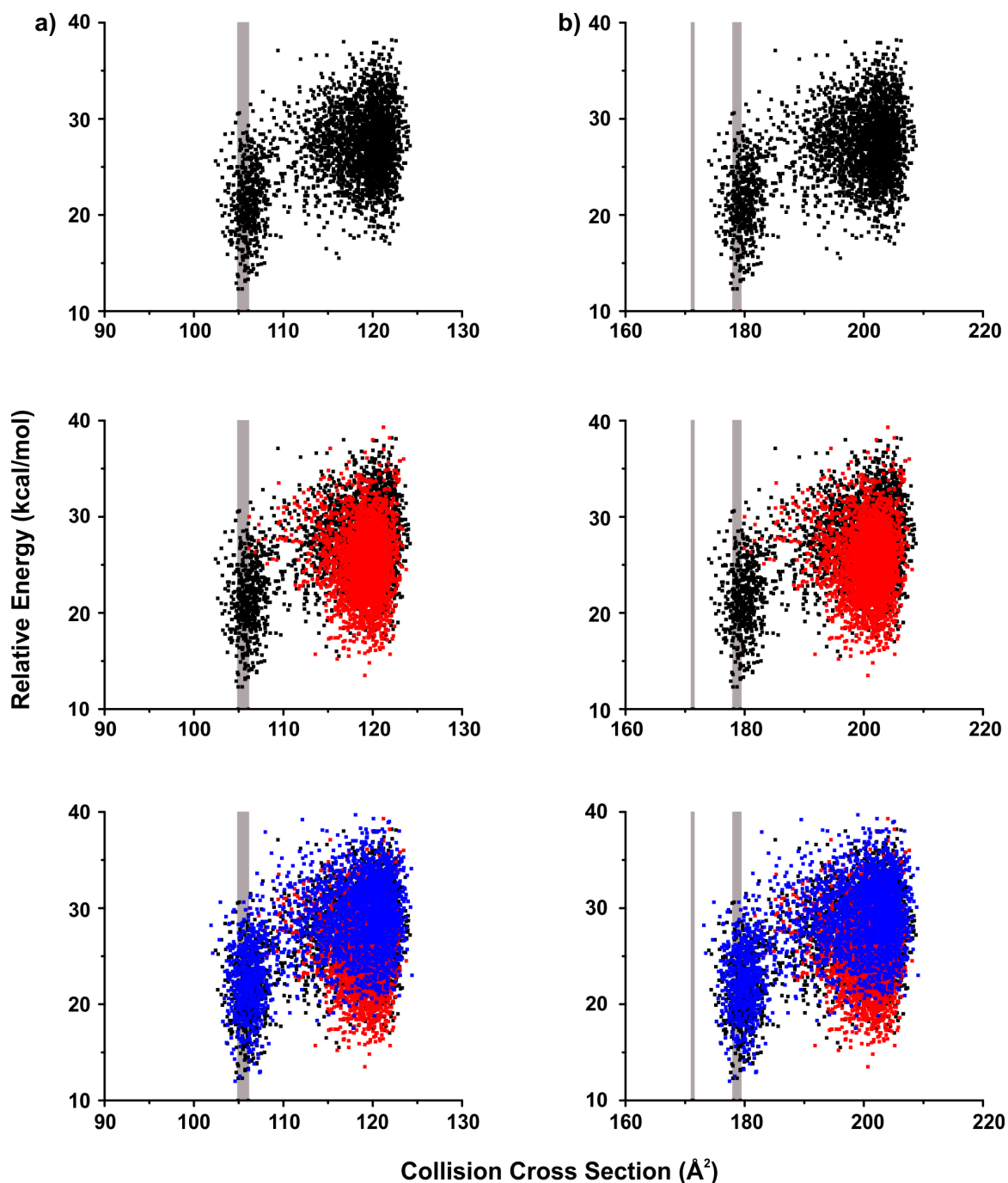


Figure B.28. Overlaid conformational space plots for the different protonation sites of 3-ring MDA. Plots are ordered to represent protonation from left to right across 3-ring MDA. Conformations from protonation on the first amine are shown in black, on the amine on the second amine in red and on the amine on the third ring in blue. These plots are zoomed in to show alignment with experimental CCS values from both a) helium and b) nitrogen. Experimental CCS ranges are indicated with the vertical gray bars. The vertical bars that align with the data are from the uniform field MS whereas the vertical bar in b) that falls to the left of the plot represents the traveling wave MS.

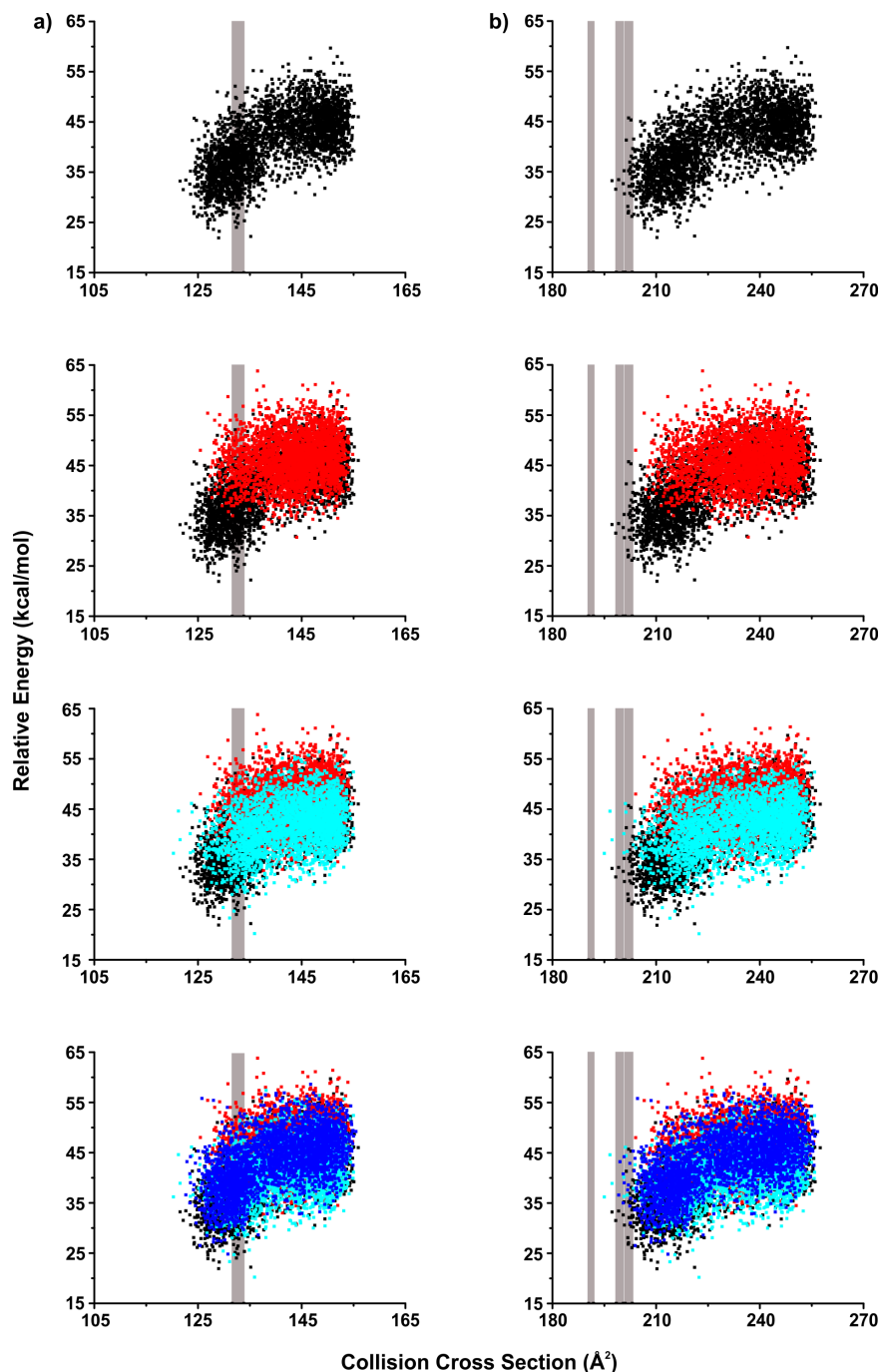


Figure B.29. Overlaid conformational space plots for the different protonation sites of 4-ring MDA. Plots are ordered to represent protonation from left to right across 4-ring MDA. Conformations from protonation on the amine on the first amine are shown in black, on the amine on the second ring in red and on the amine on the third ring in light blue, and on the amine on the fourth ring in blue. These plots are zoomed in to show alignment with experimental CCS values from both a) helium and b) nitrogen. Experimental CCS ranges are indicated with the vertical gray bars. The vertical bars that align with the data are from the uniform field MS whereas the vertical bar in b) that falls to the left of the plot represents the traveling wave MS.

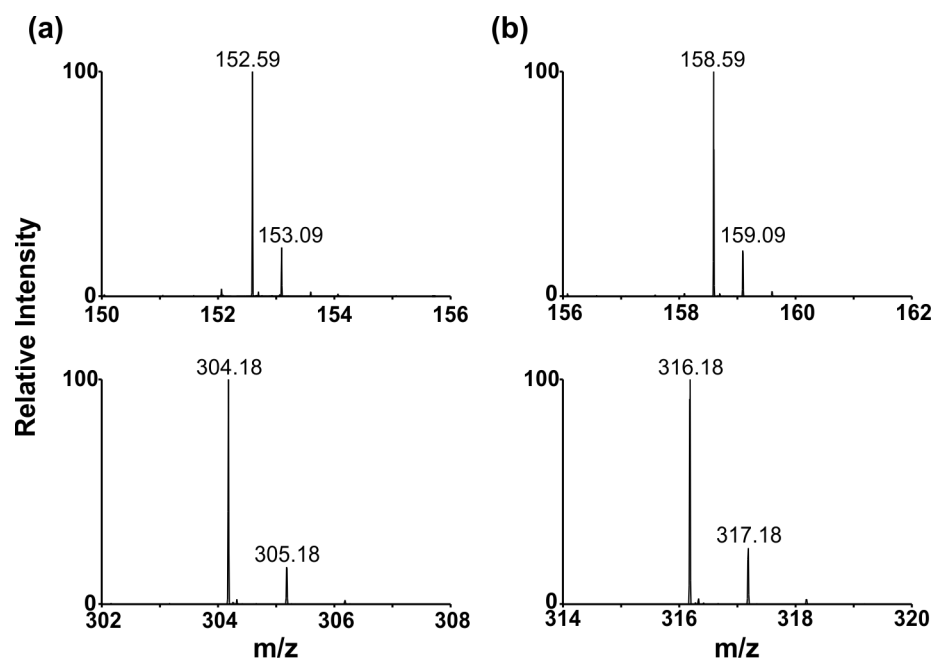


Figure B.30. Mass spectra of the doubly charged peaks and their respective singly charged peaks for a) the 3-ring MDA and b) the 4-ring MDA.

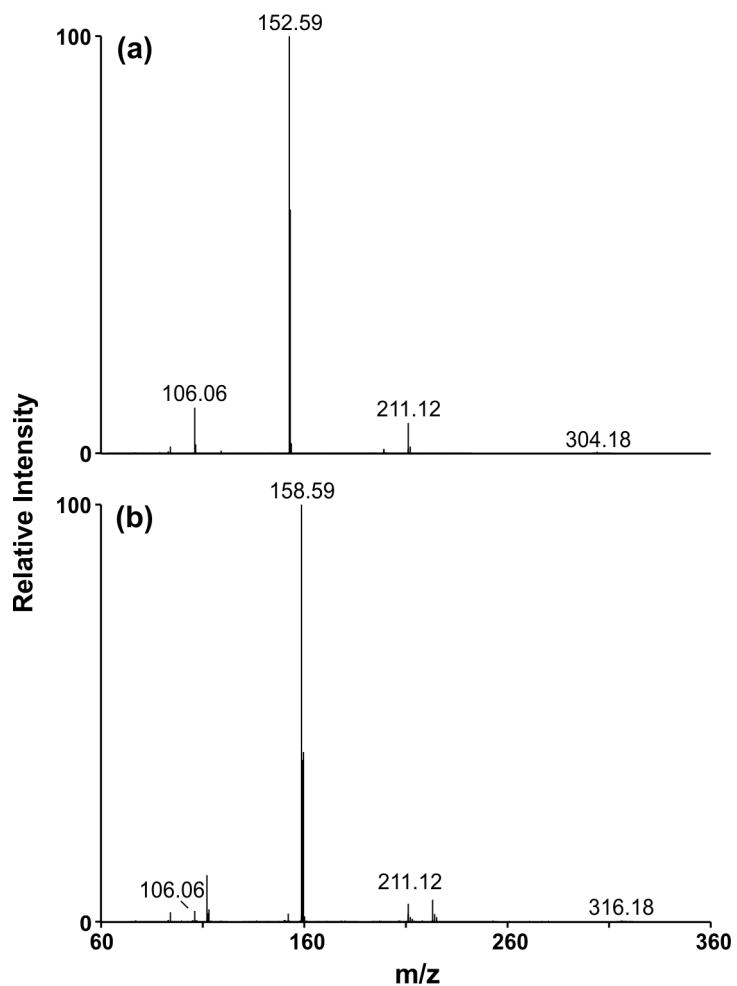


Figure B.31. Tandem mass spectra of the m/z 152.59 and m/z 158.59 doubly charged fragment ions showing the higher m/z fragments that result from fragmenting the doubly charged species.

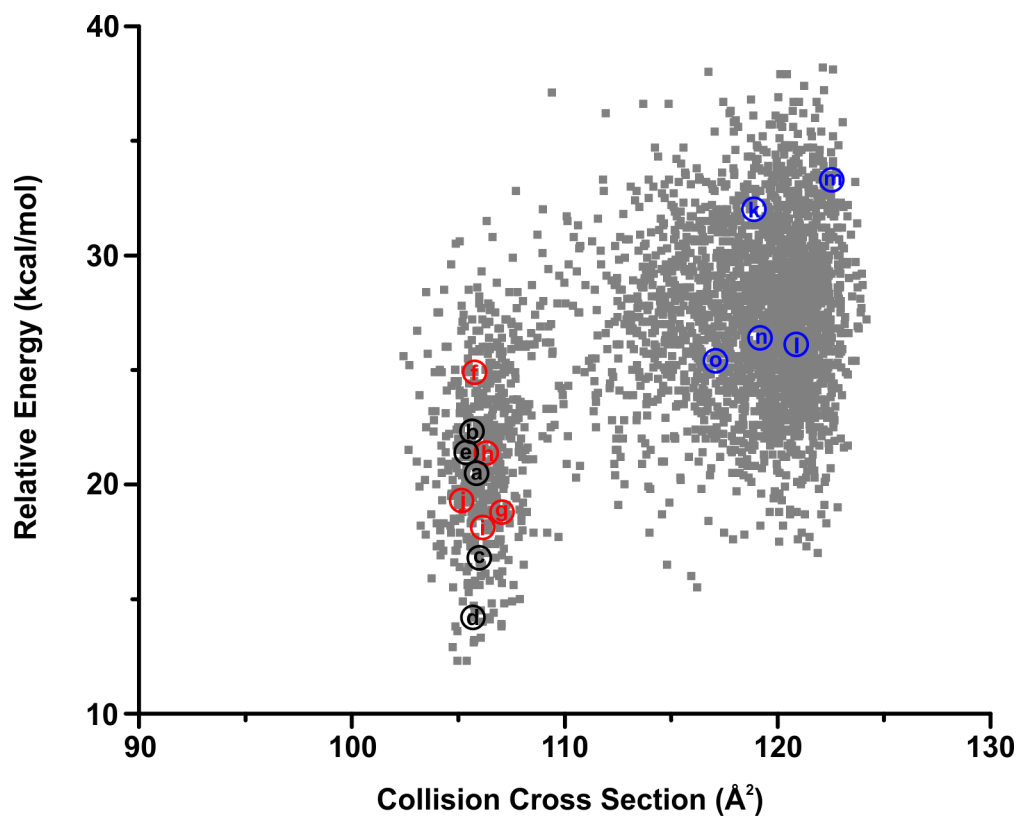


Figure B.32. Conformational space plot for the first ring amine protonated 3-ring MDA. The 3,000 generated conformations are represented in grey, the clustering representative conformations are labeled with letters that correspond to the structures in **Figures B.33-35**. The conformations labeled in black fall within the experimental range, the conformations labeled in red are representative of conformations from the left conformational cloud, and the conformations labeled in blue are representative of conformations from the right conformational cloud.

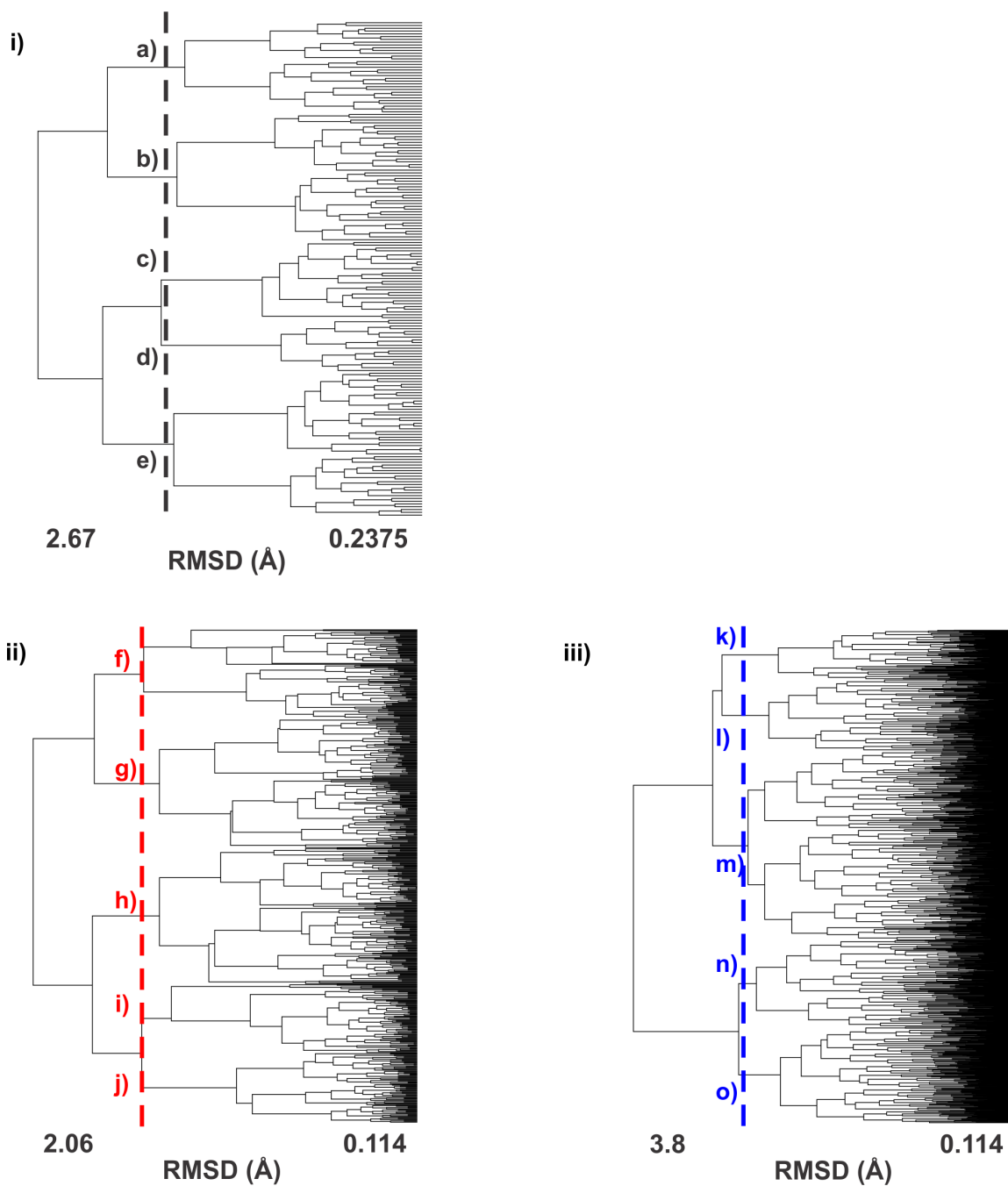


Figure B.33. Clustering analysis of 3,000 conformations of the first ring amine protonated 3-ring MDA. In i) the conformations that fall within the experimental CCS range are clustered, in ii) the conformations in the left conformational cloud are clustered, and in iii) the conformations in the right conformational cloud are clustered. Clustering is based on root mean square distance of atoms of superimposed structures. The vertical bars indicate the RMSD cutoff used to select the conformations for further analysis.

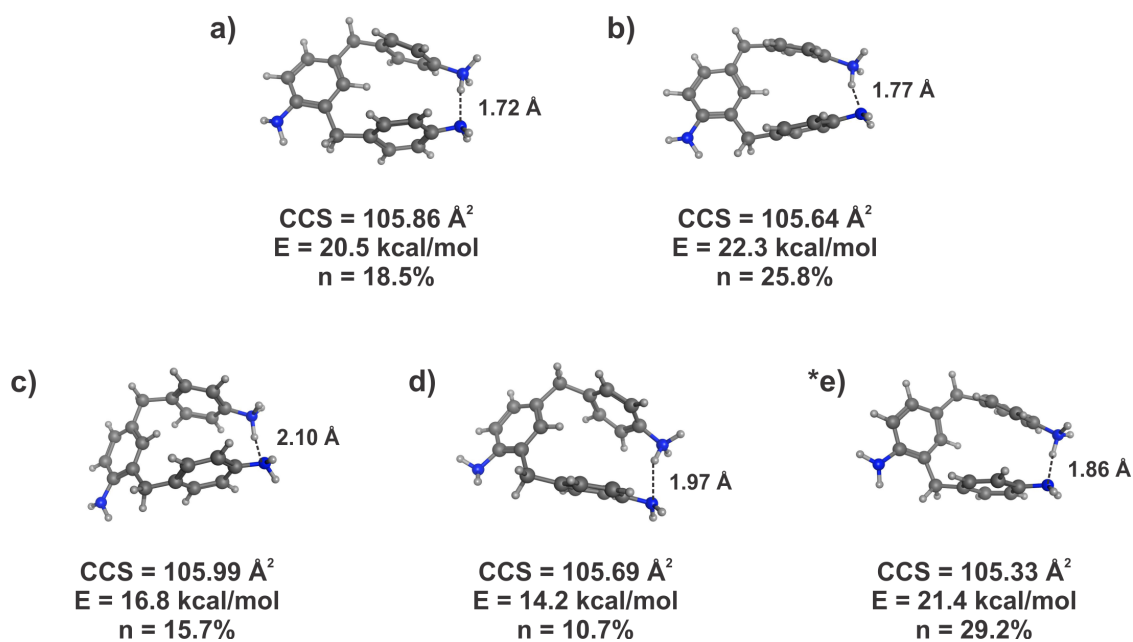


Figure B.34. Representative conformations from clustering analysis of the experimental range region of the first ring amine protonated 3-ring MDA generated from the simulated annealing calculation. Carbon atoms are shown in dark grey, hydrogen in light grey, and nitrogen in blue. Distances are labeled to show the proximity of the additional proton to other atoms in the molecule. The asterisk represents the structure shown in the manuscript. The theoretical CCS, relative energy, and percentage of conformations each of these represents from clustering are provided below each conformer.

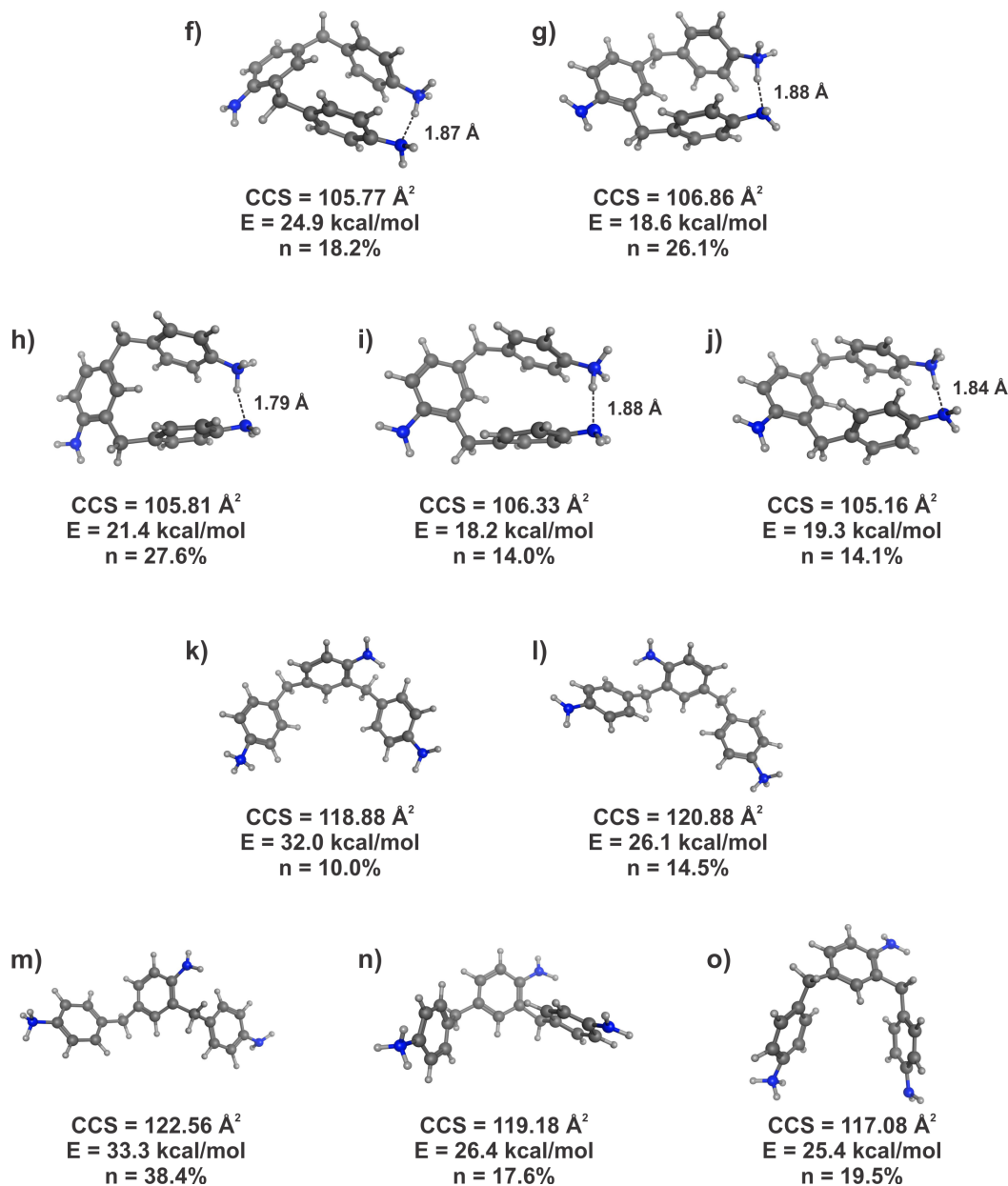


Figure B.35. Representative conformations from clustering analysis of the two conformational space clouds (left cloud (f-j) and right cloud (k-o)) of the first ring amine protonated 3-ring MDA generated from the simulated annealing calculation. Carbon atoms are shown in dark grey, hydrogen in light grey, and nitrogen in blue. Distances are labeled to show the proximity of the additional proton to other atoms in the molecule. The theoretical CCS, relative energy, and percentage of conformations each of these represents from clustering are provided below each conformer.

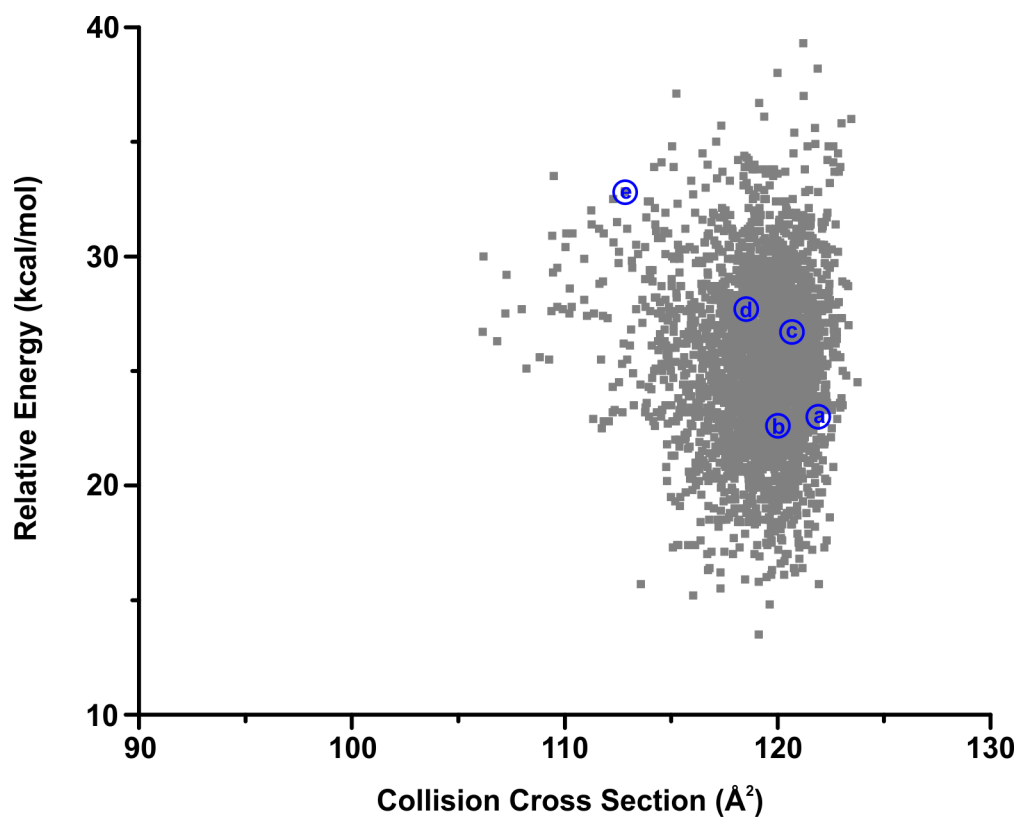


Figure B.36. Conformational space plot for the second ring amine protonated 3-ring MDA. The 3,000 generated conformations are represented in grey, the clustering representative conformations are labeled with letters that correspond to the structures in Figures B.37 and B.38.

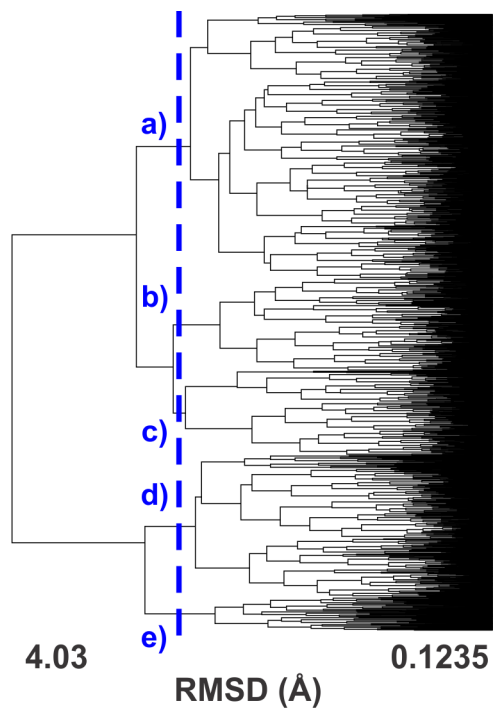


Figure B.37. Clustering analysis of 3,000 conformations of the second ring amine protonated 3-ring MDA. Clustering is based on root mean square distance of atoms of superimposed structures. The vertical bar indicates the RMSD cutoff used to select the conformations for further analysis.

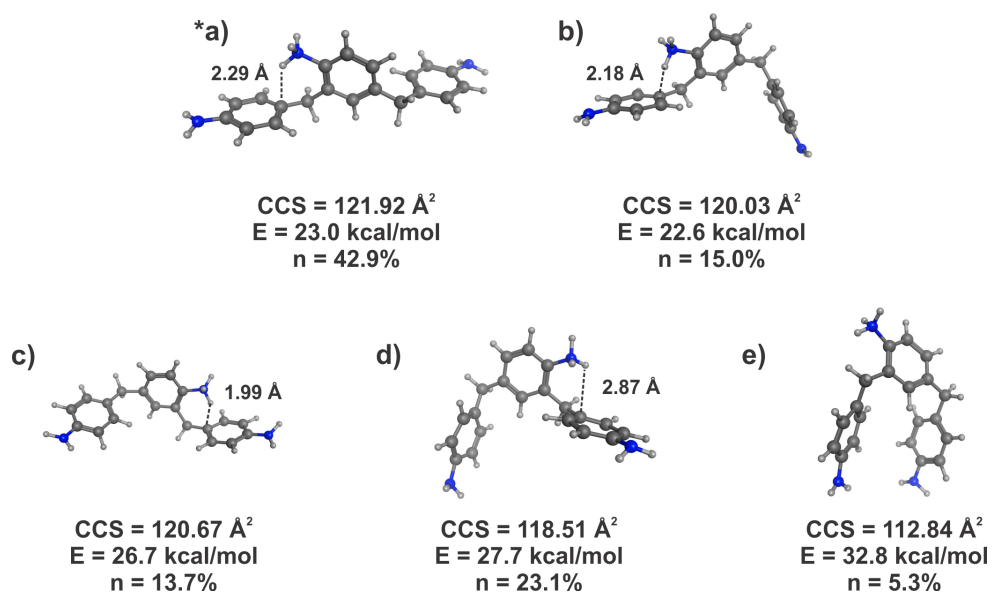


Figure B.38. Representative conformations from clustering analysis of the second ring amine protonated 3-ring MDA generated from an elevated temperature molecular dynamic protocol. Carbon atoms are shown in dark grey, hydrogen in light grey, and nitrogen in blue. The asterisk represents the structure shown in the paper. The number of conformations each of these represents from clustering is shown below the conformation.

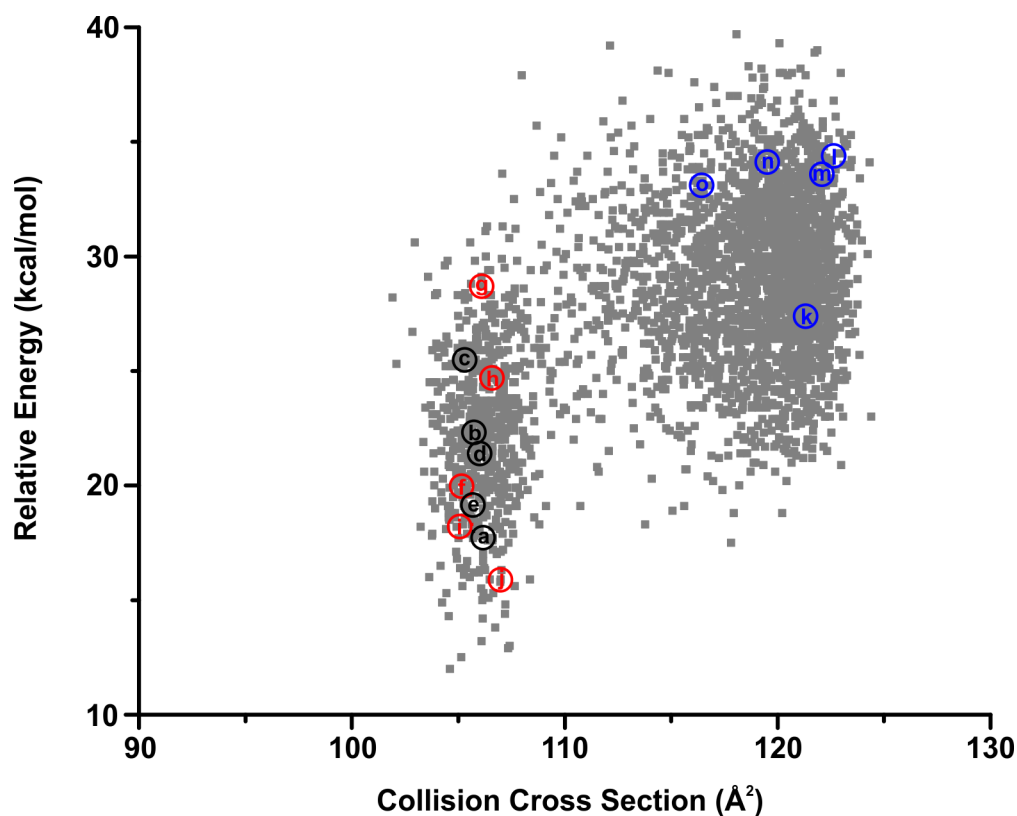


Figure B.39. Conformational space plot for the third ring amine protonated 3-ring MDA. The 3,000 generated conformations are represented in grey, the clustering representative conformations are labeled with letters that correspond to the structures in Figures **B.40-42**. The conformations labeled in black fall within the experimental range, the conformations labeled in red are representative of conformations from the left conformational cloud, and the conformations labeled in blue are representative of conformations from the right conformational cloud.

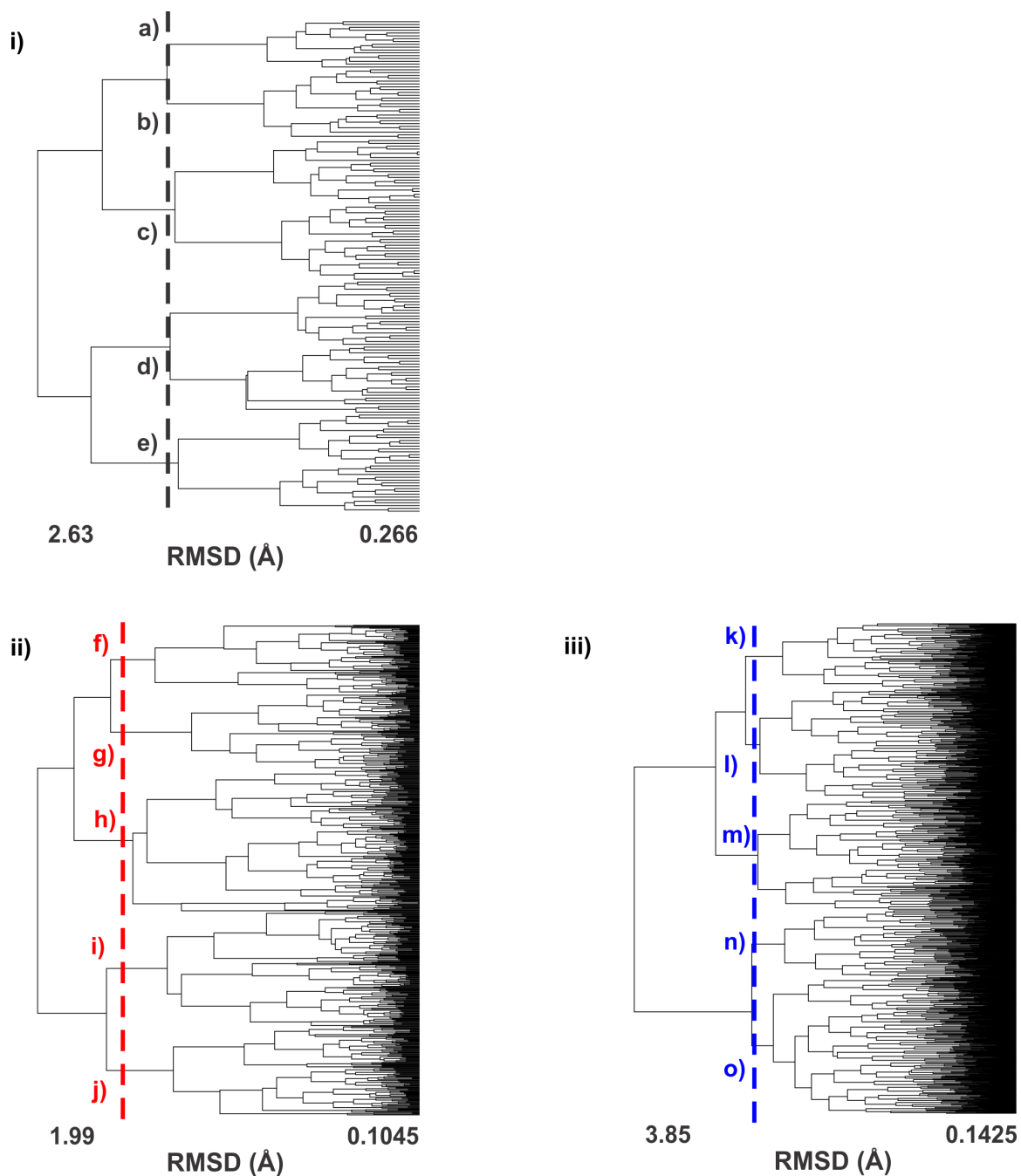


Figure B.40. Clustering analysis of 3,000 conformations of the third ring amine protonated 3-ring MDA. In i) the conformations that fall within the experimental CCS range are clustered, in ii) the conformations in the left conformational cloud are clustered, and in iii) the conformations in the right conformational cloud are clustered. Clustering is based on root mean square distance of atoms of superimposed structures. The vertical bars indicate the RMSD cutoff used to select the conformations for further analysis.

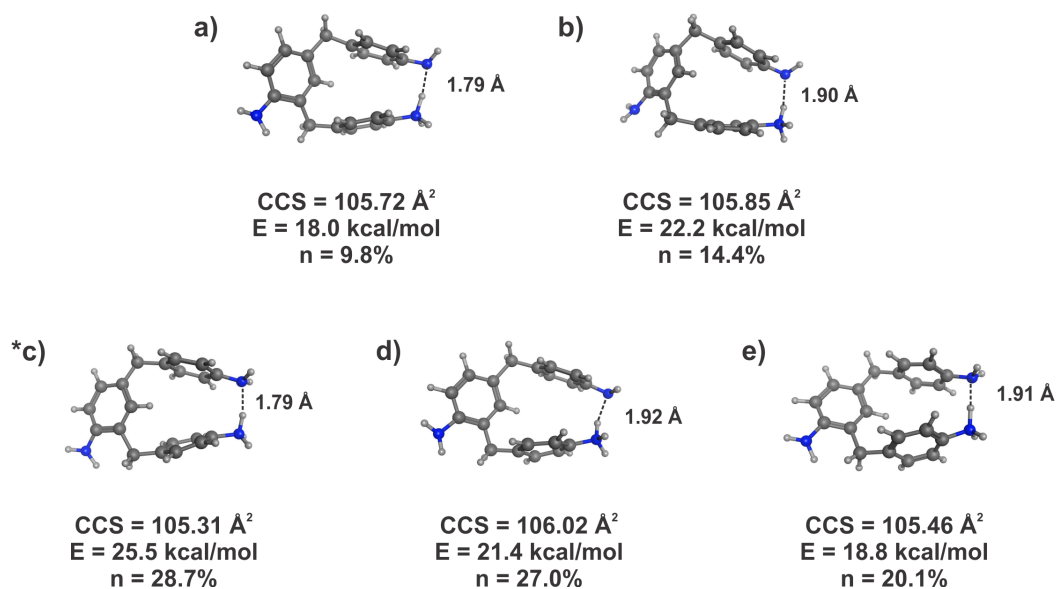


Figure B.41. Representative conformations from clustering analysis of the experimental range region of the third ring amine protonated 3-ring MDA generated from the simulated annealing calculation. Carbon atoms are shown in dark grey, hydrogen in light grey, and nitrogen in blue. Distances are labeled to show the proximity of the additional proton to other atoms in the molecule. The asterisk represents the structure shown in the manuscript. The theoretical CCS, relative energy, and percentage of conformations each of these represents from clustering are shown below the conformation

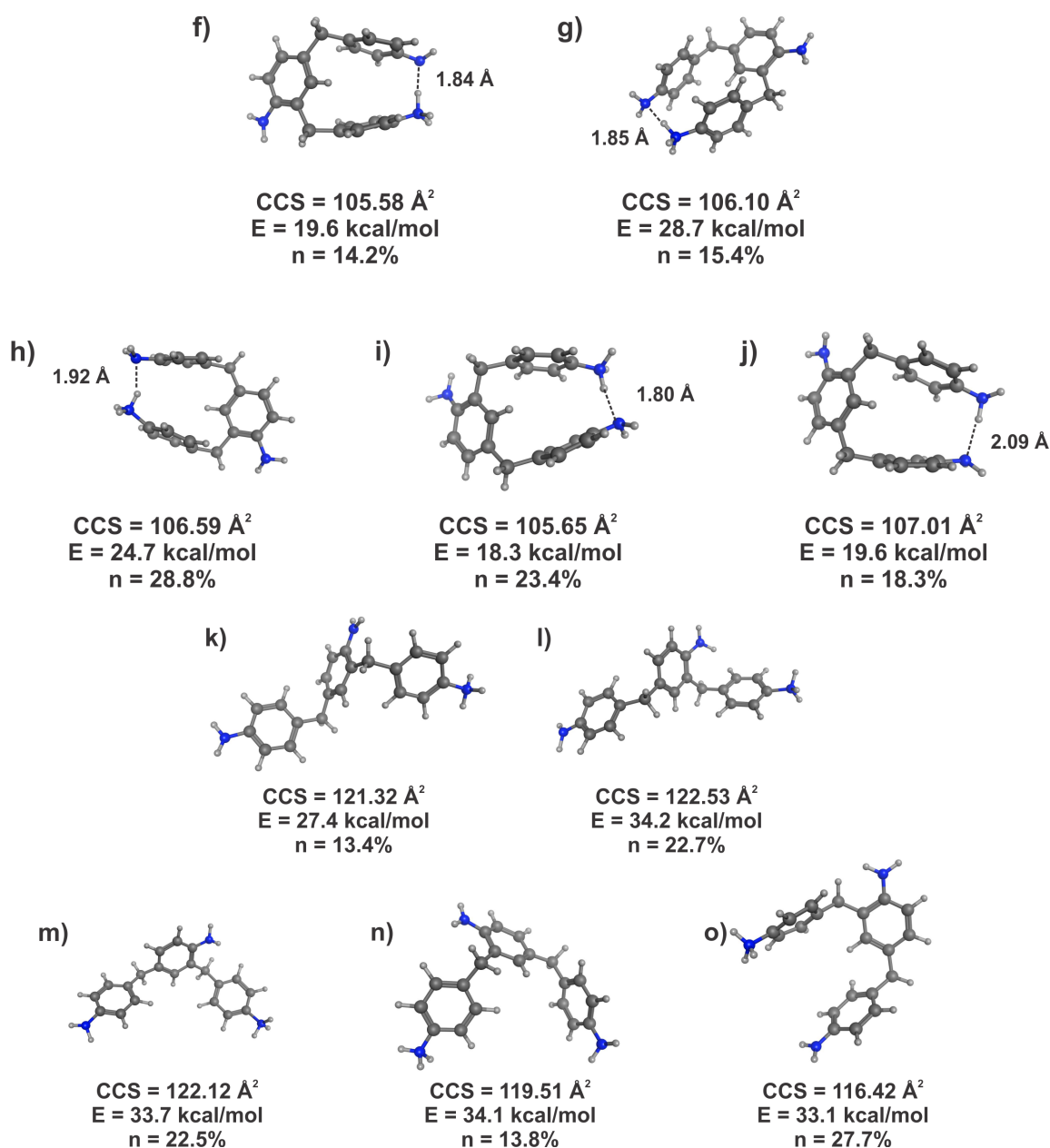


Figure B.42. Representative conformations from clustering analysis of the two conformational space clouds (left cloud (f-j) and right cloud (k-o)) of the third ring amine protonated 3-ring MDA generated from the simulated annealing calculation. Carbon atoms are shown in dark grey, hydrogen in light grey, and nitrogen in blue. Distances are labeled to show the proximity of the additional proton to other atoms in the molecule. The theoretical CCS, relative energy, and percentage of conformations each of these represents from clustering are shown below the conformation.

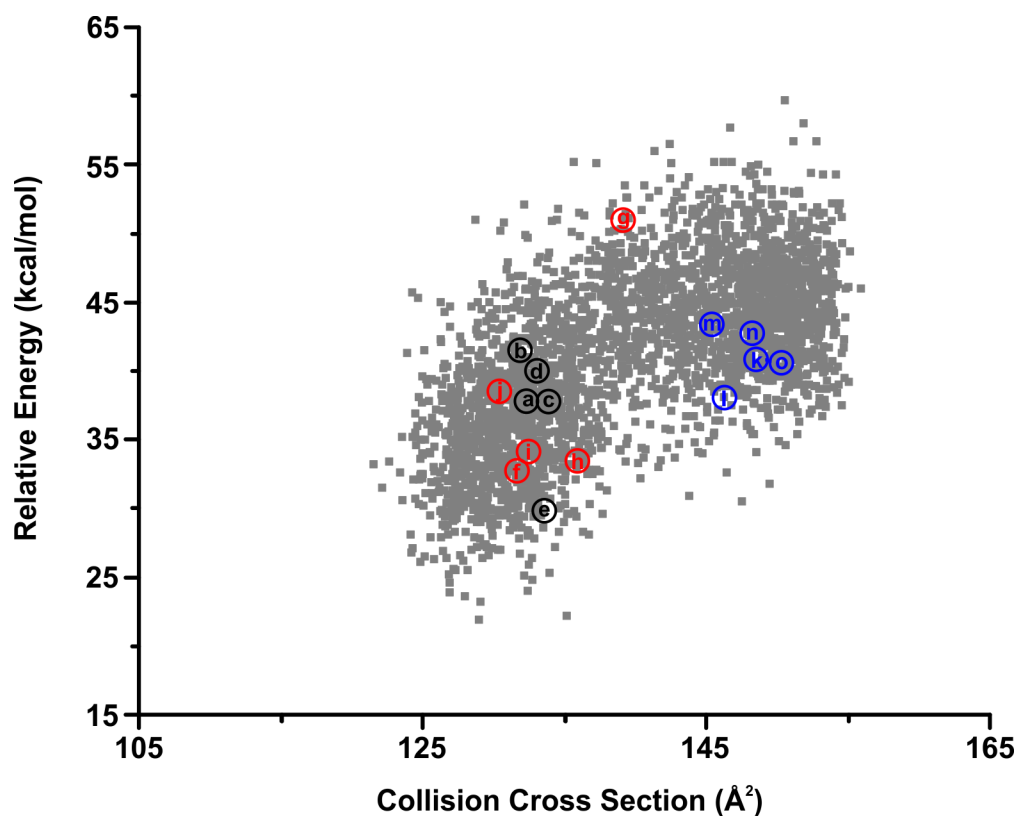


Figure B.43. Conformational space plot for the first ring amine protonated 4-ring MDA. The 3,000 generated conformations are represented in grey, the clustering representative conformations are labeled with letters that correspond to the structures in **Figures B.44-46**. The conformations labeled in black fall within the experimental range, the conformations labeled in red are representative of conformations from the left conformational cloud, and the conformations labeled in blue are representative of conformations from the right conformational cloud.

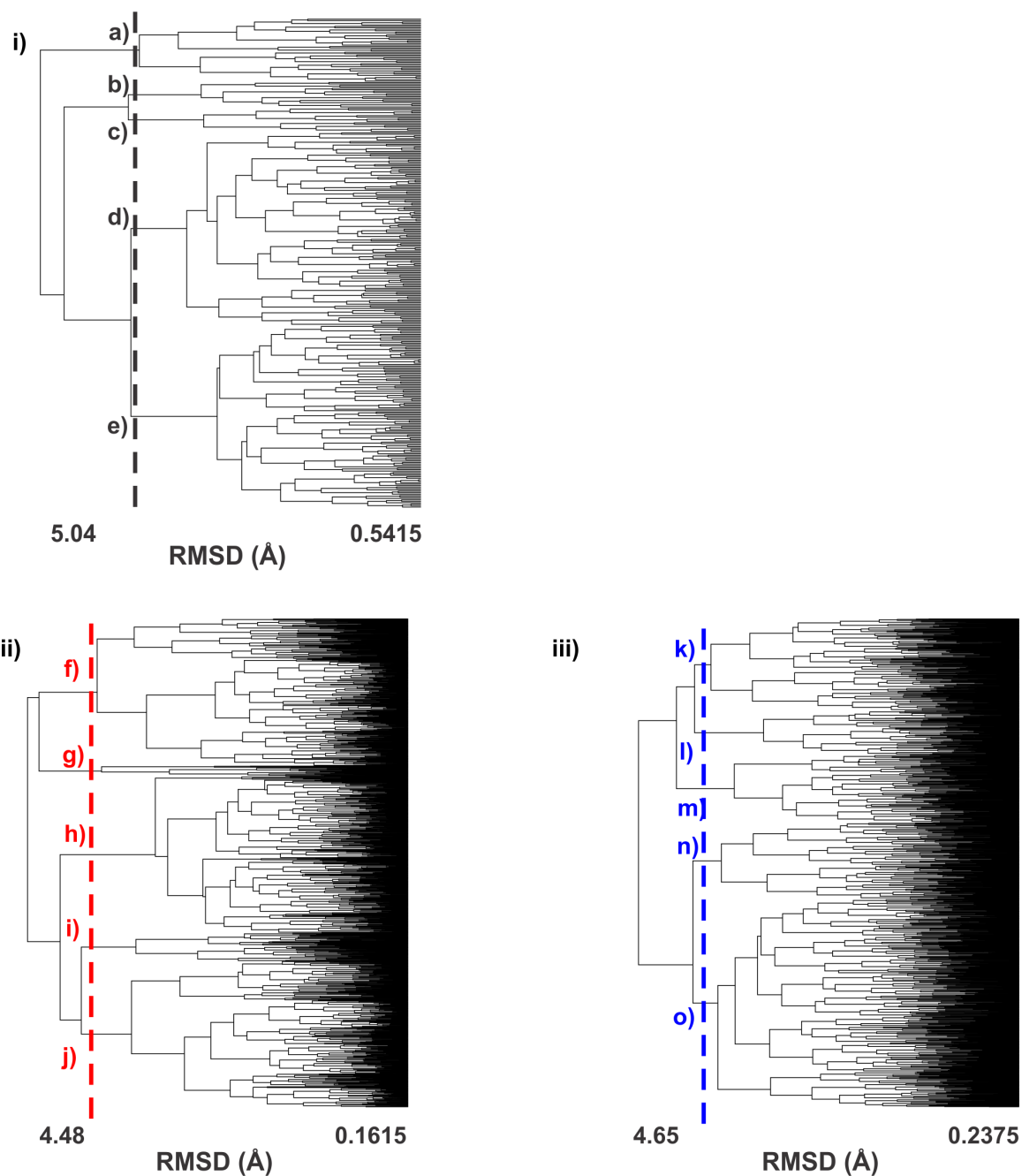


Figure B.44. Clustering analysis of 3,000 conformations of the first ring amine protonated 4-ring MDA. In i) the conformations that fall within the experimental CCS range are clustered, in ii) the conformations in the left conformational cloud are clustered, and in iii) the conformations in the right conformational cloud are clustered. Clustering is based on root mean square distance of atoms of superimposed structures. The vertical bars indicate the RMSD cutoff used to select the conformations for further analysis.

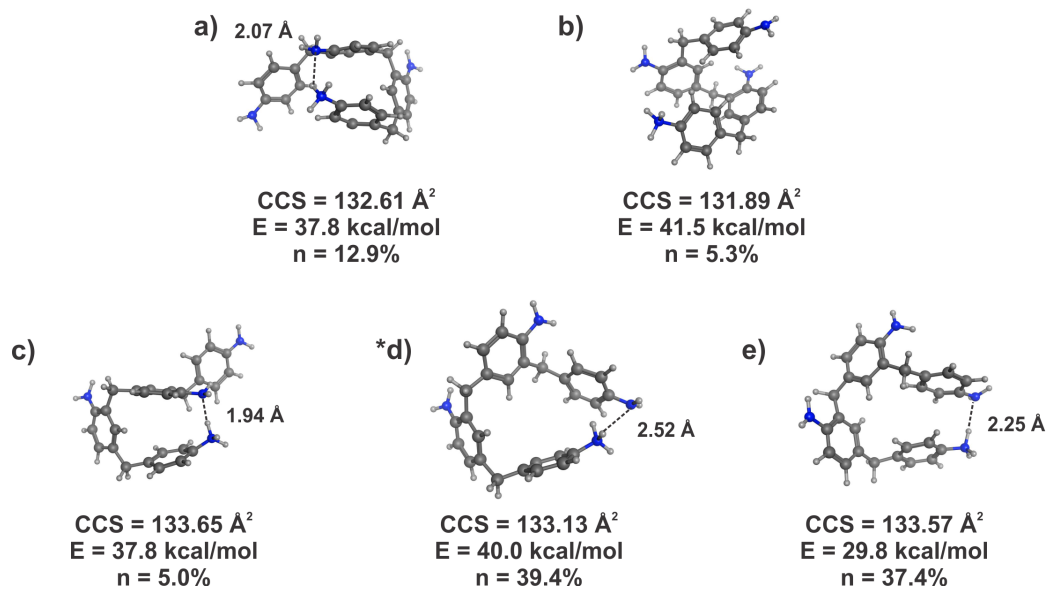


Figure B.45. Representative conformations from clustering analysis of the experimental range region of the first ring amine protonated 4-ring MDA generated from the simulated annealing calculation. Carbon atoms are shown in dark grey, hydrogen in light grey, and nitrogen in blue. Distances are labeled to show the proximity of the additional proton to other atoms in the molecule. The asterisk represents the structure shown in the manuscript. The theoretical CCS, relative energy, and percentage of conformations each of these represents from clustering are shown below the conformation.

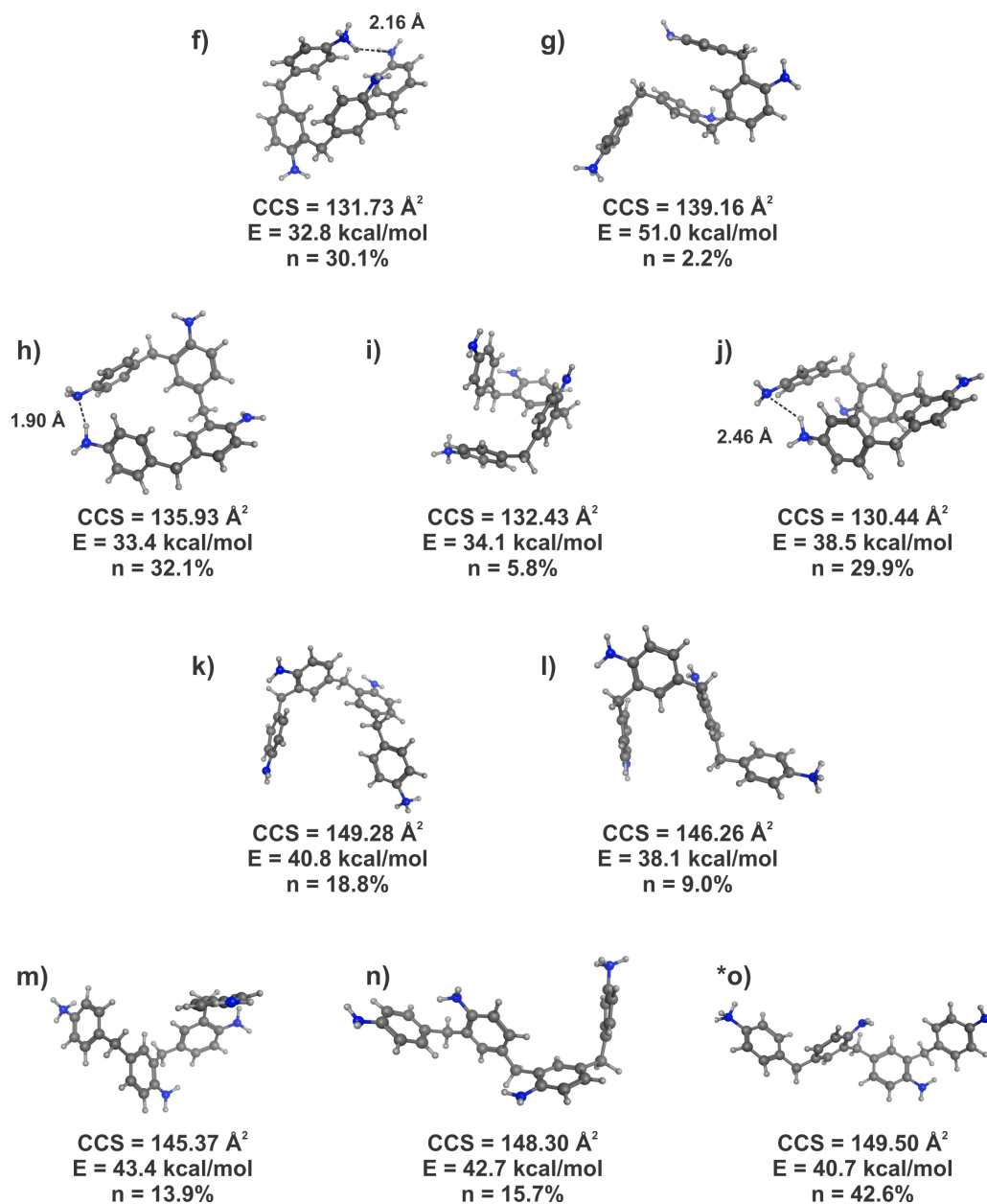


Figure B.46. Representative conformations from clustering analysis of the two conformational space clouds (left cloud (f-j) and right cloud (k-o)) of the first ring amine protonated 4-ring MDA generated from the simulated annealing calculation. Carbon atoms are shown in dark grey, hydrogen in light grey, and nitrogen in blue. Distances are labeled to show the proximity of the additional proton to other atoms in the molecule. The asterisk represents the structure shown in the manuscript. The theoretical CCS, relative energy, and percentage of conformations each of these represents from clustering are shown below the conformation.

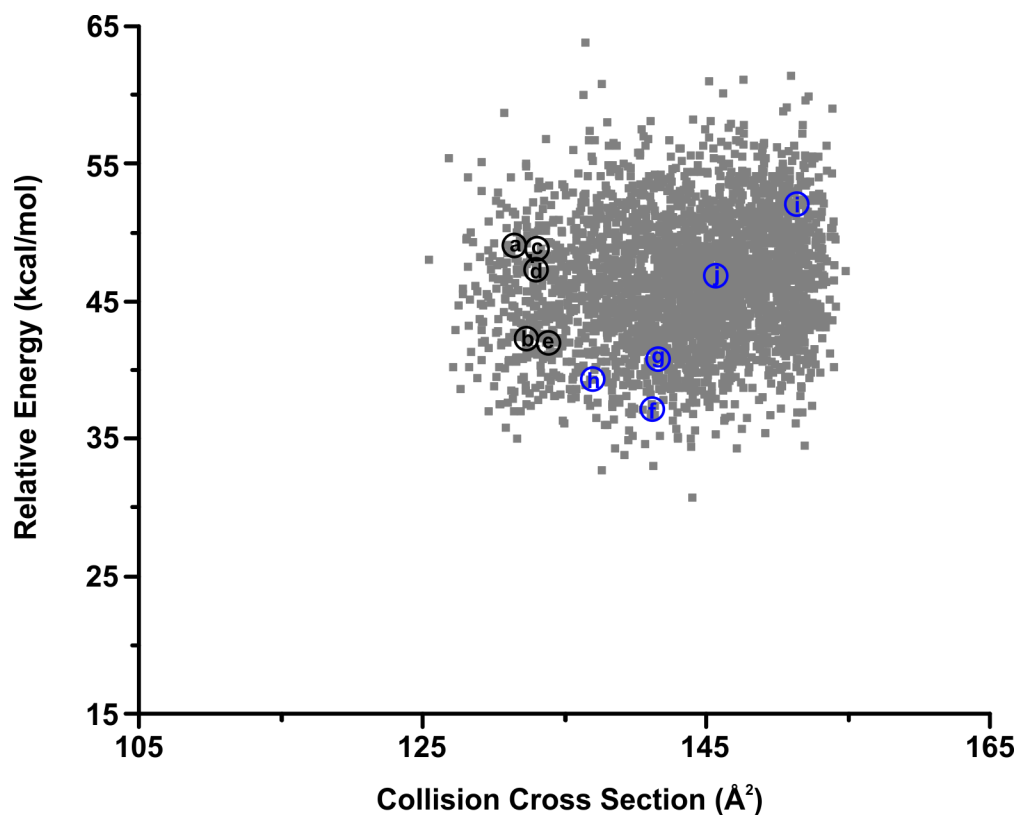


Figure B.47. Conformational space plot for the second ring amine protonated 4-ring MDA. The 3,000 generated conformations are represented in grey, the clustering representative conformations are labeled with letters that correspond to the structures in **Figures B.23,24**. The conformations labeled in black fall within the experimental range and the conformations labeled in blue are representative of conformations from the whole conformational cloud.

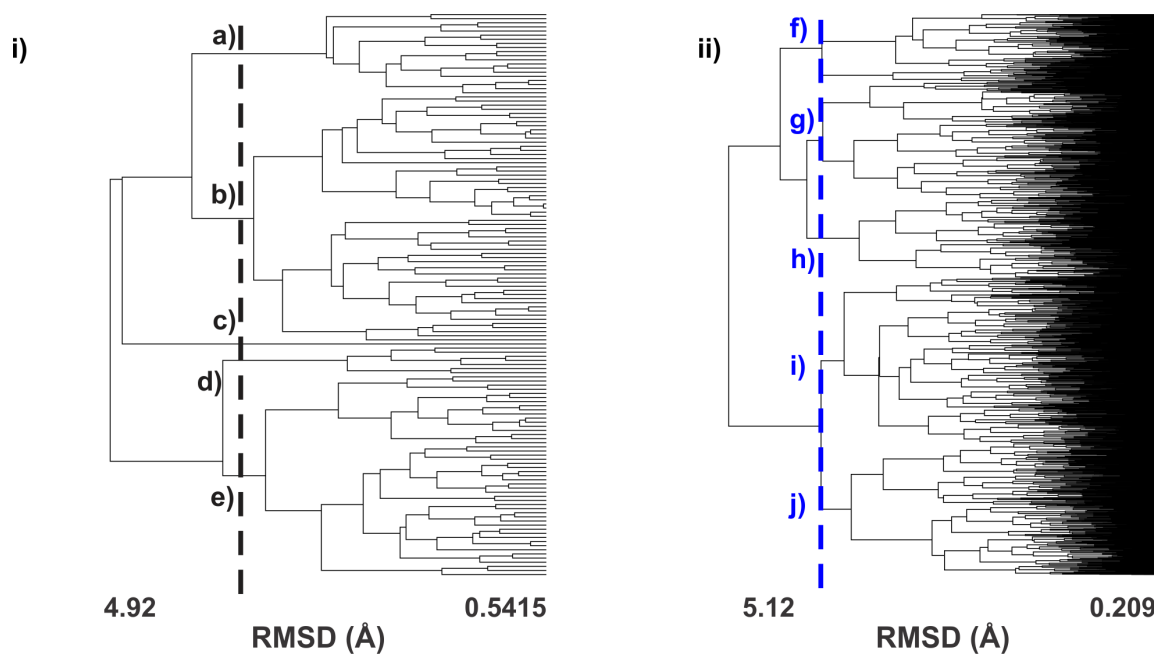


Figure B.48. Clustering analysis of 3,000 conformations of the second ring amine protonated 4-ring MDA. In i) the conformations that fall within the experimental CCS range are clustered and in ii) all 3,000 of the conformations are clustered. Clustering is based on root mean square distance of atoms of superimposed structures. The vertical bar indicates the RMSD cutoff used to select the conformations for further analysis. The asterisk represents the structures shown in the paper.

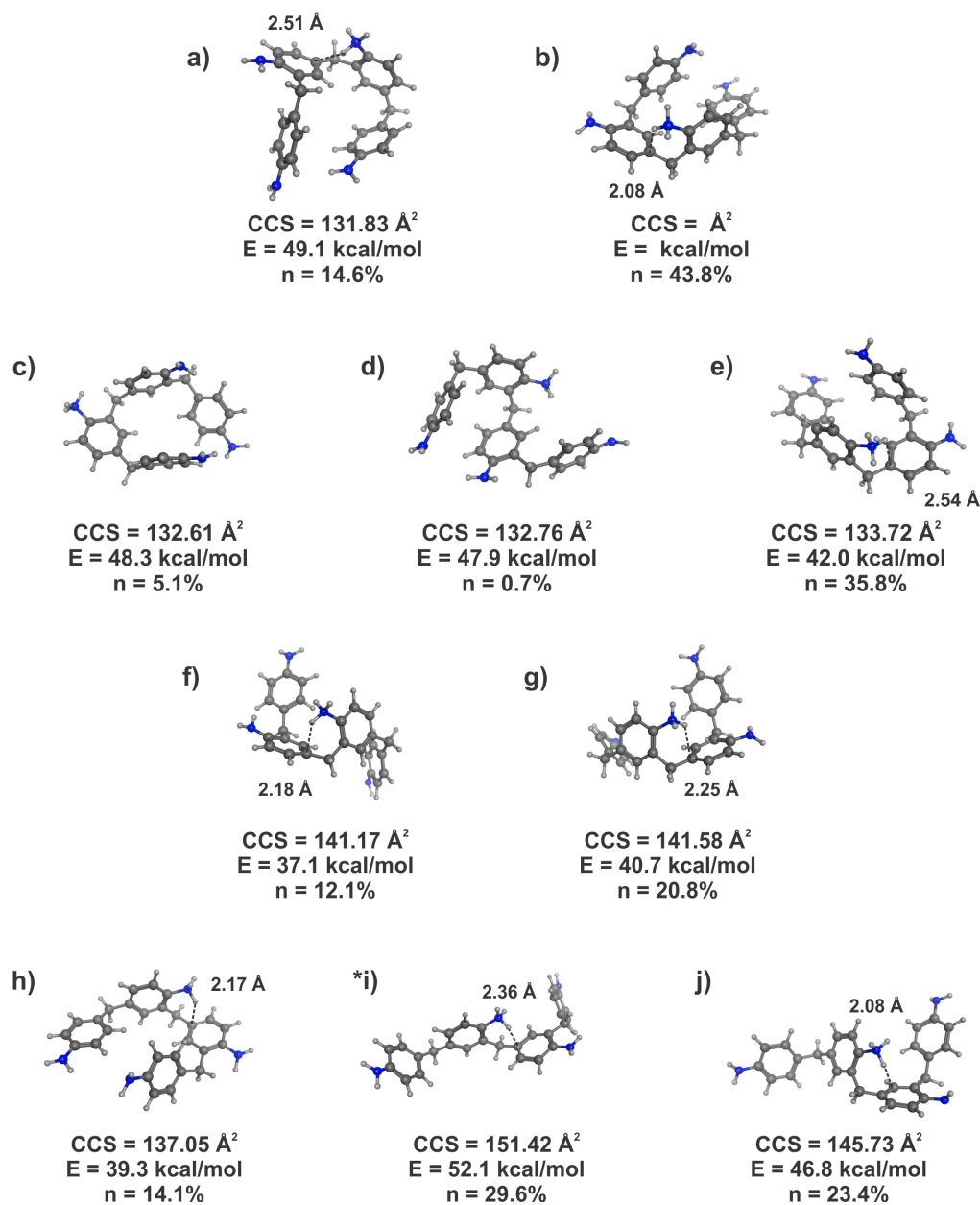


Figure B.49. Representative conformations from clustering analysis of the experimental range (a-e) and the whole conformational space cloud (f-j) of the second ring amine protonated 4-ring MDA generated from the simulated annealing calculation. Carbon atoms are shown in dark grey, hydrogen in light grey, and nitrogen in blue. Distances are labeled to show the proximity of the additional proton to other atoms in the molecule. The asterisk represents the structure shown in the manuscript. The theoretical CCS, relative energy, and percentage of conformations each of these represents from clustering are shown below the conformation.

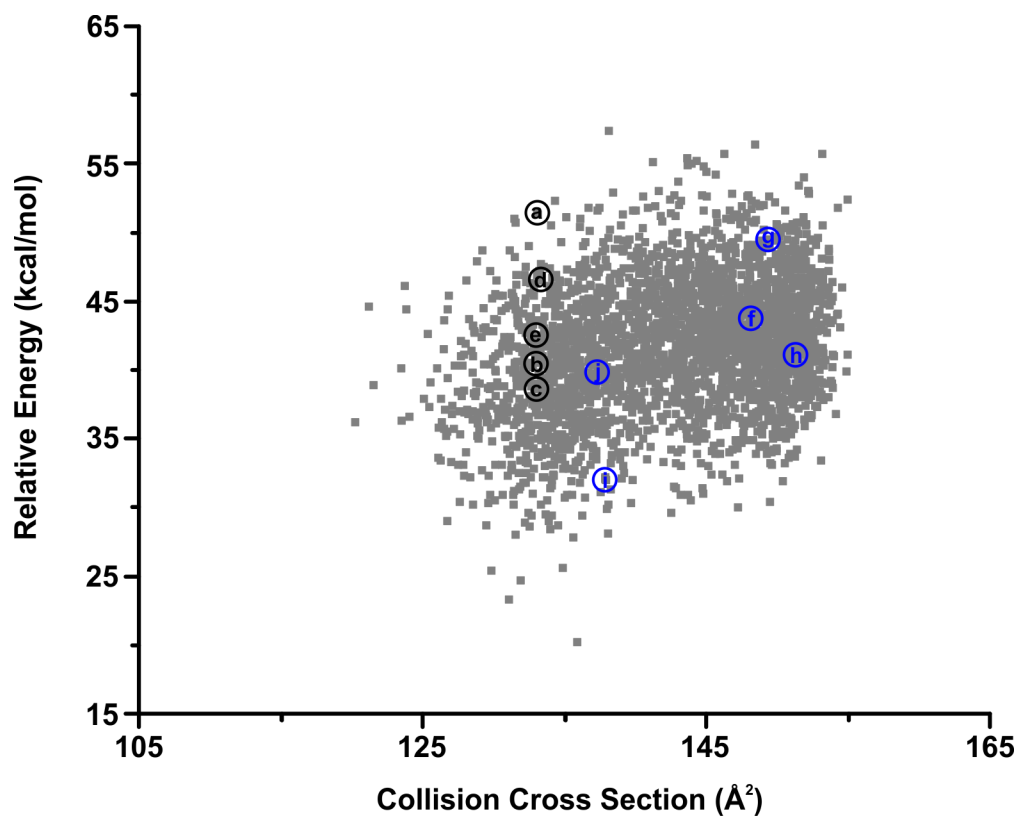


Figure B.50. Conformational space plot for the third ring amine protonated 4-ring MDA. The 3,000 generated conformations are represented in grey, the clustering representative conformation are labeled with letters that correspond to the structures in **Figures B.51 and B.52**. The conformations labeled in black fall within the experimental range and the conformations labeled in blue are representative of conformations from the whole conformational cloud.

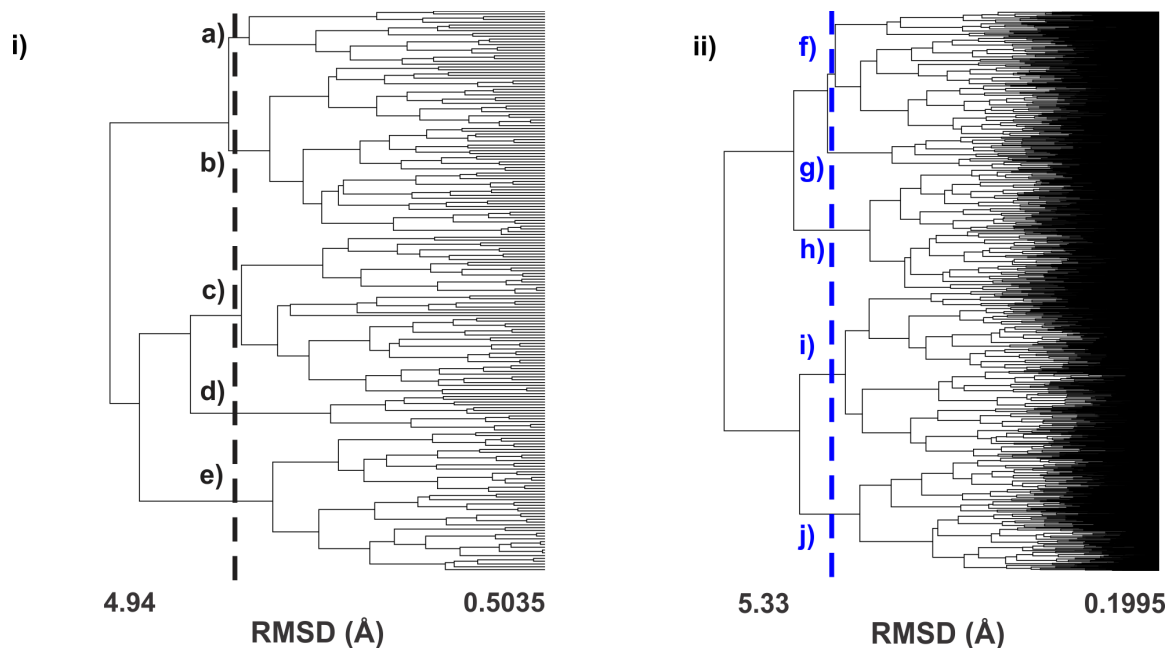


Figure B.51. Clustering analysis of 3,000 conformations of the third ring amine protonated 4-ring MDA. In i) the conformations that fall within the experimental CCS range are clustered and in ii) all 3,000 of the conformations are clustered. Clustering is based on root mean square distance of atoms of superimposed structures. The vertical bar indicates the RMSD cutoff (Å) used to select the conformations for further analysis. The asterisk represents the structures shown in the paper.

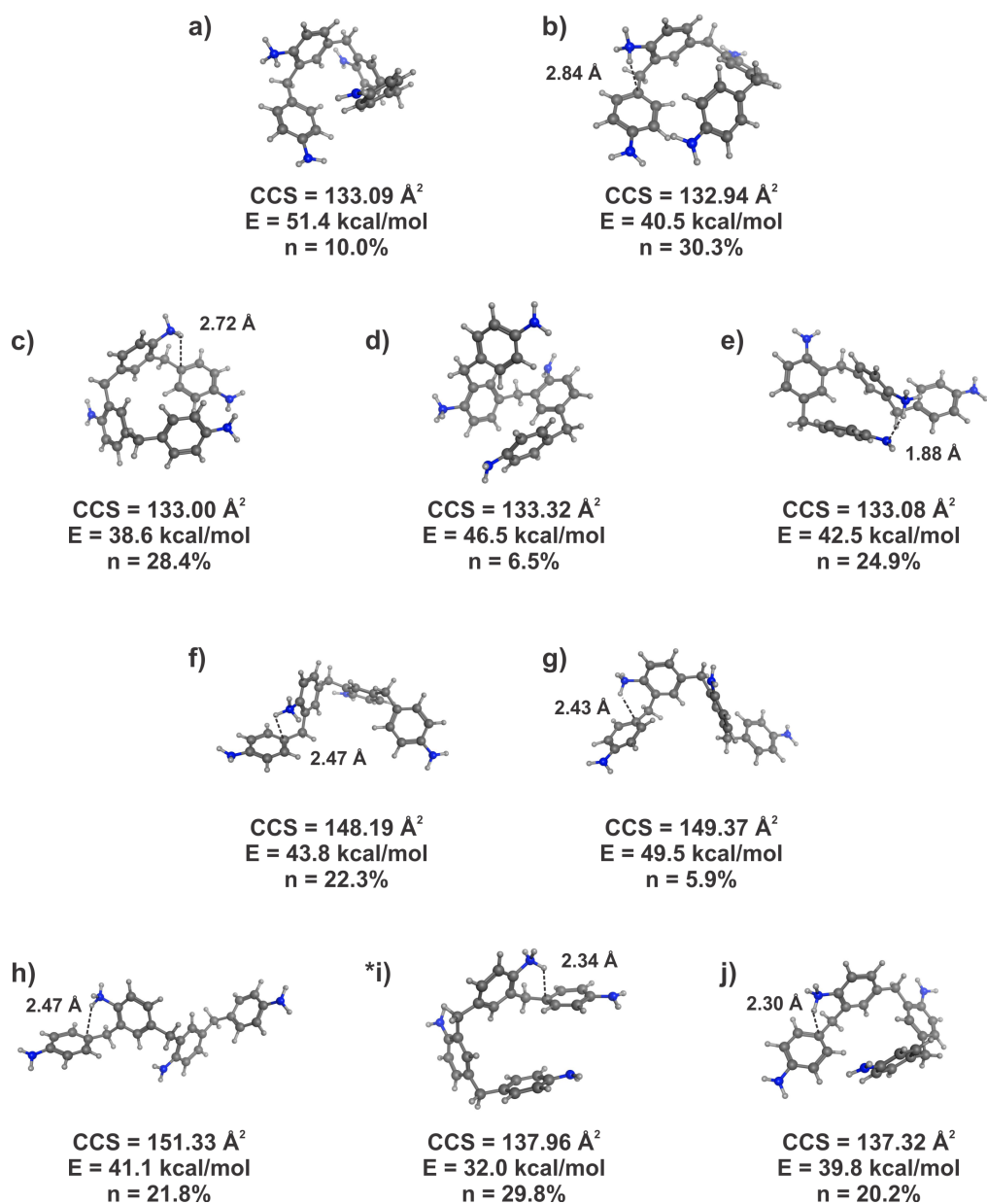


Figure B.52. Representative conformations from clustering analysis of the experimental range (a-e) and the whole conformational space cloud (f-j) of the third ring amine protonated 4-ring MDA generated from the simulated annealing calculation. Carbon atoms are shown in dark grey, hydrogen in light grey, and nitrogen in blue. Distances are labeled to show the proximity of the additional proton to other atoms in the molecule. The asterisk represents the structure shown in the manuscript. The theoretical CCS, relative energy, and percentage of conformations each of these represents from clustering are shown below the conformation.

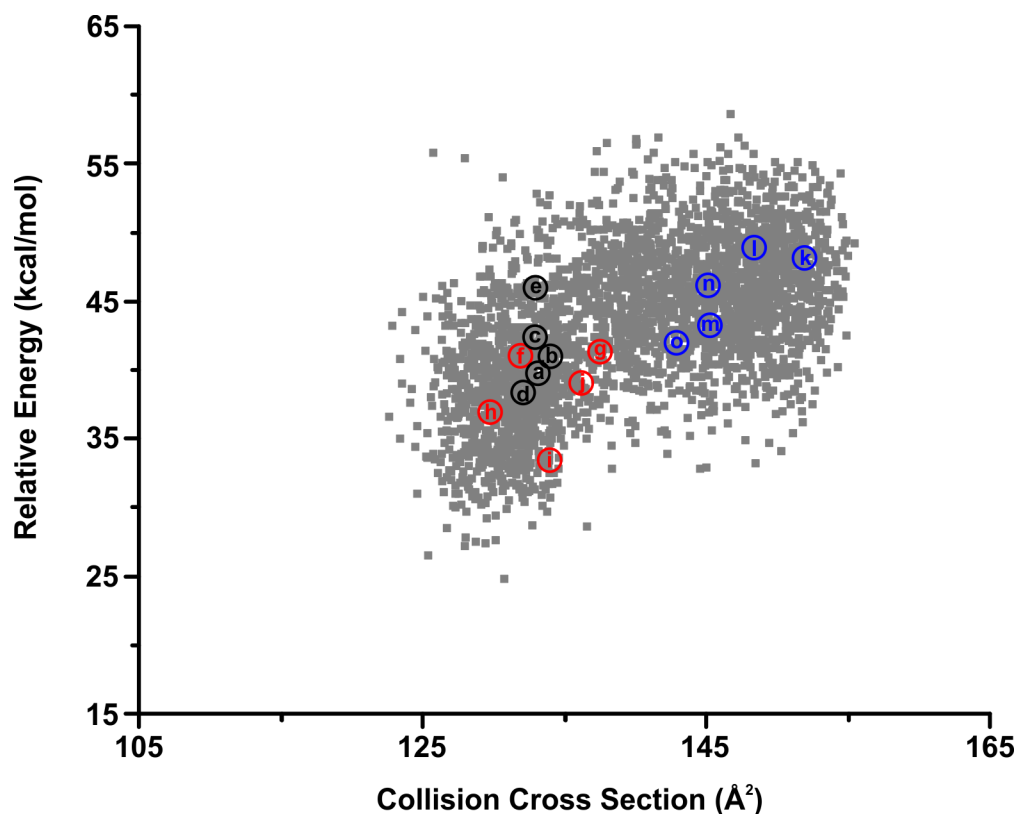


Figure B.53. Conformational space plot for the fourth ring amine protonated 4-ring MDA. The 3,000 generated conformations are represented in grey, the clustering representative conformations are labeled with letters that correspond to the structures in **Figures B.54-56**. The conformations labeled in black fall within the experimental range, the conformations labeled in red are representative of conformations from the left conformational cloud, and the conformations labeled in blue are representative of conformations from the right conformational cloud.

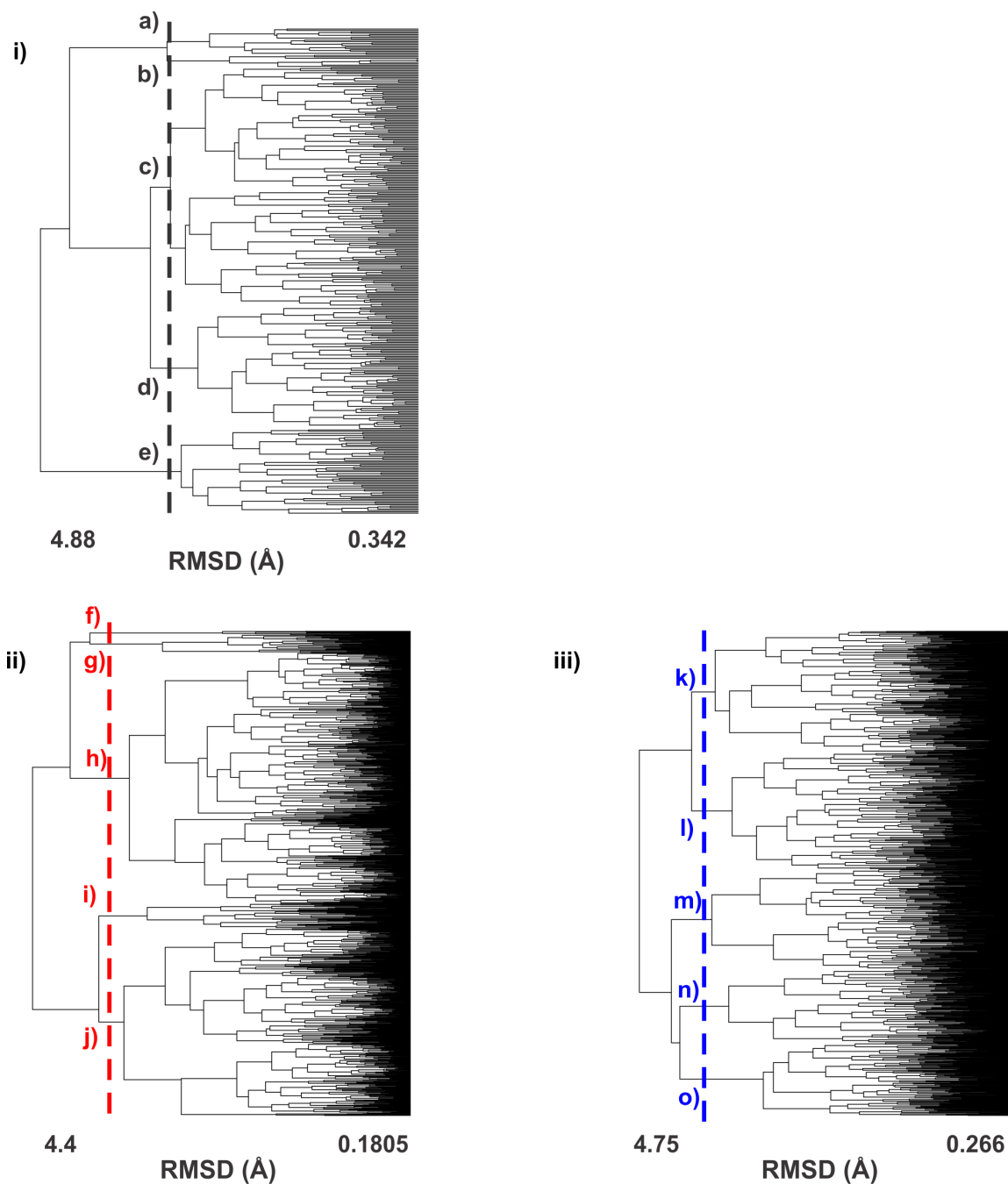


Figure B.54. Clustering analysis of 3,000 conformations of the fourth ring amine protonated 4-ring MDA. In i) the conformations that fall within the experimental CCS range are clustered, in ii) the conformations in the left conformational cloud are clustered, and in iii) the conformations in the right conformational cloud are clustered. Clustering is based on root mean square distance of atoms of superimposed structures. The vertical bars indicate the RMSD cutoff used to select the conformations for further analysis.

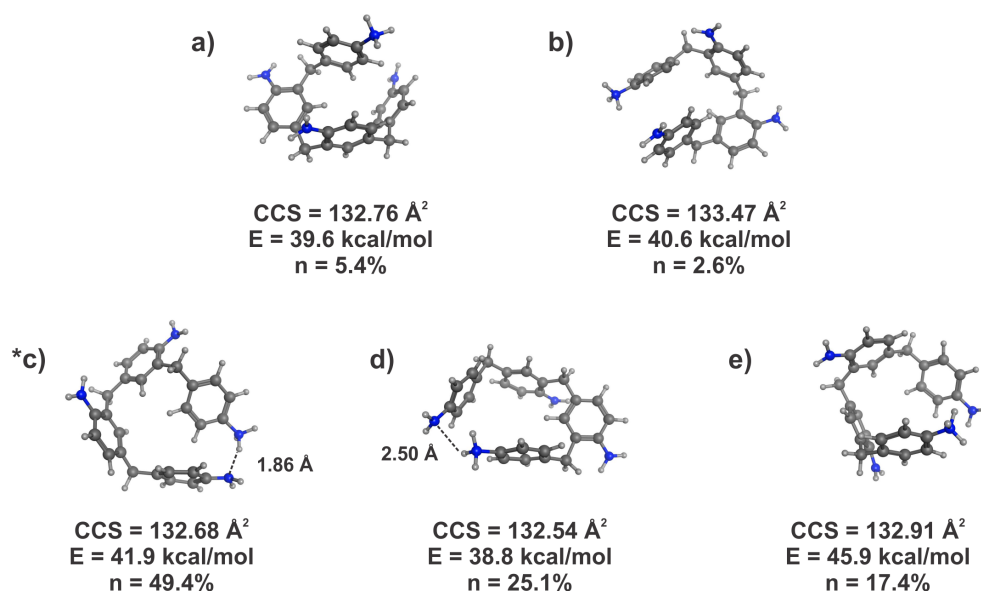


Figure B.55. Representative conformations from clustering analysis of the experimental range region of the fourth ring amine protonated 4-ring MDA generated from the simulated annealing calculation. Carbon atoms are shown in dark grey, hydrogen in light grey, and nitrogen in blue. Distances are labeled to show the proximity of the additional proton to other atoms in the molecule. The asterisk represents the structure shown in the manuscript. The theoretical CCS, relative energy, and percentage of conformations each of these represents from clustering are shown below the conformation.

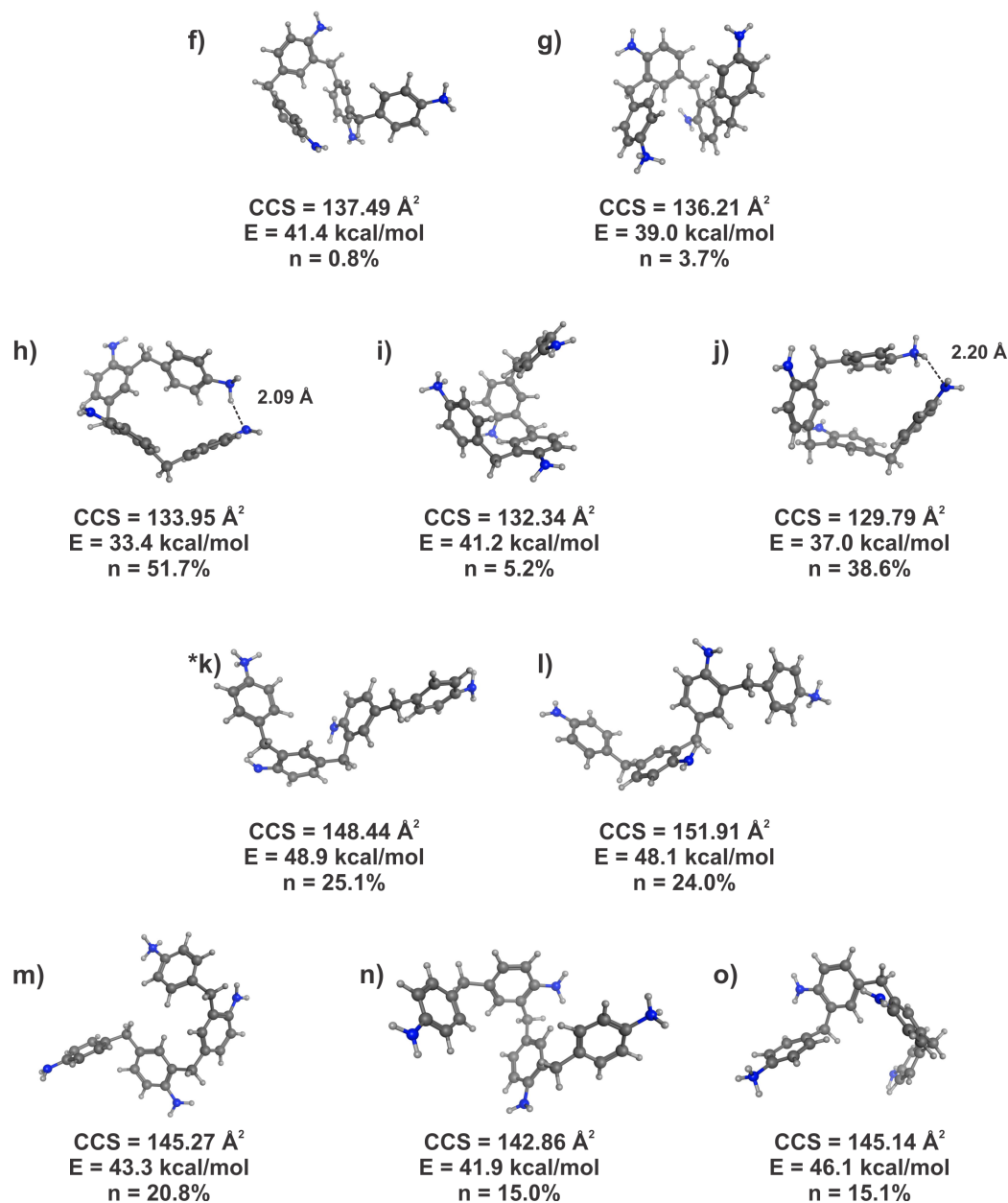


Figure B.56. Representative conformations from clustering analysis of the two conformational space clouds (left cloud (f-j) and right cloud (k-o)) of the first ring amine protonated 4-ring MDA generated from the simulated annealing calculation. Carbon atoms are shown in dark grey, hydrogen in light grey, and nitrogen in blue. Distances are labeled to show the proximity of the additional proton to other atoms in the molecule. The asterisk represents the structures shown in the manuscript. The theoretical CCS, relative energy, and percentage of conformations each of these represents from clustering are shown below the conformation.

APPENDIX C

SUPPLEMENTARY MATERIALS FOR CHAPTER III

Table C.1. Structural information concerning the 10 natural products used in this study. Number of atoms, number of rotatable bonds, number of oxygens, number of chiral centers, and number of double bonds.

Molecule	# of atoms	# of rotatable bonds	# of oxygens	# of chiral centers	# of double bonds
Brefeldin	44	0	4	5	2
Ampicillin	43	5	4	4	0
Doxorubicin	68	5	11	6	0
Capsaicin	49	10	3	0	1
Lincomycin	61	8	6	9	0
Neomycin	88	9	13	19	0
Josamycin	127	14	15	16	2
Erythromycin	118	7	13	18	0
Antimycin	79	14	9	4	0
Valinomycin	168	9	18	12	0

Table C.1. Number of structures that are generated with each method as well as the number of structures plotted after 1.0 RMSD clustering cutoff.

Molecule	# of structures generated when 20,000 requested	# of structures generated when 8,000 requested	# of structures used from 8,000 DG	# of structures used from SA	# of structures after 1.0 RMSD clustering for 8,000DG	# of structures after 1.0 RMSD clustering for SA
Brefeldin	15	15	15	3000	7	31
Ampicillin	282	268	268	3000	36	22
Doxorubicin	314	307	307	3000	152	111
Capsaicin	2864	2736	2736	9000	805	1336
Lincomycin	10995	8000	7997	9000	2580	301
Neomycin	20000	8000	8000	9000	7175	2255
Josamycin	20000	8000	7797	9000	7726	3105
Erythromycin	20000	8000	7982	9000	7509	857
Antimycin	20000	8000	7995	9000	4657	2036
Valinomycin	20000	8000	8000	9000	8000	7546

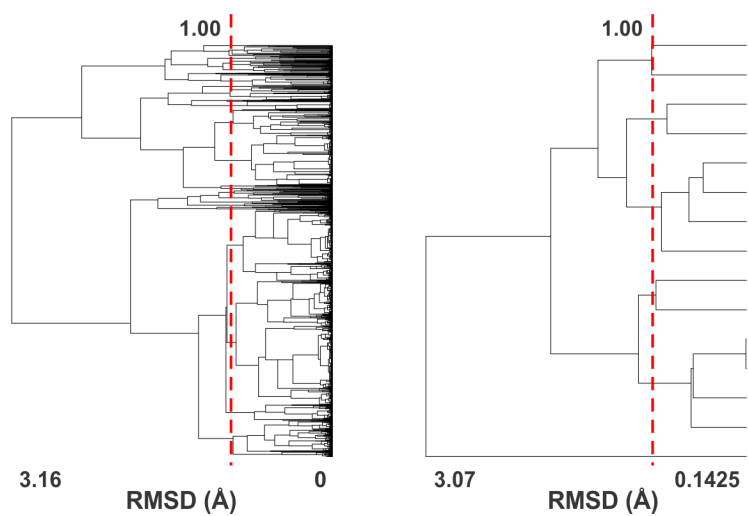


Figure C.2. Clustering analysis for brefeldin for a) simulated annealing, and b) distance geometry. The vertical bar indicates the RMSD cutoff (1.0 Å) used to select a comparable number of structures from both methods.

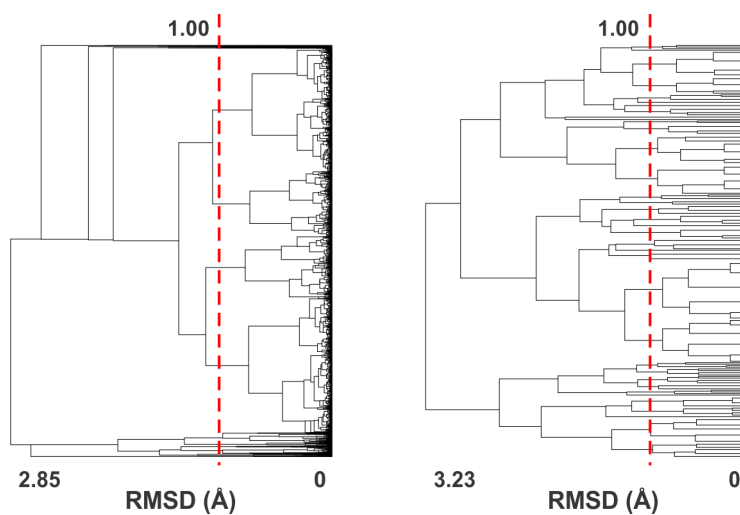


Figure C.3. Clustering analysis for ampicillin for a) simulated annealing, and b) distance geometry. The vertical bar indicates the RMSD cutoff (1.0 Å) used to select a comparable number of structures from both methods.

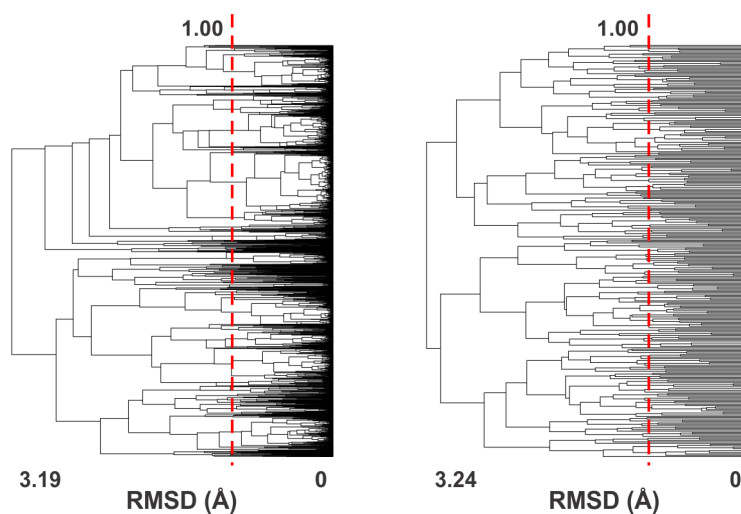


Figure C.4. Clustering analysis for doxorubicin for a) simulated annealing, and b) distance geometry. The vertical bar indicates the RMSD cutoff (1.0 Å) used to select a comparable number of structures from both methods.

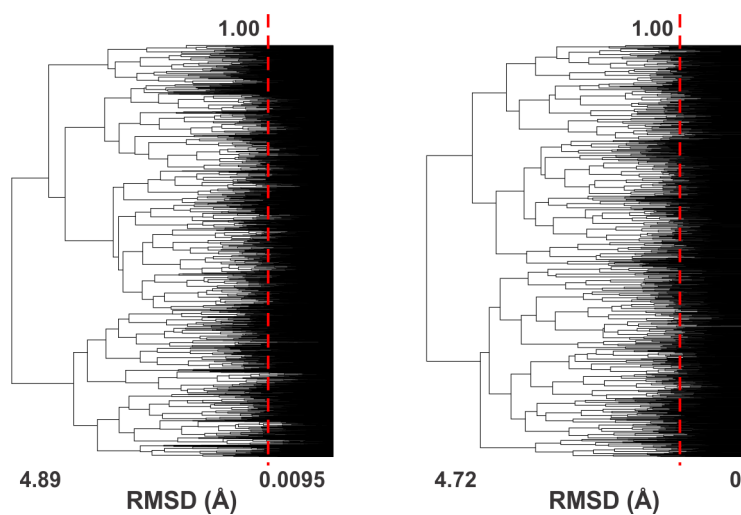


Figure C.5. Clustering analysis for capsaicin for a) simulated annealing, and b) distance geometry. The vertical bar indicates the RMSD cutoff (1.0 Å) used to select a comparable number of structures from both methods.

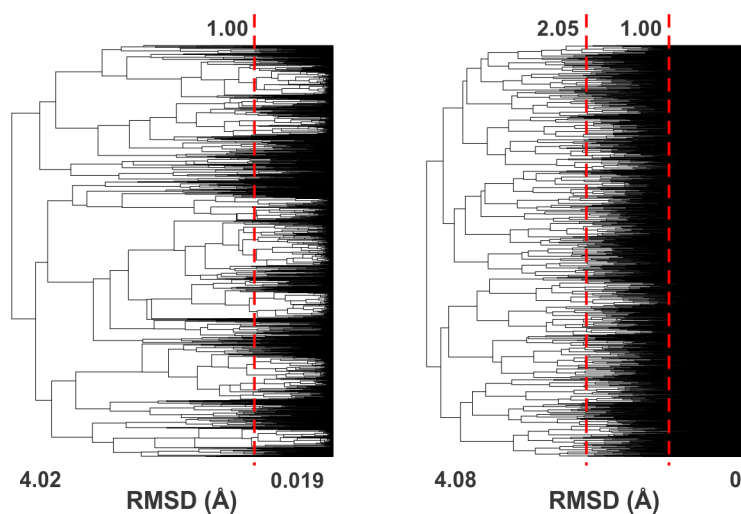


Figure C.6. Clustering analysis for lincomycin for a) simulated annealing, and b) distance geometry. The vertical bar at 1.0 Å indicates the RMSD cutoff used to select a comparable number of structures from both methods. The other vertical bar at 2.05 Å indicates the RMSD cutoff for the QM geometry optimization.

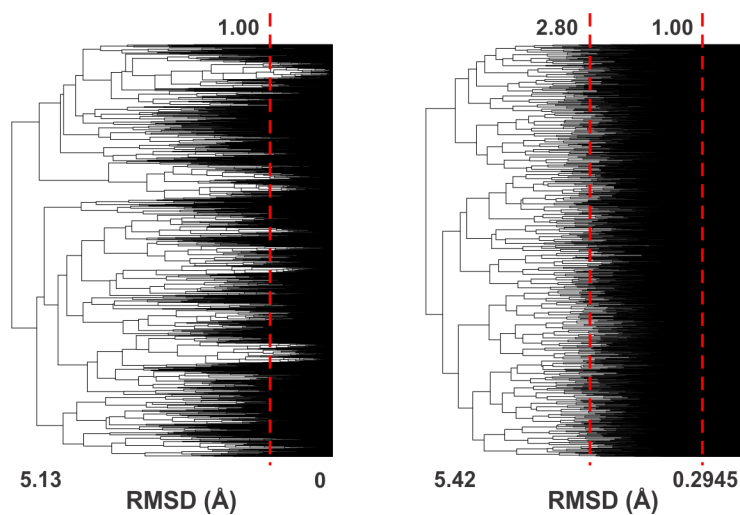


Figure C.7. Clustering analysis for neomycin for a) simulated annealing, and b) distance geometry. The vertical bar at 1.0 Å indicates the RMSD cutoff used to select a comparable number of structures from both methods. The other vertical bar at 2.80 Å indicates the RMSD cutoff for the QM geometry optimization.

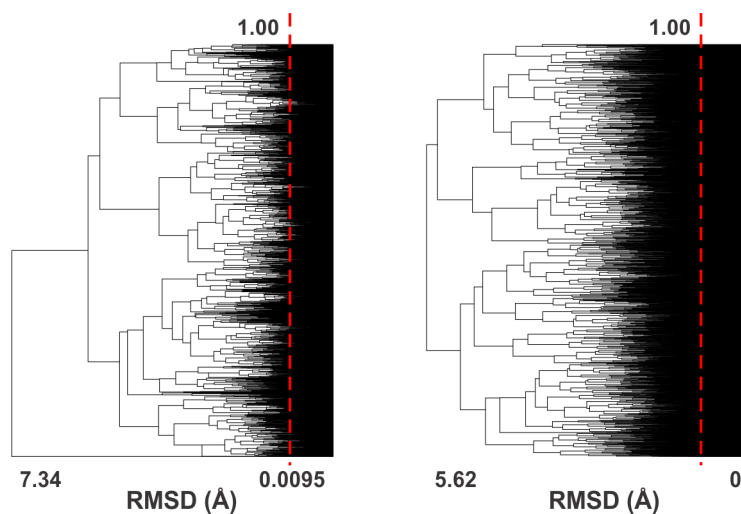


Figure C.8. Clustering analysis for antimycin for a) simulated annealing and b) distance geometry. The vertical bar indicates the RMSD cutoff (1.0 Å) used to select a comparable number of structures from both methods.

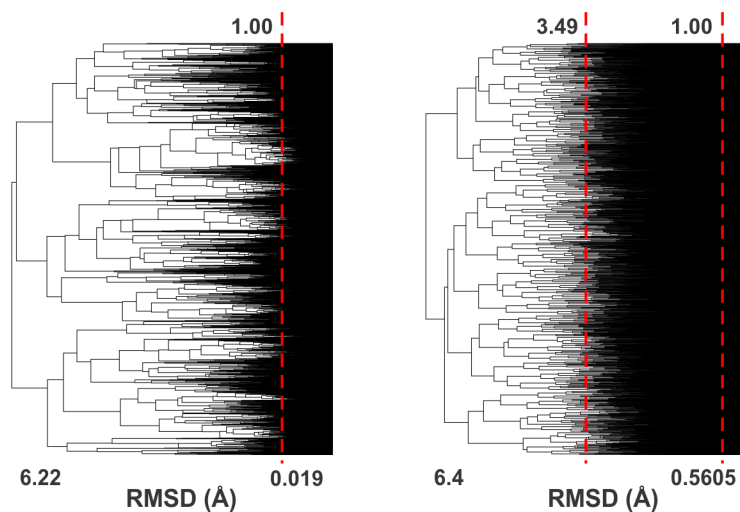


Figure C.9. Clustering analysis for josamycin for a) simulated annealing and b) distance geometry. The vertical bar at 1.0 Å indicates the RMSD cutoff used to select a comparable number of structures from both methods. The other vertical bar at 3.49 Å indicates the RMSD cutoff for the QM geometry optimization.

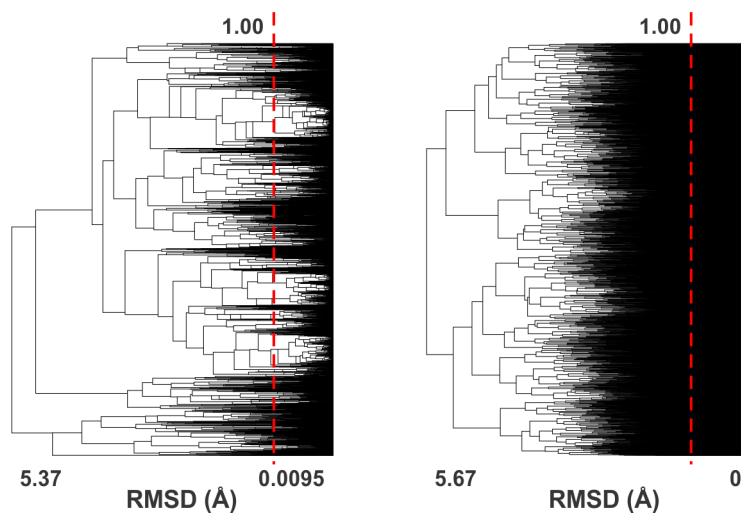


Figure C.10. Clustering analysis for erythromycin for a) simulated annealing, and b) distance geometry. The vertical bar indicates the RMSD cutoff (1.0 Å) used to select a comparable number of structures from both methods.

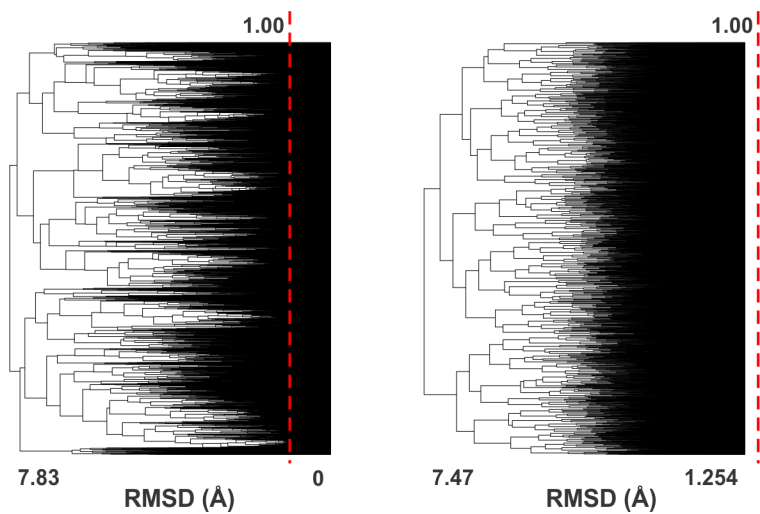


Figure C.11. Clustering analysis for valinomycin for a) simulated annealing, and b) distance geometry. The vertical bar indicates the RMSD cutoff (1.0 Å) used to select a comparable number of structures from both methods.

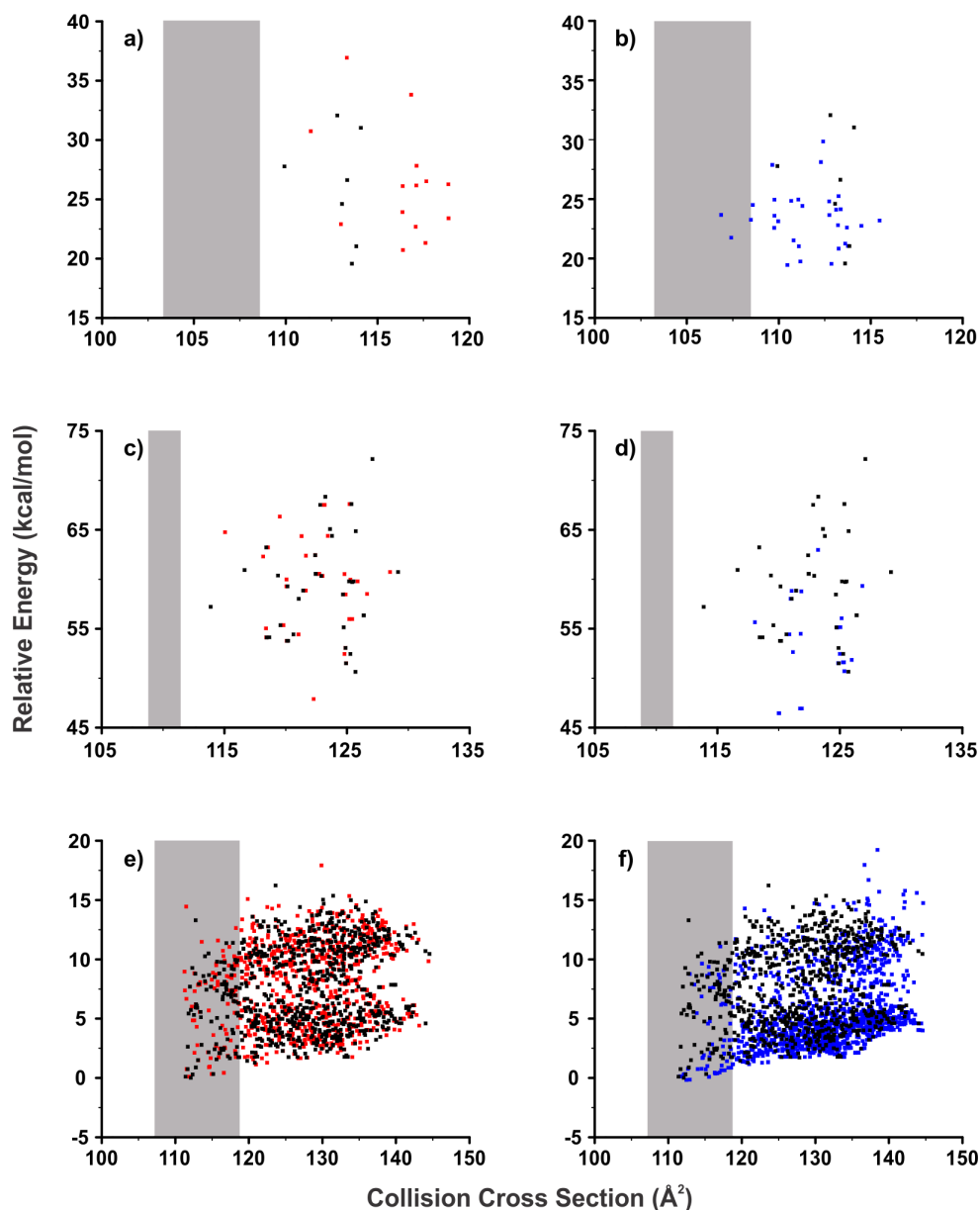


Figure C.11. Conformational space plots for three of the natural products: a,b) brefeldin, c,d) ampicillin, and e,f) capsaicin. The panel on the left shows distance geometry results when 20,000 (red) or 8,000 (black) initial structures are requested from the calculation. The panel on the right compares the distance geometry results (8,000 conformations are requested) to simulated annealing results (blue). The grey vertical bar indicated the experimental CCS range. Note that for brefeldin the distance geometry fails to generate conformations as small as the experimental range determined by IM-MS, and for ampicillin neither distance geometry nor MD-based conformational sampling generates any conformations consistent with the experimental CCS data. This most likely reflects small errors for both the experimental measurements and theoretical calculations, which is not surprising for molecules of this size (where the relative contribution of long range interaction potentials to CCS increases) under the experimental and theoretical methods presented in this manuscript.

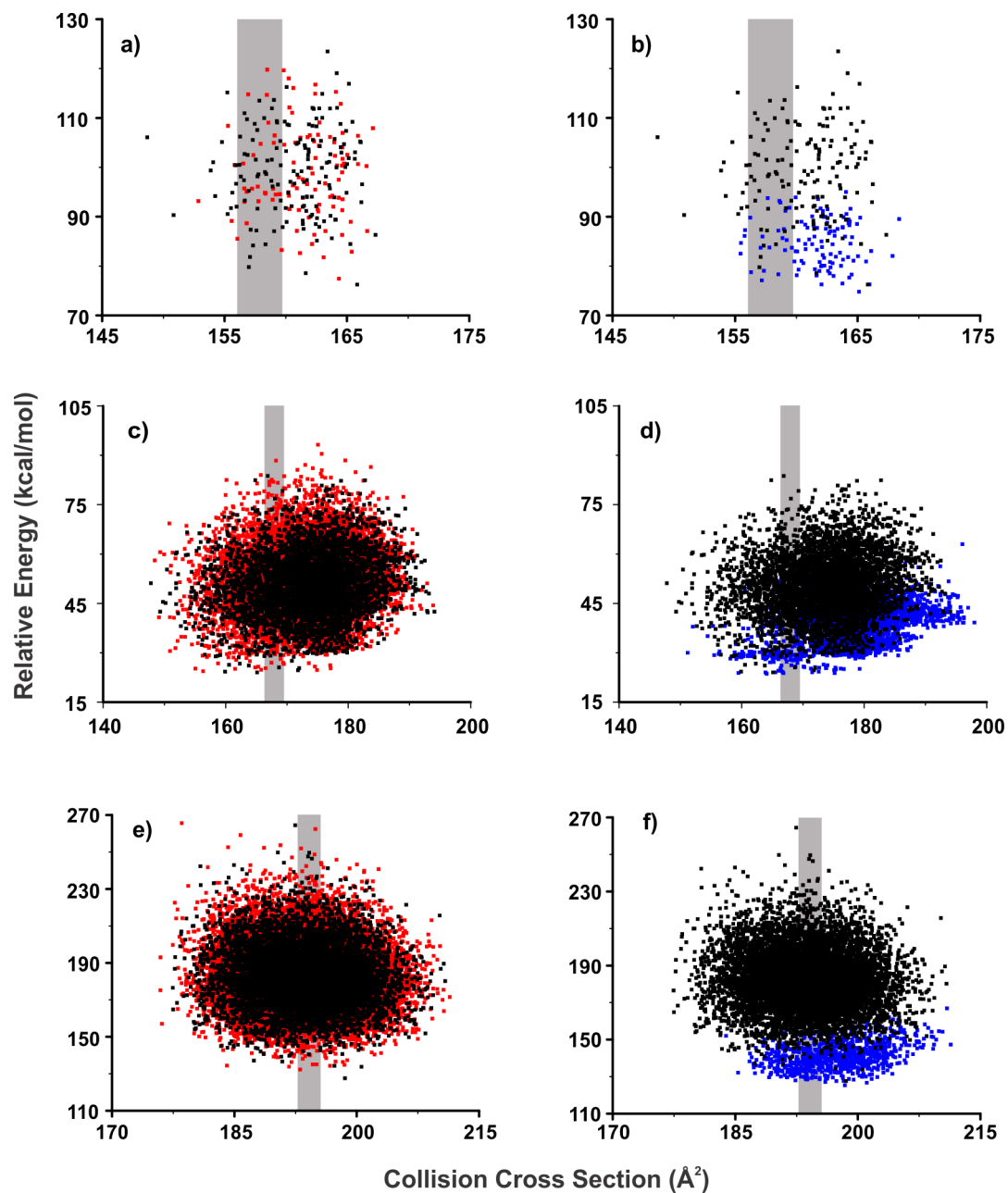


Figure C.12. Conformational space plots for three of the natural products: a,b) doxorubicin, c,d) antimycin, and e,f) erythromycin. The panel on the left shows distance geometry results when 20,000 (red) or 8,000 (black) initial structures are requested from the calculation. The panel on the right compares the distance geometry results (8,000 conformations are requested) to simulated annealing results (blue). The grey vertical bar indicated the experimental CCS range.

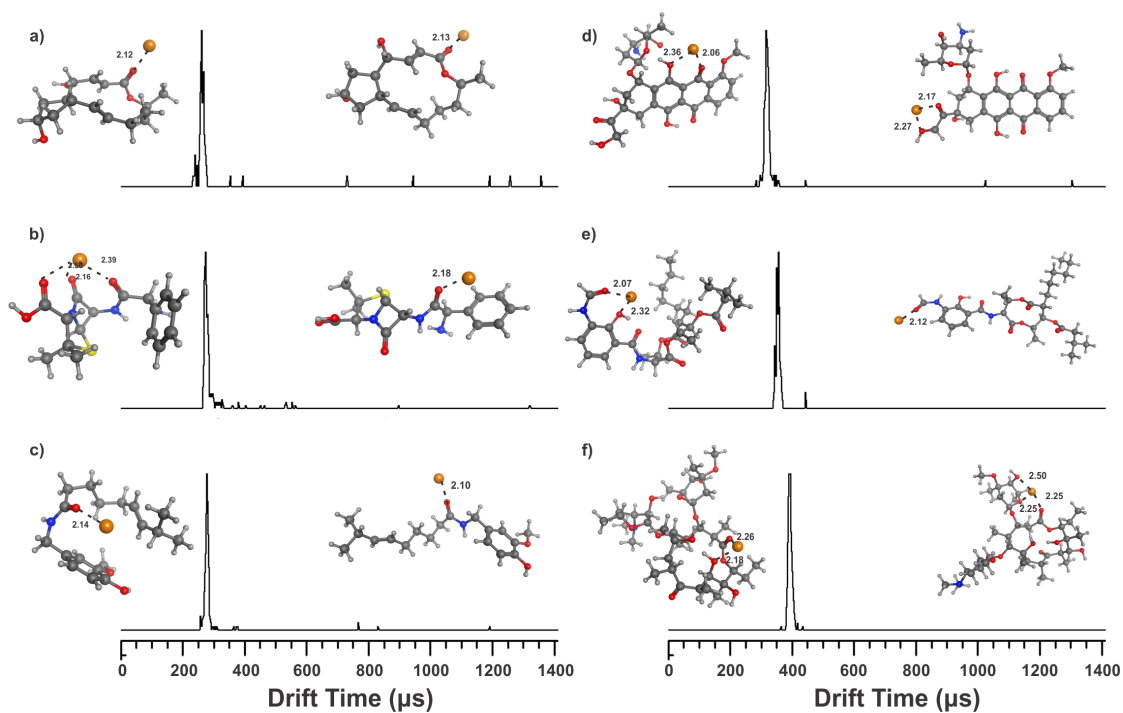


Figure C.13. IM traces for the representative natural products, namely (a) brefeldin, (b) ampicillin, (c) capsaicin, (d) doxorubicin, (e) antimycin, and (f) erythromycin. The most representative conformation generated with distance geometry from within the experimental range is shown for each natural product to the left of the mobility peak and a conformation that does not agree with the experimental measurement is shown on the right of the mobility peak to illustrate the coordination of computation with experiment for interpretation of structure.

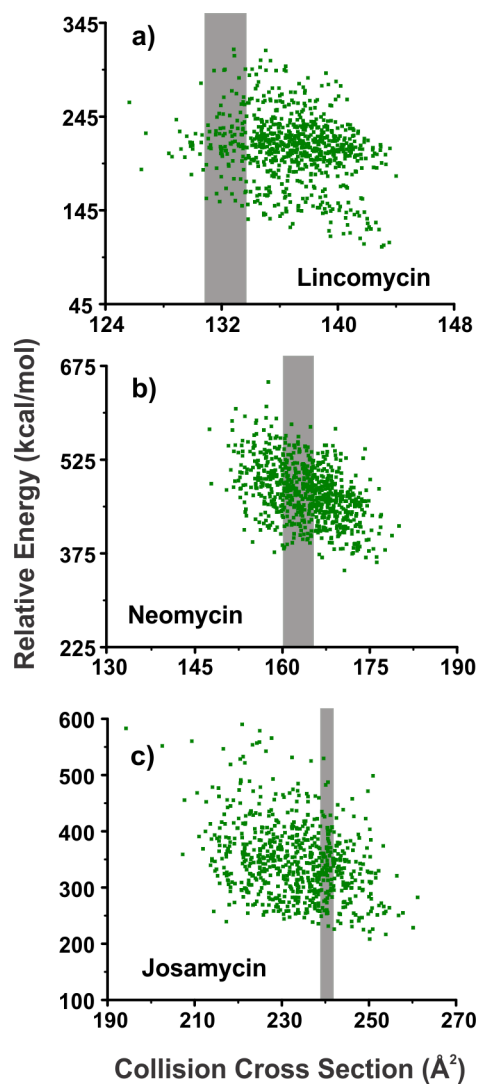


Figure C.14. Conformational space plots for three of the natural products: a) lincomycin, b) neomycin, and c) josamycin when distance geometry is performed with the Gaussian09 QM geometry optimization. The theoretical CCS value is plotted against the relative theoretical energy. The grey vertical bar indicated the experimental CCS range.

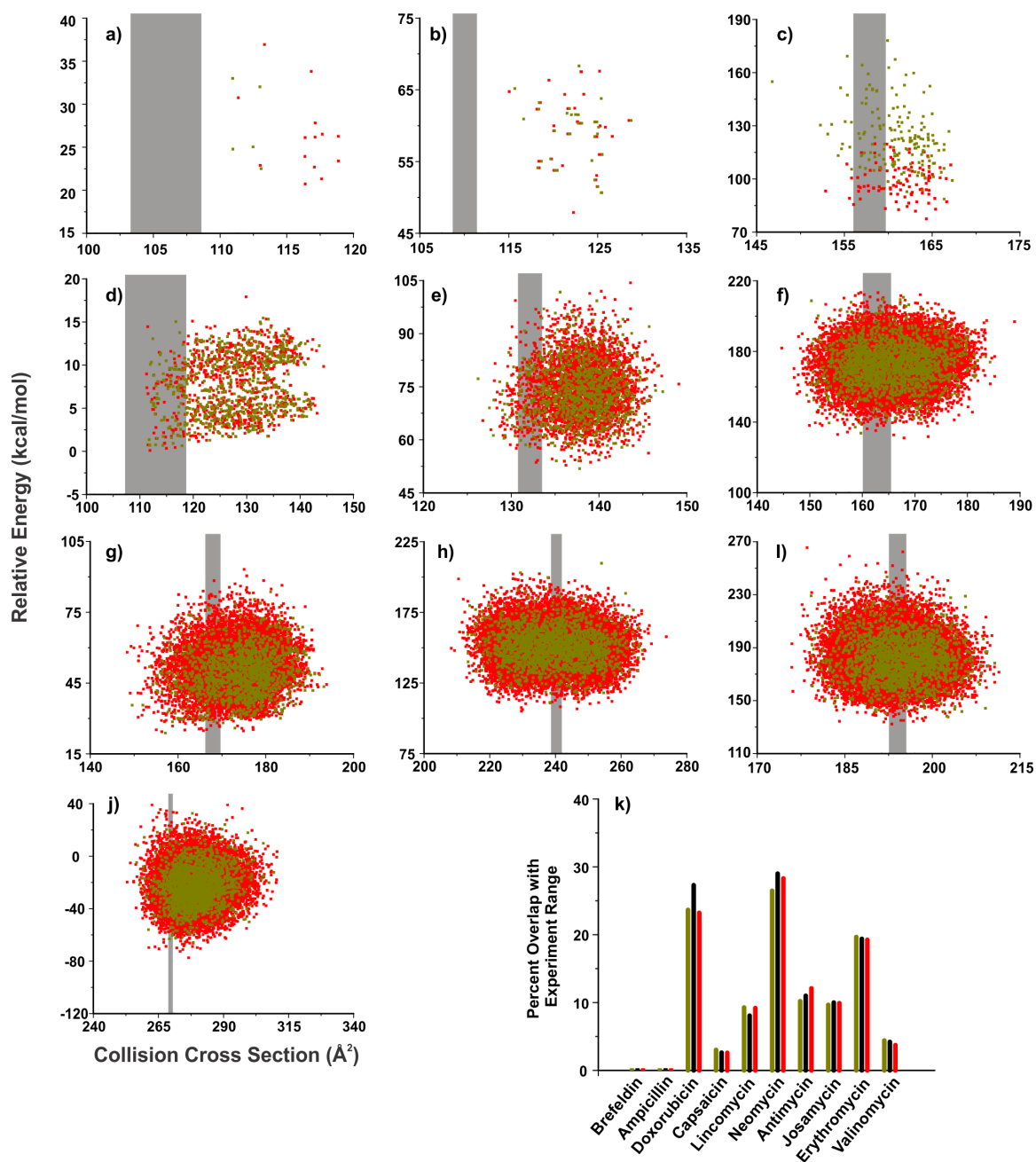


Figure C.15. Conformational space plots for the ten natural products: a) breffledin, b) ampicillin, c) doxorubicin, d) capsaicin, e) lincomycin, f) neomycin, g) antimycin, h) josamycin, i) erythromycin, and j) valinomycin. In k) the percent of generated conformations within the experimental range is shown. The results for 20,000 conformations are shown in red, for 8,000 in black, and for 2,000 in gold.

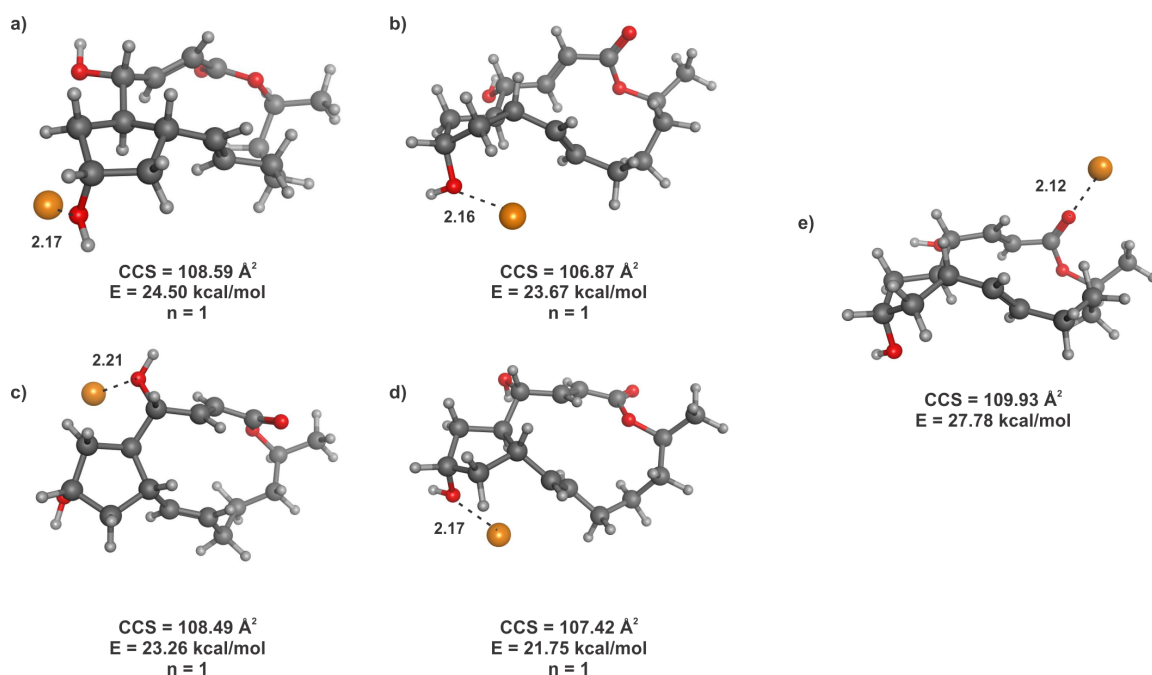


Figure C.16. Representative conformations of brefeldin generated with both simulated annealing and distance geometry. The conformations shown in a-d) were generated with simulated annealing and are the four conformations that fall within the experimental CCS range. For distance geometry, none of the generated conformations fall within the experimental range. The conformation shown in e) is the conformation with the closest theoretical CCS to the experimental range. Each conformation is labeled with its theoretical CCS value and its theoretical energy. Carbon atoms are shown in dark grey, hydrogen in light grey, oxygen in red, nitrogen in blue, sulfur in yellow, and sodium in orange. Each conformation is labeled with its theoretical CCS value and its theoretical energy. All the conformations generated with distance geometry coordinate the cation at the carbonyl oxygen, which is the most electronegative oxygen according to the electrostatic potential that introduces the sodium cation. The short energy minimization that follows the introduction of the cation is not long enough to allow the sodium cation to sample further conformational space. The conformations that have the sodium cation coordinated to the carbonyl oxygen represent larger CCS values that do not align with the experimental measurements.

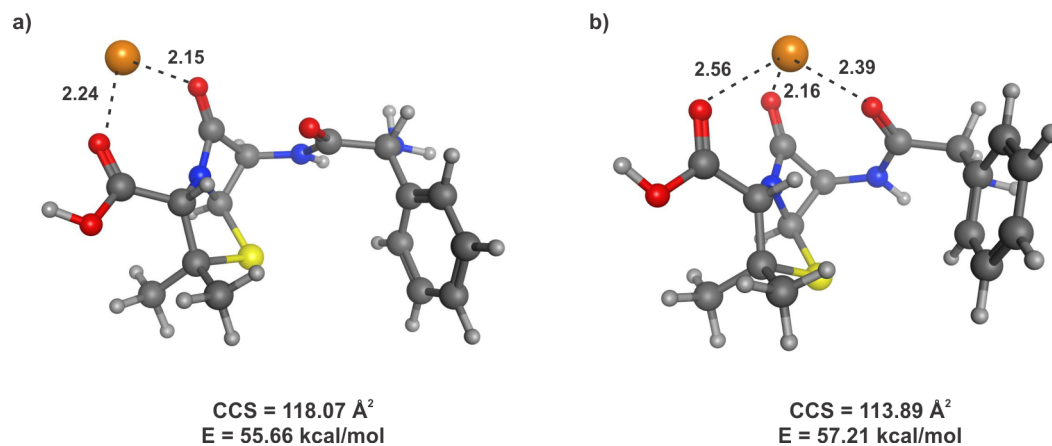


Figure C.17. Representative conformations of ampicillin generated with a) simulated annealing and b) distance geometry. Clustering data is not shown for ampicillin because none of the generated conformations aligned with the experimental CCS value. These conformations had theoretical CCS values that most closely aligned with the experimental CCS value. Carbon atoms are shown in dark grey, hydrogen in light grey, oxygen in red, nitrogen in blue, sulfur in yellow, and sodium in orange. Each conformation is labeled with its theoretical CCS value and its theoretical energy. The lack of overlap with experimental data is most likely representative of experimental conditions that were not optimized for molecules of this size.

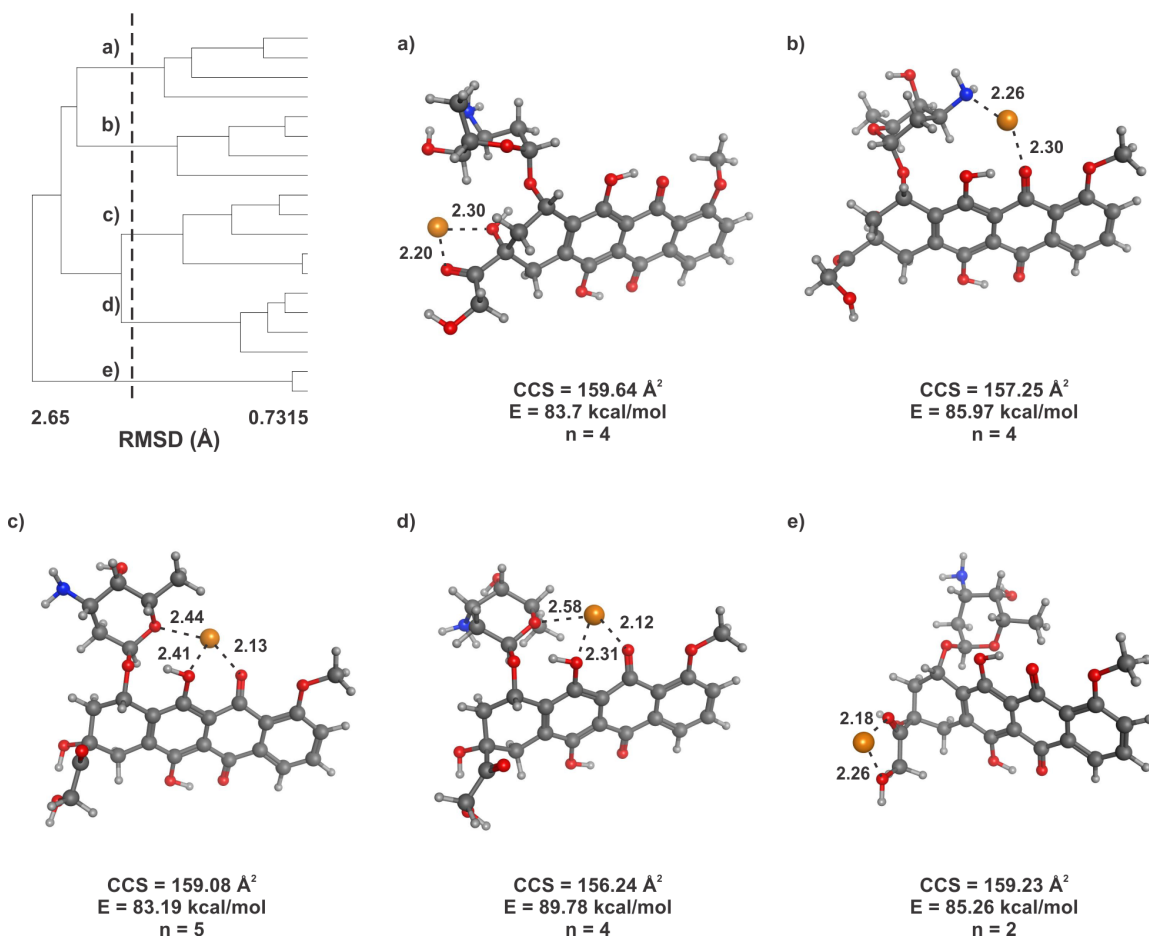


Figure C.18. Clustering analysis of 19 conformations of doxorubicin generated with simulated annealing that fall within the experimental CCS range. Clustering is based on root mean square distance of atoms of superimposed structures. The vertical bar indicates the RMSD cutoff (1.81 Å) used to select the shown conformations. The conformations indicated on the clustering tree are shown with corresponding letters. Carbon atoms are shown in dark grey, hydrogen in light grey, oxygen in red, nitrogen in blue, and sodium in orange. Each conformation is labeled with its theoretical CCS value, its theoretical energy, and the number of conformations it represents from the clustering analysis.

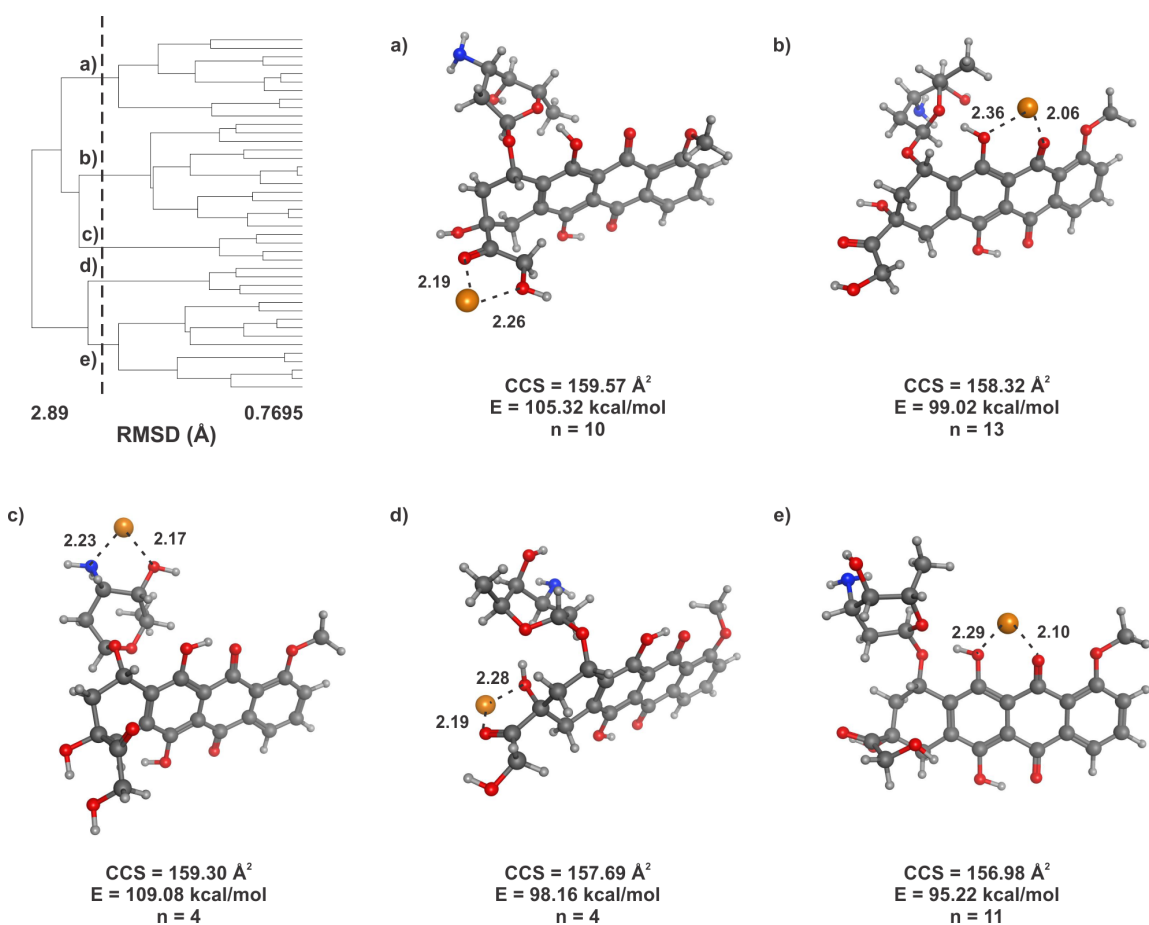


Figure C.19. Clustering analysis of 42 conformations of doxorubicin generated with distance geometry that fall within the experimental CCS range. Clustering is based on root mean square distance of atoms of superimposed structures. The vertical bar indicates the RMSD cutoff (2.40 Å) used to select the shown conformations. The conformations indicated on the clustering tree are shown with corresponding letters. Carbon atoms are shown in dark grey, hydrogen in light grey, oxygen in red, nitrogen in blue, and sodium in orange. Each conformation is labeled with its theoretical CCS value, its theoretical energy, and the number of conformations it represents from the clustering analysis.

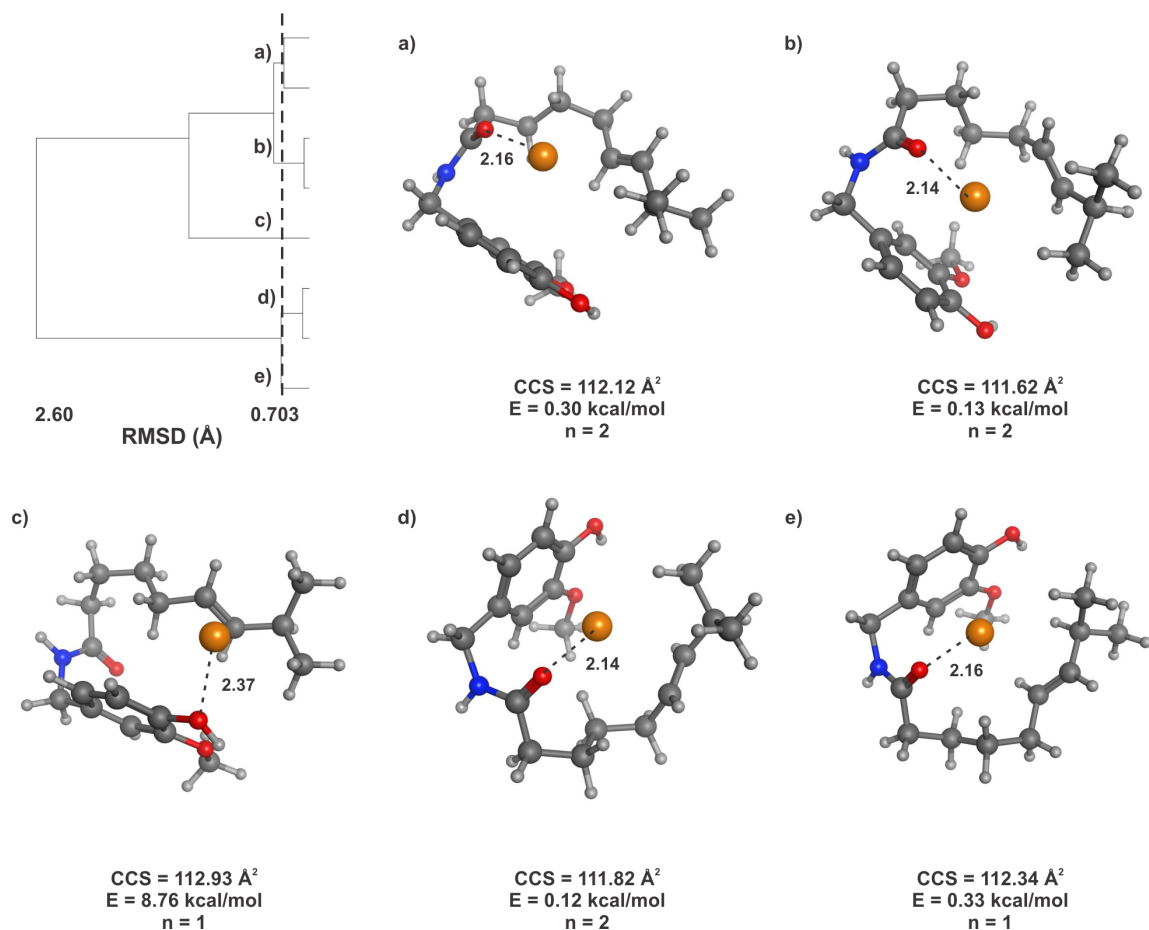


Figure C.20. Clustering analysis of 8 conformations of capsaicin generated with simulated annealing that fall within the experimental CCS range. Clustering is based on root mean square distance of atoms of superimposed structures. The vertical bar indicates the RMSD cutoff (0.89 Å) used to select the shown conformations. The conformations indicated on the clustering tree are shown with corresponding letters. Carbon atoms are shown in dark grey, hydrogen in light grey, oxygen in red, nitrogen in blue, and sodium in orange. Each conformation is labeled with its theoretical CCS value, its theoretical energy, and the number of conformations it represents from the clustering analysis.

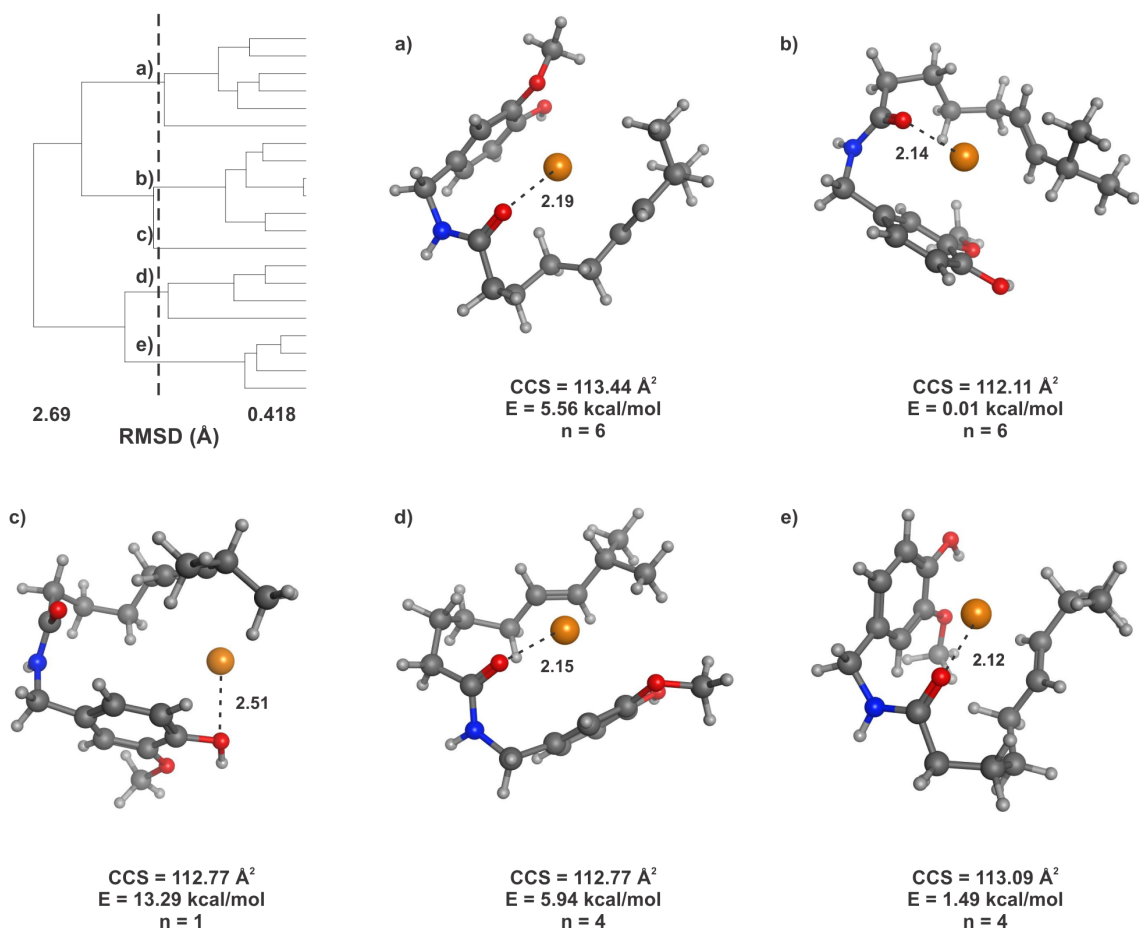


Figure C.21. Clustering analysis of 21 conformations of capsaicin generated with distance geometry that fall within the experimental CCS range. Clustering is based on root mean square distance of atoms of superimposed structures. The vertical bar indicates the RMSD cutoff (1.60 \AA) used to select the shown conformations. The conformations indicated on the clustering tree are shown with corresponding letters. Carbon atoms are shown in dark grey, hydrogen in light grey, oxygen in red, nitrogen in blue, and sodium in orange. Each conformation is labeled with its theoretical CCS value, its theoretical energy, and the number of conformations it represents from the clustering analysis.

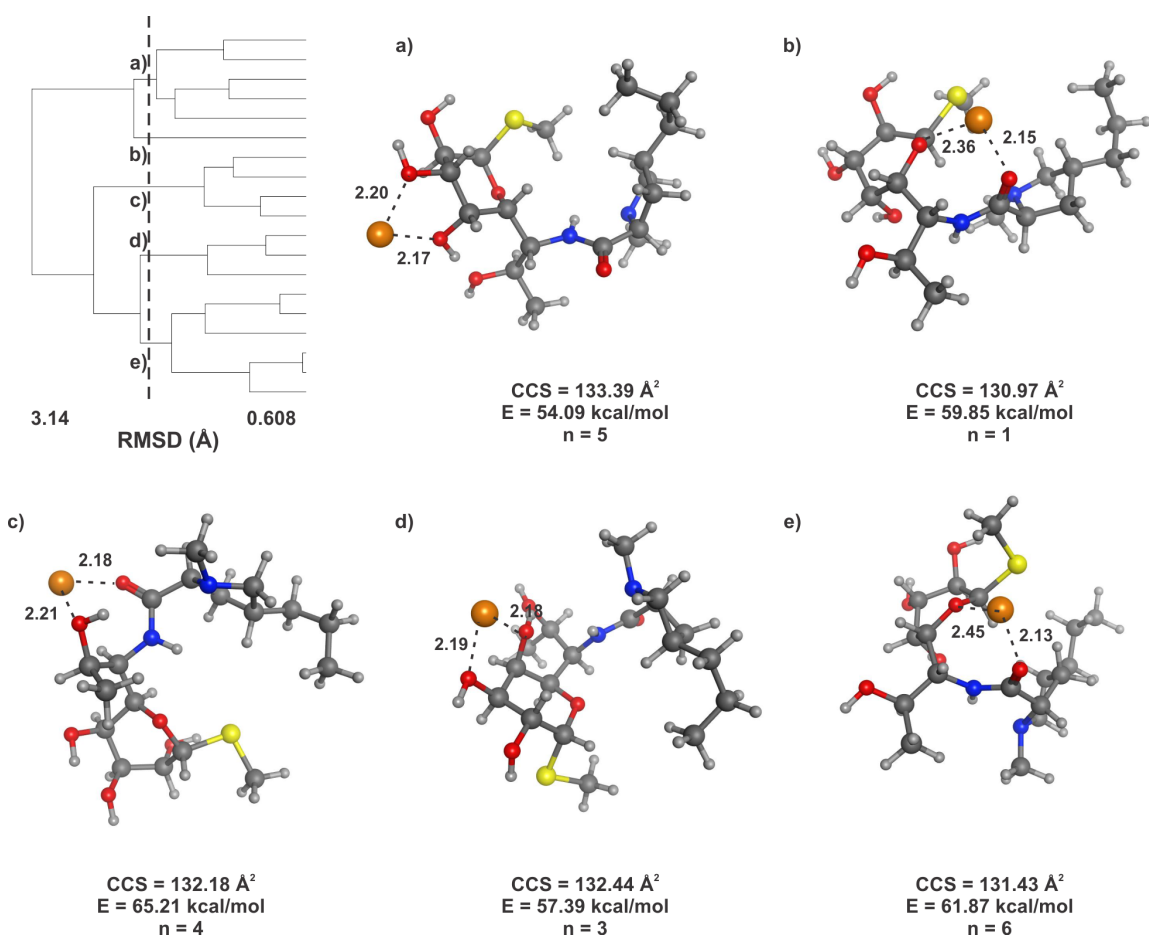


Figure C.22. Clustering analysis of 19 conformations of lincomycin generated with simulated annealing that fall within the experimental CCS range. Clustering is based on root mean square distance of atoms of superimposed structures. The vertical bar indicates the RMSD cutoff (2.10 Å) used to select the shown conformations. The conformations indicated on the clustering tree are shown with corresponding letters. Carbon atoms are shown in dark grey, hydrogen in light grey, oxygen in red, nitrogen in blue, sulfur in yellow, and sodium in orange. Each conformation is labeled with its theoretical CCS value, its theoretical energy, and the number of conformations it represents from the clustering analysis.

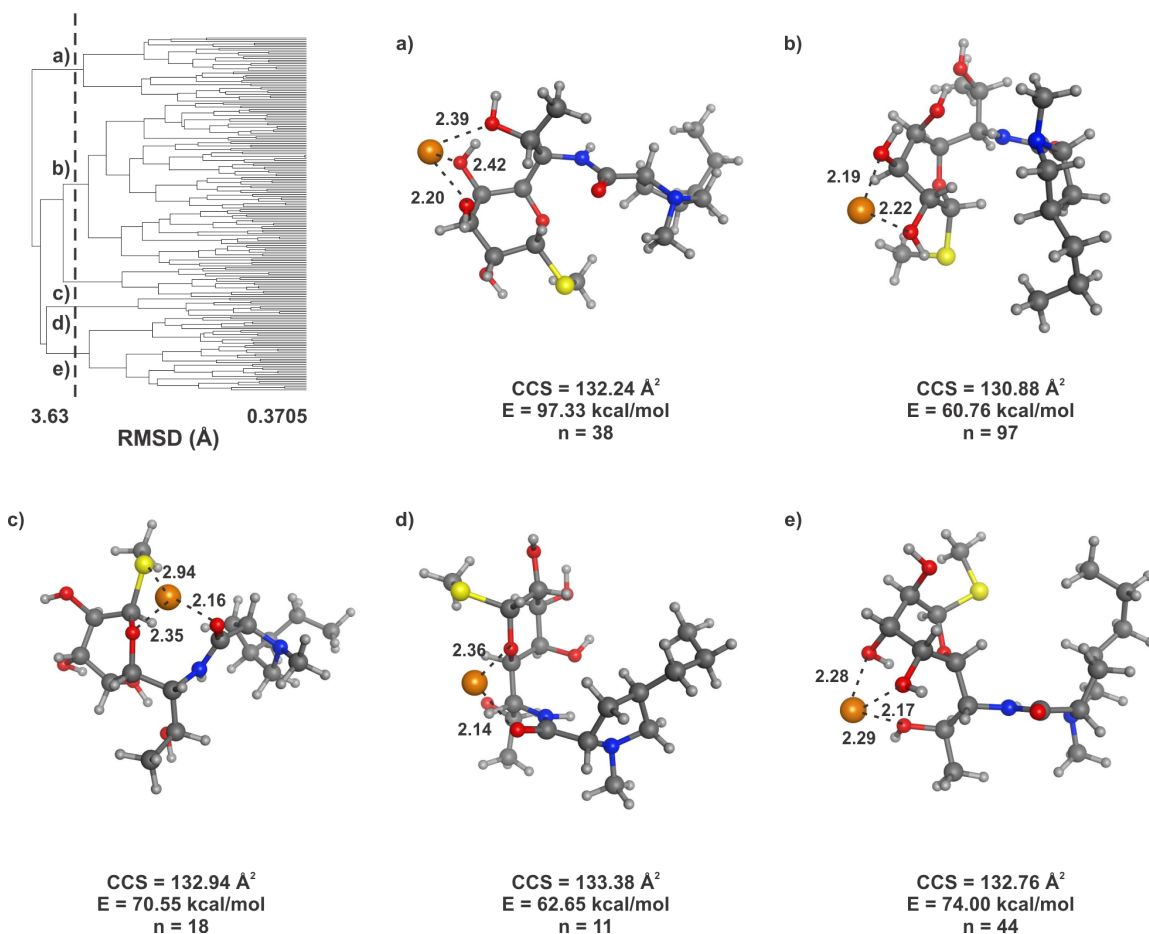


Figure C.23. Clustering analysis of 208 conformations of lincomycin generated with distance geometry and the molecular mechanics energy minimization that fall within the experimental CCS range. Clustering is based on root mean square distance of atoms of superimposed structures. The vertical bar indicates the RMSD cutoff (3.10 \AA) used to select the shown conformations. The conformations indicated on the clustering tree are shown with corresponding letters. Carbon atoms are shown in dark grey, hydrogen in light grey, oxygen in red, nitrogen in blue, sulfur in yellow, and sodium in orange. Each conformation is labeled with its theoretical CCS value, its theoretical energy, and the number of conformations it represents from the clustering analysis.

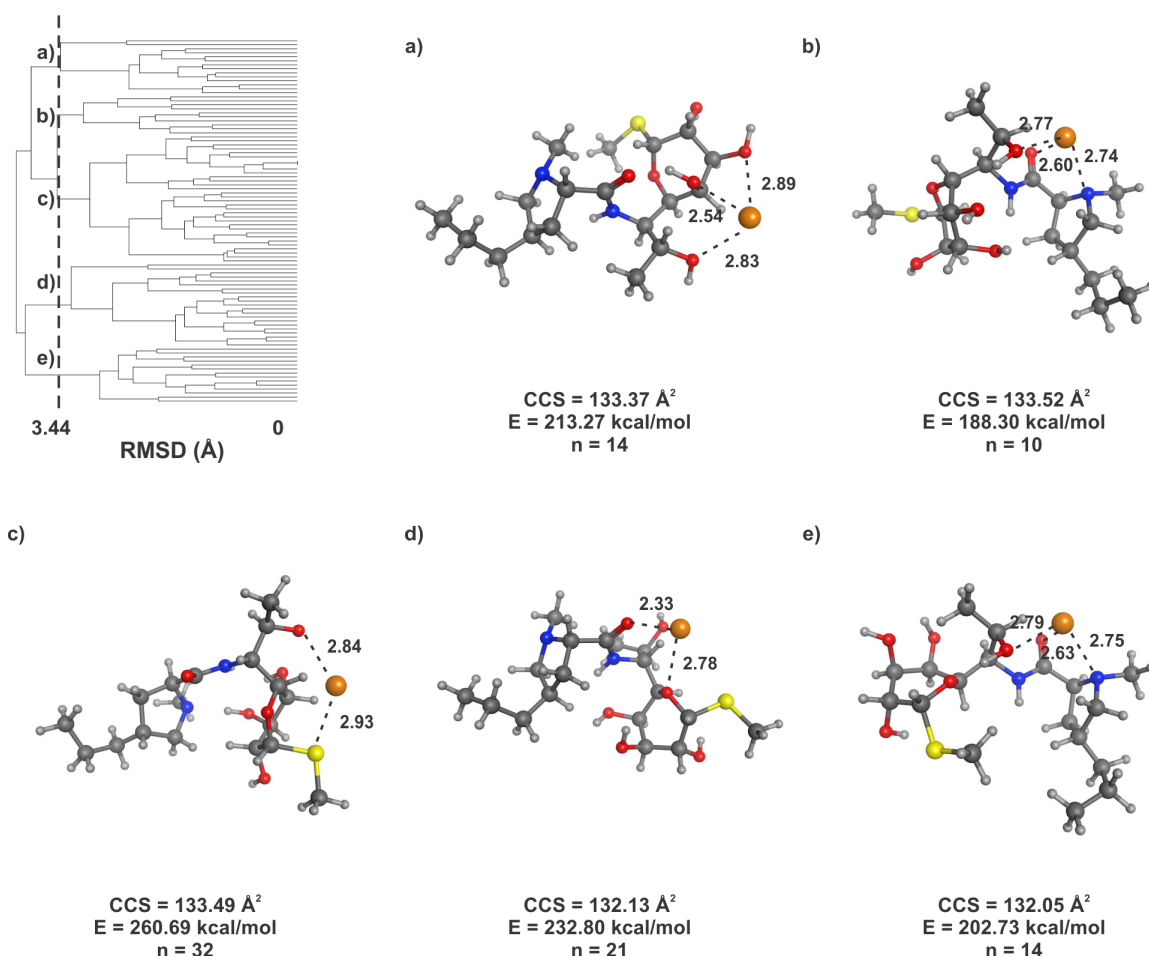


Figure C.24. Clustering analysis of 91 conformations of lincomycin generated with distance geometry and the QM geometry optimization that fall within the experimental CCS range. Clustering is based on root mean square distance of atoms of superimposed structures. The vertical bar indicates the RMSD cutoff (3.30 Å) used to select the shown conformations. The conformations indicated on the clustering tree are shown with corresponding letters. Carbon atoms are shown in dark grey, hydrogen in light grey, oxygen in red, nitrogen in blue, sulfur in yellow, and sodium in orange. Each conformation is labeled with its theoretical CCS value, its theoretical energy, and the number of conformations it represents from the clustering analysis.

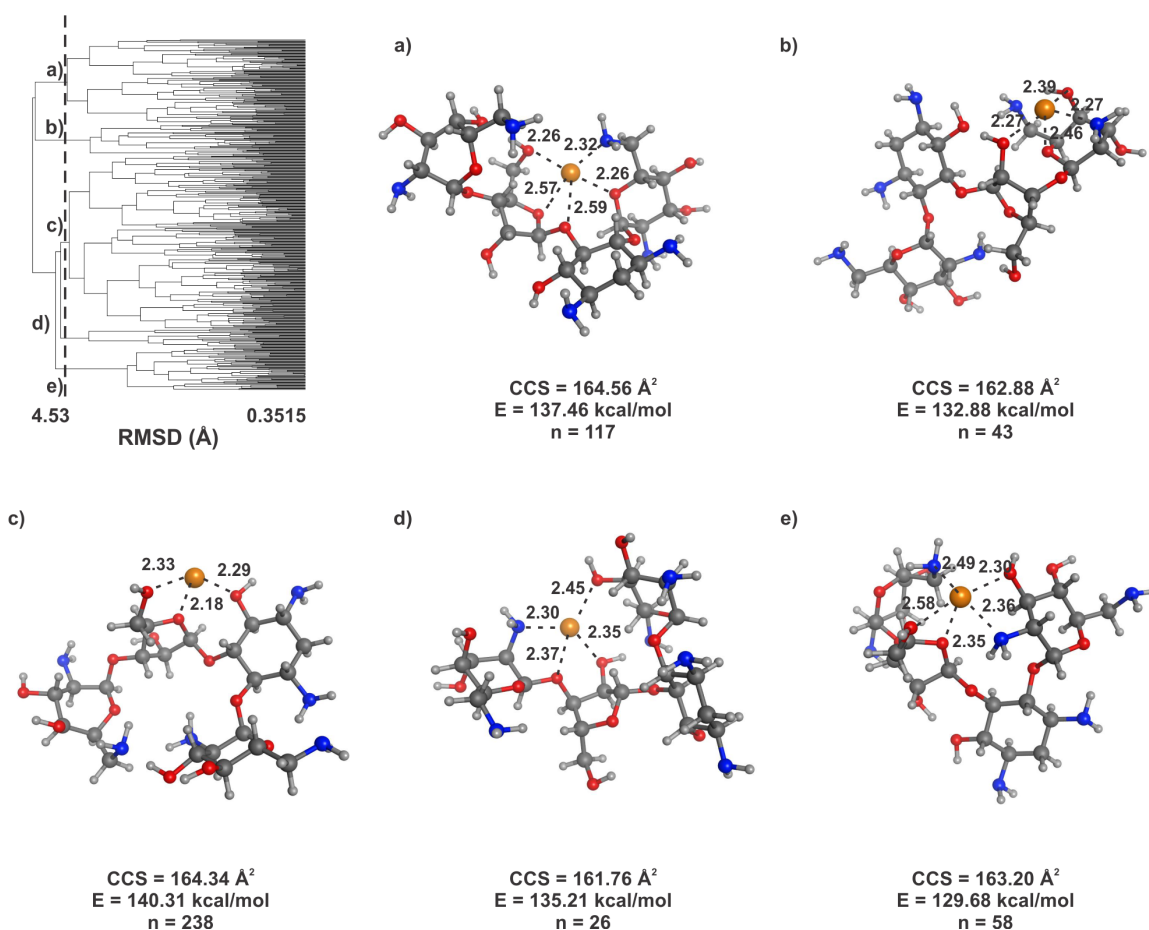


Figure C.25. Clustering analysis of 482 conformations of neomycin generated with simulated annealing that fall within the experimental CCS range. Clustering is based on root mean square distance of atoms of superimposed structures. The vertical bar indicates the RMSD cutoff (4.00 Å) used to select the shown conformations. The conformations indicated on the clustering tree are shown with corresponding letters. Carbon atoms are shown in dark grey, hydrogen in light grey, oxygen in red, nitrogen in blue, and sodium in orange. Each conformation is labeled with its theoretical CCS value, its theoretical energy, and the number of conformations it represents from the clustering analysis.

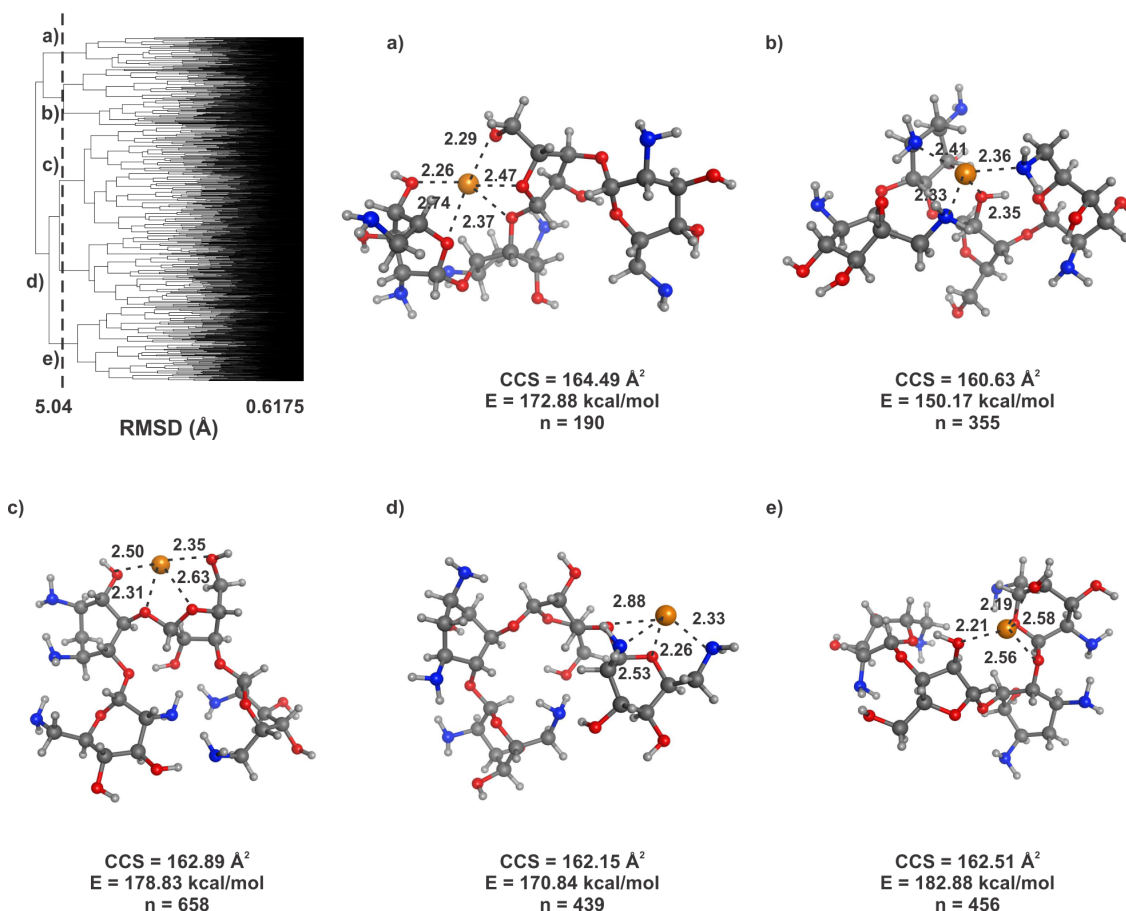


Figure C.26. Clustering analysis of 2098 conformations of neomycin generated with distance geometry and the molecular mechanics energy minimization that fall within the experimental CCS range. Clustering is based on root mean square distance of atoms of superimposed structures. The vertical bar indicates the RMSD cutoff (4.60 Å) used to select the shown conformations. The conformations indicated on the clustering tree are shown with corresponding letters. Carbon atoms are shown in dark grey, hydrogen in light grey, oxygen in red, nitrogen in blue, and sodium in orange. Each conformation is labeled with its theoretical CCS value, its theoretical energy, and the number of conformations it represents from the clustering analysis.

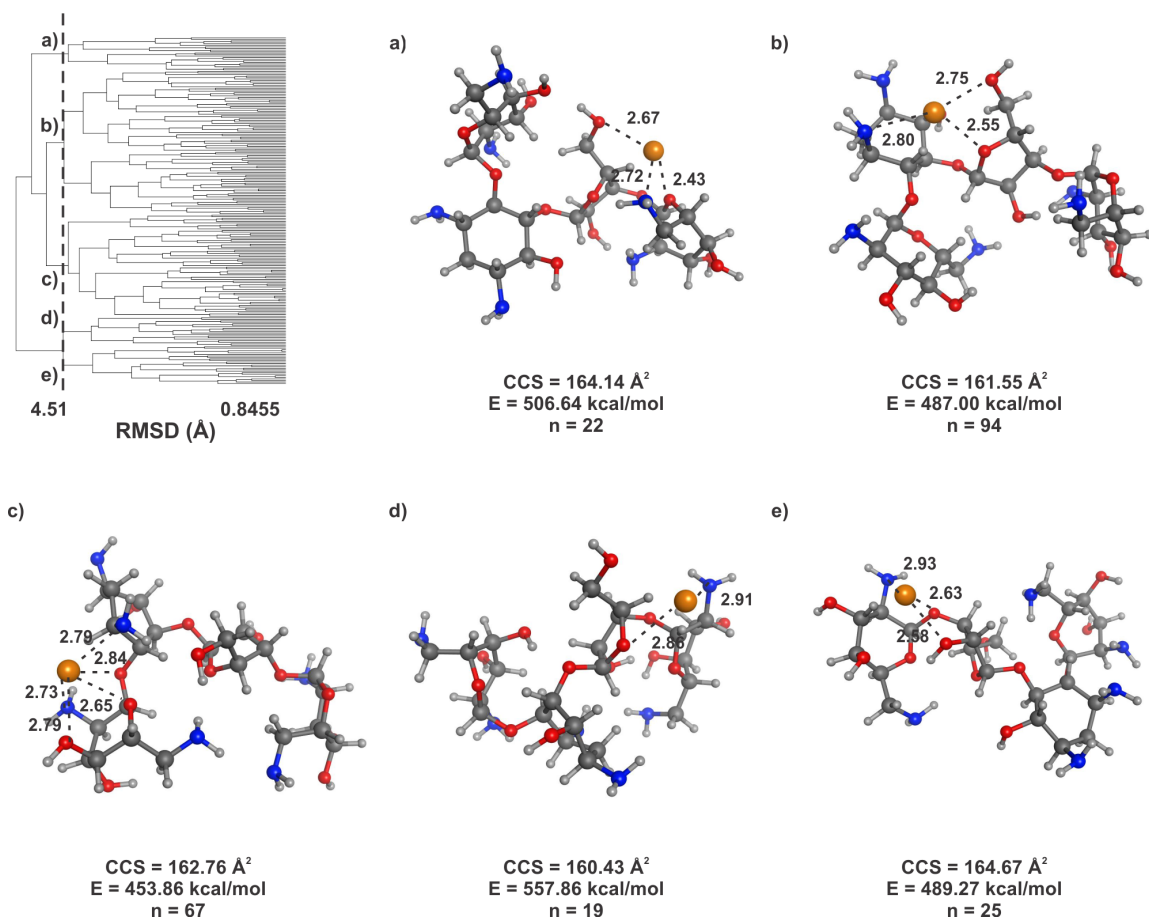


Figure C.27. Clustering analysis of 227 conformations of neomycin generated with distance geometry and the QM geometry optimization that fall within the experimental CCS range. Clustering is based on root mean square distance of atoms of superimposed structures. The vertical bar indicates the RMSD cutoff (3.86 Å) used to select the shown conformations. The conformations indicated on the clustering tree are shown with corresponding letters. Carbon atoms are shown in dark grey, hydrogen in light grey, oxygen in red, nitrogen in blue, and sodium in orange. Each conformation is labeled with its theoretical CCS value, its theoretical energy, and the number of conformations it represents from the clustering analysis.

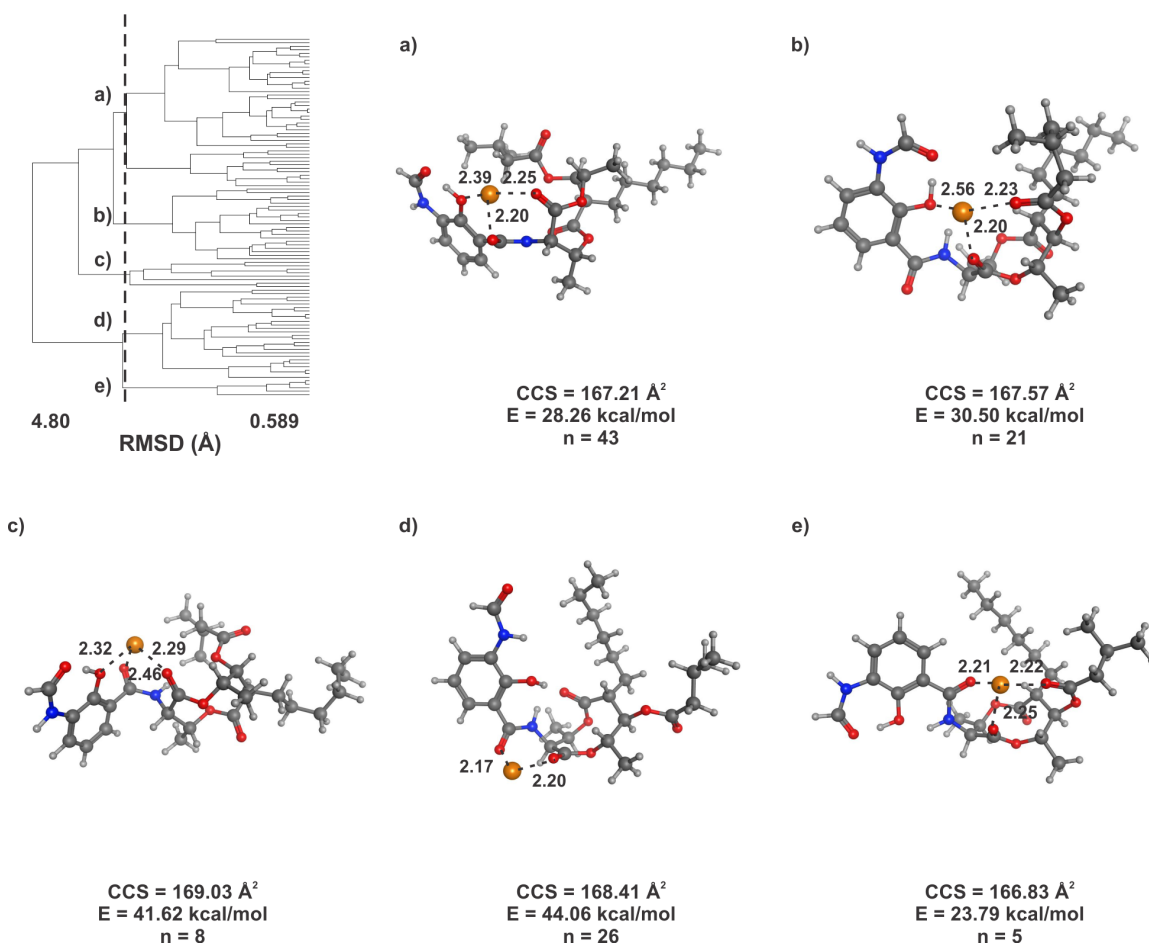


Figure C.28. Clustering analysis of 103 conformations of antimycin generated with simulated annealing that fall within the experimental CCS range. Clustering is based on root mean square distance of atoms of superimposed structures. The vertical bar indicates the RMSD cutoff (3.40 Å) used to select the shown conformations. The conformations indicated on the clustering tree are shown with corresponding letters. Carbon atoms are shown in dark grey, hydrogen in light grey, oxygen in red, nitrogen in blue, and sodium in orange. Each conformation is labeled with its theoretical CCS value, its theoretical energy, and the number of conformations it represents from the clustering analysis.

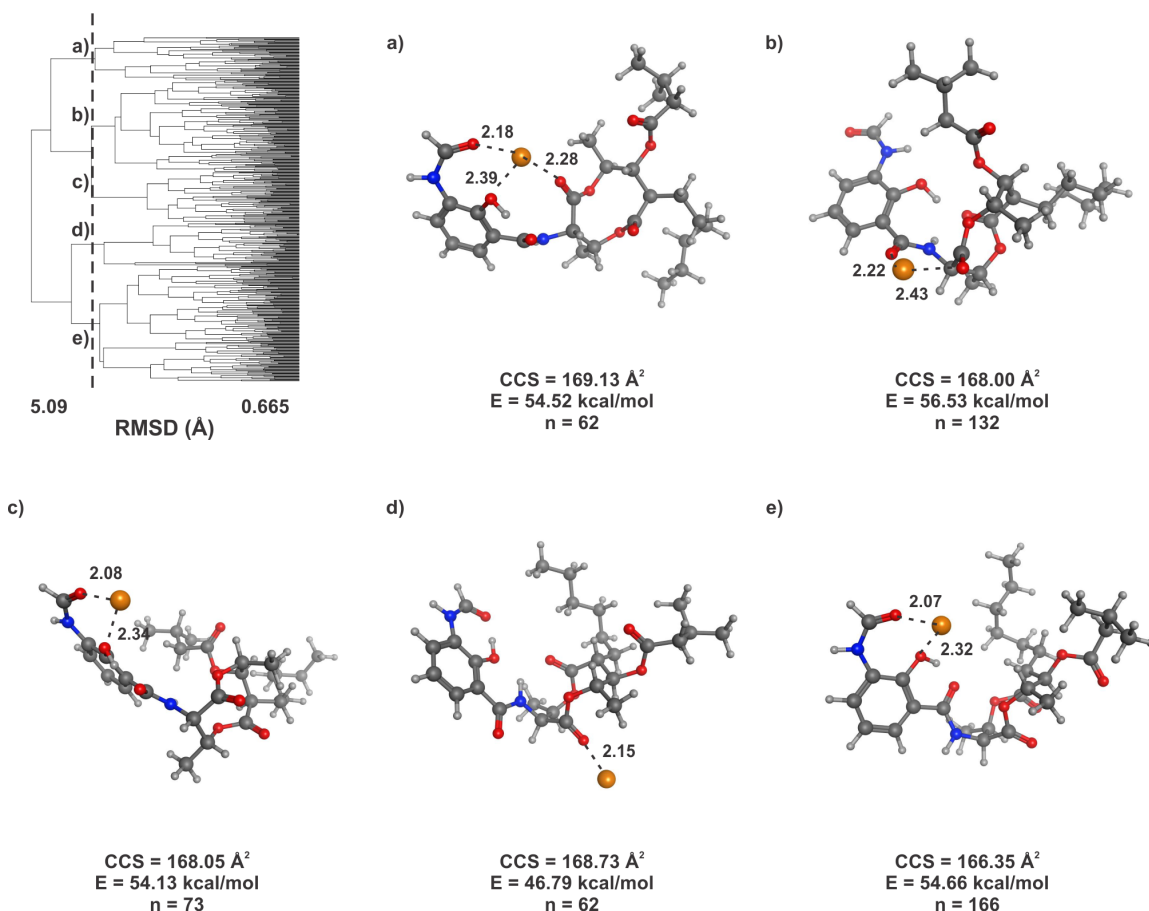


Figure C.29. Clustering analysis of 495 conformations of antimycin generated with distance geometry that fall within the experimental CCS range. Clustering is based on root mean square distance of atoms of superimposed structures. The vertical bar indicates the RMSD cutoff (4.05 Å) used to select the shown conformations. The conformations indicated on the clustering tree are shown with corresponding letters. Carbon atoms are shown in dark grey, hydrogen in light grey, oxygen in red, nitrogen in blue, and sodium in orange. Each conformation is labeled with its theoretical CCS value, its theoretical energy, and the number of conformations it represents from the clustering analysis.

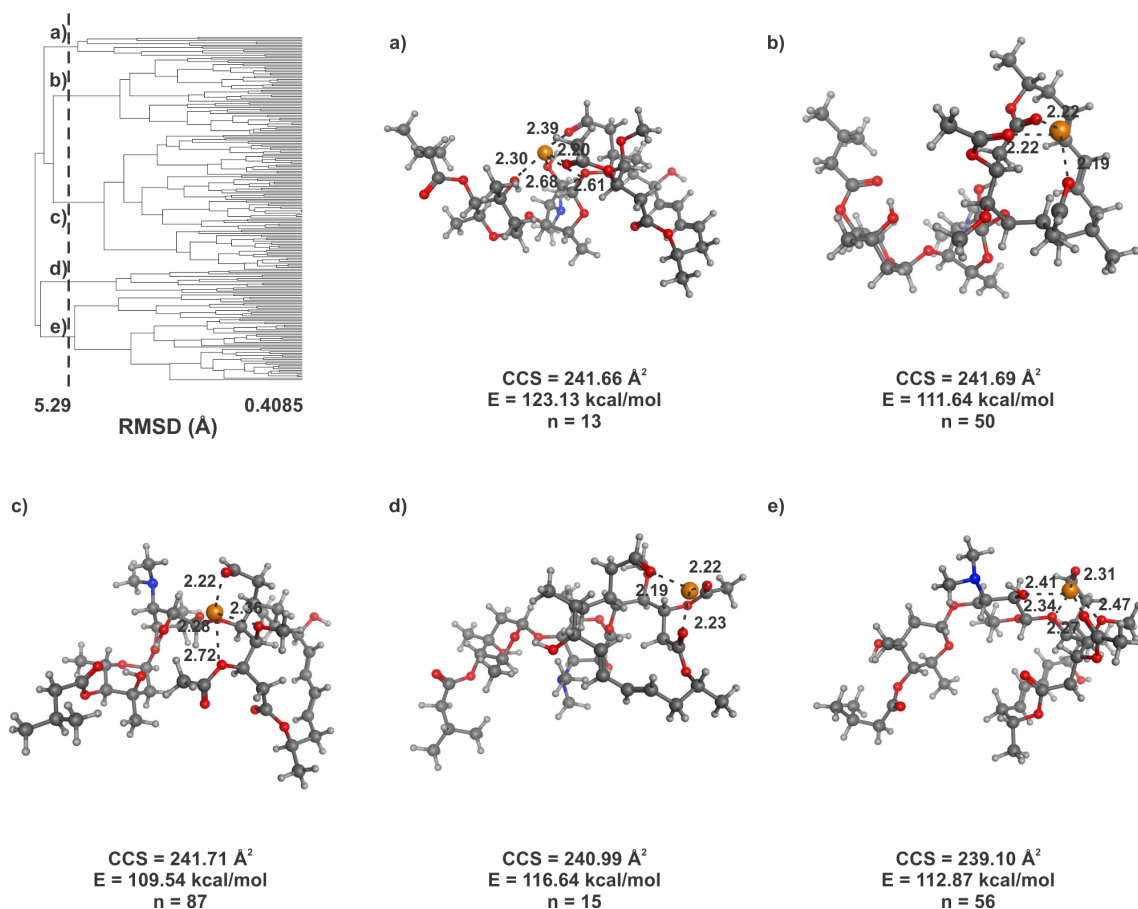


Figure C.30. Clustering analysis of 221 conformations of josamycin generated with simulated annealing that fall within the experimental CCS range. Clustering is based on root mean square distance of atoms of superimposed structures. The vertical bar indicates the RMSD cutoff (4.90 Å) used to select the shown conformations. The conformations indicated on the clustering tree are shown with corresponding letters. Carbon atoms are shown in dark grey, hydrogen in light grey, oxygen in red, nitrogen in blue, and sodium in orange. Each conformation is labeled with its theoretical CCS value, its theoretical energy, and the number of conformations it represents from the clustering analysis.

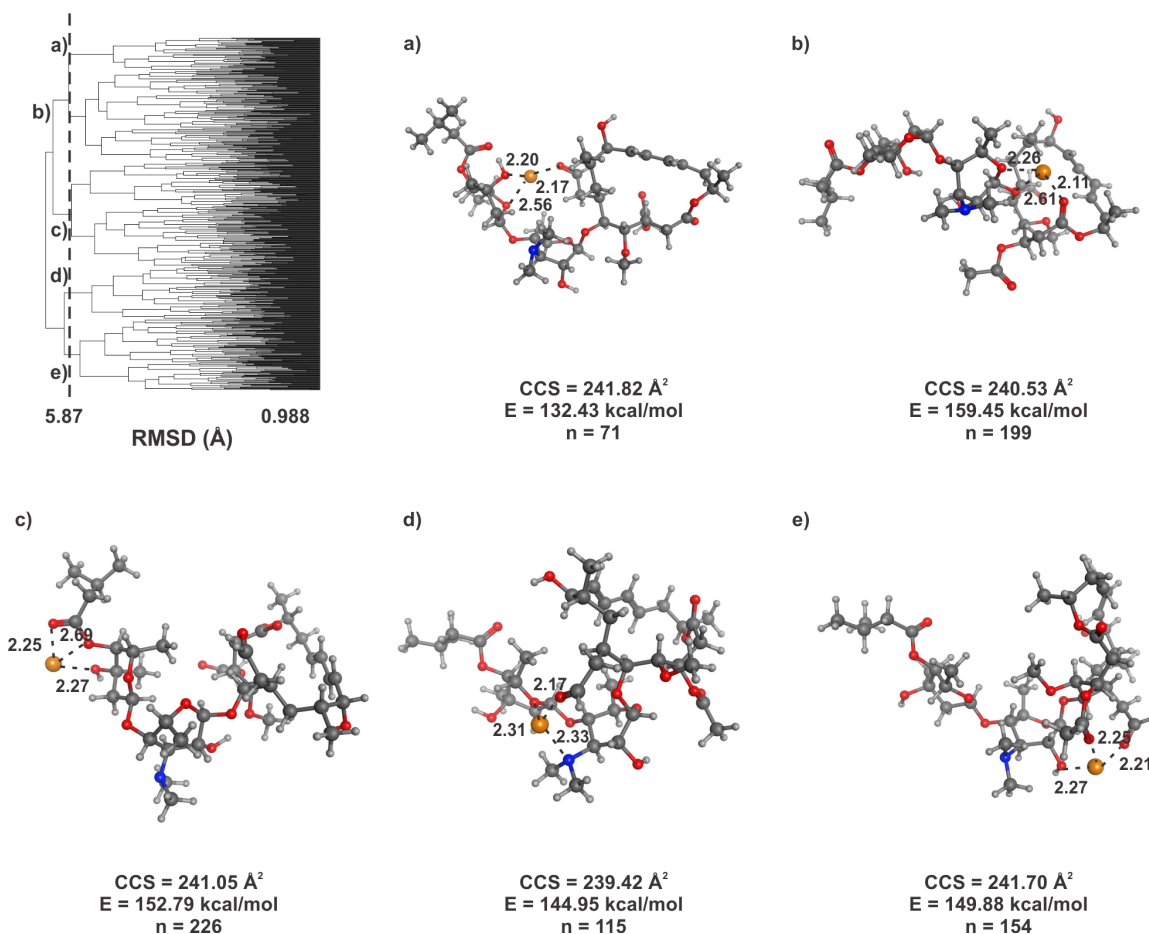


Figure C.31. Clustering analysis of 765 conformations of josamycin generated with distance geometry and the molecular mechanics energy minimization that fall within the experimental CCS range. Clustering is based on root mean square distance of atoms of superimposed structures. The vertical bar indicates the RMSD cutoff (5.45 Å) used to select the shown conformations. The conformations indicated on the clustering tree are shown with corresponding letters. Carbon atoms are shown in dark grey, hydrogen in light grey, oxygen in red, nitrogen in blue, and sodium in orange. Each conformation is labeled with its theoretical CCS value, its theoretical energy, and the number of conformations it represents from the clustering analysis.

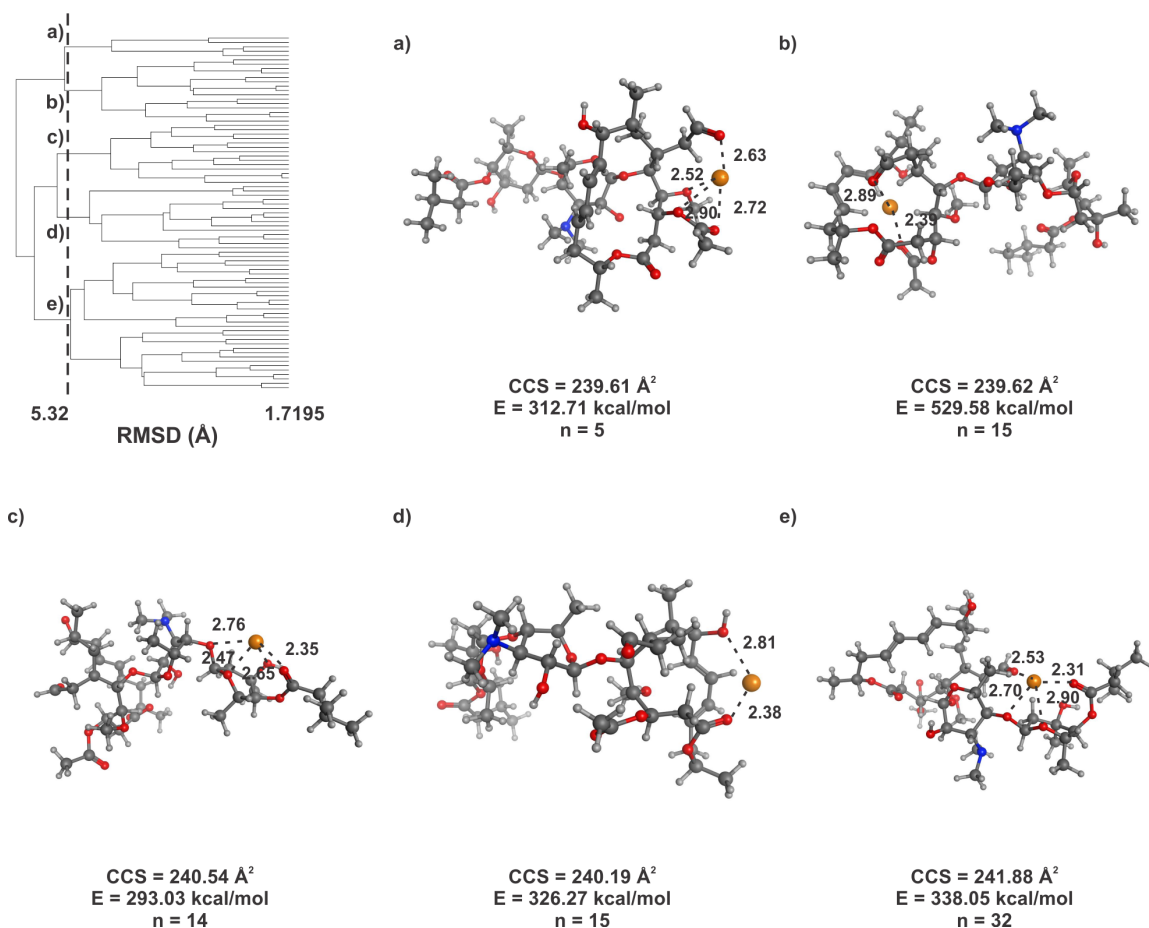


Figure C.32. Clustering analysis of 81 conformations of josamycin generated with distance geometry and the QM geometry optimization that fall within the experimental CCS range. Clustering is based on root mean square distance of atoms of superimposed structures. The vertical bar indicates the RMSD cutoff (4.60 Å) used to select the shown conformations. The conformations indicated on the clustering tree are shown with corresponding letters. Carbon atoms are shown in dark grey, hydrogen in light grey, oxygen in red, nitrogen in blue, and sodium in orange. Each conformation is labeled with its theoretical CCS value, its theoretical energy, and the number of conformations it represents from the clustering analysis.

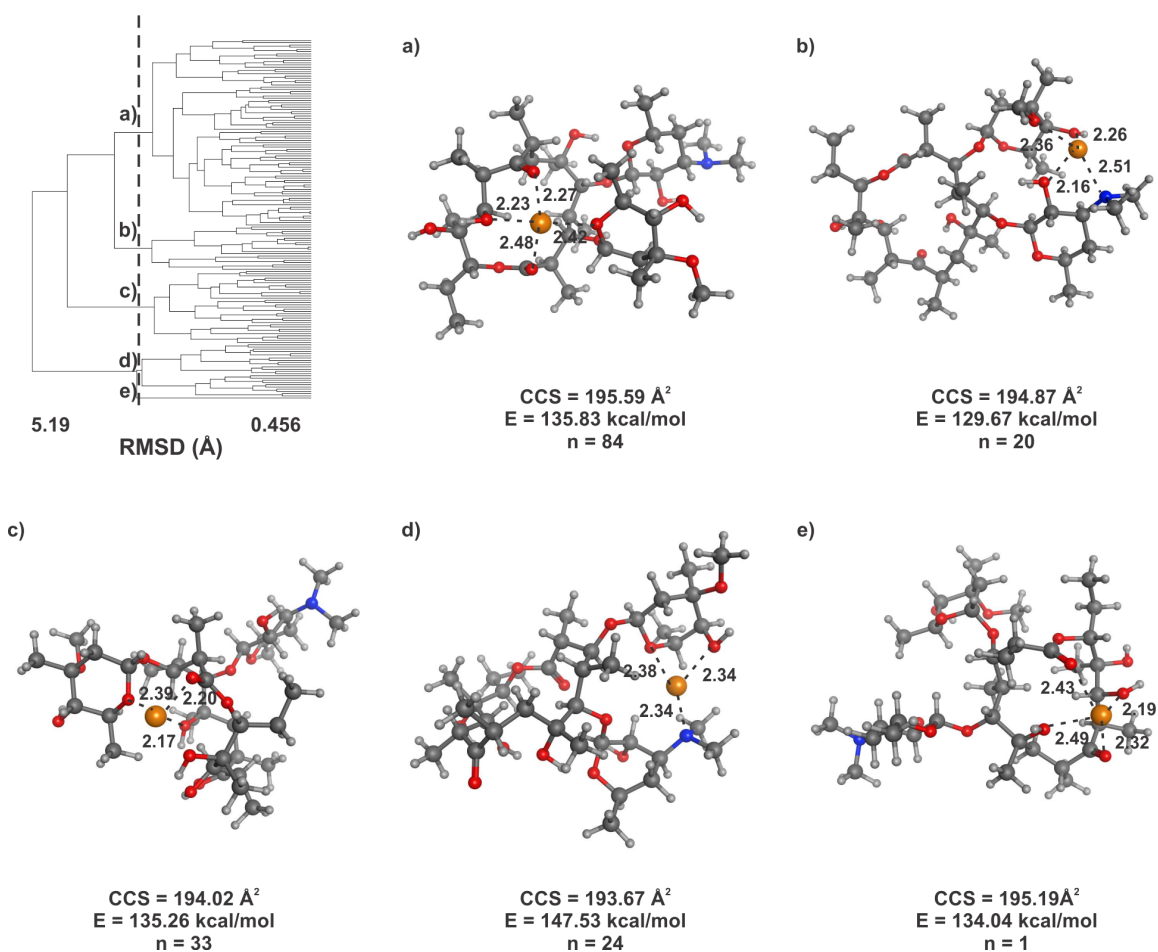


Figure C.33. Clustering analysis of 162 conformations of erythromycin generated with simulated annealing that fall within the experimental CCS range. Clustering is based on root mean square distance of atoms of superimposed structures. The vertical bar indicates the RMSD cutoff (3.40 Å) used to select the shown conformations. The conformations indicated on the clustering tree are shown with corresponding letters. Carbon atoms are shown in dark grey, hydrogen in light grey, oxygen in red, nitrogen in blue, and sodium in orange. Each conformation is labeled with its theoretical CCS value, its theoretical energy, and the number of conformations it represents from the clustering analysis.

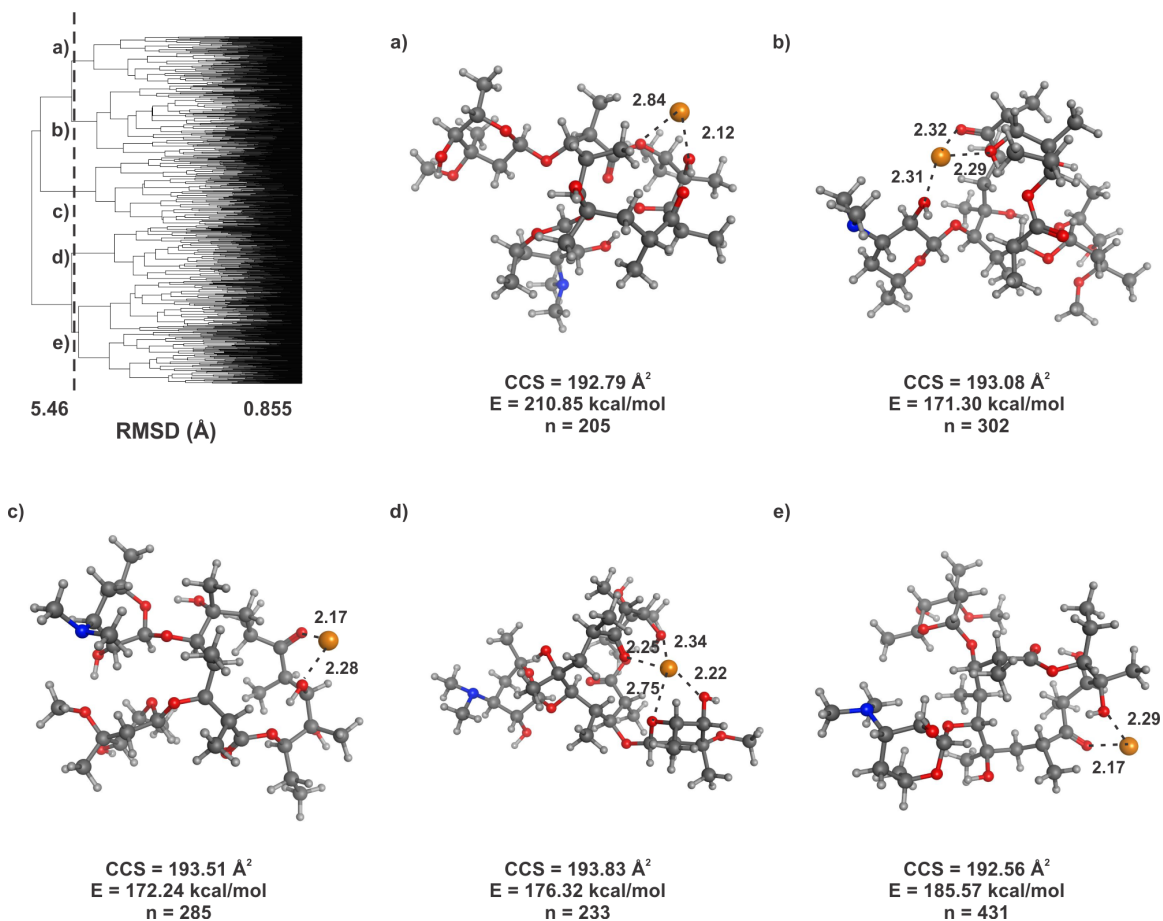


Figure C.34. Clustering analysis of 1456 conformations of erythromycin generated with distance geometry that fall within the experimental CCS range. Clustering is based on root mean square distance of atoms of superimposed structures. The vertical bar indicates the RMSD cutoff (4.70 Å) used to select the shown conformations. The conformations indicated on the clustering tree are shown with corresponding letters. Carbon atoms are shown in dark grey, hydrogen in light grey, oxygen in red, nitrogen in blue, and sodium in orange. Each conformation is labeled with its theoretical CCS value, its theoretical energy, and the number of conformations it represents from the clustering analysis.

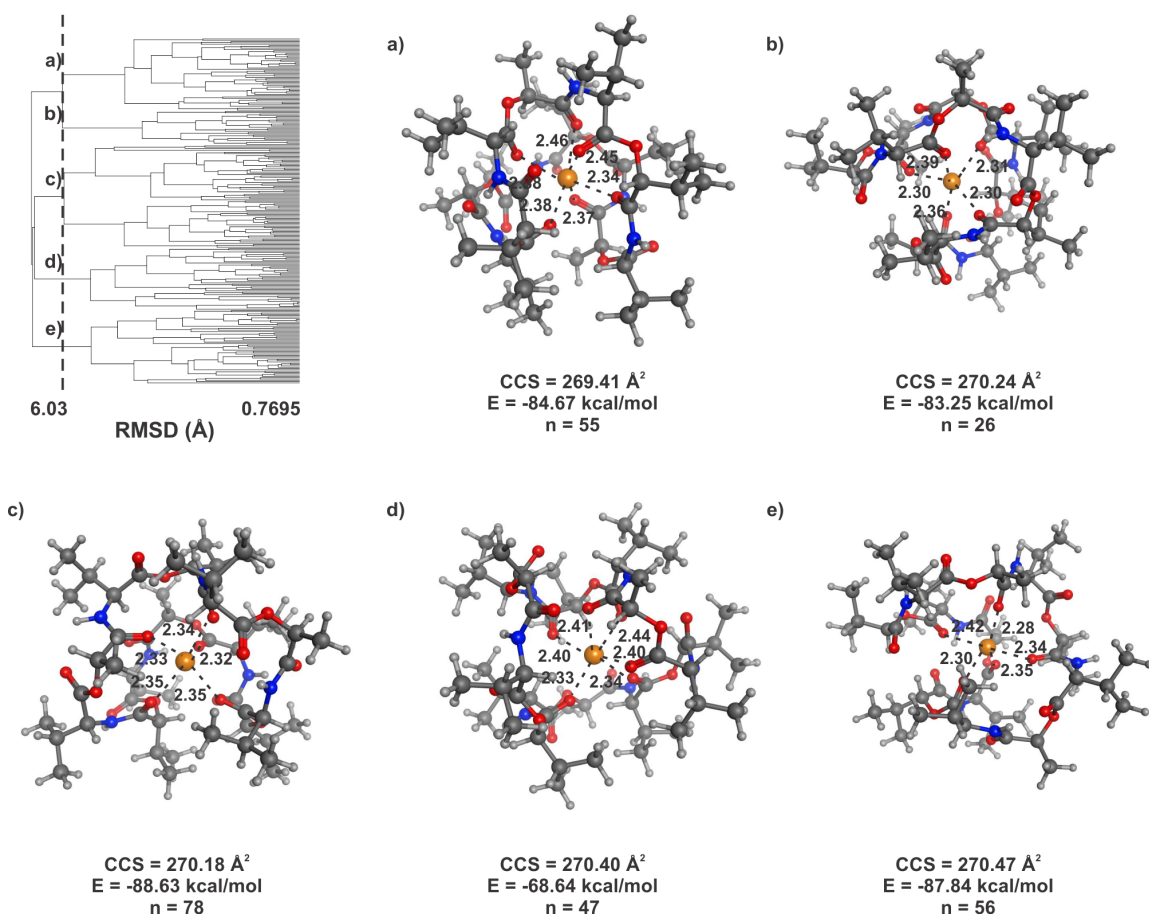


Figure C.35. Clustering analysis of 262 conformations of valinomycin generated with simulated annealing fall within the experimental CCS range. Clustering is based on root mean square distance of atoms of superimposed structures. The vertical bar indicates the RMSD cutoff (5.40 Å) used to select the shown conformations. The conformations indicated on the clustering tree are shown with corresponding letters. Carbon atoms are shown in dark grey, hydrogen in light grey, oxygen in red, nitrogen in blue, and sodium in orange. Each conformation is labeled with its theoretical CCS value, its theoretical energy, and the number of conformations it represents from the clustering analysis.

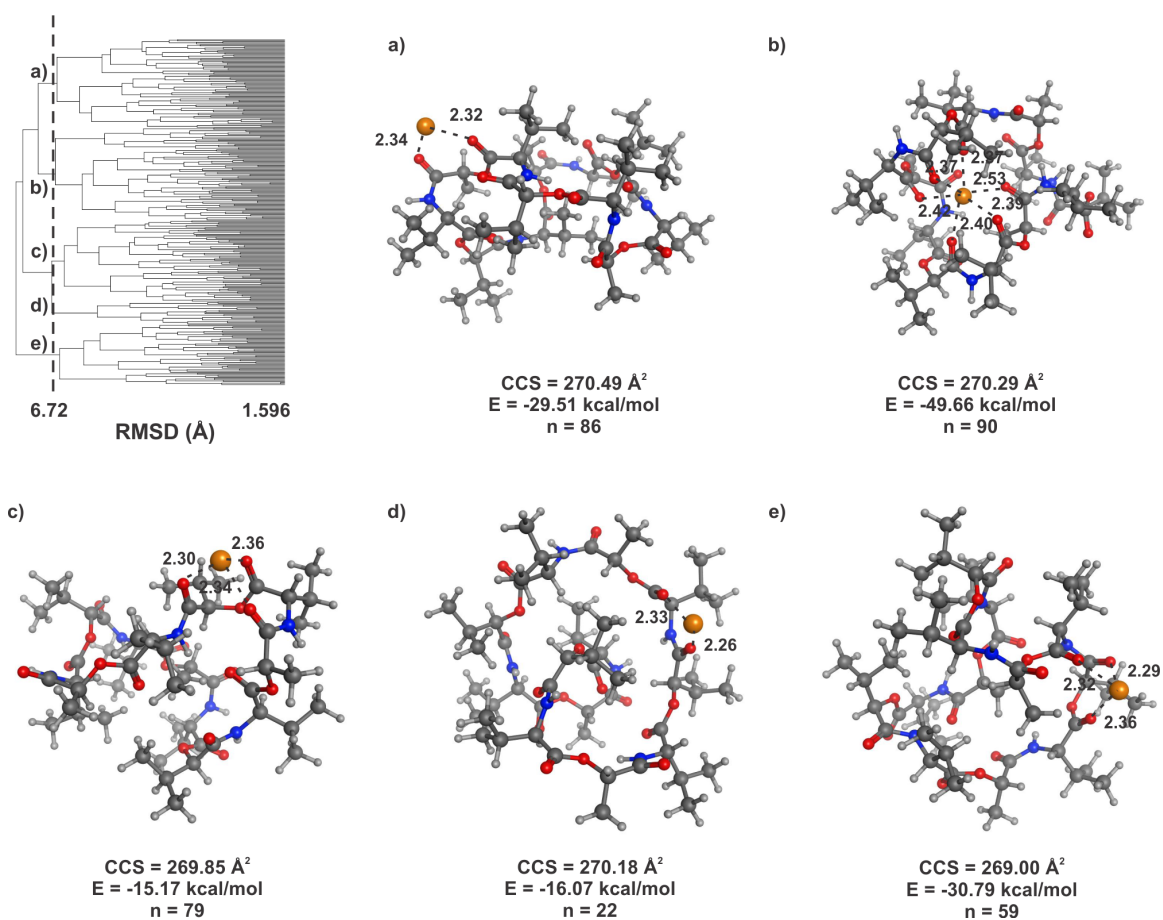


Figure C.36. Clustering analysis of 336 conformations of valinomycin generated with distance geometry that fall within the experimental CCS range. Clustering is based on root mean square distance of atoms of superimposed structures. The vertical bar indicates the RMSD cutoff (6.00 Å) used to select the shown conformations. The conformations indicated on the clustering tree are shown with corresponding letters. Carbon atoms are shown in dark grey, hydrogen in light grey, oxygen in red, nitrogen in blue, and sodium in orange. Each conformation is labeled with its theoretical CCS value, its theoretical energy, and the number of conformations it represents from the clustering analysis.

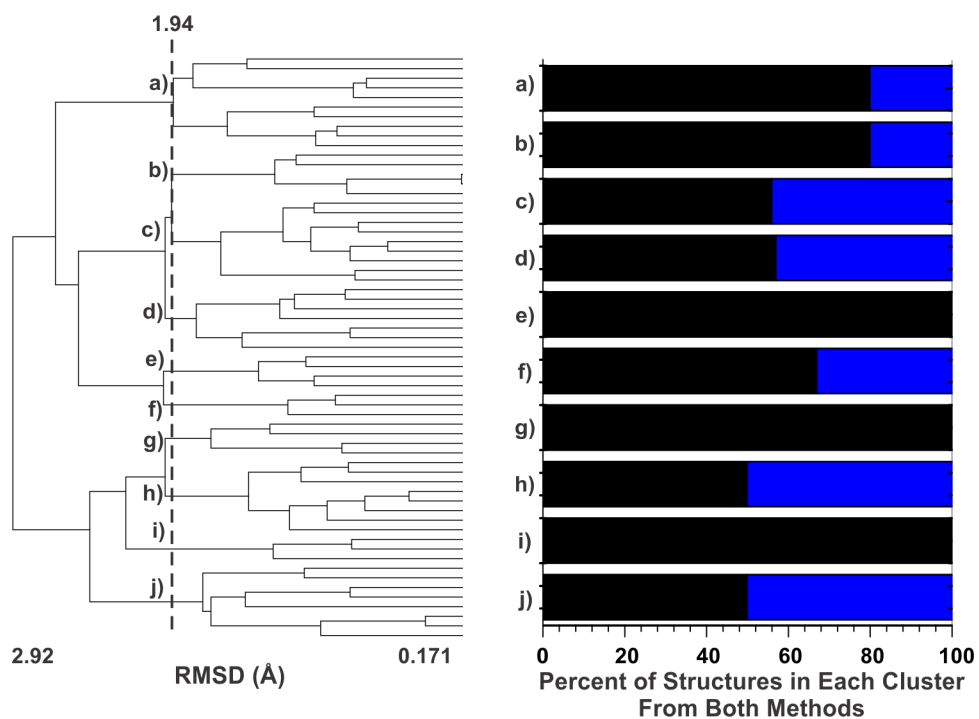


Figure C.37. Clustering analysis for the structures that align with the experimental CCS for doxorubicin from both distance geometry and simulated annealing. The structures are clustered into 10 unique clusters according to RMSD (1.94 Å) as indicated by the vertical dashed line on the cluster tree on the left. The percentage of conformations in each of the 10 clusters from either distance geometry (black) or simulated annealing (blue) is displayed in the histogram on the right.

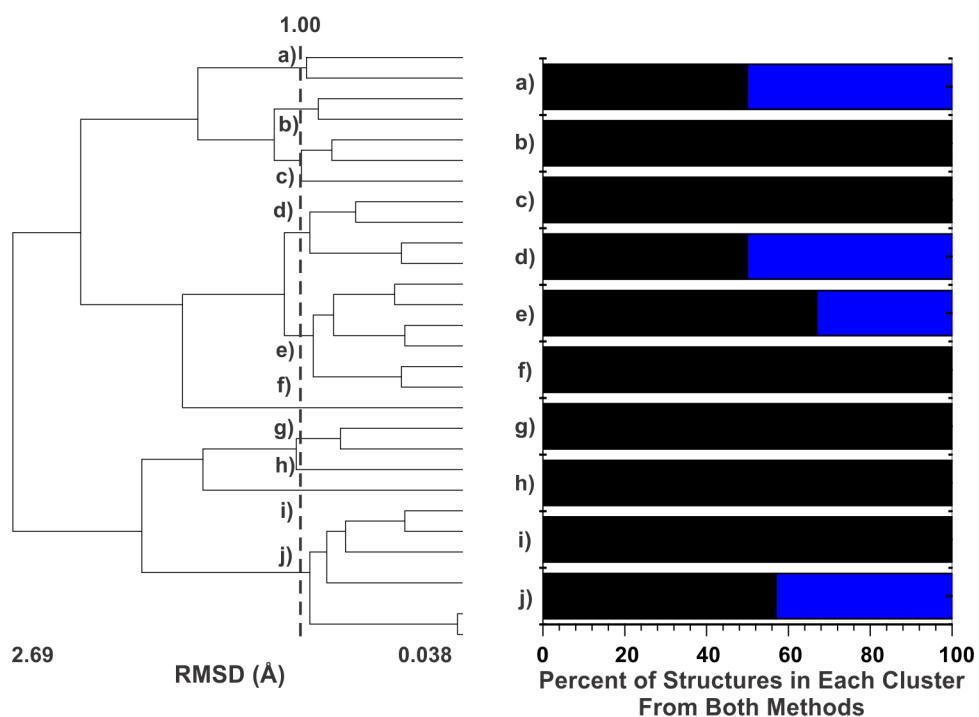


Figure C.38. Clustering analysis for the structures that align with the experimental CCS for capsaicin from both distance geometry and simulated annealing. The structures are clustered into 10 unique clusters according to RMSD (1.00 Å) as indicated by the vertical dashed line on the cluster tree on the left. The percentage of conformations in each of the 10 clusters from either distance geometry (black) or simulated annealing (blue) is displayed in the histogram on the right.

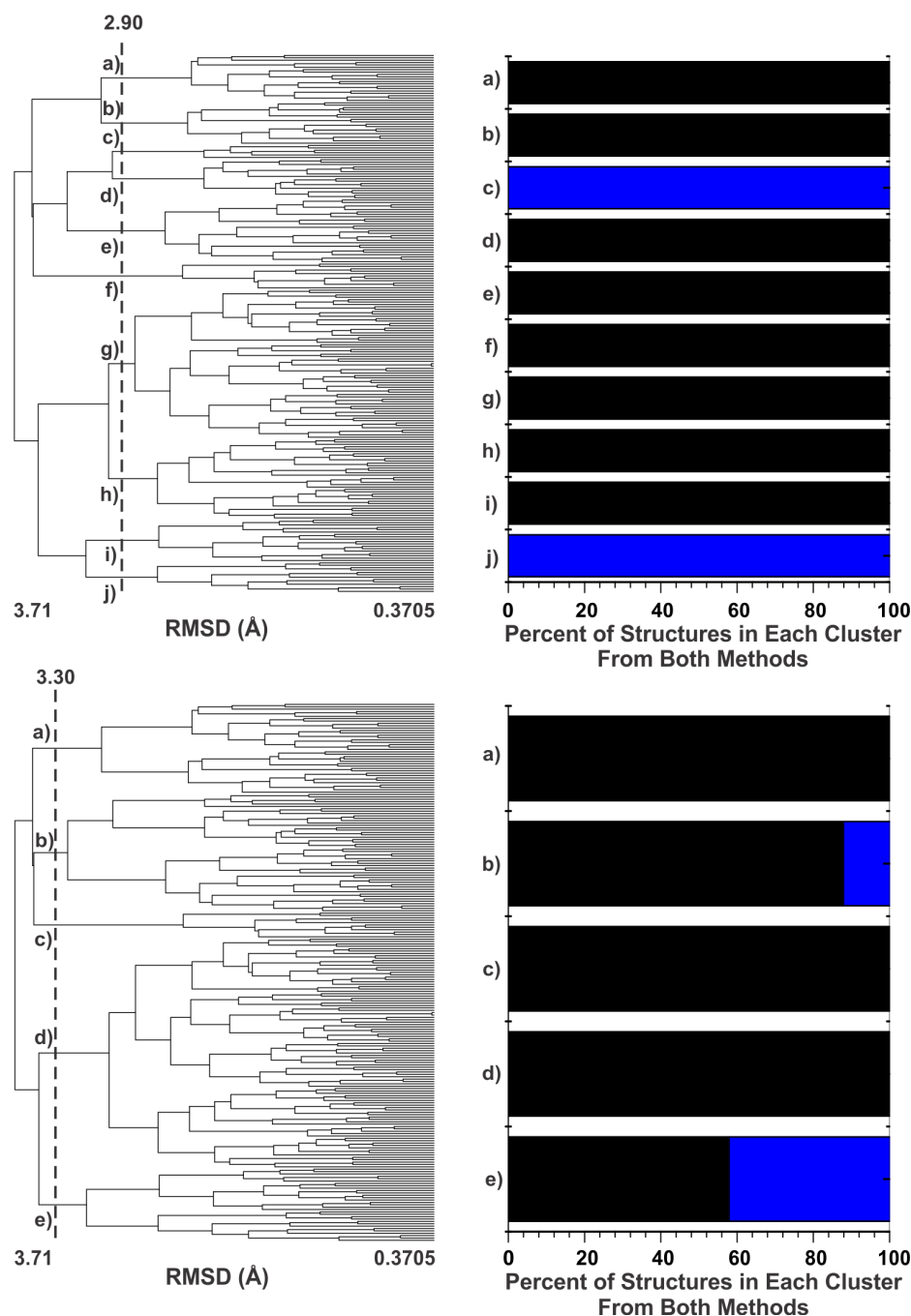


Figure C.39. Clustering analysis for the structures that align with the experimental CCS for lincomycin from both distance geometry and simulated annealing. The structures are clustered into both 10 and 5 unique clusters according to RMSD (2.90 and 3.30 Å) as indicated by the vertical dashed line on the cluster trees on the left. The percentage of conformations in each of the 10 or 5 clusters from either distance geometry (black) or simulated annealing (blue) is displayed in the histogram on the right. Analysis was performed on both 10 and 5 clusters to achieve structures from both methods in the same RMSD cluster.

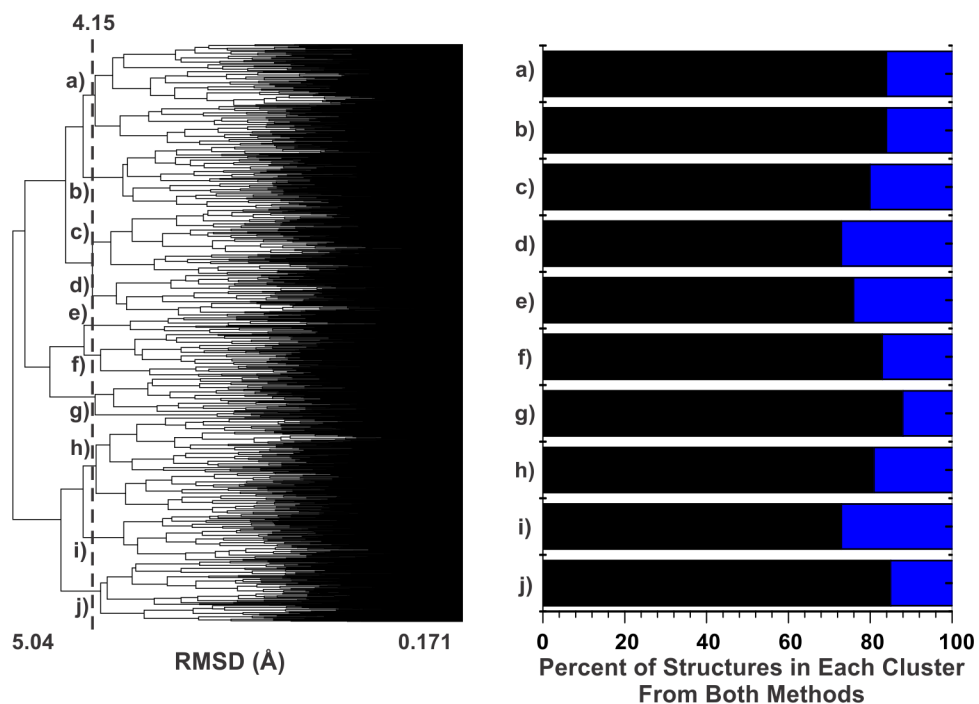


Figure C.40. Clustering analysis for the structures that align with the experimental CCS for neomycin from both distance geometry and simulated annealing. The structures are clustered into 10 unique clusters according to RMSD (4.15 Å) as indicated by the vertical dashed line on the cluster tree on the left. The percentage of conformations in each of the 10 clusters from either distance geometry (black) or simulated annealing (blue) is displayed in the histogram on the right.

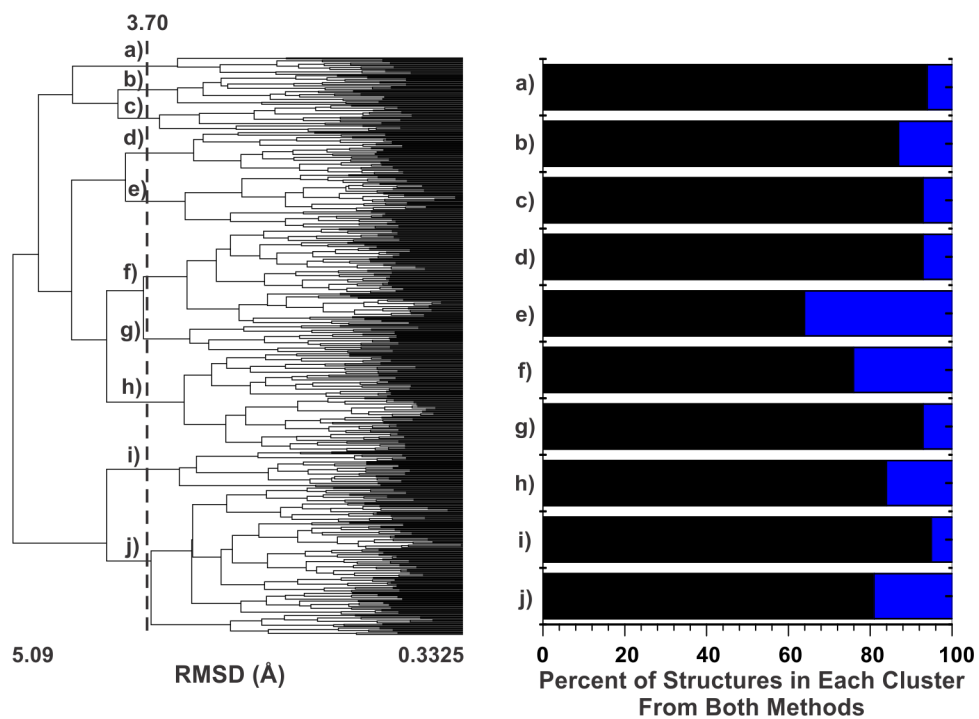


Figure C.41. Clustering analysis for the structures that align with the experimental CCS for antimycin from both distance geometry and simulated annealing. The structures are clustered into 10 unique clusters according to RMSD (3.70 \AA) as indicated by the vertical dashed line on the cluster tree on the left. The percentage of conformations in each of the 10 clusters from either distance geometry (black) or simulated annealing (blue) is displayed in the histogram on the right.

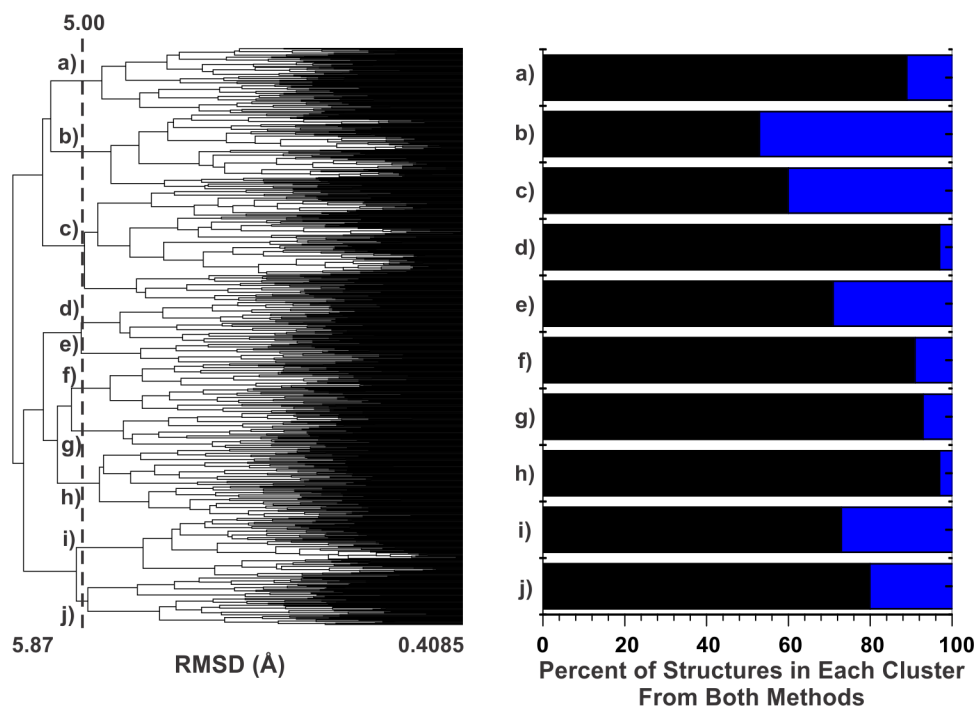


Figure C.42. Clustering analysis for the structures that align with the experimental CCS for josamycin from both distance geometry and simulated annealing. The structures are clustered into 10 unique clusters according to RMSD (5.00 Å) as indicated by the vertical dashed line on the cluster tree on the left. The percentage of conformations in each of the 10 clusters from either distance geometry (black) or simulated annealing (blue) is displayed in the histogram on the right.

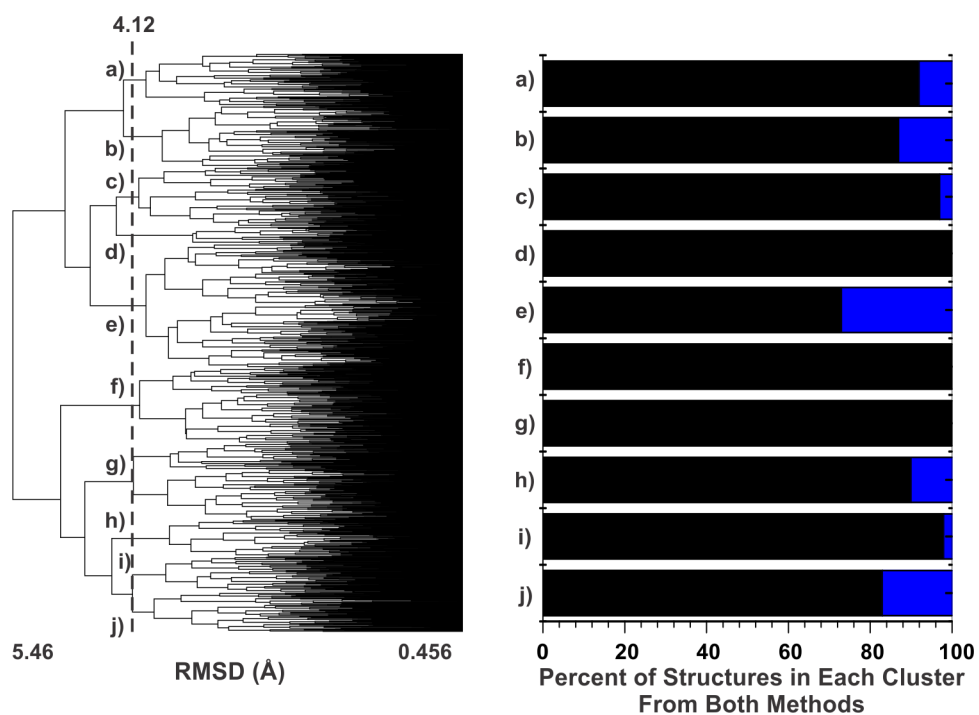


Figure C.43. Clustering analysis for the structures that align with the experimental CCS for erythromycin from both distance geometry and simulated annealing. The structures are clustered into 10 unique clusters according to RMSD (4.12 Å) as indicated by the vertical dashed line on the cluster tree on the left. The percentage of conformations in each of the 10 clusters from either distance geometry (black) or simulated annealing (blue) is displayed in the histogram on the right.

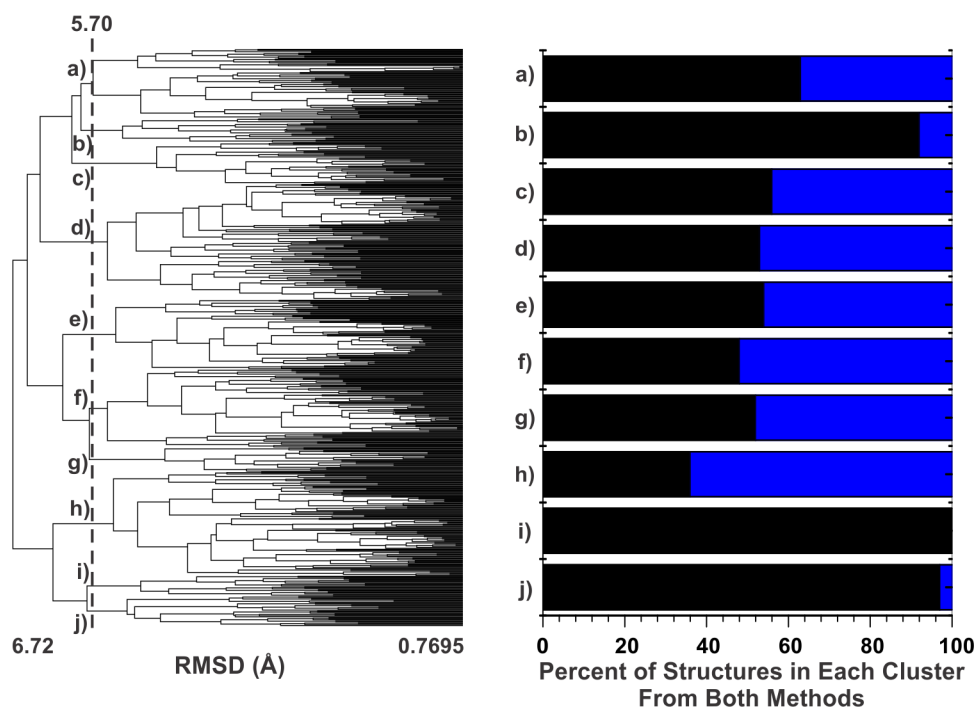


Figure C.44. Clustering analysis for the structures that align with the experimental CCS for valinomycin from both distance geometry and simulated annealing. The structures are clustered into 10 unique clusters according to RMSD (5.70 \AA) as indicated by the vertical dashed line on the cluster tree on the left. The percentage of conformations in each of the 10 clusters from either distance geometry (black) or simulated annealing (blue) is displayed in the histogram on the right.

APPENDIX D

SUPPLEMENTARY MATERIALS FOR CHAPTER IV

Table D.1. Initial Parameterization and Theoretical CCS Calculations for Selected metabolites are displayed below. The initial parameterization includes a geometry optimization and an electrostatic potential grid calculation.

<i>Molecule</i>	<i>CPU Time</i>
<i>Initial Parameterization (m/z, method)</i>	
Lactic acid [M] (90.03, HF)	4 min 54 sec
Biotin [M] (244.09, HF)	2 hours 22 min 47 sec
Maltopentose [M] (828.27, HF)	1 day 3 hours 43 min 31 sec
Amphetamine [M] (135.10, HF)	14 min 26 sec
Amphetamine [M+H] ⁺ (136.11, PM6)	42 sec
Verapamil [M] (454.28, HF)	15 hours 24 min 56 sec
Verapamil [M+H] ⁺ (455.29, PM6)	30 min 34 sec
<i>Theoretical CCS Calculation (m/z, method, number of structures)</i>	
Colchicine [M+Na] ⁺ (422.16, PA, 30)	1 min. 44 sec.
Colchicine [M+Na] ⁺ (422.16, PSA, 30)	21 min. 39 sec.
Fucose [M+Na] ⁺ (187.06, TM, 2)	~ 1 day
Raffinose [M+Na] ⁺ (527.16, TM, 2)	~ 4 days

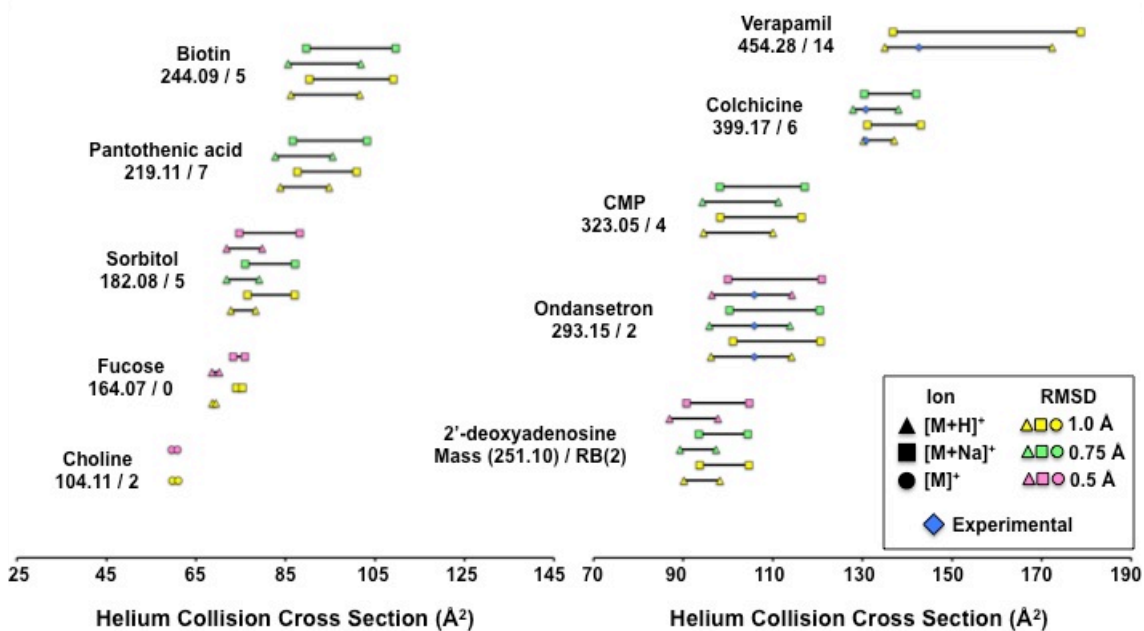


Figure D.1. Determination of RMSD cutoff for distance geometry calculations is based on the data in this plot. The CCS is on the x-axis and the theoretical ranges are plotted for these 10 metabolites for different RMSD cutoff values used in the distance geometry calculation to determine how this affects the conformational space sampled. The yellow indicates a cutoff of 1.0 Å, the green a cutoff of 0.75 Å, and the pink a cutoff of 0.5 Å. The different shapes represent different gas phase ions. Based on the results above, a 0.5 Å cutoff was used for metabolites with a molecular weight less than 200 Da, a 0.75 Å cutoff was used for metabolites with a molecular weight less between 200 and 400 Da, and a 1.0 Å cutoff was used for metabolites with a molecular weight more than 400 Da.

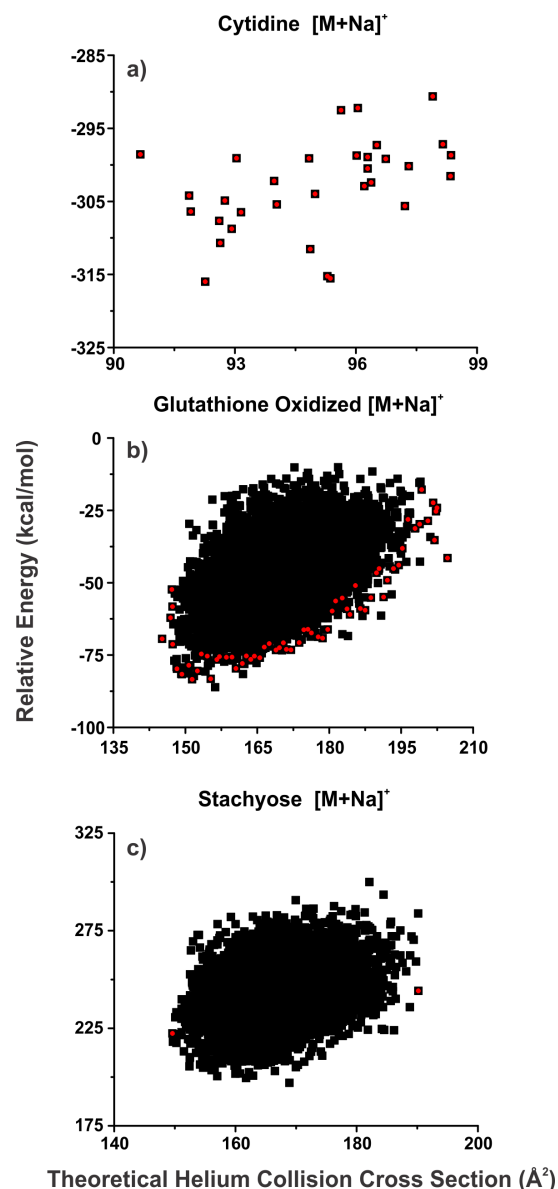


Figure D.2. Sample theoretical conformational space plots to show which conformations were selected for nitrogen CCS calculations. The data is shown for helium, and the conformations that were used for nitrogen are shown in red. For metabolites where 100 or less conformations were generated with distance geometry they were all submitted to PSA N₂ calculations as shown in a) for cytidine. When more than 100 conformations were generated with distance geometry as shown in b) for glutathione oxidized low energy conformations than span the CCS range were selected for the PSA N₂ calculations. For molecules that do not contain the appropriate ratio of carbon, oxygen and nitrogen atoms as is the case for stachyose as shown in c) the trajectory method in MOBCAL must be used to get nitrogen CCS value. This calculation is very computationally expensive and only the smallest and largest CCS conformations are used to the MOBCAL N₂ calculation.

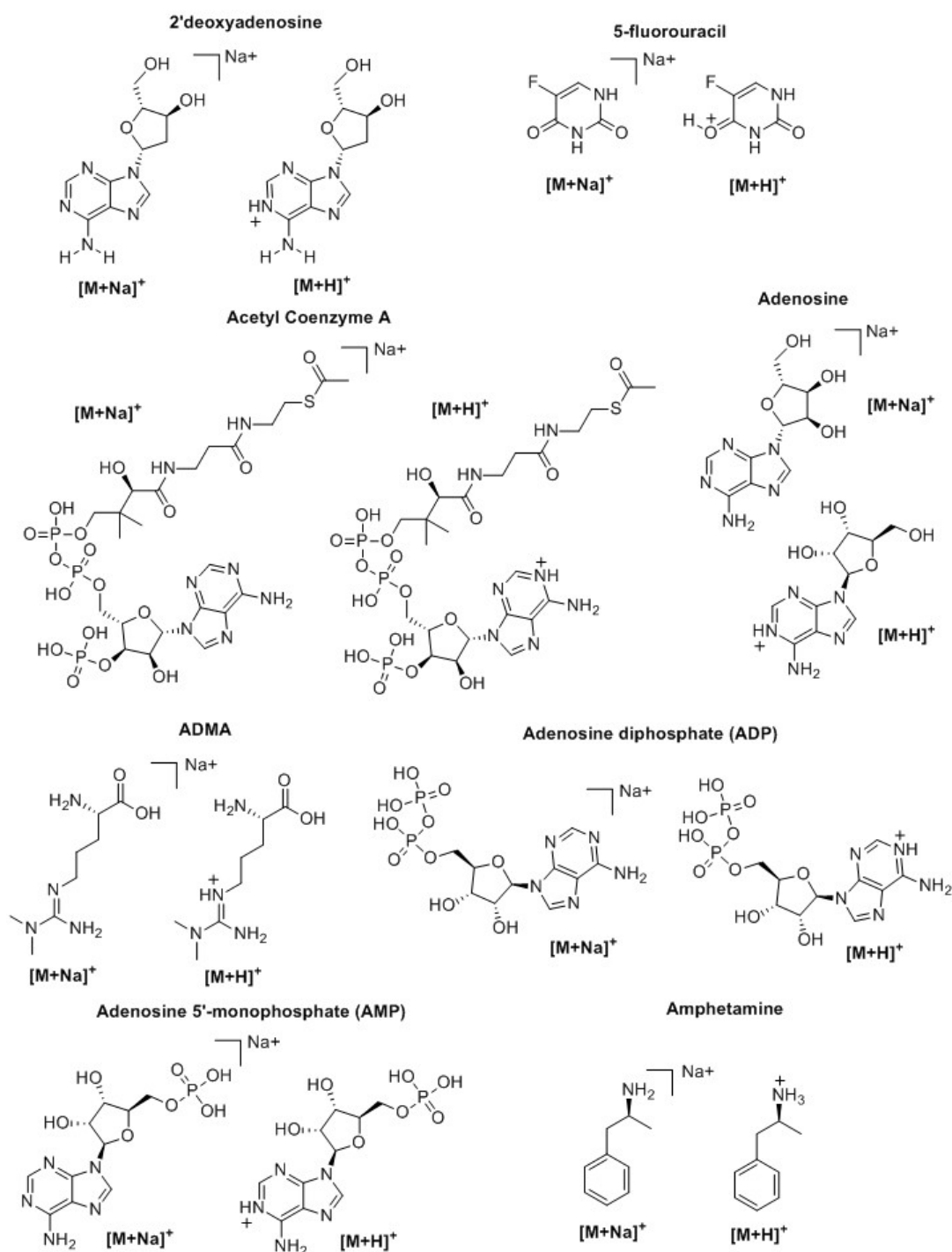


Figure D.3. Structures of the metabolites examined in the study. The cation coordinating species as well as the attached protonated species are shown.

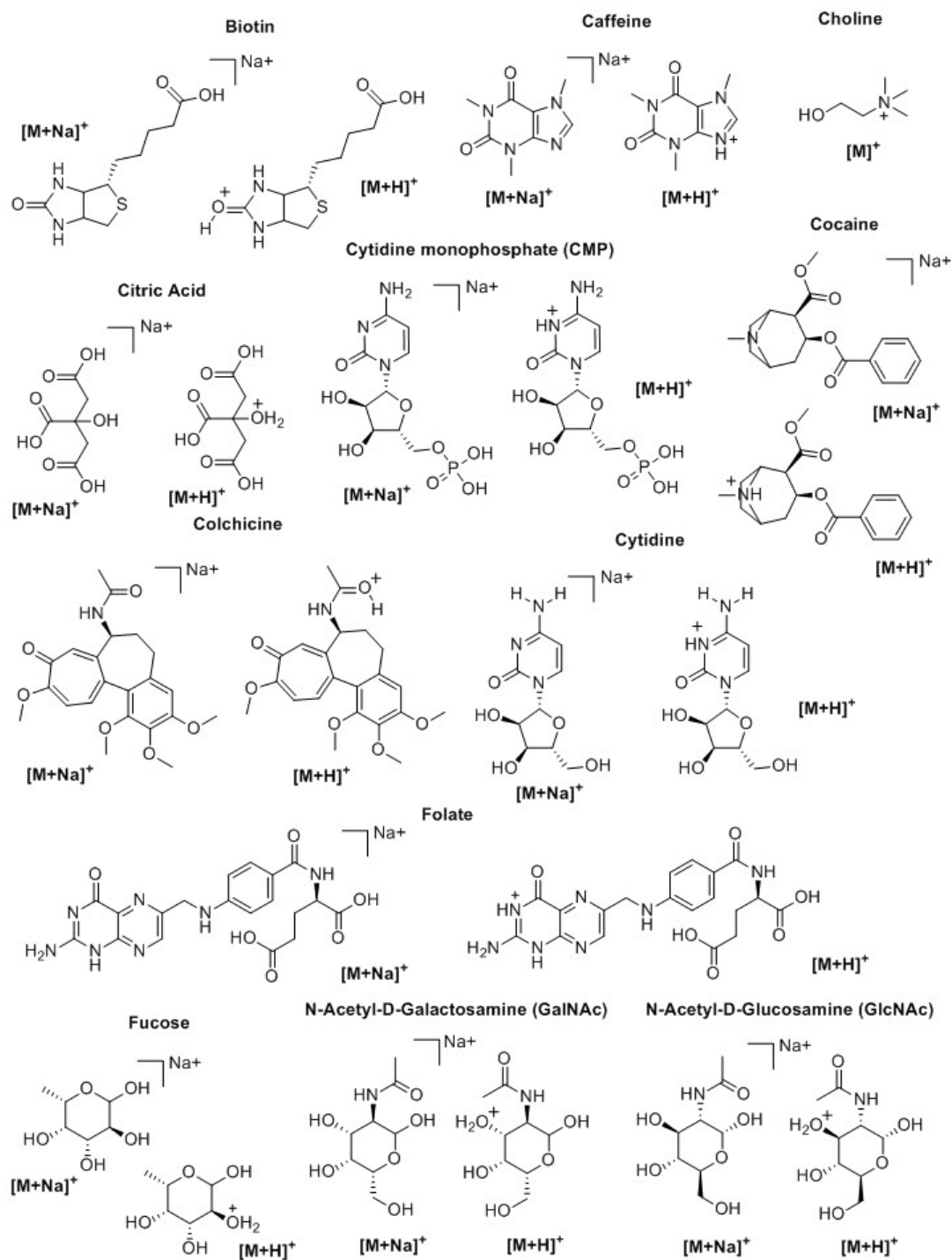


Figure D.4. Structures of the metabolites examined in the study. The cation coordinating species as well as the attached protonated species are shown.

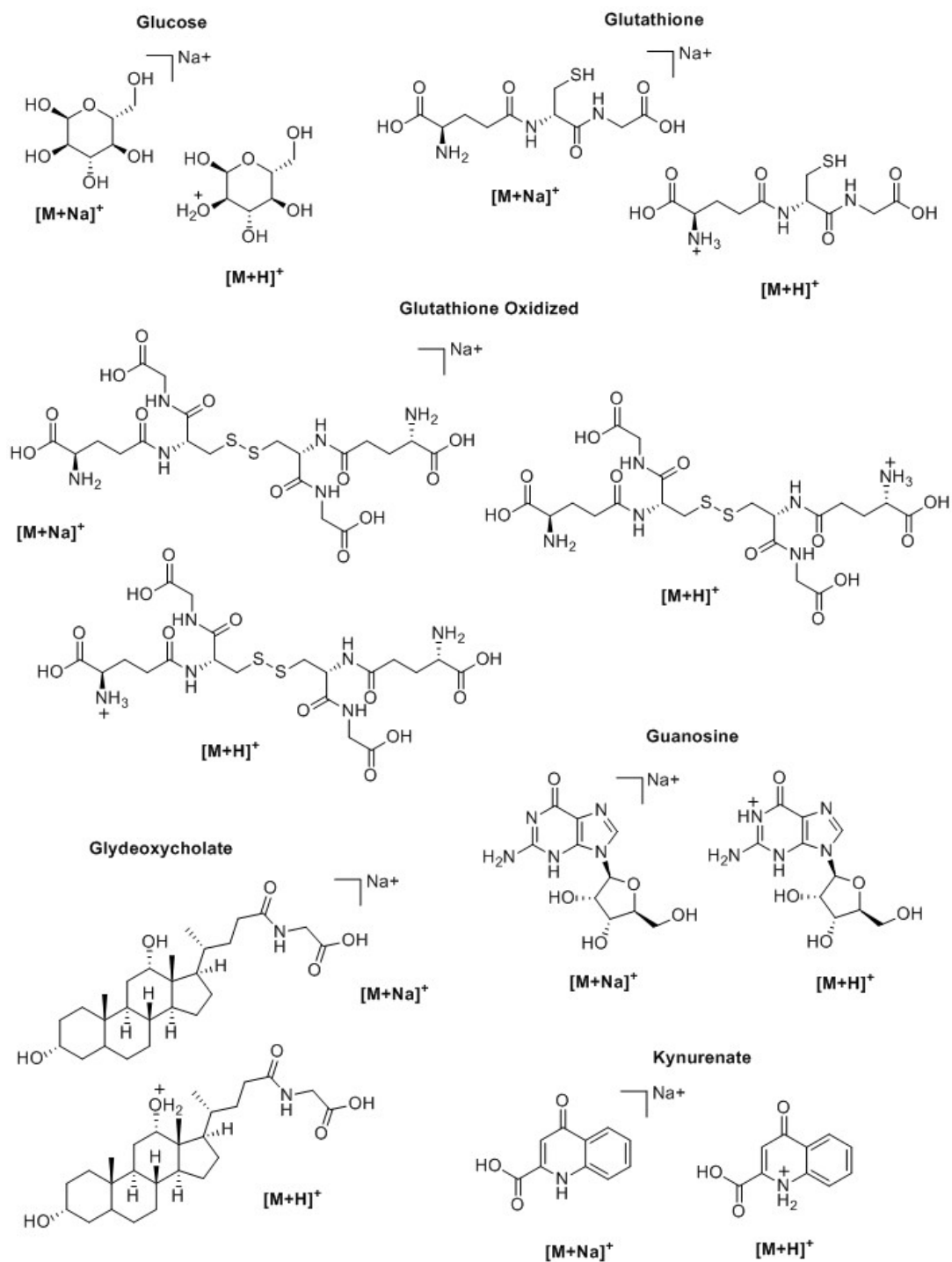


Figure D.5. Structures of the metabolites examined in the study. The cation coordinating species as well as the attached protonated species are shown.

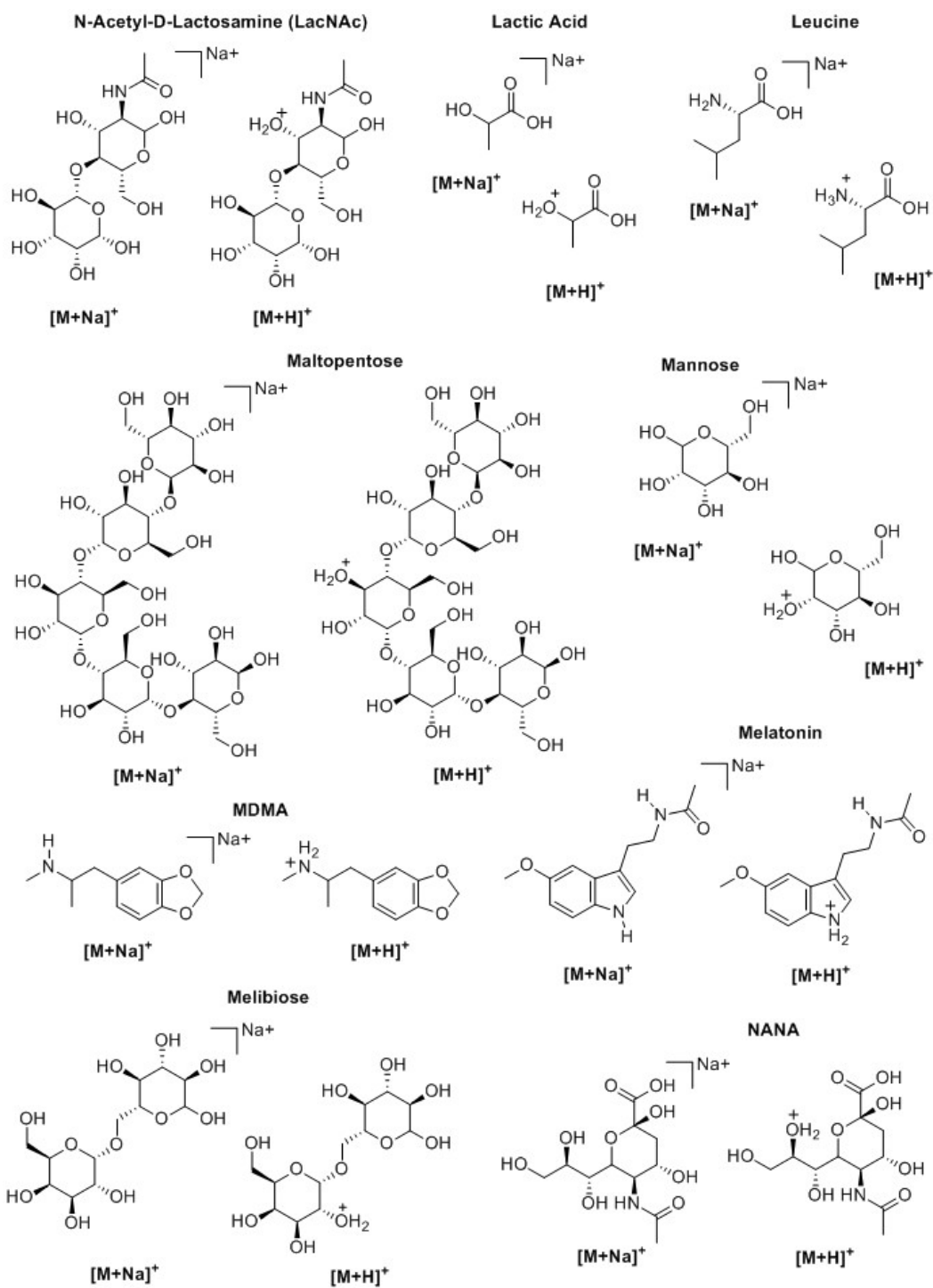


Figure D.6. Structures of the metabolites examined in the study. The cation coordinating species as well as the attached protonated species are shown.

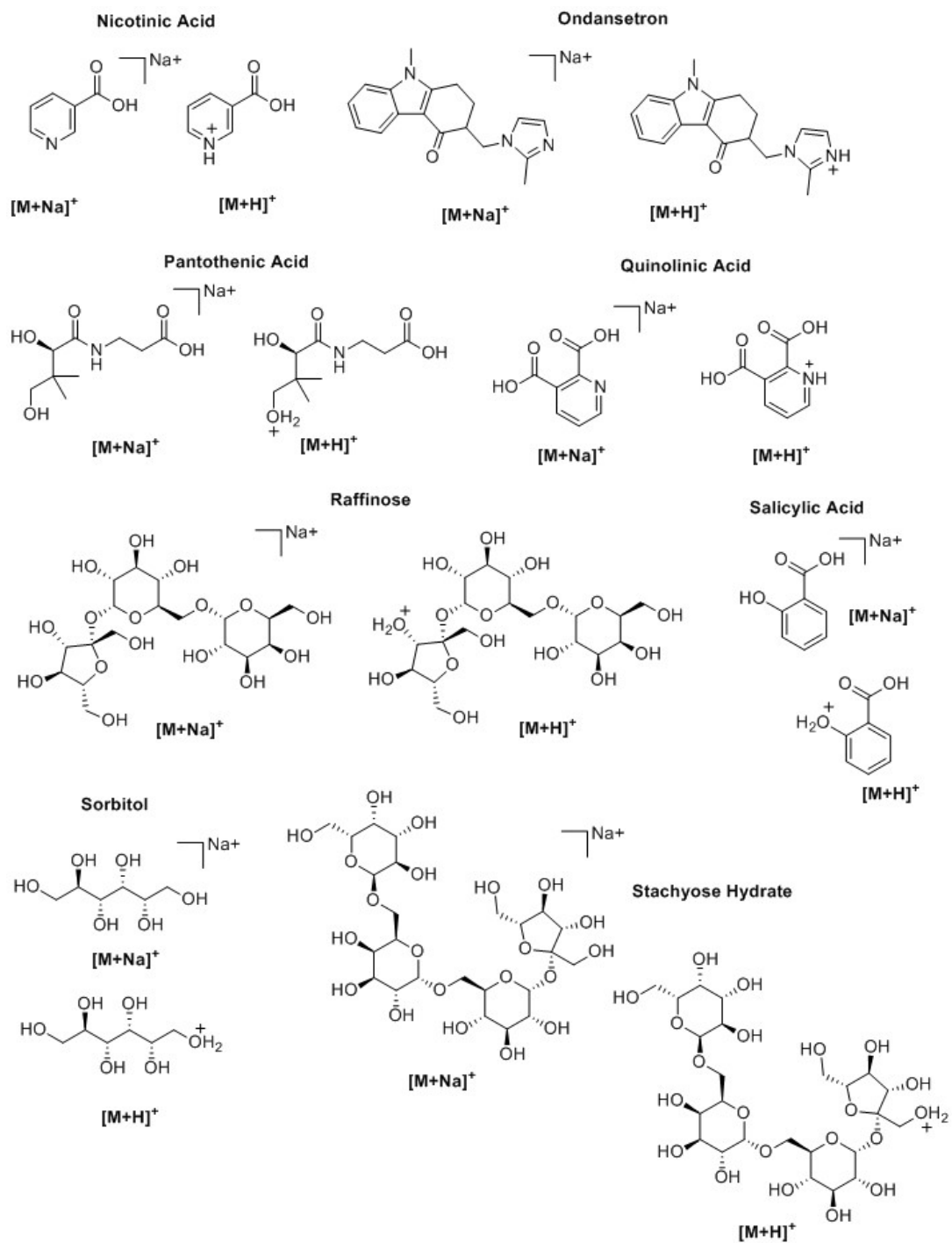


Figure D.7. Structures of the metabolites examined in the study. The cation coordinating species as well as the attached protonated species are shown.

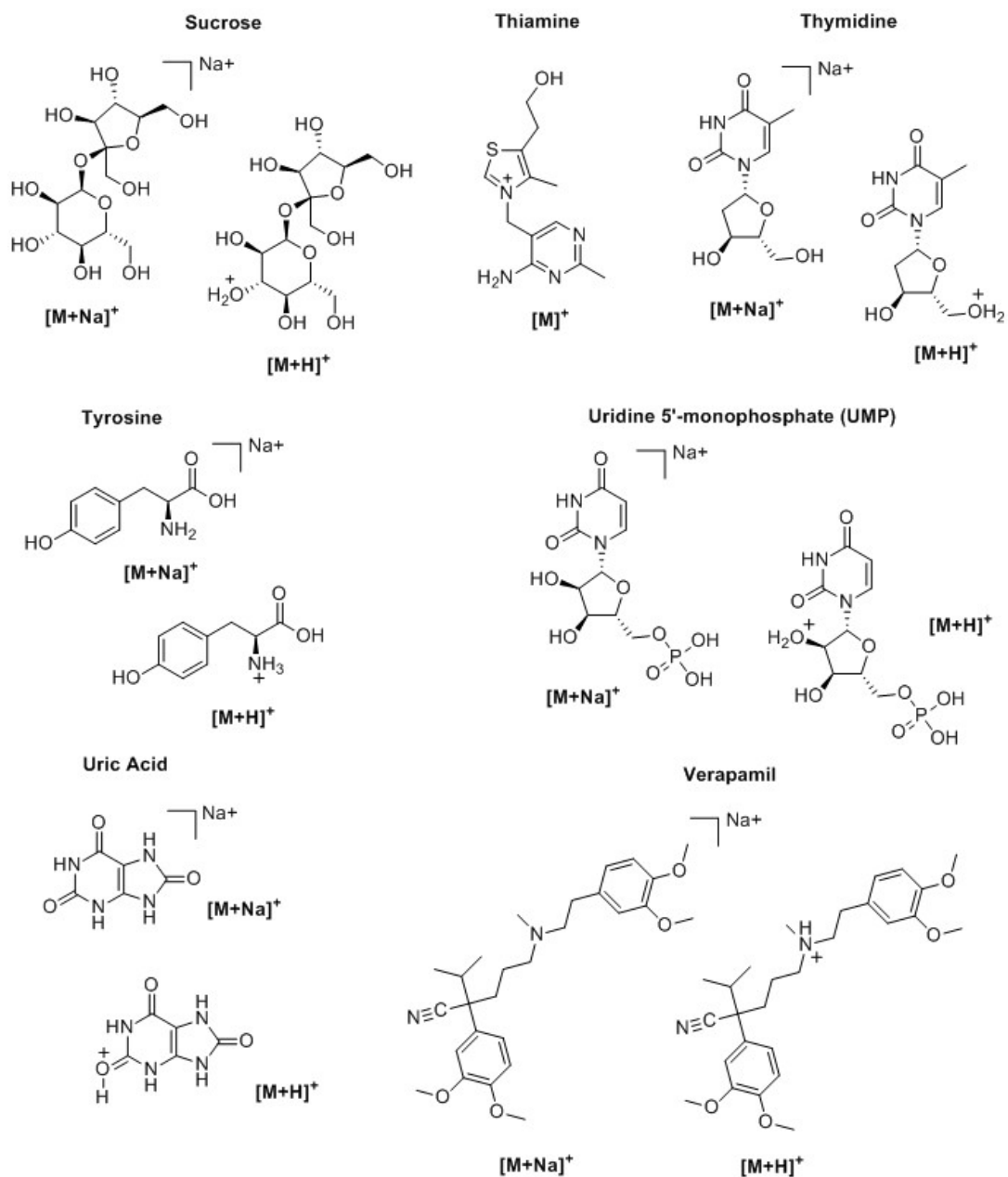


Figure D.8. Structures of the metabolites examined in the study. The cation coordinating species as well as the attached protonated species are shown.

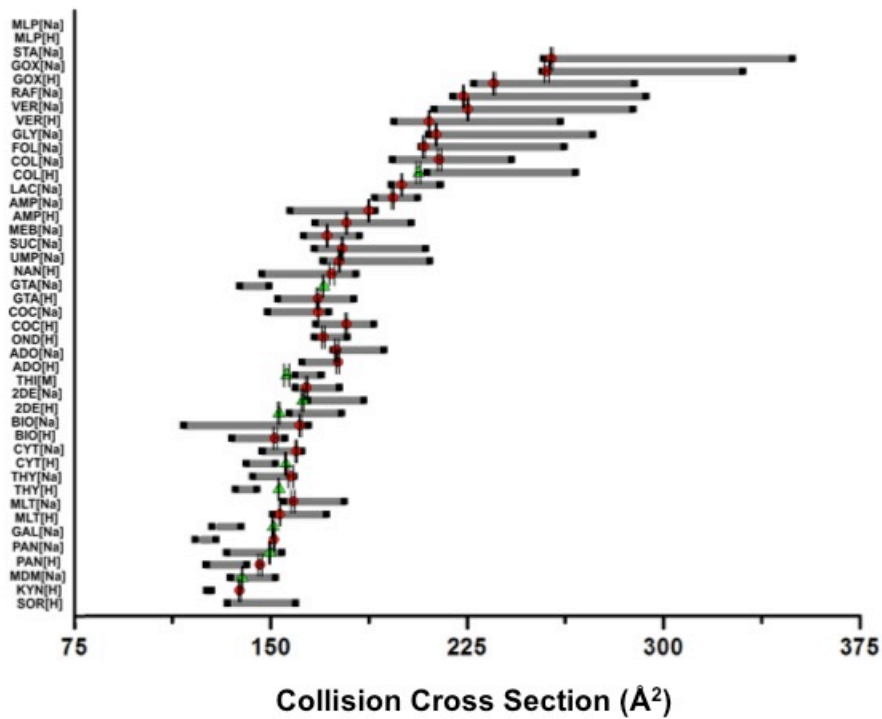


Figure D.9. Comparison of theoretical CCS ranges with experimental CCS values from DTIM mass spectrometer. Error bars have been added for the experimental CCS values.

APPENDIX E

CURRICULUM VITAE

Sarah Markley Stow

Vanderbilt University Department of Chemistry
7330 Stevenson Center
Station B 351822
Nashville, TN 37235
Lab: 615-343-4563
sarah.m.stow@vanderbilt.edu
smstow8@gmail.com

Education

Vanderbilt University, Nashville, TN

Advisor: Dr. John A. McLean
Degree expected: Ph.D. (May 4, 2015)
Current GPA: 3.49

University of Georgia, Athens, GA

Degrees Obtained: Bachelor of Science B.S. Chemistry Degree (May 2010)
Bachelor of Science Mathematics Degree (May 2012)
Cumulative GPA: 3.05
GRE Scores: Quantitative: 730, Verbal: 530, Writing: 4.0

Research Experience

Graduate Student

Structural Mass Spectrometry Laboratory (January 2011 – Present)
Advisor: Dr. John A. McLean

This interface between experimental and theoretical CCS calculations from structural IM-MS studies has been the focus of my dissertation research. Specifically, I have looked at three different classes of molecules (polymer precursors, natural products, and metabolites) and developed protocols based on existing computational methods that best offer the conformational information needed to support the experimental measurements. Selecting the appropriate computational method that accurately describes the molecule of interest and provides the desired information needed to support the experimental observations is important when structurally interpreting IM-MS results.

Dissertation Title: Strategies for Selecting Computational Protocols in Support of Small Molecule Structural Analysis by Ion Mobility-Mass Spectrometry

Publications

7. **S. M. Stow**, T. M. Onifer, J. G. Forsythe, H. Nefzger, N. W. Kwiecien, J. C. May, J. A. McLean, and D. M. Hercules, *Structural Characterization of Methylenedianiline Regioisomers by Ion Mobility-Mass Spectrometry, Tandem Mass Spectrometry, and Computational Strategies: II. Electrospray Spectra of 3-Ring and 4-Ring Isomers*, Analytical Chemistry (2015).
6. A. P. Gies, **S. M. Stow**, John A. McLean, and D. M. Hercules, *Matrix-Assisted Laser Desorption/Ionization-Time-of-Flight/Time-of-Flight Collision Induced Dissociation Study of Poly(1,4-dihydroxybenzene terephthalate) Fragmentation Reactions*, Polymer 64 (2015) 100-111.
5. **S. M. Stow**, C. R. Goodwin, M. Kliman, B. O. Bachmann, J. A. McLean, and T. P. Lybrand, *A Distance Geometry Protocol to Generate Conformations of Natural Products to Structurally Interpret Ion Mobility-Mass Spectrometry Collision Cross Sections*, Journal of Physical Chemistry B 118 (2014) 13812-13820.
4. N. G. Hendricks, N. M. Lareau, **S. M. Stow**, J. A. McLean, and R. R. Julian, *Bond-Specific Dissociation Following Excitation Energy Transfer for Distance Constraint Determination in the Gas Phase*, Journal of the American Chemical Society 136 (2014) 13363-13370.
3. J. G. Forsythe, **S. M. Stow**, H. Nefzger, N. W. Kwiecien, J. C. May, J. A. McLean, and D. M. Hercules, *Structural Characterization of Methylenedianiline Regioisomers by Ion Mobility-Mass Spectrometry, Tandem Mass Spectrometry, and Computational Strategies: I. Electrospray Spectra of 2-Ring Isomers*, Analytical Chemistry 86 (2014) 4362-4370.
2. A. P. Gies, S. T. Ellison, **S. M. Stow**, and D. M. Hercules, *Matrix-Assisted Laser Desorption/Ionization-Time-of-Flight/Time-of-Flight Collision Induced Dissociation Study of Poly(p-phenylenediamine terephthalamide) Fragmentation Reactions*, Analytica Chimica Acta 808 (2014) 124-143.
1. **S. M. Stow**, N. M. Lareau, K. M. Hines, C. R. McNeese, C. R. Goodwin, B. O. Bachmann, and J. A. McLean, *Classification of Natural Product Classes by Ion Mobility-Mass Spectrometry* in **Natural Product Analysis: Instrumentation, Methods, and Applications**. Wiley-Blackwell (2014). **Book Chapter**

Presentations

18. **S. M. Stow**, N. M. Lareau, J. C. May, T. P. Lybrand, E. E. Rennie, R. T. Kurulugama, J. C. Fjeldsted, J. A. McLean, *Fast Approach for Obtaining Theoretical Conformations for Collision Cross Section Ranges to Aid in Metabolite Identification*, 63rd American Society for Mass Spectrometry Conference on Mass Spectrometry and Allied Topics, St. Louis, MO (May 2015). **Poster**

17. J. P. Williams, J. Abdel-Khalik, Y. Wang, **S. M. Stow**, M. Towers, G. Astarita, J. Langridge, W. Griffiths, *The Analysis of Bile Acids: Enhancement of Specificity Using an Ion Mobility-TOFMS Based Approach*, 63rd American Society for Mass Spectrometry Conference on Mass Spectrometry and Allied Topics, St. Louis, MO (May 2015). **Poster**
16. N. M. Lareau, **S. M. Stow**, J. C. May, E. Darland, R. T. Kurulugama, E. E. Rennie, J. C. Fjeldsted, J. A. McLean, *Mining Secondary Metabolites by HPLC Chip Cube and Ion Mobility-Mass Spectrometry*, 63rd American Society for Mass Spectrometry Conference on Mass Spectrometry and Allied Topics, St. Louis, MO (May 2015). **Poster**
15. T. M. Onifer, **S. M. Stow**, J. G. Forsythe, J. C. May, J. A. McLean, D. M. Hercules, *Structural Characterization of Isomeric Polymer Precursors by Electrospray Ion Mobility-Mass Spectrometry and Computational Strategies*, 63rd American Society for Mass Spectrometry Conference on Mass Spectrometry and Allied Topics, St. Louis, MO (May 2015). **Poster**
14. **S. M. Stow**, B. O. Bachmann, T. P. Lybrand, J. A. McLean, *Development and evaluation of a distance geometry protocol to generate conformations of natural products to structurally interpret ion mobility-mass spectrometry absolute collision cross sections*, The 66th Southeastern Regional Meeting of the American Chemical Society, Nashville, TN (October 2014). **Oral**
13. **S. M. Stow**, B. O. Bachmann, T. P. Lybrand, J. A. McLean, *Insight into Emerging Computational Techniques for Structural Ion Mobility-Mass Spectrometry*, Vanderbilt Institute of Chemical Biology 2014 Student Symposium, Nashville, TN (August 2014). **Poster**
12. **S. M. Stow**, J. G. Forsythe, T. M. Onifer, H. Nefzger, N. W. Kwiecien, J. C. May, D. M. Hercules, J. A. McLean, *Structural Characterization of Methylenedianiline Regioisomers by Ion Mobility-Mass Spectrometry, Tandem Mass Spectrometry, and Computational Strategies*, 62nd American Society for Mass Spectrometry Conference on Mass Spectrometry and Allied Topics, Baltimore, MD (June 2014). **Oral**
11. R. T. Kurulugama, A. Mordehai, N. Sanders, **S. M. Stow**, J. C. May, J. A. McLean, G. C. Stafford, J. C. Fjeldsted, *Evaluation of High Performance Ion Mobility – MS Platform for Structural Measurements in Different Drift Gases Combined with Computational Strategies*, 62nd American Society for Mass Spectrometry Conference on Mass Spectrometry and Allied Topics, Baltimore, MD (June 2014). **Poster**
10. T. M. Onifer, **S. M. Stow**, J. G. Forsythe, D. M. Hercules, J. A. McLean, *Structural Characterization of Polyurethane Precursors: Methylenedianiline Trimer and Tetramers*, The Pittsburgh Conference of Analytical Chemistry and Applied Spectroscopy (March 2014). **Poster**
9. **S. M. Stow**, J. G. Forsythe, C. R. Goodwin, J. C. May, D. M. Hercules, B. O. Bachmann, T. P. Lybrand, J. A. McLean, *Structure Prediction of Small Molecules From*

Ion Mobility Measurements Obtained Under Different Operating Conditions, Vanderbilt Institute of Chemical Biology 2013 Student Symposium, Nashville, TN (August 2013). **Poster**

8. T. M. Onifer, **S. M. Stow**, J. G. Forsythe, D. M. Hercules, J. A. McLean, *The Structural Characterization of Polyurethane Precursors: Methylenedianiline Trimer and Tetramers* Vanderbilt Institute of Chemical Biology 2013 Student Symposium, Nashville, TN (August 2013). **Poster**

7. **S. M. Stow**, C. R. Goodwin, M. Kliman, R. Kurulugama, E. Darland, B. O. Bachmann, T. P. Lybrand, J. A. McLean, *Distance Geometry: A Time Efficient Approach for Sampling Conformational Space in Support of Ion Mobility Structural Mass Spectrometry*, 61st American Society for Mass Spectrometry Conference on Mass Spectrometry and Allied Topics, Minneapolis, MN (June 2013). **Poster**

6. **S. M. Stow**, C. R. Goodwin, M. Kliman, B. O. Bachmann, T. P. Lybrand, J. A. McLean, *Using Distance Geometry in Support of Ion Mobility-Mass Spectrometry Data to Study the Conformational Space of Natural Products*, Aegis Sciences Corporation-Vanderbilt University Department of Chemistry Research Symposium, Nashville, TN (December 2012). **Oral**

5. **S. M. Stow**, C. R. Goodwin, M. Kliman, B. O. Bachmann, T. P. Lybrand, J. A. McLean, *Exploring the Conformational Space of Natural Products Using Distance Geometry and Ion Mobility-Mass Spectrometry*, Vanderbilt Institute of Chemical Biology 2012 Student Symposium, Nashville, TN (August 2012). **Poster**

4. **S. M. Stow**, C. R. Goodwin, M. Kliman, B. O. Bachmann, T. P. Lybrand, J. A. McLean, *Using Distance Geometry to Explore the Conformational Space of Natural Products in Support of Ion Mobility-Mass Spectrometry Data*, North America User Group Meeting and Conference, Montreal, QC Canada (June 2012). **Poster**

3. **S. M. Stow**, C. R. Goodwin, M. Kliman, B. O. Bachmann, T. P. Lybrand, J. A. McLean, *Exploring Conformational Space Using Distance Geometry and Other Computational Methods in Support of Ion Mobility-Mass Spectrometry Data*, 60th American Society for Mass Spectrometry Conference on Mass Spectrometry and Allied Topics, Vancouver, BC Canada (May 2012). **Poster**

2. **S. M. Stow**, C. R. Goodwin, M. Kliman, B. O. Bachmann, T. P. Lybrand, J. A. McLean, *Using Distance Geometry with Ion Mobility-Mass Spectrometry Data to Study the Conformational Space of Natural Products*, American Society for Mass Spectrometry Sanibel Conference on Mass Spectrometry Technologies for Structural Biology, St Pete Beach, FL (January 2012). **Poster**

1. M. Kliman, L. Xu, **S. M. Stow**, N. A. Porter, J. A. McLean, *Analysis of Human SLOS Fibroblast Cholesterol and 7-Dehydrocholesterol via Silver Sputtering Laser Desorption Ionization – Ion Mobility – Mass Spectrometry and Computational Modeling*, American

Society for Mass Spectrometry Sanibel Conference on Mass Spectrometry Technologies for Structural Biology, St Pete Beach, FL (January 2012). **Poster**

Teaching and Leadership Experience

Chemical Biology Association of Students Executive Board Member

Plan and host career development, volunteer, and social events for graduate students (2013-2015)

Vice President (2013-2014)

Secretary (2014-2015)

General Chemistry Tutor

Tutor for General Chemistry Students at UGA (2007)

Tutor for General Chemistry Students at Vanderbilt (2013)

Teaching Assistant

General Chemistry (August 2010 – May 2011)

Advanced Integrated Laboratory (August 2011 – May 2012)

Course Preparation

Advanced Integrated Laboratory (May 2011 – August 2011)

Awards

University of Georgia One UGA Diversity Scholarship

Four-year merit scholarship; value \$54,000

Student Travel Stipend for the 24th Sanibel Conference on Mass Spectrometry

Professional Membership

American Chemical Society

Member since May 2011

American Society of Mass Spectrometry

Member since January 2012

Volunteer Activities

Brentwood United Methodist Church

Volunteer Church Time Leader (October 2011 – May 2014)

Nashville Delta Delta Delta Alumnae Chapter

Volunteer for Local Philanthropic Events (August 2011 – Present)